Western University

Scholarship@Western

Electronic Thesis and Dissertation Repository

2-21-2020 2:30 PM

Incipient deformation of small volumes of fcc metals

Mahdi Bagheripoor, *The University of Western Ontario*

Supervisor: Klassen, Robert J., *The University of Western Ontario*
A thesis submitted in partial fulfillment of the requirements for the Doctor of Philosophy degree in Mechanical and Materials Engineering
© Mahdi Bagheripoor 2020

Follow this and additional works at: https://ir.lib.uwo.ca/etd

Part of the Computational Engineering Commons, and the Mechanics of Materials Commons

Recommended Citation

Abstract

In the area of mechanics of materials, the classic theories can not describe the material behaviour as the volume of deformation or sample size is small enough to be compared with the size scales of the imperfections of the crystal. So, there has been a great deal of interest in investigating the plasticity of micron and nano-sized materials, in the last 20 years. As a Ph.D. research project, the deformation mechanism at small scales of fcc metals is studied based on dislocations behaviour. The effect of main parameters that haven't been studied in detail, including, crystal orientation, pre-existing faults, grain boundaries, and free surface is considered. Atomistic simulation is used to investigate the deformation at nanoscales and experimental observation is used to tailor findings at the submicron scale.

The coupling effects of crystallographic orientation and internal structural defects on the load distribution at the onset of plasticity are investigated during Au nanoindentation to clarify the anisotropic characteristics of material responses to crystallographic orientation. In the absence of pre-existing defects, deformation is dominated by nucleation of Shockley partial dislocations regardless of crystal orientation. The relation of hardening and dislocation density shows that conventional Taylor hardening captures the plasticity after a certain amount of indentation depth in the presence of enough dislocation density. Indentation simulations in the presence of sessile dislocation loops in the structure show that the greatest reduction in the pop-in load happens for the [111] oriented sample. Indentation near a defect can lead to small, subcritical events that lead to a smoother "pop- in" at the onset of plasticity.

The influence of GB on the plasticity is mainly related to the misorientation angle, its intrinsic structure, and GB energy. Our simulation on various symmetric <110> tilt GBs with a wide range of misorientation angles show that high energy GBs affect the dislocation nucleation beneath the indenter and accommodate plasticity by providing the necessary dislocations to make the imposed deformation.

The simulation results of Au nanopillars show that the plasticity always starts with the nucleation of dislocations at the free surface and the crystal orientation affects the subsequent

microstructural evolution. The Schmid factor of leading and trailing partials plays a decisive role in leading to the twinning deformation or slip deformation. [100] oriented pillars deform by the glide of the twin boundary planes while [110] and [111] oriented pillars deform by the slip of stacking fault loops and planes. A significant difference is observed in the strength of pillars of the same size with different orientations. The power-law equation exponent is completely dependent on the crystal orientations and a week or no size effect is observed in the compression of [100] and [110] oriented Au pillars with sizes less than 40 nm. In the absence of free surface, the nucleation of initial dislocations happens in a much higher stress and trapping of dislocations in the pillar will result in the smooth increase of stress with strain.

Experimental micro-compression of sub-micron and micron-sized (0.7 – 3 μm) Au spheres at different strain rates showed an increase of yield stress with decreasing the sphere diameter (the yield point increases from 24MPa to 227Mpa for 3 µm and 0.7 µm spheres, respectively with a loading rate of 0.005mN/s). The apparent activation volume (V*) remains almost constant, ranging 1.6-2.4b^3 with changes of strain up to 20% for the smallest sphere while it ranges 8.6-10.6 b^3, 9.4-10.2 b^3, and 8.9-10.5 b^3 for the 1.5μm, 2.2μm, and 3μm diameter spheres respectively. These results indicate that the operative mechanism in the deformation of considered spheres is dependent on their size. Our obtained data for apparent activation volume (V*) and energy (Q*) suggest that the dislocation-obstacle limited glide mechanism is dominant or plays the main role in the deformation of larger spheres while the smallest sphere deformed by dislocation nucleation and starvation mechanism.

The force-displacement curves of the W and Al_2O_3 coated samples display a significantly higher strength than the non-coated samples. Analyses of the V* and Q* show a significant increase for the W coated samples than the noncoated ones. Values of apparent activation energy changed from 0.062-0.091 (eV) to 0.297-0.430 (eV) for the 0.7 µm spheres by having the W coating layer which reflects the activation of dislocation-obstacle mechanism in the coated layer samples and indicates the surface nucleation and exhaustion mechanism activation in the noncoated samples of 0.7 µm dimeter size.

Keywords

Summary for Lay Audience

The mechanical properties of materials change distinctly when specimen dimension changes to smaller than a few micrometers. With the continuing development of small-scale structures with small dimensions in the micron range, there is an impending need for understanding the fundamentals of plasticity at the micron and nanoscale. In the area of mechanics of materials, classic continuum-based theories describing the material behaviour become inaccurate when the deformation volume being considered is very small, on the size scale of the actual crystal imperfections. In this thesis, the operative deformation mechanisms of face-centered cubic (fcc) small-scale material volumes is studied using both laboratory experimentation and numerical atomistic-simulation. New data are presented on the effect of crystal orientation, pre-existing crystal defects, grain boundaries, and free surfaces on the operative mechanisms of dislocation nucleation and dislocation-obstacle interactions.

Co-Authorship Statement

The research presented in this thesis is composed of six manuscripts, Chapter two has now been published as a review paper in the Reviews on Advanced Material Science Journal, Chapter three has been submitted to Mechanics of Materials and is in the final stages of review, Chapters four and five were submitted to Computational Materials and International Journal of Plasticity and are presently in review. All of the manuscripts are co-authored by Mahdi Bagheripoor and Prof. Robert J. Klassen.

The simulations, experiments, analysis of data and manuscript preparation were performed by Mahdi Bagheripoor. Professor Klassen contributed by editing all the manuscript and, where necessary providing additional interpretation of data and suggestions for analysis.

Acknowledgments

I am overwhelmingly grateful to every person, organization, and institution that has supported this project. First and foremost, I like to express my sincere gratitude to Professor Robert J. Klassen for providing me with this opportunity and for all his guidance, supports, and ideas provided throughout this project. Without his help, the successful completion of this thesis and the quality of work achieved would not have been possible. His willingness to give time and feedback so generously is very much appreciated. I also wish to thank my advisory committee, Prof. Andy Sun and Prof. Liyang Jiang for their guides, useful feedbacks, supports and valuable time during my Ph.D. program.

I like to thank the great computing facility of Compute Canada. The completion of this project was not possible without using the sources of Compute Canada. I wish to thank the great staff of Western Nanofabrication Facility for helping us to fabricate the micro compression samples. I also wish to thank Dr. Yang Zhao from Prof. Sun's group for helping us to coat our samples with ALD and MLD techniques. I like to express my thanks to National Sciences and Engineering Research Council of Canada (NSERC) Discovery Grant for financially supporting this project.

In particular, I wish to thank my parents and loving family members for their support and encouragement throughout my study. In addition, my close friends, colleagues and classmates for shaping an amazing graduate student experience. I look forward to reflecting on our experiences with each other in the future.

Table of Contents

List of Tables

List of Figures

Nomenclature

Symbols	Definition
σ	Flow stress
σ_y	Yield strength
ε_p	Plastic strain
n	Work hardening exponent
m	Strain rate sensitivity constant
Q	Thermal activation energy
R	Boltzmann constant
T	Temperature
τ_{CRSS}	Critical resolved shear stress
b	Burgers vector
k_S	Anisotropic shear modulus
ρ_{tot}	Total dislocation density
$\bar{\lambda}_{max}$	Statistical average length of the weakest single-arm dislocation source
ε_p	Engineering plastic strain
P	Indentation force
h	Indentation depth
R	Indenter radius
$E*$	Reduced elastic modulus
υ	Poisson's ratio
a_c	Contact radius

R_{pl}	Radius of the hemispherical plastic zone
λ	Total dislocation line length
ρ	Dislocation density
H	Hardness
μ	Shear modulus
α	Empirical constant
γ_{GB}	Grain boundary energy
γ_{utf}	Unstable twin-fault energy
γ_{usf}	Unstable stacking fault energy
γ_{sf}	Stacking fault energy
m_L	Schmid factor for leading partial
m_T	Schmid factor for trailing partial
V^*	Apparent activation volume
k	Boltzmann's constant
τ_{0K}	Athermal stress
Q^*	Apparent activation energy

Abbreviations	Definition
FCC	Face centered cubic
BCC	Body centered cubic
HCP	Hexagonal close packing
MD	Molecular dynamics
GB	Grain Boundary
ALD	Atomic layer deposition
MLD	Molecular layer deposition
ISE	Indentation size effect
AFM	Atomic force microscopy
SEM	Scanning electron microscopy
TEM	Transmission electron microscopy
NEMS	Nano electro-mechanical systems
MEMS	Micro electro-mechanical systems
DS	Dislocation Starvation
SAD	Single arm dislocations
FIB	Focused ion beam
DD	Dislocation dynamics
SAS	Single arm source
SPD	Shockley partial dislocation

SFT	Stacking fault tetrahedron
LAMMPS	Large-scale Atomic/Molecular Massively Parallel Simulator
EAM	Embedded-atom method
CNA	Common neighbor analysis
DXA	Dislocation extract algorithm
OVITO	Open visualization tool
FEM	Finite element method
CG	Conjugate gradient
SF	Stacking fault
CLS	Confined layer slip
TB	Twin boundary
TPS	Twin partial slip
GND	Geometrically necessary dislocation
DT	Deformation twinning
DS	Dislocation slip
PMMA	Polymethyl methacrylate

Chapter 1

1. Introduction

1.1. Overview

The mechanical properties of materials change distinctly when the volume of deformation or specimen dimension changes to smaller than a few micrometers. With the continuing development of small-scale structures with small dimensions in the micron range, there is an impending need for understanding the fundamentals of plasticity at the micron and nanoscale. Mechanical tests at small scales are difficult to perform, but they provide guidance to develop new technologies and new theories of plasticity. Intrinsic size scale effects, resulting from internal microstructural features, are often utilized to improve a material's bulk mechanical properties (for example, Hall-Petch hardening) [1, 2]. In contrast, extrinsic length scale effects resulting from, for example, micrn-scale size of a deforming sample have, until recently, been largely overlooked in research.

In the category of extrinsic length scale dependence, the first work on assessing the mechanical properties of small, sub-micrometer size, material samples was performed on thin metal whiskers with diameters of ~100 μm was performed by Herring and Galt [3] more than 50 years ago. Other experiments have repeatedly indicated that metallic materials display a strong size effect at the micron and sub-micron scales. Increasing the micro-indentation hardness of metallic materials (e.g., aluminum, silver, copper, tungsten) has been reported as the indentation depth decreased to microns and sub-micron [4-11]. Fleck et al. [12], reported increase of plastic work hardening in micro torsion tests of thin copper wires with decreasing the wire diameter from 170 to 12 μm. Stolken and Evans [13] observed a significant increase in work hardening in micro bending tests of micron thick nickel foils and similar results have been obtained by Haque and Saif [14], in bending sub-micron thick aluminum beams. These size effects have been attributed to geometrically necessary dislocations associated with non-uniform plastic deformation. Plastic flow in bulk specimens results from the collective behavior of a large, and increasing, number of dislocations. In recent years, many studies have been done to analyze this behavior in small, submicron size, samples by the extrapolation of laws

established for statistically homogeneous samples, e.g. the Taylor hardening or the Schmid law. So, the existence of a material length scale for plasticity is now completely supported by direct dislocation simulations and by many types of laboratory experiments: micro-torsion, -bending, -compression, etc [15].

To describe material behaviour at small length scales, Greer et al. [16] explained the exceptionally high strength of micro-pillars based on the concept of dislocation starvation. Benzerga and Shaver [17] used a mesoscopic plasticity model to capture the size-dependence of flow strength in micro-pillars. Parthasarathy et al. [18] proposed the same idea. According to these pioneering works on revealing the plasticity mechanism of small scale material, currently there are two generally accepted explanations. One is the dislocation starvation model, which describes that increase of flow stress in small samples results from a loss of dislocation sources by quick surface annihilation [19]. The other is the dislocation source truncation model, which says that the smaller samples contain shorter sources that require higher flow stress to activate [18, 20].

1.2. Scope and Objectives

The aim of this study is to use nanomechanical testing and numerical simulation techniques to understand the mechanisms of small scale plastic deformation of face center cubic (fcc) crystal structure metals. The objectives of this study are as follows;

Molecular Dynamics (MD) modeling will be used to explore the coupled effects of crystallographic orientation, and pre-existing crystal defects on the operative deformation mechanisms during nanoindentation of Au. A general view of the defect generation mechanisms and its evolution during the nanoindentation will then be proposed. The onset of plasticity and its evolution will be analyzed by quantifying dislocation density and identifying the dislocation evolution mechanisms. The validity of conventional continuum mechanic work hardening theory; i.e. Taylor hardening model, which has not been previously studied with full atomistic detail, and the effect of orientation on the hardening model will be investigated.

The correlation of Grain Boundary (GB) structure and properties with local small scale plasticity will be studied by analyzing interaction of lattice nucleated dislocations with various GB structures over a wide range of GB energy levels.

Molecular dynamics simulation of the deformation of compressed Au and Pt nanopillars will then be studied to further investigate the effect of the crystal orientation and proximity to free surfaces on the developments of crystal defects during deformation.

Laboratory experimentation, involving compression of single- and poly-crystalline Au micro-spheres of 700 nm to 3 µm diameter will be undertaken to obtain direct experimental characterization of the operative small-scale deformation process. Analysis of the resulting apparent activation volume and activation energy of the deformation process will provide to clues to the details of operative plastic deformation mechanisms at the micron and submicron length scales for these Au samples. Furthermore, Au microspheres that have been coated with thin W and Al_2O_3 constraining layers are also tested in compression to gain a better understanding of the effect of extrinsic surface constraint on the length-scale mechanisms of plastic deformation.

1.3. Structure of the Thesis

The structure of this thesis is based on the Integrated Format of the school of Graduate and Post-graduate studies (SGPS) at The University of Western Ontario, ON, Canada. It includes eight chapters, five of which are simulation results and experimental research papers, investigating the dominant mechanisms of small scale plasticity of FCC metals and their affecting parameters.

Chapter two of this thesis presents a review of the relevant previously published information, experimentally-based and numerical simulation-based, related to the unique properties obtained by the small scale deformation of materials. It covers the existing information in the literature about the dislocation nucleation and defect structure development during the nanoindentation of fcc metals and compression of small-sized materials. It also provides information about the current small scale deformation experimental testing technique and possible simulation methods. A modified version of

this chapter has been published as a review paper in Reviews on Advanced Materials Science Journal [21].

Chapter three of the thesis quantifies the initial plastic deformation mechanisms of gold as a model face-centered cubic (fcc) metal in the nanoindentation process using molecular dynamics simulation. It investigates the coupling effects of crystallographic orientation and internal structural defects on the resulting load distribution at the onset of plasticity. A part of this chapter has been presented in the 30th Canadian Material Science Conference, Edmonton, Canada, June 2018; and Canadian Society for Mechanical Engineering (CSME) Congress, London, Canada, June 2019.

Chapter four discusses MD simulations of the effect of grain boundaries on the incipient plasticity associated with small scale deformation. It analyses a wide range of misorientation angles and GB energies and studies the relation of GB structure and energy with its role as a source of dislocation nucleation. It also describes the effect of the GB distance from the indentation surface on the deformation mechanism. A part of this chapter has been presented in the 31st Canadian Materials Science Conference, Vancouver, Canada, June 2019.

Chapter five presents MD simulations of the effect of free surface on the dislocation behavior and deformation mechanisms of small-sized samples. It investigates the operative deformation mechanisms at different crystal orientations of Au and Pt nanopillars of various diameters and also considers the effect of the constraining surface layers on their deformation. A part of this chapter has been presented in the Materials Science & Technology Conference, Columbus, USA, October 2018.

Chapter six contains experimental results and analyses of Au submicron and micron-sized sphere compression. The spheres tested were of diameter ranging between 700 nm to 3 μm. The experiments were performed at various ranges of strain rate and thus allow calculation of the apparent activation volume and activation energy of the deformation process for the different sizes of spheres.

Chapter seven presents the results of the deformation of microspheres which are coated with a thin, 80 nm, Al_2O_3 or W constraining layer. These layers are deposited on the micro-spheres by three techniques, Atomic Layer Deposition (ALD) and Molecular

Layer Deposition (MLD) and Ar+ sputtering. The resulting apparent activation volume and energy values for the coated spheres are compared with those obtaine from similar uncoated Au spheres (Chapter 6) to deduce the effect of surface constraint on the operative deformation mechanisms.

Chapter 8 presents a discussion of all the results of the previous chapters and arrives at a final conclusion on the dominant plasticity mechanisms of samples that are in the micron and submicron length scale and the effect of microstructural properties on theses mechanisms.

1.4. Contributions

While recent experimental tests and numerical simulations have achieved significant results in understanding the length-scale dependence of the mechanical deformation of metals, there are still unanswered questions related to the effect of crystal condition on the incipient plastic deformation process and the evolution of dislocations in the early stages of small scale plasticity. This project explores the coupled effects of crystallographic orientation and pre-existing structural defects on the distribution of pop-in loads and deformation mechanisms during the nanoindentation of Au. A general view of the defect generation mechanisms and its evolution during the nanoindentation is provided. The validity of conventional continuum mechanic work hardening theory; i.e. Taylor hardening model, which has not been previously studied with full atomistic detail, and the effect of orientation on the hardening model is investigated for nanoindentation.

Published studies have revealed that the mechanical behavior and deformation mechanisms are mainly related to the GB structure and various scholars have focused their studies on a certain geometry of GB. Moreover, most of the atomistic studies on the effect of GB on deformation mechanisms are limited to the tensile tests without local deformation and interaction of lattice dislocation with GB. Therefore, the role of the GB on the local deformation and the complex interaction of lattice dislocations and GB geometry is still not fully studied. In this study, the correlation of GB structure and properties with local small scale plasticity is studied by analyzing the interaction of lattice nucleated dislocations with various GB structures over a wide range of GB energy levels. The results lead to an understanding of the role of GBs as the internal sources of

dislocation nucleation on the small scale deformation mechanisms based on the GB energy levels.

Although different theories have been proposed to explain the plasticity of sub-micron and nanoscale samples, a clear understanding of the effect of crystal orientations combined with free surface is still missing. Moreover, most of the conducted experiments are on the FIB machined samples which have some initial dislocation density imparted by the FIB milling process. In this study, the effect of the crystal orientation and free surface are investigated focusing on the changes in the dislocation density and stress and development and movements of the crystal faults. Based on the results the Schmid factor of leading and trailing partials plays a decisive role in leading to the twinning deformation or slip deformation. [100] oriented pillars deform by the glide of the twin boundary planes while [110] and [111] oriented pillars deform by the slip of stacking fault loops and planes. A significant difference is observed in the strength of pillars of the same size with different orientations. For the first time, it is described that the power-law equation exponent is completely dependent on the crystal orientations and a week or no size effect is observed in the compression of [100] and [110] oriented Au pillars with sizes less than 40 nm. The results of the compression of pillars with rigid constraining layers show that in the absence of free surface the nucleation of initial dislocations happens in a much higher stress and trapping of dislocations in the pillar will result in the smooth increase of stress with strain.

Current analyses of thermal and energy activation mechanisms of micron and sub-micron samples are limited to a low range of strain rates. In this study, micro-compression of micron and submicron spheres are performed on a wide range of strain rates which will result in a more accurate analysis of the apparent activation energy and thus better understanding of the deformation mechanisms of micron and sub-micron scales. Moreover, the deposition of the constraining layer of Al_2O_3 and W on the spheres in this study has resulted in a better understanding of the effect of free surface on the dominant small scale plasticity mechanisms.

References

[1] E.O. Hall, The Deformation and Ageing of Mild Steel .3. Discussion of Results, P Phys Soc Lond B 64(381) (1951) 747-753.

[2] N.J. Petch, The Cleavage Strength of Polycrystals, J Iron Steel I 174(1) (1953) 25-28.

[3] J.K. Galt, C. Herring, Elastic and Plastic Properties of Very Small Metal Specimens, Phys Rev 86(4) (1952) 656-656.

[4] M.S. Deguzman, G. Neubauer, P. Flinn, W.D. Nix, The Role of Indentation Depth on the Measured Hardness of Materials, Thin Films: Stresses and Mechanical Properties Iv 308 (1993) 613-618.

[5] N.A. Stelmashenko, M.G. Walls, L.M. Brown, Y.V. Milman, Microindentations on W and Mo Oriented Single-Crystals - an Stm Study, Acta Metallurgica Et Materialia 41(10) (1993) 2855-2865.

[6] Q. Ma, D.R. Clarke, Size-Dependent Hardness of Silver Single-Crystals, J Mater Res 10(4) (1995) 853-863.

[7] W.D. Nix, Elastic and plastic properties of thin films on substrates: nanoindentation techniques, Mat Sci Eng a-Struct 234 (1997) 37-44.

[8] K.W. McElhaney, J.J. Vlassak, W.D. Nix, Determination of indenter tip geometry and indentation contact area for depth-sensing indentation experiments, J Mater Res 13(5) (1998) 1300-1306.

[9] R. Saha, Z.Y. Xue, Y. Huang, W.D. Nix, Indentation of a soft metal film on a hard substrate: strain gradient hardening effects, J Mech Phys Solids 49(9) (2001) 1997-2014.

[10] N.I. Tymiak, D.E. Kramer, D.F. Bahr, T.J. Wyrobek, W.W. Gerberich, Plastic strain and strain gradients at very small indentation depths, Acta Mater 49(6) (2001) 1021-1034.

[11] J.G. Swadener, E.P. George, G.M. Pharr, The correlation of the indentation size effect measured with indenters of various shapes, J Mech Phys Solids 50(4) (2002) 681-694.

[12] N.A. Fleck, G.M. Muller, M.F. Ashby, J.W. Hutchinson, Strain Gradient Plasticity - Theory and Experiment, Acta Metall Mater 42(2) (1994) 475-487.

[13] J.S. Stolken, A.G. Evans, A microbend test method for measuring the plasticity length scale, Acta Mater 46(14) (1998) 5109-5115.

[14] M.A. Haque, M.T.A. Saif, Strain gradient effect in nanoscale thin films, Acta Mater 51(11) (2003) 3053-3061.

[15] H.J. Gao, Y.G. Huang, Geometrically necessary dislocation and size-dependent plasticity, Scripta Mater 48(2) (2003) 113-118.

[16] J.R. Greer, W.C. Oliver, W.D. Nix, Size dependence of mechanical properties of gold at the micron scale in the absence of strain gradients, Acta Mater 53(6) (2005) 1821-1830.

[17] A.A. Benzerga, N.F. Shaver, Scale dependence of mechanical properties of single crystals under uniform deformation, Scripta Mater 54(11) (2006) 1937-1941.

[18] T.A. Parthasarathy, S.I. Rao, D.M. Dimiduk, M.D. Uchic, D.R. Trinkle, Contribution to size effect of yield strength from the stochastics of dislocation source lengths in finite samples, Scripta Mater 56(4) (2007) 313-316.

[19] J.R. Greer, W.D. Nix, Nanoscale gold pillars strengthened through dislocation starvation, Phys Rev B 73(24) (2006).

[20] R. Beanland, Dislocation Multiplication Mechanisms in Low-Misfit Strained Epitaxial Layers, J Appl Phys 77(12) (1995) 6217-6222.

[21] M. Bagheripoor, R. Klassen, Length Scale Plasticity: A Review from the Perspective of Dislocation Nucleation, Rev Adv Mater Sci 56(1) (2018) 21-61.

Chapter 2

2. Review of the relevant literature

The mechanical properties of materials change distinctly when specimen dimension changes to smaller than a few micrometers. With the continuing development of small-scale structures with small dimensions in the micron range, there is an impending need for understanding the fundamentals of plasticity at the micron and nanoscale. Mechanical tests at small scales are difficult to perform, but they provide guidance to develop new technologies and new theories of plasticity. Size scale effects because of the internal microstructural features are observed and are often utilized to improve bulk properties (Hall-Petch hardening) [1, 2]. In contrast, size scale effects because of the physical geometry of a sample have been overlooked, especially for samples smaller than 100 μm.

In this category, the first work on small scales (thin metal whiskers with diameters of ∼100 μm) was performed by Herring and Galt [3] more than 50 years ago. Other experiments have repeatedly indicated that metallic materials display a strong size effect at the micron and sub-micron scales. Increasing the micro-indentation hardness of metallic materials (e.g., aluminum, silver, copper, tungsten) has been reported as the indentation depth decreased to microns and sub-micron [4-11]. Fleck et al. [12], reported increase of plastic work hardening in micro torsion tests of thin copper wires with decreasing the wire diameter from 170 to 12 μm. Stolken and Evans [13] observed a significant increase in work hardening in micro bending tests of micron thick nickel foils and similar results have been obtained by Haque and Saif [14], in bending sub-micron thick aluminum beams. These size effects have been attributed to geometrically necessary dislocations associated with non-uniform plastic deformation. Plastic flow in bulk specimens results from the collective behavior of a large, and increasing, number of dislocations at a sufficiently large density. In recent years, many studies have been done to analyze this behavior which has been caused by specimen size reduction and describe it by extrapolating systematically laws established for statistically homogeneous samples, e.g. Taylor hardening or Schmid law, downing to the micron-scale. So, the existence of a material length scale for plasticity is now completely supported by direct dislocation

simulations and by four kinds of laboratory experiments: micro-torsion, micro-bending, particle-reinforced metal-matrix composites and micro-indentation hardness tests [15].

To describe material behaviour in the small scale, Greer et al. [16] explained the exceptionally high strength of micro-pillars based on the concept of dislocation starvation. Benzerga and Shaver [17] used a mesoscopic plasticity model to capture the size-dependence of flow strength in micro-pillars. Parthasarathy et al. [18] proposed the same idea. According to these pioneering works on revealing the plasticity mechanism of small scale material, currently, there are two generally accepted explanations. One is the dislocation starvation model, which describes that increase of flow stress in small samples results from a loss of dislocation sources by quick surface annihilation [19]. The other is the dislocation source truncation model, which says that the smaller samples contain shorter sources that require higher flow stress to activate them [18, 20].

2.1. Micro and nanoscale flow behaviour

2.1.1. Small scale plasticity

Mechanical behaviour of materials has the main importance in materials science and applied mechanics and has been a subject of interest for a long time. Therefore, many theories have been developed to describe the material behaviour. However, the mechanical response based on the classical continuum plasticity models are size-independent. Recent studies on small scale materials and small-scale deformation showed that the mechanical properties can change significantly when the scale of deformation or the specimen size is in the range of sub-micron and nano scales. Based on the recent observations, the material strength increases when the only a small volume is under strain or the structure size is small. The term "size effect" is generally used to cover mechanical properties related to the scale of deformation. One of the scale dependent phenomena is the yield or flow stress increase which is observed when the sample size or the deformation volume is small as the micrometer or nanometer scales. It is accepted that such scale-dependent changes in strength are due to particular deformation mechanisms that can only be observed when the specimen dimensions exceed the normal spacing of the dislocation and when a limited number of defects influence the plastic deformation.

One of the important size-dependent behaviour is observed in nanoindentation testing when the hardness is dependent to the depth of indentation, resulting to indentation size effect (ISE). Figure 2.1 shows the size effect observed for several nanoindentation experiments in the literature in which the hardness increases as the indentation depth decreases [21]. H_0 in Figure 2.1 is the value of hardness at large indentation depths where the hardness becomes independent of the indentation depth. A lot of research has addressed this issue in order to establish a relationship between the decreasing hardness and the thin film structures. Nix and Gao [22] established a law on strain gradient plasticity to explain these effects based on the concept of copper geometrically required dislocations.
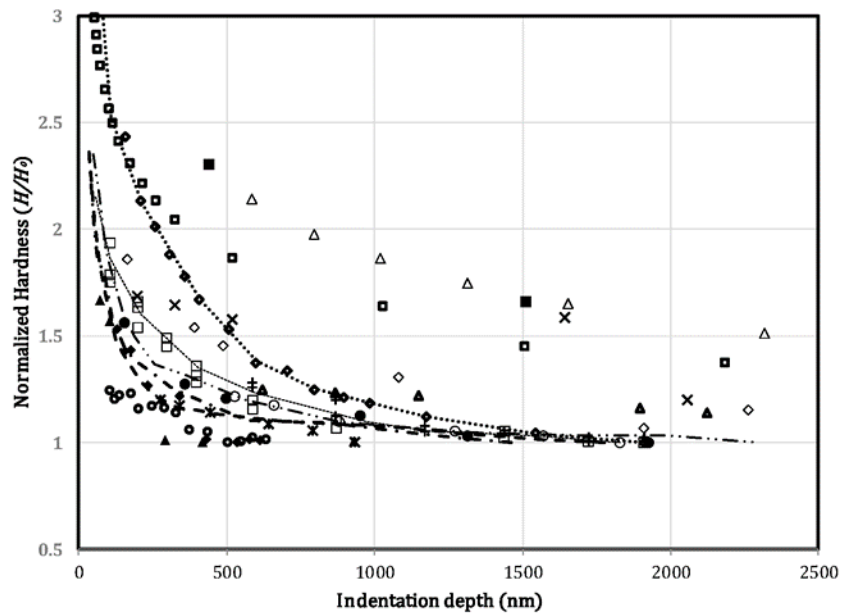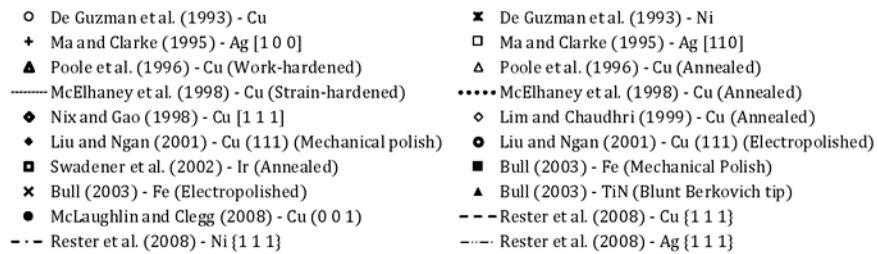
Figure 2.1: Size effect during nanoindentation [21].

Nix and Gao model on the small scale plasticity [22] is based on two assumptions . The first assumption is that the indentation is accommodated by the geometry necessary dislocation loops with Burgers vectors normal to the plane of indentation. Second assumption is that the geometry necessary loops remain in the hemispherical plastic volume defined by the contact radius (Figure 2.2).
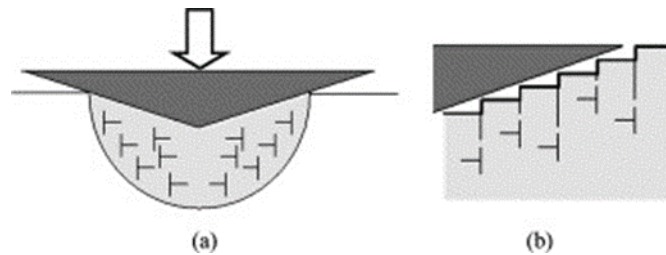
Figure 2.2: Geometrically necessary dislocations underneath an indenter, b) Detailed view of the deformation and associated GNDs on the atomic level [23].

2.1.2. Plasticity of small scale materials (effect of the free surface)

For typical face-centered cubic (FCC) metals like Ag, Au, Cu, Ni and Al with various stacking fault energy values (~22, ~45, ~78, ~128 and ~166 mJ/m^2, respectively) [24], it was found that when the sample size is reduced to nano-scale, the mechanical properties such as yield strength and plasticity would both increase [19, 24-26].

As the first example, stress-strain curves of [111] Ni pillarhs with diameters ranging from 165 nm to 2 μm is presented in Figure 2.3 [27]. Two interesting observations can be found from these curves. The first one is the evolution of the yield strength during compression as a function of the micropillar diameters. The second observation seen from the compression of micropillars (Figure 2.4) is that all curves display fast transients of strain during compression, i.e., rapid bursts of strain separated by elastic loading segments [27]. Uniaxial compression stress strain curves obtained by deforming micropillars of as-rolled martensitic steel with various diameters are shown in Figure 2.4 a and b. The stress–strain curves in Figure 2.4 a are for pillars that equal or bigger than 2 μm in diameter whereas those presented in Figure 2.4 b correspond to submicron pillars. In Figure 2.4 a, micropillars 1 and 2 (diameter of 2.0 μm) begin yielding at 1200 MPa and show elastic–nearly perfectly plastic behavior. Micropillars 3 and 4, which have

diameters of 3.6 µm and 2.8 µm, respectively, display a slightly higher proportional limit but pronounced hardening [28]. Stress–strain curves of Ta and W micropillars compression are depicted in Figure 2.5 a and b, respectively [29]. The stress–strain curves of the micropillars with diameters larger than 2 µm are continuous, while, for diameters between 500 nm and 1 µm, the loading curves showed pronounced stress drops along the whole strain range, indicating that the stress–strain behavior became more stochastic as the diameter decreases. The most acceptable description of this behavior is the reduction of the number of available dislocation sources as sample size decreases [29].

As it is seen in all of the presented graphs, the material strength is increased significantly in small scale and because of their size which includes less dislocation density than the bulk materials, a great amount of studies have been done to investigate their plasticity and deformation mechanisms. In the following some of the theories will be reviewed briefly.
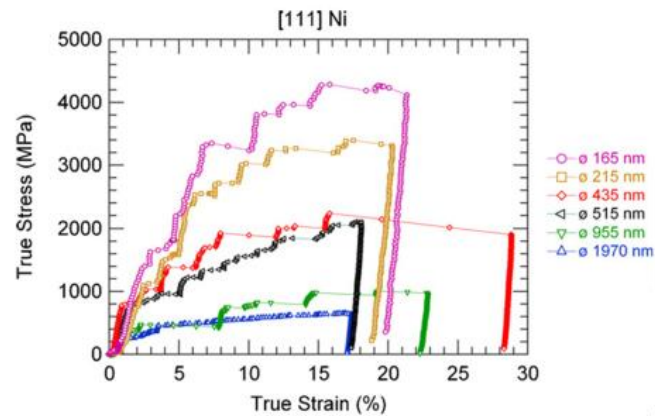
Figure 2.3: Stress-strain curves for [111] Ni pillars of different diameters [27]**.**
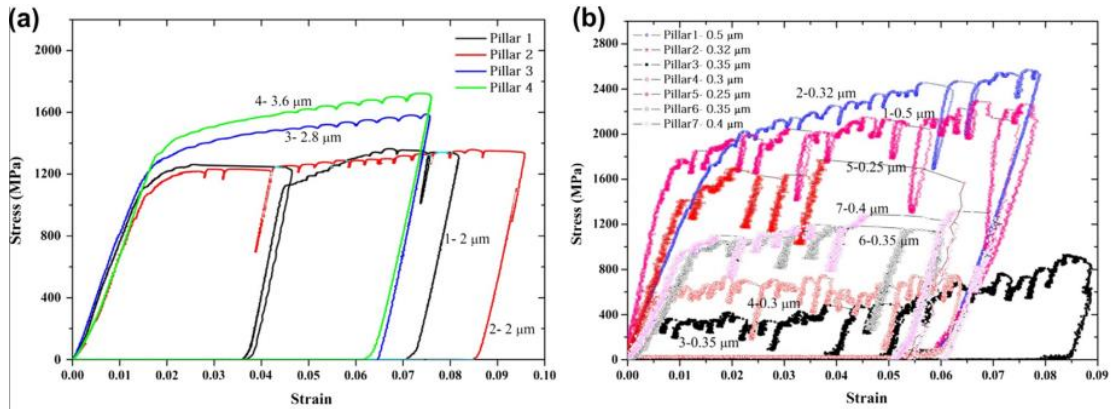
Figure 2.4: Micropillar compression stress–strain curves for the as-rolled martensitic steel (a) diameters >1 µm, (b) diameters <1 µm [28].
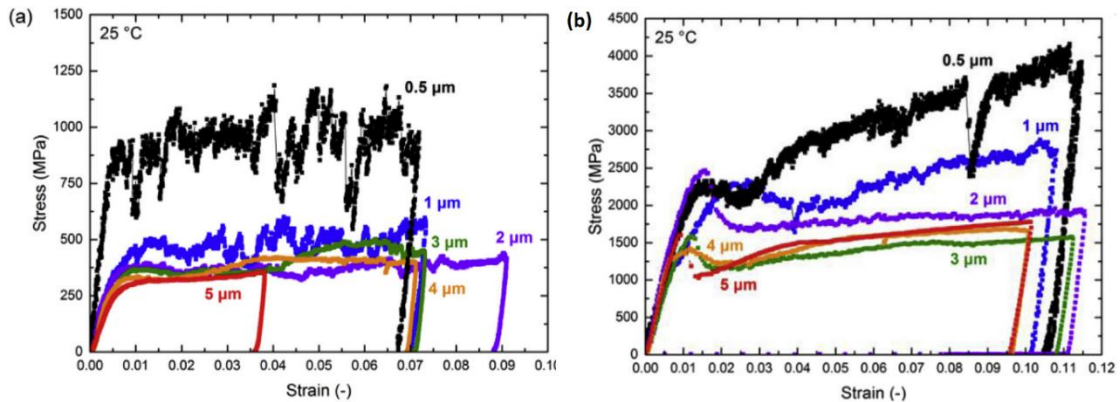
Figure 2.5: Typical compressive stress–strain curves of different micropillars with diameters ranging from 0.5 to 5 µm tested at different temperatures (a) Ta, (b) W [29].

2.2. Micro compression test

A various range of methods has been used to study the mechanical properties of materials. For the nanomechanical properties, the possibility of using all these methods is reduced because of either technical or monetary reasons. The methods that have been applied to study nano or small scale mechanics are as follows: nanoindentation [30], uniaxial compression [31], uniaxial tension [32], three/four-point pressing [33], the plane-strain bulge test [34]. Some of these techniques are shown in Figure 2.6. All these methods should presumably lead to the same conclusion about a certain property. However, there are some properties that cannot be studied by all of the mentioned

methods. For example, the yield strength cannot be determined by nanoindentation. The physical property of the sample is another factor that limits the applicable tests, nanoindentation can not be applied on graphene since there is no thickness for graphene to be penetrated. Moreover, there is some inaccuracy with experimental condition. For example, nanoindantation with sharp tips introduces a nonuniform distribution of the mechanical strains or strain gradients within the contact area. The cost of the experiments is another factor that limits the available techniques for studying material properties at the nano scale. For instance, uniaxial tensile test of nanopillars is very costly and requires more complicated procedure in sample fabrication and experimental testing [35].
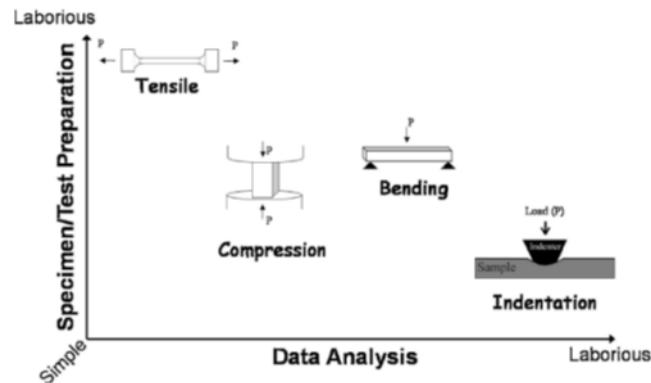
Figure 2.6: Different mechanical testing methods for micron to sub-micron length samples [36].

In light of the above factors, the most common technique for exploring nanoscale mechanical properties with the fewest limitations and drawbacks – especially that of the presence of strong strain gradients –is the uniaxial compressive loading of cylindrical nanopillars which was first introduced in 2004 by Uchic et al. [26] for compression of microsized pillars, and later extended to the nanoscale compression in 2005 by Greer et al. [16]. In these test, mimicking the bulk compression experiment, compression is applied using a diamond flat punch which could be controlled by a nanoindentation pendulum or an AFM tip, and the load displacement curve is simultaneously drawn as the pillar or particle compresses [31, 35]. Advent of higher resolution testing equipment, has made it possible to continuously control and monitor the indenter loads and

displacements as it is driven into and withdrawn from a sample material in nano indentation test [36]. This expands the capabilities of the traditional hardness testing method and can potentially produce very reliable measurements of stress–strain curves from fairly small indentation depths and recently, a variant on nanoindentation has been developed which is called micropillar compression. In this technique, a nanoindenter with a flat punch is used to compress a small cylindrical volume (1µm diameter by 2µm length cylinders) to obtain a uniaxial stress-strain behavior (Figure 2.7) [37]. The popularity of indentation tests is because of its versatility, ease of use and its potential for high throughput. This is the most currently used methods for interrogating the local mechanical properties at micron and sub-micron length size that rely largely on testing miniaturized samples in homogeneous deformation modes [36].
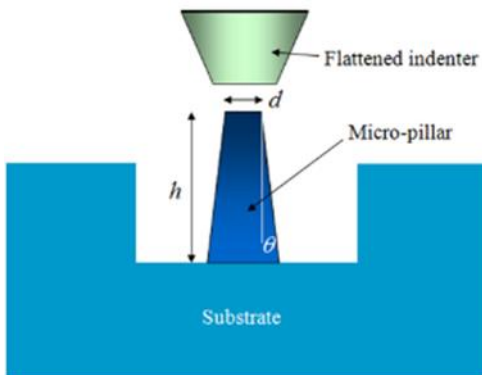
Figure 2.7: Schematic of the micro-pillar compression test [37].

Nanoindentation or instrumented indentation is a technique, appeared in the early 1980s and consists in measuring the force and displacement of a hard tip forced into the material. The load and displacement are measured through a change in capacitance between a reference and a movable electrostatic plate attached to the tip [38, 39]. Oliver and Pharr [40], who have played a leading role in presenting models for quantitative nanoindentation, have presented a general overview of the development and recent advances of nanoindentation techniques [40]. In situ nanoindentation was reviewed in 2006 by Schuh [41], in which an excellent overview of in situ techniques with particular emphasis on technological advancements was provided. Nili et al. [42] traced developments and pinpoints significant recent advances, with emphasis on the

applications of in situ nanoindentation techniques to materials systems, and highlighting the new insights gained from these in situ techniques.

Recently and with the advancement of technology, nanoindentation has been combined with different microscopic techniques to make it possible to observe material behavior during the deformation and investigate active mechanisms while the experiment is doing and in situ experimentation has gained significant attention due to its ability to enhance material characterization. Performing nanomechanical tests inside of a microscope device with real-time imaging, elucidate the specific deformation mechanisms that occur, as well as its occurrence time, and thus allows us a better understanding of the material's properties and overall performance [42, 43].

As Ghisleni et al. [44] pointed out, the main advantage of in situ SEM indentation techniques is the continuous observation of the surface deformation during the application of an external load on the specimen surface by an indenter. The large field of view, which helps to locate the feature of interest, and the submicron precision positioning allowed by the high magnification available through the SEM are the other advantages of doing nanoindentation in SEM instrument [44]. By performing the nanoindentation experiments in situ with a SEM instrument, one can observe how the specimen deforms under an applied load, which allows correlating the variation in the load-displacement curves to the variation in the specimen's topography. In particular, the influence of coating failure such as delamination, crack formation and propagation [45-48], and surface shear band formation [49-52] can be correlated to a single discontinuity in the load-displacement data. Figure 2.8 shows the Greer group's [53] in situ mechanical tester, SEMentor, in which the dynamic contact module (DCM) of the nanoindenter (Agilent Corp., Oak Ridge, TN, USA) inserted into a free port in the SEM (FEI Quanta 200, FEI Company, Hillsboro, OR, USA) and equipped with a custom-fabricated conductive diamond tension/compression grips. Instrumentation companies like Hysitron, has provided PicoIndenters that could be installed on the SEM and used for in situ mechanical testing. However, even though in situ SEM indentation can observe the deformation on the surface of the indented specimen, some physical phenomena that

might take place underneath the surface such as phase transformation, or nucleation and propagation of dislocations are hardly visible by SEM observation.
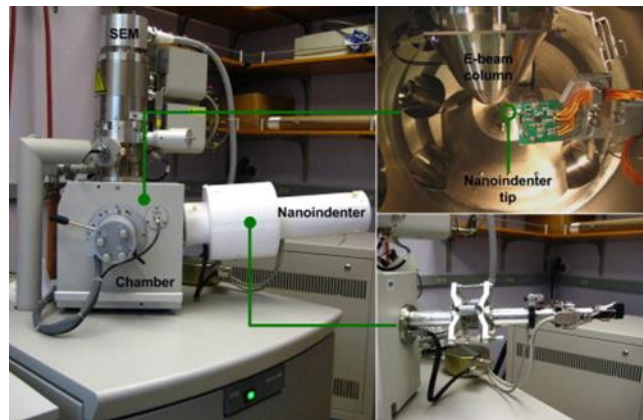
Figure 2.8: Pictures of the SEMentor (SEM + Nanoindenter) and the inside of chamber [53].

Lee et al [54, 55], developed an in-situ cryogenic nanomechanical testing system by combining the nanomechanical tester (InSEMTM, Nanomechanics, inc), SEM (Quanta, FEI), and cryogenic systems (Janis Research Company, LLC), to study small-scale mechanical behavior of materials at low temperatures. Figure 2.9 shows the schematic diagram of cryogenic system consisting cold finger, Si-diode temperature sensors, joule heaters, radiation-shielded oxygen-free high thermal conductivity copper (OFHC) lines, vacuum shielded coolant transfer line, the liquid nitrogen dewar, and temperature controller [54].
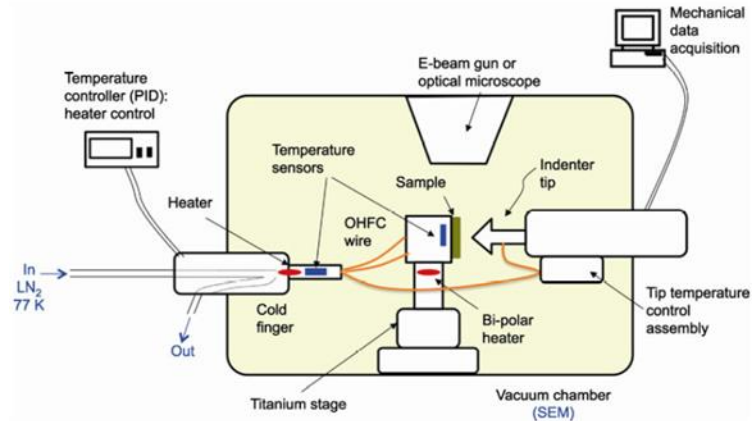
Figure 2.9: Schematic diagram of an in-situ nanomechanical tester integrated with the cryogenic system [54].

Following early load sensor integration developments, in situ TEM mechanical testing with quantitative load measurement including mechanical probing modes such as nanoindentation expanded toward commercialization in the last decade [56]. These developments are particularly useful for conducting size effects experiments, whereby quantitative in situ TEM mechanical testing is an ideal tool for studying the origin and principles of the material deformation through dislocation and twining observation. Figure 2.10 shows some the of involved deformation mechanisms in size effects which can be studied by in situ TEM.
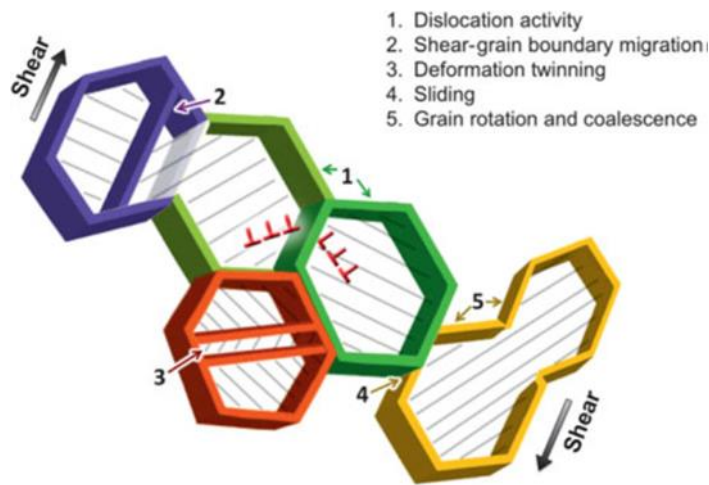
Figure 2.10: Schematic of various deformation mechanisms that can be studied by in situ TEM mechanical testing [56].

Various approaches of mechanical testing inside a TEM exist today. They span from using TEM holders with a simple mechanical actuation to elaborated testing units that fit inside the pole pieces. From 2003 to 2005, Hysitron® and Nanofactory Instruments AB® companies further implemented the indenting holders by adjoining them with a micro load cell [57].

In recent years, nanoindentation, AFM, MEMS-based testing device and scanning tunneling microscope [58] probe were integrated with the TEM platform [56, 57, 59]. In situ mechanical testing via nanoindentation, AFM and MEMS device have revealed novel deformation phenomena and size-dependent responses in nano-sized materials [31, 60-64]. Different holder setups have been developed based on the desired mechanical test and sample geometry (Figure 2.11).
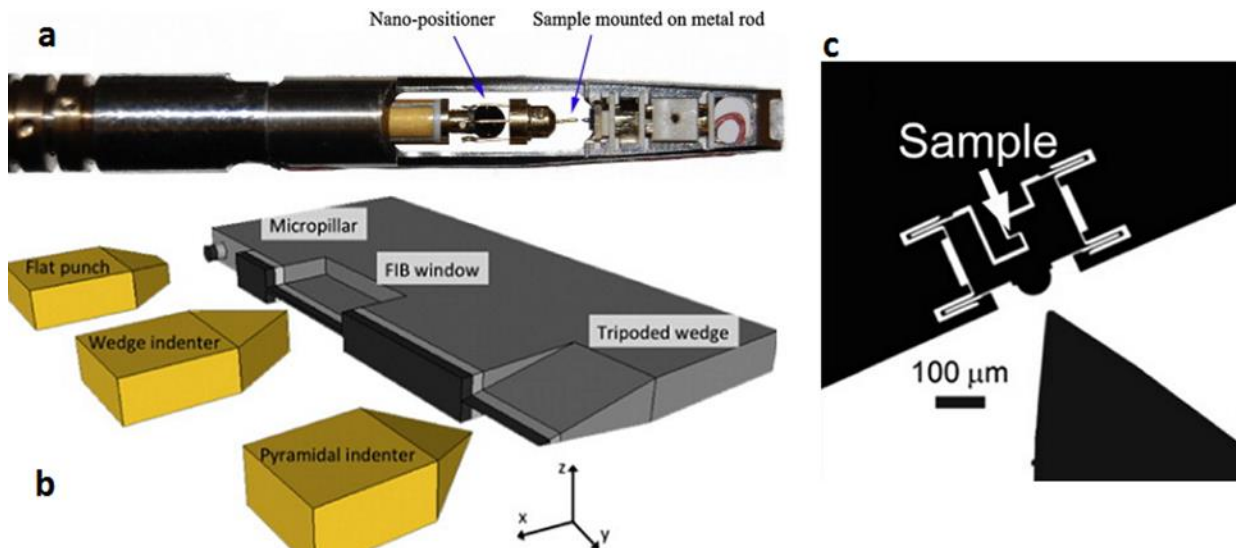
Figure 2.11: Examples of in situ TEM mechanical testing techniques: (a) Tip of a classical straining holder (b) sketch of the various types of straining configurations used in nanoindentation holders, (c) Push to pull device with a Hysitron PI-95 nanoindenter [57, 65, 66].

For compression tests carried out inside TEM, one of the main concern is always whether the high energy electron beam (e-beam) affect the measured mechanical properties or not. The answer is, for materials with metallic bond, no obvious effect has been observed so far [67]. However, for materials with covalent and ionic bonds, significant e-beam effect has been confirmed. One typical example is Zheng et al.'s [68] study on amorphous SiO_2

spheres. As they found during the compression test at room temperature, the flow stress can be decreased by four times when the e-beam is illuminating the sample comparing the condition e-beam is shielded from the sample (Figure 2.12) [67].
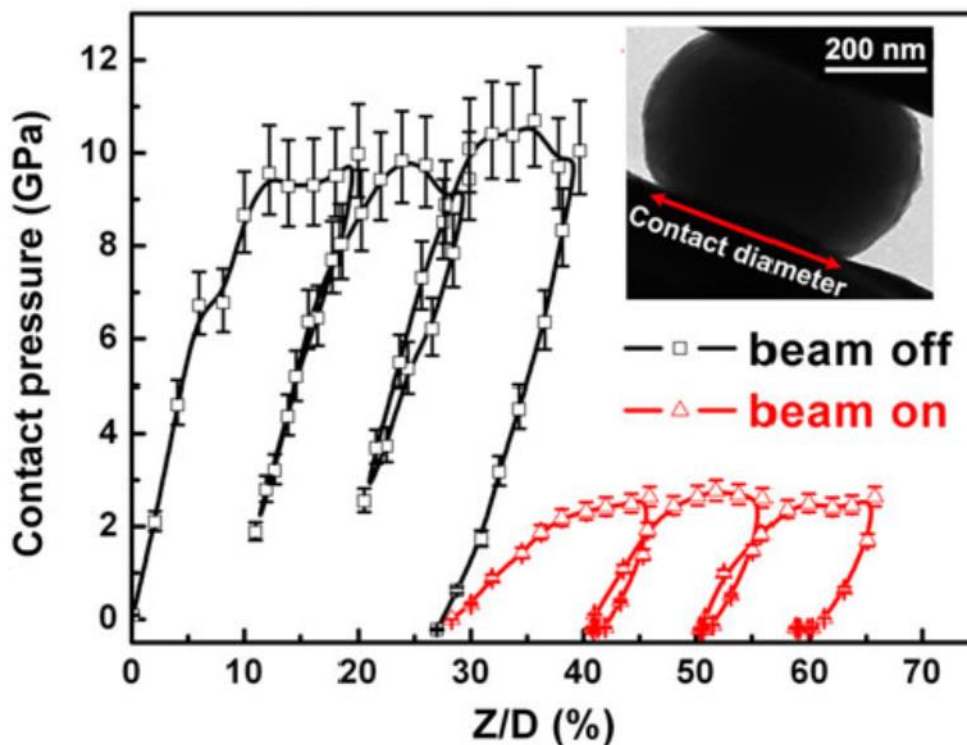
Figure 2.12: The effect of E-beam on the mechanical behavior of an amorphous silica particle. The contact pressure decreased about four times when electron beam was switched from off (black curve) to on (red curve). The inset is a frame from the recorded movie during compression test [67], [68].

With the advent of the atomic force microscope (AFM) and specialized depth sensing indenters, the probing of mechanical properties on the micro- and nanoscale under ultra-low loads has become possible [69]. This advancement in technology has proven useful for understanding the mechanical behavior of micro- and nano scale materials [70-75]. As an example, a Hysitron SPM-3800 Atomic Force Microscope (AFM) with a pyramidal-shape Berkovich diamond indenter was used by Gan et al. [76], to perform the nanoindentation measurements of the individual phases. Wood et al. [77] used AFM nanoindentation to examine the local plasticity and size-dependent hardness of bimetallic Ni–Au NWs with small dimensions attached to chemically functionalized flat substrates.

2.3. Deformation mechanisms

Two basic models have been used to explain the size effects on plasticity of fcc single crystals. The first is the "dislocation starvation" (DS) model, in which dislocations can escape from nearby free surfaces in a small sample prior to dislocation multiplication, leaving samples in a dislocation-free state. The continuous plastic flow would then require increasing of applied load to nucleate dislocations at the surface. Thus the basic idea behind the DS model is that plastic deformation at small scales is dislocation nucleation dominated [78]. This model indicates that the rate of dislocation escape from the free surface is greater than that of dislocation multiplication in the small scale crystal [79]. The other model is the "single-arm dislocation" (SAD) model, which is based on the idea that size effects on the plasticity of small single crystals can be rationalized almost completely by considering the stochastics of single-arm dislocation source lengths in the sample [78]. These single-arm dislocations can be readily described as Frank–Read (F-R) source that changed into two single-arm sources when truncated by free surfaces [80, 81]. In contrast to the DS model, the SAD model assumes that plastic deformation is derived by multiplication of internal dislocation sources rather than nucleation of surface dislocations.

2.3.1.   Dislocation starvation and nucleation control

One of the most likely deformation modes that can result in the observed high strengths is explained by the concept of dislocation starvation. According to this scenario [19], in small volumes mobile dislocations are thought to escape from the crystal at the nearest free surface before multiplying and interacting with other dislocations. Such processes lead to a dislocation-starved state, and nucleation of new dislocations in the newly-formed perfect crystal is required to accommodate further plastic deformation. According to Greer et al. [16, 82-84] description, a dislocation must travel a minimum distance, δ (also called breeding distance) before it replicates itself, and when crystals are smaller than this characteristic length, it might behave quite differently from bulk crystals. When the conditions for multiplication are not met, the dislocations would leave the small crystals before having the chance of multiplication, leading to dislocation starvation. Once the dislocation-starved conditions are reached, very high stresses would be required

to nucleate new dislocations, either at surfaces or in the bulk of the crystal, which could describe the observed near-theoretical-strengths at small scales.

Figure 2.13 shows Shan et al. [31] results as they evaluated the dislocation starvation theory. As they observed, the dislocation content of the nanopillars dropped markedly when deformed in the TEM. With this exhaustion, which the authors call 'mechanical annealing', the process controlling the strength and plasticity changes from dislocation propagation and interaction to dislocation nucleation [85].
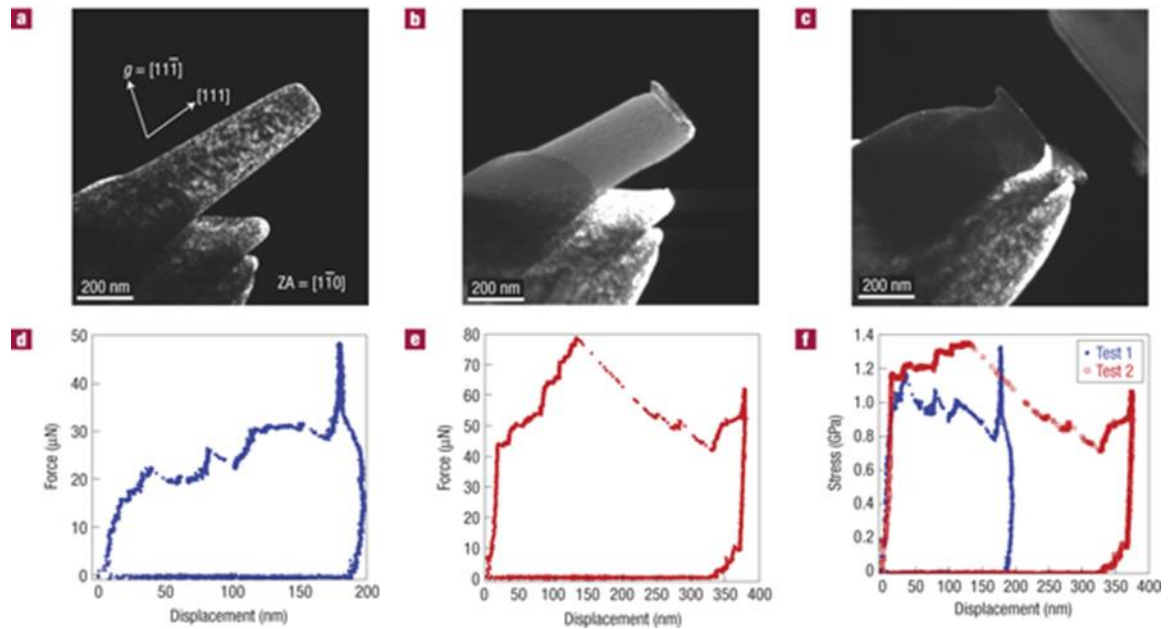
Figure 2.13: In situ TEM compression of <111> oriented 160nm Ni pillar. a) The dark-field TEM image of the pillar before the test, showing high initial dislocation density, b) Dark-field TEM image of the same pillar after the first test which is now free of dislocation c) Dark-field TEM image of the same pillar after the second test. d) Force versus displacement curve of the first and e) the second test. f) Instantaneous stress versus compressive displacement for the two tests; the apparent yield stress is similar for both tests [31].

Jerusalem et al [86], proposed a continuum model accounting for dislocation starvation and nucleation. As they described, a reference of the average dislocation resistance shear stress for each slip system i can be described as,

$$\tau_0^i = Min\left(\left(1 - \frac{\varepsilon_p}{\varepsilon_p^{starv}}\right)\tau_{0,starv} + \frac{\varepsilon_p}{\varepsilon_p^{starv}}\tau_{0,nucl}, \tau_{0,nucl}\right) \tag{2.1}$$

where

$$\tau_{0,starv} = 0.5\mu b\sqrt{\rho_0} + 1.4\frac{\mu b}{4\pi a_0(1-v)}\ln\left(\frac{\alpha a_0}{b}\right) \tag{2.2}$$

and ε_p^{starv} considers the plastic strain for which nucleation dislocation is more favorable than dislocation starvation, and at which the nucleation critical resolved shear stresses (CRSS) $\tau_{0,nucl}$ is reached.

According to Zhu et al.'s [87] theory, the required stress for dislocation nucleation is proportional to the logarithm of the number equivalent surface nucleation sites; N, which is directly affected by the sample geometry. Since nucleation stress is a function of the logarithm of N, the size effect arising from surface nucleation is expected to be weak, compared to that in micropillars showing a power-law scaling exponent in the range of −0.6 to −0.7 [16, 88-91]. As Zhu et al. [87] assumed, a transition in the scaling behavior of yield stress could be expected on the sample size in an approximate range of tens of nanometers, as illustrated by Figure 2.14.
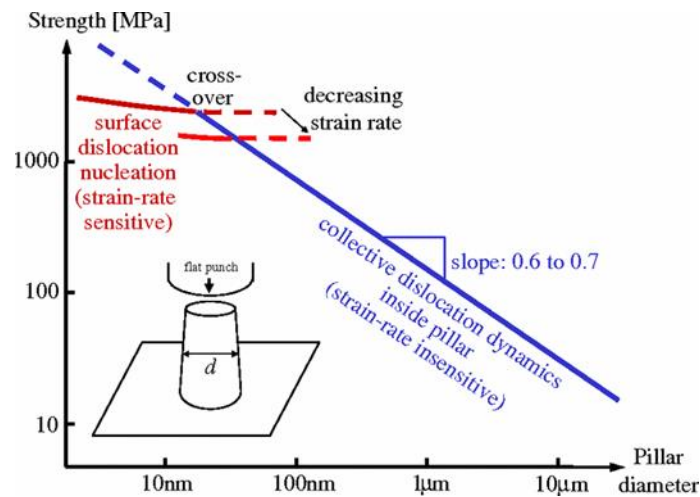
Figure 2.14: Transition in the scaling behavior of yield stress on the sample size range of tens of nanometers [87].

TEM studies on partial dislocation nucleation have highlighted the role of various surface defects in dislocation nucleation. This is most obvious in the case of thin films where dislocations preferentially nucleate at voids as they serve as stress concentrations sites during tensile experiments [92, 93]. The effect of surface steps on decreasing the elastic threshold and assisting the nucleation of dislocations [94-102]. As Navarro et al. [102] calculated, the critical stress for dislocation nucleation at the steps is approximately half that on the flat surface.

Large strain bursts were universally observed during the compression of sub-micron and nano-sized fcc pillars. However, depending on the sample size, the underlying physical mechanisms are different. As Wang et al. [103] concluded on his studies on Al pillars, for small pillars (with D=80 to 300 nm, group A), the bursts originate from explosive and highly correlated dislocation nucleation, characterized by very high ultimate stresses and nearly dislocation-free microstructure after the sample failure. Figure 2.15 shows a 165nm Al pillar as an example of this group. The single crystal is loaded along the $[2\bar{2}0]$ direction and observed under <110> zone axis. FIB induced dislocations are clearly seen in the darkfield image (Figure 2.15(c)). The first burst observed in the stress-strain and load time curves (Figure 2.15 (a, b)) is caused by the cleaning-up of pre-existing dislocation which were driven out of the pillar, in a process known as mechanical annealing [31, 60, 85, 103-105]. Here, the CRSS is equal to the starvation CRSS in equation 1 and then linearly increases as a function of ε_p as the mobile dislocations are moving towards the free surface. Once all mobile dislocations are annihilated, plasticity is fully nucleation driven and second drop at stress, marked point 2, happens when new dislocations nucleate from the contact interface between the pillar and the indenter. However, since there is no dislocation in the pillar, the new ones move through it very fast and escape immediately out of the pillar. The drastic strain burst happens in point 3, where the structural collapse occurred, in the result of a major shape change within a small fraction of a second [103]. Post-test, dark-field observation under multiple conditions confirmed that this test left behind a dislocation-free pillar (Figure 2.15 (d)) [31, 103]. The pronounced decrease in dislocation density during the nano-compression tests provides direct support for the dislocation starvation theory that has been hypothesized based on experiments [16, 19, 53, 82, 106] and simulations [78, 86, 87,

107]. As Shan et al. [31] pointed out, even the surface oxide layer [108] and the FIB damage layer [109], cannot trap dislocations inside the pillar during deformation [67]. The driving force for the dislocation starvation within the pillars is a combination of the applied stress which will activate or nucleate dislocations and the image forces from the surface which will assist the dislocations in moving towards the free surfaces of the crystal [31]. The mechanical annealing phenomena is more significant in smaller the samples [67].
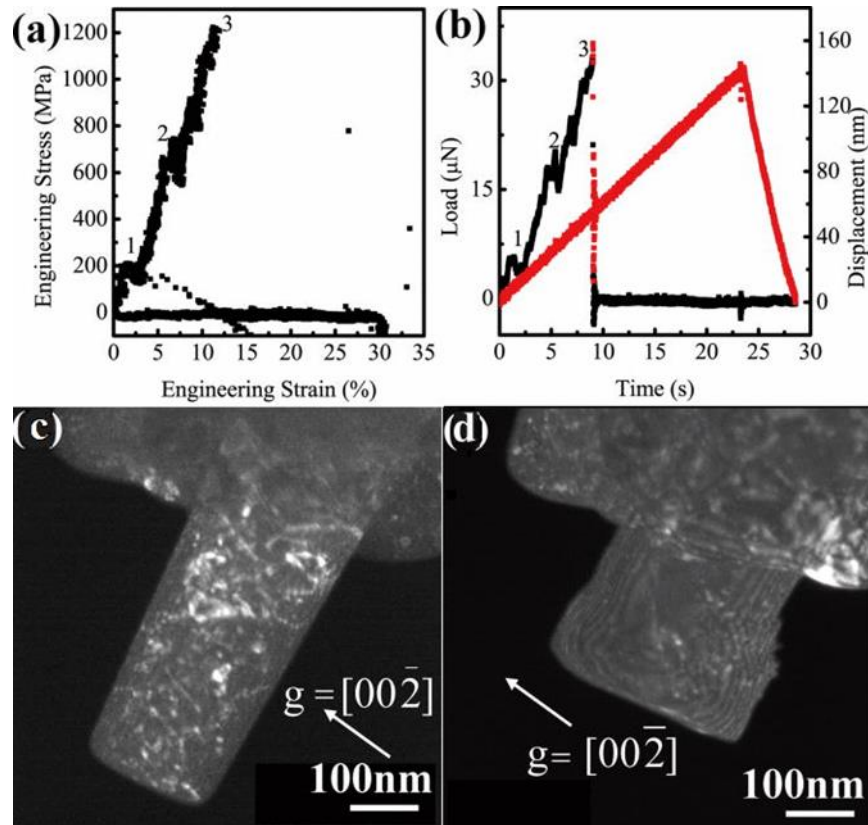
Figure 2.15: Snapshots of the microstructural evolution in 165 nm Al nanopillar compression. (a) Engineering stress-strain curve (b) The load-time and displacement-time curves. (c) Dark-field images of the pillar before compression. (d) Dark-field images of the pillar after the collapse (∼20% strain) reproduced from reference [103] with the permission of AIP.

Figure 2.16 shows the result of a dislocation dynamics (DD) simulation on the behavior of a 150 nm Cu pillar in which all dislocations escape the crystal during the early stages

of loading and half-loop dislocations are introduced into the crystal from the surface when the stress reaches the critical dislocation nucleation stress. If the applied load is not dropped, then these new dislocations will traverse the pillar and subsequently escape and this process is then repeated with the flow stress reaching a plateau without any significant hardening [110].
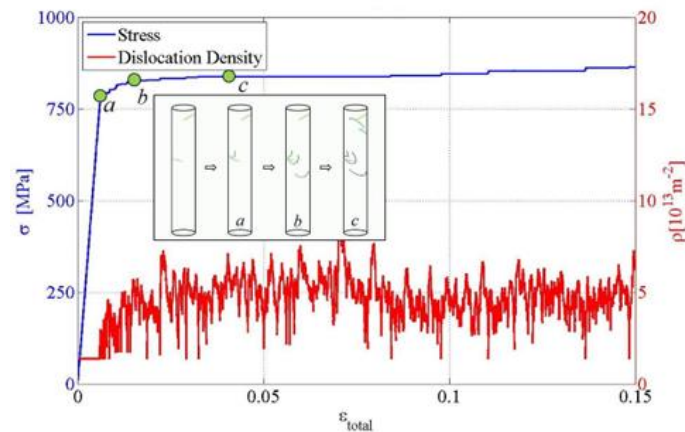
Figure 2.16: Stress and dislocation density evolution versus strain for a 150 nm diameter Cu pillar. Insets show the dislocation microstructures at different points along with the stress-strain curve [110].

2.3.2. Source truncation (single-arm dislocation source control)

Some scholars have proposed a mechanism based on the operation and stochastic effects of a single-arm dislocation source within a pillar in the scale of micrometer, believing that the micropillars contain several dislocation sources, but only one or two for the slip plane in the small pillars [18, 111]. As Parthasarathy et al. [18] described, in finite samples, where the sample dimensions are of the same order of magnitude as the source lengths, all sources end up as being single-ended due to interaction with the free surface, as in Figure 2.17 b. Figure 2.18 shows one of single-arm sources operating in a 750 nm wide Al fiber [112]. In Fig. 18a, the spiral source is captured while generating dislocation loops in a (111) glide plane by turning clockwise around a fixed arm. The moving arm propagates to the right and forms a pile-up because of the non-immediate evacuation of dislocations to the free surfaces. Thick slip traces (noted Tr. in Figure 2.18a) are evidence

of the slow shear of the native oxide by the dislocations. The slip traces are erased when the source stops by cross-slipping of the fixed arm, meaning that the dislocations have completely escaped the crystal (Figure 2.18b). This single-arm mechanism has been found acceptable and used in discrete dislocation dynamics simulations [78, 81, 113-119]. Moreover, some physical models have been developed based on this stochastic effect, such as the single arm source (SAS) model [18, 25, 114, 120, 121]. Pan et al. [122], examined the dislocation pile-up mechanism quantitatively and provided a revised SAS model for describing the size dependent strength by reconsidering the back stress and activation stress.
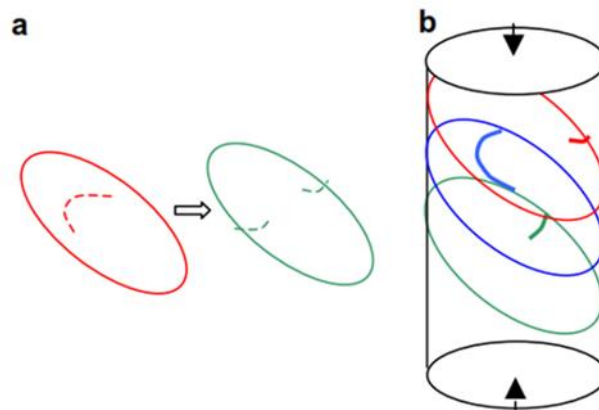
Figure 2.17: (a) A schematic description of changing a double-pinned Frank–Read sources to single-arm sources in a small volume. (b) Representation of single-arm sources in a finite cylindrical sample in critical configuration, which occurs where the distance from the pin to the free surface is the shortest. The longest arm determines the critical resolved shear stress [18].
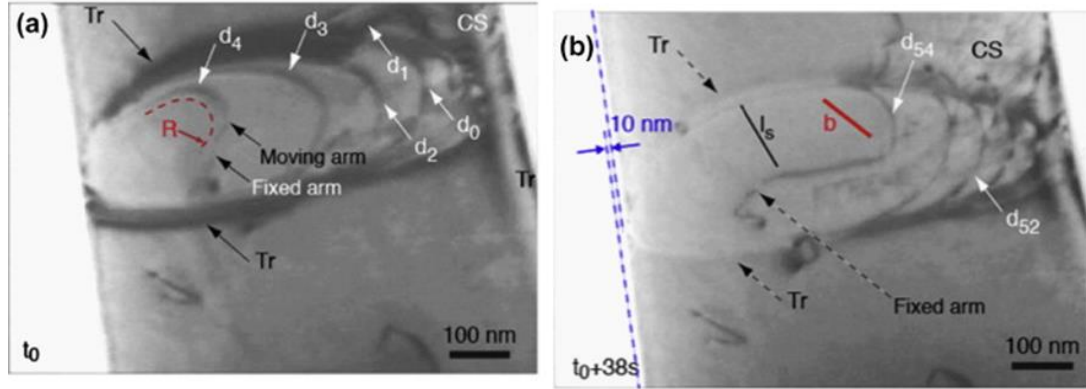
Figure 2.18: Single-arm source operating in a 750 nm wide Al fiber for a finite time (54 loop emissions in 38 s). (a) and (b) are video frames that correspond to the source operating and stopping, respectively [112].

The critical resolved shear stress to activate a single-arm dislocation source is generally computed by summing the friction stress, the elastic interaction stress, and the line tension stress. Choosing Parthasarathy et al.'s [18] equation and considering material parameters, Lee and Nix [25] expressed the required CRSS as,

$$\tau_{CRSS} = \tau_0 + 0.5 k_S b \sqrt{\rho_{tot}} + \frac{\alpha k_S b}{\bar{\lambda}_{max}(D, \rho_{tot}, \beta)} \qquad (2.3)$$

where τ_{CRSS} is the CRSS for the activation of the weakest single-arm source, τ_0 is the friction stress, k_S is the anisotropic shear modulus, b is the magnitude of Burgers vector, ρ_{tot} is the total dislocation density, α is a constant of the order of unity, and $\bar{\lambda}_{max}$ is the statistical average length of the weakest single-arm dislocation source, D is the pillar diameter, ρ_{tot} is the dislocation density, and β is the slip plane orientation. As Lee and Nix [25] described if all of the samples have a similar dislocation density and slip plane orientation, $\bar{\lambda}_{max}$ becomes only diameter dependent, which indicates the capability of SAS theory for describing size scale properties.

The stability of dislocation sources has been studied in the literature. Molecular dynamics simulations have shown that jogs on Lomer–Cottrell dislocations that might form the pinned part of single arm sources are unstable in the high stress loading conditions required to deform Al nanopillars of diameter 16–50 nm [123], while 3D discrete dislocation plasticity (DDP) simulations approved the importance of image stresses and

cross-slip in controlling the lifetime of intermittent sources which tend to be longer lived in larger diameter samples [78]. However, TEM observations of deformation of Al fibers of diameter 120 nm confirm that although operating intermittently, an individual single arm dislocation source is sufficiently stable to generate large plastic strain [124].

Investigating single arm source controlled plastic flow in the micropillars with diameters from 200 to 800 nm is extensively investigated by a statistically, Cui et al. [114] noted that the SAS mechanism itself is not suitable to explain the hardening behavior of very small or very large samples. As the sample size decreases, the image force becomes larger and together with the external applied stress, the dislocations can be easily driven out of the crystal, resulting that available dislocation sources become progressively exhausted, even causing dislocation starvation. The similar conclusion was made by Gu et al. [125], pointing out that in fcc single crystalline metals, dislocations are generated by the operation of the single arm dislocation sources in micrometer-sized structures and via dislocation nucleation at surfaces in nanometer-sized structures [121, 125-127].

Hu et al. [128], studied the behavior 300 to 700 nm diameter gold particles and resulted that abundant dislocations nucleation and storage exist inside their 400 and 500nm particles during the compression, while few dislocations nucleate inside the smaller particles, concluding that the accumulated emission mechanism controls the collapse of relative larger particles and correlated emission is dominant for the smaller ones. As Jennings et al. [129] stated, the same deformation mechanisms govern flow behavior of nano-scale samples regardless of fabrication methods.

Modifying Jerusalem et al.'s [86] model (equation 1) and considering SAS operation mechanism, Cui et al [114], developed a more general theoretical model to quantitatively describe the sub-micron plastic behavior as follows,

$$\tau = Min\left(\left(1 - \frac{\varepsilon_p}{\varepsilon_p^{star}}\right)\left(\tau_0 + \alpha\mu b\sqrt{\rho} + \frac{k\mu b}{\bar{\lambda}}\right) + \frac{\varepsilon_p}{\varepsilon_p^{star}}\tau_{nucl}, \tau_{nucl}\right) \tag{2.4}$$

where ε_p is the engineering plastic strain, and ε_p^{star} is the plastic strain for which dislocation nucleation is more favorable than SAS operation, and at which the CRSS for dislocation nucleation τ_{nucl} is reached. Cui [130] summarized possible mechanisms of

FCC single crystal plastic deformation in a phase diagram shown in Figure 2.19. As is described, dislocation starvation is dominant in the smaller sample with lower dislocation density ($\sim<10^{12}$ m^{-2}). Continuing deformation, dislocations gradually escape from the crystal, and surface nucleation controls plasticity. By increasing the sample size, it becomes more difficult to reach the dislocation starvation state and dislocation sources emerge because of the interaction between internal dislocations. Here, the activation of single-arm source plays the main role. If the sample size further increases, classical dislocation multiplication mechanism controls the deformation. The critical size between different mechanisms depends on dislocation density and internal microstructure, as shown schematically in Figure 2.19. While there is still no quantitative expression, it is generally believed that the critical size decreases with the decline of dislocation density [130].
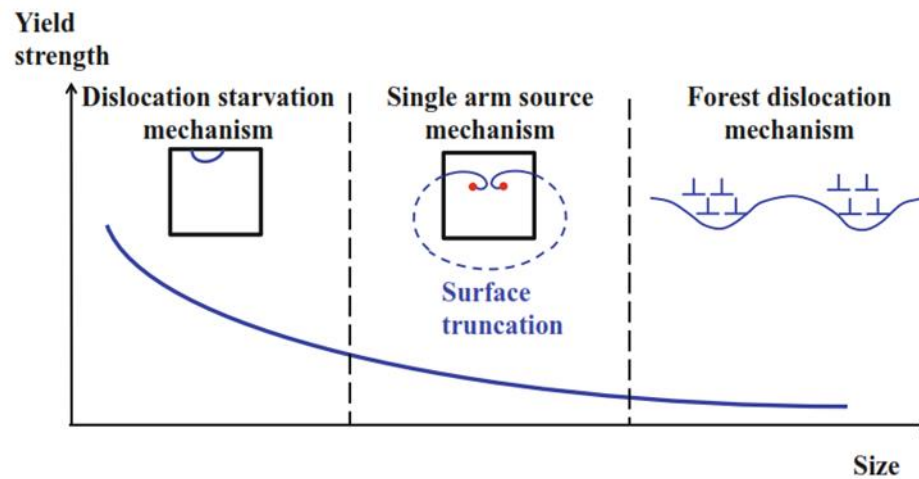
Figure 2.19: Plastic deformation mechanisms in FCC single crystal [130].

2.4. Numerical simulation

Different methods have been used to simulate the material behaviour at small scales. Between modelling approaches, Dislocation Dynamics (DD), Molecular Dynamics (MD), and Continuum Mechanics have been the most applied techniques to study plasticity of micron and nano-sized materials, based on the size of the simulation and desired outputs.
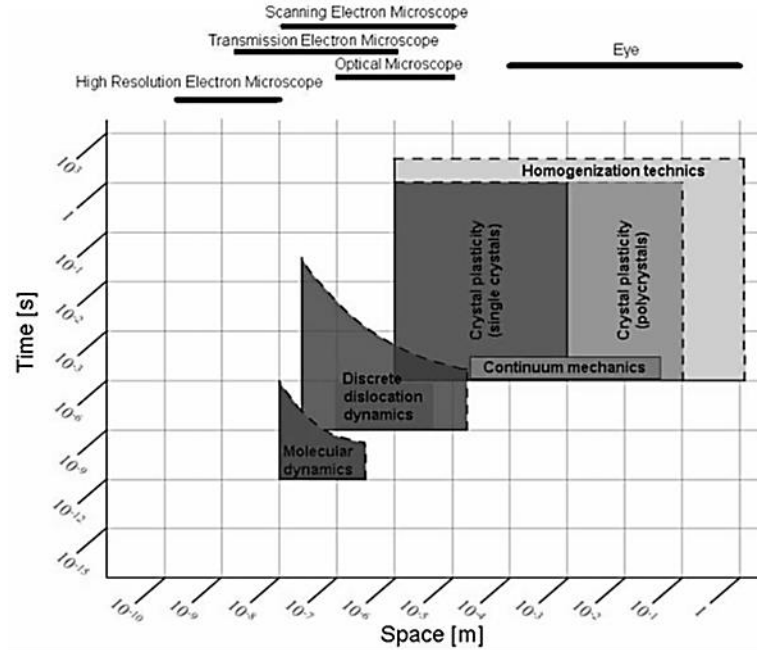
Figure 2.20: Typical volume size and physical time covered by three models devoted to crystal plasticity [131].

In DD methods, dislocation lines are represented explicitly. Each dislocation line is considered as an elastic inclusion embedded in an elastic medium. The collective evolution of interacting dislocations under an external loading is simulated using elastic properties of the crystal. Core properties of dislocations such as line mobility and junction strength are input parameters of DD simulations that can be derived from MD simulations. DD simulations give access to the dislocation behaviour and the mechanical response of the simulated volume (<(50μm)) [131].

Three-dimensional (3-D) DD simulations, in which dislocations are the simulated entities, have been the primary modeling tool employed to study the various aspects of plastic behavior in nano- and microscale samples. Ouyang et al. [132] performed 2D discrete dislocation dynamic modeling on compressed micro pillars attached on a huge base to study the size-dependent microplastic behavior of micro-pillars. They assumed micro-pillar and the base to be linear elastic isotropic material with Young's modulus E = 70GPa and Poisson's ratio $\upsilon = 0.33$, representative of aluminum. Resulted dislocation pattern and total slip Γ distribution are shown in Figure 2.21, with Γ computed as follows [132];

$$\Gamma = \left|\gamma^{\varphi=45^o}\right| + \left|\gamma^{\varphi=-45^o}\right| \tag{2.5}$$

and

$$\gamma^{(\varphi)} = s_i^{\varphi} s_{ij} m_j^{(\varphi)} \tag{2.6}$$

where s_i^{φ} is the tangent and $m_j^{(\varphi)}$ the normal to the slip system φ, respectively. Comparing Figure 2.21 (a)–(c), it gets clear that there exist some slip bands in the micro-pillar, and these bands in the slender micropillars are more intense than that in the podgier ones. It is important that the slip bands in the slender micro-pillar (such as h = 2.0µm, w = 0.5µm) intersect with two sidewalls of the micro-pillar, thus few dislocations reside in the micro-pillar. Nevertheless, the slip bands in the podgy micropillars (such as h = 2.0µm, w = 2.0µm) usually intersect with at least one of the two ends of micro-pillar (the indenter end of the base end), thus more dislocations are observed in the micro-pillar and some dislocations pile-up near the micro-pillar ends. Another observation from Figure 2.21 (c) is the numerous same-signed dislocations that are distributed on the slip planes in the base. The pile-up dislocations repress follow-up dislocations nucleation and enhance flow resistance and strain hardening [132]. However, the dislocation slip-out mechanism is dominant in slender micro-pillars, especially when more slip planes intersect with the micro-pillar free sidewalls. Moreover, the well-known Schmid law may fail in podgy micro-pillars and result in a complicated and even "reverse" size effect [132].
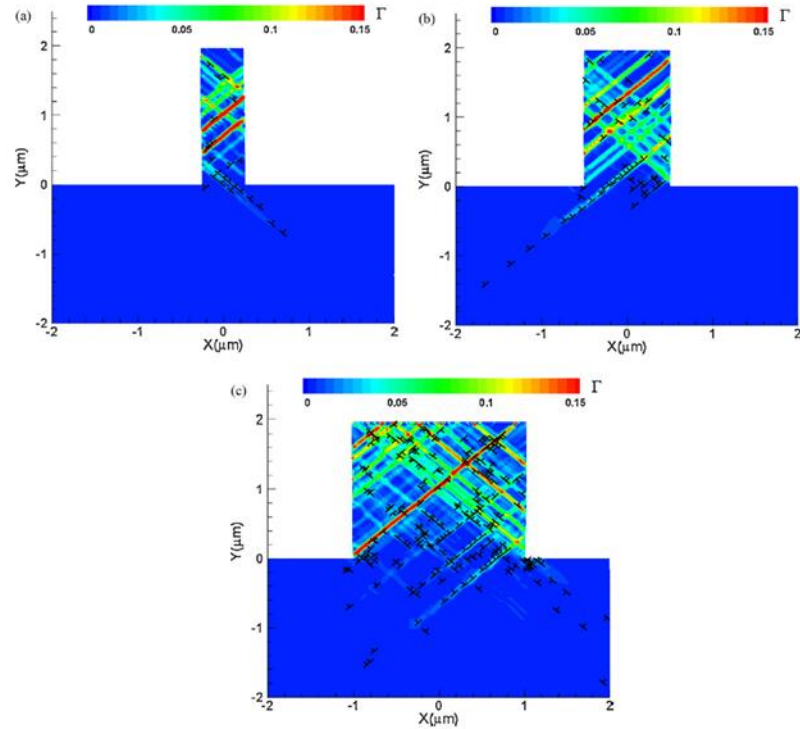
Figure 2.21: Distribution of the total slip Γ and the dislocation pattern at the strain ε= 1.8% for pillars with height h = 2.0 μm and width (a) w = 0.5μm, (b) w = 1.0μm, and (c) w = 2.0μm [132].

Here the simulation result of Cui et al. [114] based on discrete dislocation dynamic is presented to analyze the detail of SAD operation. Simulations were performed for compression test of Ni single crystal micropillars with different 200 nm diameter. Initially, several SAD were arranged in a network (Figure 2.22a) connected by dislocation junctions. As stress increases, the weakest SAD begins to recede along the direction shown in Figure 2.22a, meanwhile a strain burst event takes place. The plastic strain is then generated by the spiral motion of SAD. However, SAD usually only operates for a short time before they stop to work. For example, the activated sources of Figure 2.22a–c form new junctions by the interaction with other dislocations, and could not be activated any more under the current stress. The activated source in Figure 2.22d disappears because of the destruction of pinning point under high stress and the subsequent surface annihilation. The dynamic source in Figure 2.22e is broken as the pinning point glides out of the crystal in that limited size. The number of times that SAD

sweeps the slip plane can be defined as the lifetime of SAD. According to Cui et al. [114] analysis, SAD lifetime depends on the neighboring dislocation microstructure, the instantaneous stress, and the relative position to the surface. When dislocation sources cease to operate, the current strain burst finishes. Then the stress increases almost elastically to activate new sources. Because of the stochastic distribution of the strength and lifetime of SAD, the stress usually increases in a discontinuous and stochastic manner during deformation.
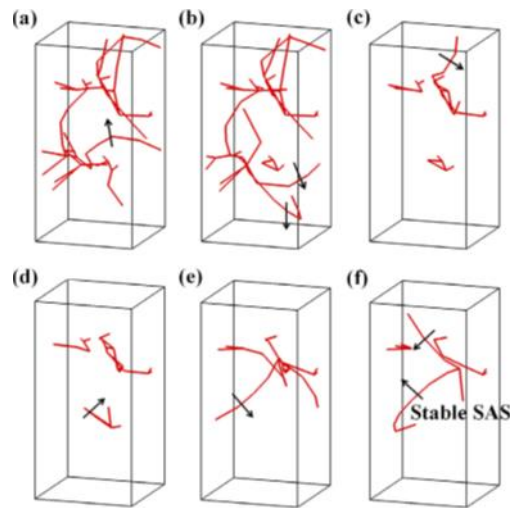
Figure 2.22: (a–f) Snapshots of dislocation configurations during compression for 200 nm diameter Ni micropillar, where the arrows show the receding directions of the activated SAD [114].

In all the DD simulations, the stress and strain fields were assumed to be homogeneous and no surface effects were accounted for. However, as shown in all the experiments, the deformation field in sub-micron scale specimens is far from being homogenous, and becomes highly heterogeneous and localized with increased strain [133].

The molecular dynamics (MD) modelling approach is based on the interactions of the particles that constitute the material. In the framework of material science, these particles are the atoms that making the microstructure, and MD is used to describe how the position and velocity of these changes with time. Since MD operates on the atomistic scales the method is supposed to have the capacity to capture all possible mechanical phenomena related to the hierarchical structures of materials. However, the method is

constrained by assumptions, approximations, and the enormous computational effort is needed to model all the atoms in even a small material specimen. The method is based on classical Newton's laws of motion, where the position of a particle is governed by:

$$m\ddot{x} = f(x) = \nabla U(x) \tag{2.7}$$

where f is the force acting on the particle and can be determined from a potential U(x) [134].

Interaction between particles can then be simulated if the correct potential energy relation can be described. Numerical integration of (2.7) will yield the particle velocities and positions, from which statistical averages over a large number of particles can be formed to give information about the macroscopic evolution of the modeled system [134].

Two atomic configuration of the simulation cell for MD simulation of nanoindentation of Au particles and compression of MgO nanocubes have been shown in Figure 2.23.
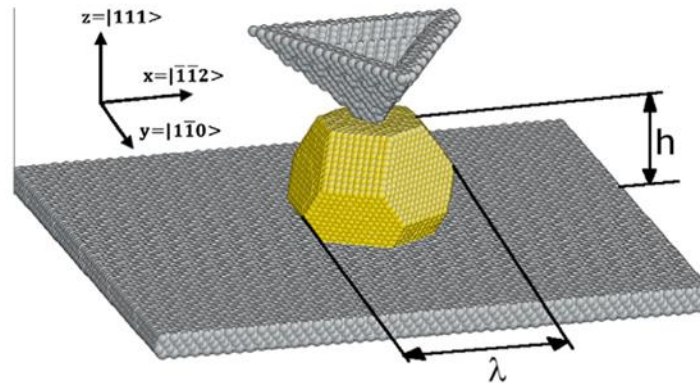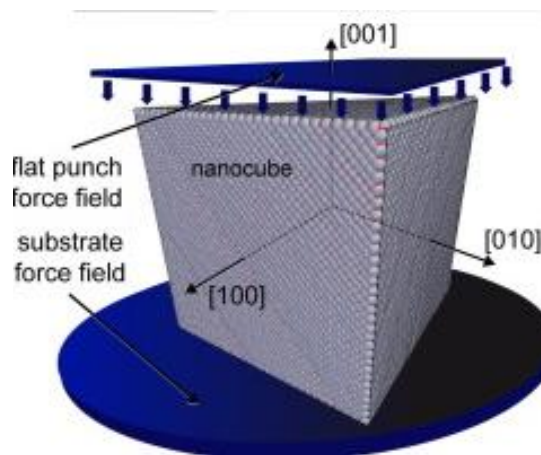
Figure 2.23: The atomic configuration of the MD simulation cell for a) indentation of a 4.9 nm high Au particle [135] and b) nanocompression of 100 nm MgO nanocube [136].

On the basis of a series of MD simulations of the compressive deformation of <111> oriented Au nanopillars, Rabkin and Srolovitz [137] demonstrated that slip nucleates at surface features for which the amplitude of thermal vibrations is a maximum. Figure 2.24c demonstrates clearly that slip nucleates in the vicinity of thin stripes of atoms, marked by red color in Figure 2.24a (consisting of several rows of atoms oriented along the cylinder axis, <111>), on otherwise flat terraces. The arrow in Figure 2.24c shows the position of a slip trace associated with the nucleation and motion of a Shockley partial into the cylinder. This trace is centered around the three <111> atomic rows thick stripe of atoms. For all temperatures below 300 K, slip always nucleated in the vicinity of the marked <111> stripes. It should be emphasized that these stripes are aligned along the loading axis and cannot serve as stress concentrators for the present uniaxial load. Figure 2.24b shows the smoothed or polished nanopillar in which the <111> stripes of surface atoms have been removed. The atomic configuration of the atomically polished cylinder at the onset of plasticity is shown in Figure 2.24d. A comparison of this figure with that for the as-carved cylinder (Figure 2.24c) indicates that removing the thin <111> stripes has changed the location of slip nucleation at the surface.
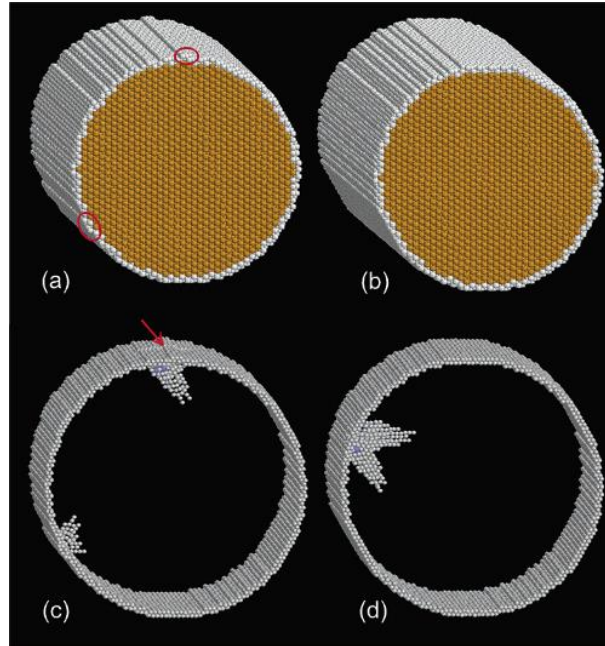
Figure 2.24: Atomic structures of (a) as-carved and (b) atomically polished nanopillars. The "atomically polished" cylinder was created by removing a total of 294 atoms ordered in <111> strings (marked by red color in (a)) from the "as-carved" cylinder. The atomic structure immediately following slip nucleation in configuration (a) is shown in (c). Fig (d) shows the same thing for the atomically polished structure of (b). Atoms with fcc symmetry haven't been shown in (c) and (d) [137].

References

[1] E.O. Hall, The Deformation and Ageing of Mild Steel .3. Discussion of Results, P Phys Soc Lond B 64(381) (1951) 747-753.

[2] N.J. Petch, The Cleavage Strength of Polycrystals, J Iron Steel I 174(1) (1953) 25-28.

[3] J.K. Galt, C. Herring, Elastic and Plastic Properties of Very Small Metal Specimens, Phys Rev 86(4) (1952) 656-656.

[4] M.S. Deguzman, G. Neubauer, P. Flinn, W.D. Nix, The Role of Indentation Depth on the Measured Hardness of Materials, Thin Films: Stresses and Mechanical Properties Iv 308 (1993) 613-618.

[5] N.A. Stelmashenko, M.G. Walls, L.M. Brown, Y.V. Milman, Microindentations on W and Mo Oriented Single-Crystals - an Stm Study, Acta Metallurgica Et Materialia 41(10) (1993) 2855-2865.

[6] Q. Ma, D.R. Clarke, Size-Dependent Hardness of Silver Single-Crystals, J Mater Res 10(4) (1995) 853-863.

[7] W.D. Nix, Elastic and plastic properties of thin films on substrates: nanoindentation techniques, Mat Sci Eng a-Struct 234 (1997) 37-44.

[8] K.W. McElhaney, J.J. Vlassak, W.D. Nix, Determination of indenter tip geometry and indentation contact area for depth-sensing indentation experiments, J Mater Res 13(5) (1998) 1300-1306.

[9] R. Saha, Z.Y. Xue, Y. Huang, W.D. Nix, Indentation of a soft metal film on a hard substrate: strain gradient hardening effects, J Mech Phys Solids 49(9) (2001) 1997-2014.

[10] N.I. Tymiak, D.E. Kramer, D.F. Bahr, T.J. Wyrobek, W.W. Gerberich, Plastic strain and strain gradients at very small indentation depths, Acta Mater 49(6) (2001) 1021-1034.

[11] J.G. Swadener, E.P. George, G.M. Pharr, The correlation of the indentation size effect measured with indenters of various shapes, J Mech Phys Solids 50(4) (2002) 681-694.

[12] N.A. Fleck, G.M. Muller, M.F. Ashby, J.W. Hutchinson, Strain Gradient Plasticity - Theory and Experiment, Acta Metall Mater 42(2) (1994) 475-487.

[13] J.S. Stolken, A.G. Evans, A microbend test method for measuring the plasticity length scale, Acta Mater 46(14) (1998) 5109-5115.

[14] M.A. Haque, M.T.A. Saif, Strain gradient effect in nanoscale thin films, Acta Mater 51(11) (2003) 3053-3061.

[15] H.J. Gao, Y.G. Huang, Geometrically necessary dislocation and size-dependent plasticity, Scripta Mater 48(2) (2003) 113-118.

[16] J.R. Greer, W.C. Oliver, W.D. Nix, Size dependence of mechanical properties of gold at the micron scale in the absence of strain gradients, Acta Mater 53(6) (2005) 1821-1830.

[17] A.A. Benzerga, N.F. Shaver, Scale dependence of mechanical properties of single crystals under uniform deformation, Scripta Mater 54(11) (2006) 1937-1941.

[18] T.A. Parthasarathy, S.I. Rao, D.M. Dimiduk, M.D. Uchic, D.R. Trinkle, Contribution to size effect of yield strength from the stochastics of dislocation source lengths in finite samples, Scripta Mater 56(4) (2007) 313-316.

[19] J.R. Greer, W.D. Nix, Nanoscale gold pillars strengthened through dislocation starvation, Phys Rev B 73(24) (2006).

[20] R. Beanland, Dislocation Multiplication Mechanisms in Low-Misfit Strained Epitaxial Layers, J Appl Phys 77(12) (1995) 6217-6222.

[21] G.Z. Voyiadjis, M. Yaghoobi, Review of Nanoindentation Size Effect: Experiments and Atomistic Simulation, Crystals 7(10) (2017).

[22] W.D. Nix, H.J. Gao, Indentation size effects in crystalline materials: A law for strain gradient plasticity, J Mech Phys Solids 46(3) (1998) 411-425.

[23] H. Gao, Y. Huang, Geometrically necessary dislocation and size-dependent plasticity, Scripta Mater 48(2) (2003) 113-118.

[24] D. Kiener, W. Grosinger, G. Dehm, R. Pippan, A further step towards an understanding of size-dependent crystal plasticity: In situ tension experiments of miniaturized single-crystal copper samples, Acta Mater 56(3) (2008) 580-592.

[25] S.-W. Lee, W.D. Nix, Size dependence of the yield strength of fcc and bcc metallic micropillars with diameters of a few micrometers, Philos Mag 92(10) (2012) 1238-1260.

[26] M.D. Uchic, D.M. Dimiduk, J.N. Florando, W.D. Nix, Sample dimensions influence strength and crystal plasticity, Science 305(5686) (2004) 986-989.

[27] M. Diobet, Characterization of Microdevices by Nanoindentation, (2012).

[28] H. Ghassemi-Armaki, P. Chen, S. Bhat, S. Sadagopan, S. Kumar, A. Bower, Microscale-calibrated modeling of the deformation response of low-carbon martensite, Acta Mater 61(10) (2013) 3640-3652.

[29] O.T. Abad, J.M. Wheeler, J. Michler, A.S. Schneider, E. Arzt, Temperature-dependent size effects on the strength of Ta and W micropillars, Acta Mater 103 (2016) 483-494.

[30] A.C. Fischer-Cripps, Nanoindentation, Springer, New York, 2002.

[31] Z.W. Shan, R.K. Mishra, S.A.S. Asif, O.L. Warren, A.M. Minor, Mechanical annealing and source-limited deformation in submicrometre-diameter Ni crystals, Nat Mater 7(2) (2008) 115-119.

[32] A.T. Jennings, J.R. Greer, Tensile deformation of electroplated copper nanopillars, Philos Mag 91(7-9) (2011) 1108-1120.

[33] S. Barakat, P. Lee-Sullivan, S.A. Vitale, T.Y. Tsui, The effects of low temperature and pressure on the fracture behaviors of organosilicate thin films, J Mater Res 26(19) (2011) 2524-2532.

[34] L. Yang, S.G. Long, Z.S. Ma, Z.H. Wang, Accuracy analysis of plane-strain bulge test for determining mechanical properties of thin films, T Nonferr Metal Soc 24(10) (2014) 3265-3273.

[35] O. Alshehri, Mechanical Behaviour of Nanocrystalline Rhodium Nanopillars under Compression, Mechanical Engineering, University of Waterloo, Waterloo, Ontario, Canada, 2012.

[36] S. Pathak, S.R. Kalidindi, Spherical nanoindentation stress-strain curves, Mat Sci Eng R 91 (2015) 1-36.

[37] H.Y. Fei, A. Abraham, N. Chawla, H.Q. Jiang, Evaluation of Micro-Pillar Compression Tests for Accurate Determination of Elastic-Plastic Constitutive Relations, J Appl Mech-T Asme 79(6) (2012).

[38] J.B.P. Warren C. Oliver, Method for continuous determination of the elastic stiffness of contact between two bodies, 1988.

[39] J.B. Pethica, R. Hutchings, W.C. Oliver, Hardness Measurement at Penetration Depths as Small as 20-Nm, Philos Mag A 48(4) (1983) 593-606.

[40] W.C. Oliver, G.M. Pharr, Nanoindentation in materials research: Past, present, and future, Mrs Bull 35(11) (2010) 897-907.

[41] C.A. Schuh, Nanoindentation studies of materials, Mater Today 9(5) (2006) 32-40.

[42] H. Nili, K. Kalantar-zadeh, M. Bhaskaran, S. Sriram, In situ nanoindentation: Probing nanoscale multifunctionality, Prog Mater Sci 58(1) (2013) 1-29.

[43] C. Rudolf, B. Boesl, A. Agarwal, In Situ Mechanical Testing Techniques for Real-Time Materials Deformation Characterization, Jom-Us 68(1) (2016) 136-142.

[44] R. Ghisleni, K. Rzepiejewska-Malyska, L. Philippe, P. Schwaller, J. Michler, In Situ SEM Indentation Experiments: Instruments, Methodology, and Applications, Microsc Res Techniq 72(3) (2009) 242-249.

[45] R. Rabe, J.M. Breguet, P. Schwaller, S. Stauss, F.J. Haug, J. Patscheider, J. Michler, Observation of fracture and plastic deformation during indentation and scratching inside the scanning electron microscope, Thin Solid Films 469 (2004) 206-213.

[46] X.W. Gu, M. Jafary-Zadeh, D.Z. Chen, Z.X. Wu, Y.W. Zhang, D.J. Srolovitz, J.R. Greer, Mechanisms of Failure in Nanoscale Metallic Glass, Nano Lett 14(10) (2014) 5858-5864.

[47] M.L.B. Palacio, B. Bhushan, Depth-sensing indentation of nanomaterials and nanostructures, Mater Charact 78 (2013) 1-20.

[48] Q.N. Han, W.H. Qiu, Y.B. Shang, H.J. Shi, In-situ SEM observation and crystal plasticity finite element simulation of fretting fatigue crack formation in Ni-base single-crystal superalloys, Tribol Int 101 (2016) 33-42.

[49] B. Moser, J. Kuebler, H. Meinhard, W. Muster, J. Michler, Observation of instabilities during plastic deformation by in-situ SEM indentation experiments, Adv Eng Mater 7(5) (2005) 388-392.

[50] Q.P. Cao, J.W. Liu, K.J. Yang, F. Xu, Z.Q. Yao, A. Minkow, H.J. Fecht, J. Ivanisenko, L.Y. Chen, X.D. Wang, S.X. Qu, J.Z. Jiang, Effect of pre-existing shear bands on the tensile mechanical properties of a bulk metallic glass, Acta Mater 58(4) (2010) 1276-1292.

[51] D.Z. Chen, D. Jang, K.M. Guan, Q. An, W.A. Goddard, J.R. Greer, Nanometallic Glasses: Size Reduction Brings Ductility, Surface State Drives Its Extent, Nano Lett 13(9) (2013) 4462-4468.

[52] H.E. Weekes, V.A. Vorontsov, I.P. Dolbnya, J.D. Plummer, F. Giuliani, T.B. Britton, D. Dye, In situ micropillar deformation of hydrides in Zircaloy-4, Acta Mater 92 (2015) 81-96.

[53] J.Y. Kim, J.R. Greer, Tensile and compressive behavior of gold and molybdenum single crystals at the nano-scale, Acta Mater 57(17) (2009) 5245-5253.

[54] S.W. Lee, Y.T. Cheng, I. Ryu, J.R. Greer, Cold-temperature deformation of nano-sized tungsten and niobium as revealed by in-situ nano-mechanical experiments, Sci China Technol Sc 57(4) (2014) 652-662.

[55] S.W. Lee, L. Meza, J.R. Greer, Cryogenic nanoindentation size effect in [001]-oriented face-centered cubic and body-centered cubic single crystals, Appl Phys Lett 103(10) (2013).

[56] Q. Yu, M. Legros, A.M. Minor, In situ TEM nanomechanics, Mrs Bull 40(1) (2015) 62-68.

[57] M. Legros, In situ mechanical TEM: Seeing and measuring under stress with electrons, Cr Phys 15(2-3) (2014) 224-240.

[58] E.T. Selig, R.S. Ladd, ASTM Committee D-18 on Soil and Rock for Engineering Purposes., ASTM International., Evaluation of relative density and its role in geotechnical projects involving cohesionless soils, American Society for Testing and Materials, Philadelphia, 1973.

[59] J. Wang, S.X. Mao, Atomistic perspective on in situ nanomechanics, Extreme Mechanics Letters (2016).

[60] S.H. Oh, M. Legros, D. Kiener, G. Dehm, In situ observation of dislocation nucleation and escape in a submicrometre aluminium single crystal, Nat Mater 8(2) (2009) 95-100.

[61] Q. Yu, Z.W. Shan, J. Li, X.X. Huang, L. Xiao, J. Sun, E. Ma, Strong crystal size effect on deformation twinning, Nature 463(7279) (2010) 335-338.

[62] J. Wang, Z. Zeng, C.R. Weinberger, Z. Zhang, T. Zhu, S.X. Mao, In situ atomic-scale observation of twinning-dominated deformation in nanoscale body-centred cubic tungsten, Nat Mater 14(6) (2015) 594-600.

[63] D. Kiener, P. Hosemann, S.A. Maloy, A.M. Minor, In situ nanocompression testing of irradiated copper, Nat Mater 10(8) (2011) 608-13.

[64] H. Zheng, A.J. Cao, C.R. Weinberger, J.Y. Huang, K. Du, J.B. Wang, Y.Y. Ma, Y.N. Xia, S.X. Mao, Discrete plasticity in sub-10-nm-sized gold crystals, Nat Commun 1 (2010).

[65] C.E. Carlton, P.J. Ferreira, In situ TEM nanoindentation of nanoparticles, Micron 43(11) (2012) 1134-1139.

[66] J. Kacher, Q. Yu, C. Chisholm, C. Gammer, A.M. Minor, In Situ TEM Nanomechanical Testing, (2016) 9-16.

[67] Z.W. Shan, In Situ TEM Investigation of the Mechanical Behavior of Micronanoscaled Metal Pillars, Jom-Us 64(10) (2012) 1229-1234.

[68] K. Zheng, C.C. Wang, Y.Q. Cheng, Y.H. Yue, X.D. Han, Z. Zhang, Z.W. Shan, S.X. Mao, M.M. Ye, Y.D. Yin, E. Ma, Electron-beam-assisted superplastic shaping of nanoscale amorphous silica, Nat Commun 1 (2010).

[69] D. Maharaj, B. Bhushan, Scale effects of nanomechanical properties and deformation behavior of Au nanoparticle and thin film using depth sensing nanoindentation, Beilstein J Nanotech 5 (2014) 822-836.

[70] R. Kositski, O. Kovalenko, S.W. Lee, J.R. Greer, E. Rabkin, D. Mordehai, Cross-Split of Dislocations: An Athermal and Rapid Plasticity Mechanism, Sci Rep-Uk 6 (2016).

[71] D. Liu, Mechanical characterization of isolated nanostructures, Rensselaer Polytechnic Institute, Troy, New York, 2004.

[72] S. Varghese, New method for estimating local strains using nanoindentation and atomic force microscopy, Oklahoma State University, 2006.

[73] X. Wei, Mechanical properties of nanoscale and atomic scale materials: Nanocrystalline copper and graphene Columbia University, 2009.

[74] W.H. Roos, R. Bruinsma, G.J.L. Wuite, Physical virology, Nature Physics 6(10) (2010) 733-743.

[75] K. Daeinabi, M.H. Korayem, Indentation analysis of nano-particle using nano-contact mechanics models during nano-manipulation based on atomic force microscopy, Journal of Nanoparticle Research 13(3) (2010) 1075-1091.

[76] B. Gan, H. Murakami, R. Maass, L. Meza, J.R. Greer, T. Ohmura, S. Tin, NANOINDENTATION AND NANO-COMPRESSION TESTING OF Ni3Al PRECIPITATES, Superalloys 2012 (2012) 83-91.

[77] E.L. Wood, T. Avant, G.S. Kim, S.K. Lee, Z. Burchman, J.M. Hughes, F. Sansoz, Size effects in bimetallic nickel-gold nanowires: Insight from atomic force microscopy nanoindentation, Acta Mater 66 (2014) 32-43.

[78] C.Z. Zhou, I.J. Beyerlein, R. LeSar, Plastic deformation mechanisms of fcc single crystals at small scales, Acta Mater 59(20) (2011) 7673-7682.

[79] X.Y. Li, W. Yang, Size Dependence of Dislocation-Mediated Plasticity in Ni Single Crystals: Molecular Dynamics Simulations, J Nanomater (2009).

[80] A.T. Jennings, C.R. Weinberger, S.W. Lee, Z.H. Aitken, L. Meza, J.R. Greer, Modeling dislocation nucleation strengths in pristine metallic nanowires under experimental conditions, Acta Mater 61(6) (2013) 2244-2259.

[81] H.D. Fan, Z.H. Li, M.S. Huang, Size effect on the compressive strength of hollow micropillars governed by wall thickness, Scripta Mater 67(3) (2012) 225-228.

[82] W.D. Nix, J.R. Greer, G. Feng, E.T. Lilleodden, Deformation at the nanometer and micrometer length scales: Effects of strain gradients and dislocation starvation, Thin Solid Films 515(6) (2007) 3152-3157.

[83] J.R. Greer, W.D. Nix, Size dependence in mechanical properties of gold at the micron scale in the absence of strain gradients, Appl Phys a-Mater 90(1) (2008) 203-203.

[84] M.B. Julia R. Greer, Bridging the gap between computational and experimental length scales: a review on nanoscale plasticity, Rev Adv Mater Sci 13 (2006) 59-70.

[85] K.J. Hemker, W.D. Nix, Nanoscale deformation - Seeing is believing, Nat Mater 7(2) (2008) 97-98.

[86] A. Jerusalem, A. Fernandez, A. Kunz, J.R. Greer, Continuum modeling of dislocation starvation and subsequent nucleation in nano-pillar compressions, Scripta Materialia 66(2) (2012) 93-96.

[87] T. Zhu, J. Li, A. Samanta, A. Leach, K. Gall, Temperature and strain-rate dependence of surface dislocation nucleation, Phys Rev Lett 100(2) (2008).

[88] D. Mordehai, S.W. Lee, B. Backes, D.J. Srolovitz, W.D. Nix, E. Rabkin, Size effect in compression of single-crystal gold microparticles, Acta Mater 59(13) (2011) 5202-5215.

[89] C.A. Volkert, E.T. Lilleodden, Size effects in the deformation of sub-micron Au columns, Philos Mag 86(33-35) (2006) 5567-5579.

[90] C.P. Frick, B.G. Clark, S. Orso, A.S. Schneider, E. Arzt, Size effect on strength and strain hardening of small-scale [111] nickel compression pillars, Materials Science and Engineering: A 489(1-2) (2008) 319-329.

[91] D.M. Dimiduk, M.D. Uchic, T.A. Parthasarathy, Size-affected single-slip behavior of pure nickel microcrystals, Acta Mater 53(15) (2005) 4065-4077.

[92] P.A. Gruber, C. Solenthaler, E. Arzt, R. Spolenak, Strong single-crystalline Au films tested by a new synchrotron technique, Acta Mater 56(8) (2008) 1876-1889.

[93] S.H. Oh, M. Legros, D. Kiener, P. Gruber, G. Dehm, In situ TEM straining of single crystal Au films on polyimide: Change of deformation mechanisms at the nanoscale, Acta Mater 55(16) (2007) 5558-5571.

[94] J.D. Kiely, J.E. Houston, Nanomechanical properties of Au (111), (001), and (110) surfaces, Phys Rev B 57(19) (1998) 12588-12594.

[95] J.D. Kiely, R.Q. Hwang, J.E. Houston, Effect of surface steps on the plastic threshold in nanoindentation, Phys Rev Lett 81(20) (1998) 4424-4427.

[96] A. Gouldstone, K.J. Van Vliet, S. Suresh, Nanoindentation - Simulation of defect nucleation in a crystal, Nature 411(6838) (2001) 656-656.

[97] J.A. Zimmerman, C.L. Kelchner, P.A. Klein, J.C. Hamilton, S.M. Foiles, Surface step effects on nanoindentation, Phys Rev Lett 87(16) (2001) art. no.-165507.

[98] H.B. Lu, Y.S. Ni, Effect of surface step on nanoindentation of thin films by multiscale analysis, Thin Solid Films 520(15) (2012) 4934-4940.

[99] D.B. Shan, L. Yuan, B. Guo, Multiscale simulation of surface step effects on nanoindentation, Mat Sci Eng a-Struct 412(1-2) (2005) 264-270.

[100] M.R. Shankar, Surface steps lead to heterogeneous contact mechanics and facilitate dislocation nucleation in nanoindentation, Appl Phys Lett 90(17) (2007).

[101] C. Li, G. Xu, Critical conditions for dislocation nucleation at surface steps, Philos Mag 86(20) (2006) 2957-2970.

[102] V. Navarro, O.R. de la Fuente, A. Mascaraque, J.M. Rojo, Uncommon dislocation processes at the incipient plasticity of stepped gold surfaces, Phys Rev Lett 100(10) (2008).

[103] Z.-J. Wang, Q.-J. Li, Z.-W. Shan, J. Li, J. Sun, E. Ma, Sample size effects on the large strain bursts in submicron aluminum pillars, Appl Phys Lett 100(7) (2012) 071906.

[104] C.Z. Zhou, S.B. Biner, R. LeSar, Discrete dislocation dynamics simulations of plasticity at small scales, Acta Mater 58(5) (2010) 1565-1577.

[105] S.W. Lee, S.M. Han, W.D. Nix, Uniaxial compression of fcc Au nanopillars on an MgO substrate: The effects of prestraining and annealing, Acta Mater 57(15) (2009) 4404-4415.

[106] J.R. Greer, C.R. Weinberger, W. Cai, Comparing the strength of f.c.c. and b.c.c. sub-micrometer pillars: Compression experiments and dislocation dynamics simulations, Mat Sci Eng a-Struct 493(1-2) (2008) 21-25.

[107] H. Tang, K.W. Schwarz, H.D. Espinosa, Dislocation escape-related size effects in single-crystal micropillars under uniaxial compression, Acta Mater 55(5) (2007) 1607-1616.

[108] J.J. Gilman, Oxide surface films on metal crystals, Science 306(5699) (2004) 1134-1134.

[109] D. Kiener, C. Motz, M. Rester, M. Jenko, G. Dehm, FIB damage of Cu and possible consequences for miniaturized mechanical tests, Mat Sci Eng a-Struct 459(1-2) (2007) 262-272.

[110] I. Ryu, W. Cai, W.D. Nix, H. Gao, Stochastic behaviors in plastic deformation of face-centered cubic micropillars governed by surface nucleation and truncated source operation, Acta Mater 95 (2015) 176-183.

[111] D.M. Norfleet, D.M. Dimiduk, S.J. Polasik, M.D. Uchic, M.J. Mills, Dislocation structures and their relationship to strength in deformed nickel microcrystals, Acta Mater 56(13) (2008) 2988-3001.

[112] F. Mompiou, M. Legros, A. Sedlmayr, D.S. Gianola, D. Caillard, O. Kraft, Source-based strengthening of sub-micrometer Al fibers, Acta Mater 60(3) (2012) 977-983.

[113] J. Senger, D. Weygand, P. Gumbsch, O. Kraft, Discrete dislocation simulations of the plasticity of micro-pillars under uniaxial loading, Scripta Mater 58(7) (2008) 587-590.

[114] Y.N. Cui, P. Lin, Z.L. Liu, Z. Zhuang, Theoretical and numerical investigations of single arm dislocation source controlled plastic flow in FCC micropillars, Int J Plasticity 55 (2014) 279-292.

[115] S.W. Lee, W.D. Nix, Geometrical analysis of 3D dislocation dynamics simulations of FCC micro-pillar plasticity, Mat Sci Eng a-Struct 527(7-8) (2010) 1903-1910.

[116] Y.N. Cui, Z.L. Liu, Z. Zhuang, Quantitative investigations on dislocation based discrete-continuous model of crystal plasticity at submicron scale, Int J Plasticity 69 (2015) 54-72.

[117] Y.N. Cui, Z.L. Liu, Z. Zhuang, Theoretical and numerical investigations on confined plasticity in micropillars, J Mech Phys Solids 76 (2015) 127-143.

[118] H.J. Chang, J. Segurado, J.M. Molina-Aldareguia, R. Soler, J. LLorca, A 3D dislocation dynamics analysis of the size effect on the strength of [111] LiF micropillars at 300K and 600K, Model Simul Mater Sc 24(3) (2016).

[119] Y.N. Cui, Z.L. Liu, Z.J. Wang, Z. Zhuang, Mechanical annealing under low-amplitude cyclic loading in micropillars, J Mech Phys Solids 89 (2016) 1-15.

[120] P. Lin, Z.L. Liu, Y.N. Cui, Z. Zhuang, A stochastic crystal plasticity model with size-dependent and intermittent strain bursts characteristics at micron scale, Int J Solids Struct 69-70 (2015) 267-276.

[121] S.W. Lee, A.T. Jennings, J.R. Greer, Emergence of enhanced strengths and Bauschinger effect in conformally passivated copper nanopillars as revealed by dislocation dynamics, Acta Mater 61(6) (2013) 1872-1885.

[122] B. Pan, Y. Shibutani, X. Zhang, F. Shang, Effect of dislocation pile-up on size-dependent yield strength in finite single-crystal micro-samples, J Appl Phys 118(1) (2015) 014305.

[123] C.R. Weinberger, W. Cai, The stability of Lomer-Cottrell jogs in nanopillars, Scripta Mater 64(6) (2011) 529-532.

[124] E. Tarleton, D.S. Balint, J. Gong, A.J. Wilkinson, A discrete dislocation plasticity study of the micro-cantilever size effect, Acta Mater 88 (2015) 271-282.

[125] X.W. Gu, C.N. Loynachan, Z.X. Wu, Y.W. Zhang, D.J. Srolovitz, J.R. Greer, Size-Dependent Deformation of Nanocrystalline Pt Nanopillars, Nano Lett 12(12) (2012) 6385-6392.

[126] S.I. Rao, D.M. Dimiduk, T.A. Parthasarathy, M.D. Uchic, M. Tang, C. Woodward, Athermal mechanisms of size-dependent crystal flow gleaned from three-dimensional discrete dislocation simulations, Acta Mater 56(13) (2008) 3245-3259.

[127] J.K. Diao, K. Gall, M.L. Dunn, J.A. Zimmerman, Atomistic simulations of the yielding of gold nanowires, Acta Mater 54(3) (2006) 643-653.

[128] J.Q. Hu, Z.L. Liu, Y.N. Cui, Z.J. Wang, Z.W. Shan, Z. Zhuang, Sensitive Material Behavior: Theoretical Model and Experiment for Compression Collapse of Gold Particles at Submicron Scale, J Appl Mech-T Asme 81(9) (2014).

[129] A.T. Jennings, M.J. Burek, J.R. Greer, Microstructure versus Size: Mechanical Properties of Electroplated Single Crystalline Cu Nanopillars, Phys Rev Lett 104(13) (2010).

[130] Y. Cui, The Investigation of Plastic Behavior by Discrete Dislocation Dynamics for Single Crystal Pillar at Submicron Scale, Springer Singapore2017.

[131] M. FIVEL, Discrete Dislocation Dynamics: Principles and Recent Applications, in: O. Cazacu (Ed.), Multiscale Modeling of Heterogenous Materials: From Microstructure to Macro-Scale Properties, John Wiley & Sons 2008.

[132] C.J. Ouyang, Z.H. Li, M.S. Huang, L.L. Hu, C.T. Hou, Combined influences of micro-pillar geometry and substrate constraint on microplastic behavior of compressed single-crystal micro-pillar: Two-dimensional discrete dislocation dynamics modeling, Mat Sci Eng a-Struct 526(1-2) (2009) 235-243.

[133] S. Akarapu, H.M. Zbib, D.F. Bahr, Analysis of heterogeneous deformation and dislocation dynamics in single crystal micropillars under compression, Int J Plasticity 26(2) (2010) 239-257.

[134] C.F.O. Dahlberg, On the role of interfaces in small scale plasticity, Department of Solid Mechanics, Royal Institute of Technology, 2011.

[135] D. Mordehai, M. Kazakevich, D.J. Srolovitz, E. Rabkin, Nanoindentation size effect in single-crystal nanoparticles and thin films: A comparative experimental and simulation study, Acta Mater 59(6) (2011) 2309-2321.

[136] I. Issa, J. Amodeo, J. Réthoré, L. Joly-Pottuz, C. Esnouf, J. Morthomas, M. Perez, J. Chevalier, K. Masenelli-Varlot, In situ investigation of MgO nanocube deformation at room temperature, Acta Mater 86 (2015) 295-304.

[137] E. Rabkin, D.J. Srolovitz, Onset of plasticity in gold nanopillar compression, Nano Lett 7(1) (2007) 101-107.

Chapter 3

3. The effect of crystal anisotropy and pre-existing defects on the incipient plasticity of FCC single crystals during nanoindentation

Molecular dynamics simulation is used to identify and quantify the initial plastic deformation mechanisms of gold as a model face-centered cubic (fcc) metal in the nanoindentation process. The coupling effects of crystallographic orientation and internal structural defects on the resulting load distribution at the onset of plasticity are investigated to clarify the anisotropic characteristics of material responses to crystallographic orientation. Homogenous defect nucleation is studied by correlating the indentation force-displacement curve with the instantaneous defect structure. In the absence of pre-existing defects, nanoindentation deformation is dominated by nucleation of Shockley partial dislocations regardless of crystal orientation. Various forms of dislocation propagation are observed in different crystal orientations. The elastic-plastic transition point appears later for the [111]-oriented surface than the ones for [001]-, and [011]-oriented surfaces. The relation of hardening and dislocation density shows that conventional Taylor hardening captures the plasticity after a certain amount of indentation depth in the presence of enough dislocation density. The crystal's sensitivity to the presence of internal structural faults is strongly dependent on the crystallographic orientation. Nanoindentation simulations in the presence of sessile dislocation loops in the structure show that the most significant reduction in the pop-in load happens for the [111] oriented sample. Our simulations suggest that the indentation near a defect can lead to small, subcritical events that lead to a smoother "pop- in" at the onset of plasticity. Since internal defects in materials are nearly inevitable, a defect-based model can be useful to understand the stochastic pop- in loads in nanoindentation tests.

3.1. Introduction

Nanoindentation testing is widely used to study the mechanical response of small volumes of materials and continuous improvements in load- and depth- measurement precision has allowed this technique to provide important insight into the initiation and

evolution of plasticity resulting from the movement of individual, or small groups of, dislocations [1]. As the deformation volume of a material decreases the effect of crystal orientation on its elastic and plastic mechanical response increases [2-4]. An ongoing limitation to the impact of high-resolution nanoindentation testing is the considerable difficulty in deducing the atomic scale activities occurring in the metal during the nanoindentation process [5]. In principle, molecular dynamics (MD) simulation can provide a complete representation of the near-field (core) and far-field atomic structure of a typical crystal defect, such as a dislocation, and is therefore an attractive technique for studies of the fundamental crystal defect nucleation and mobility during small-volume deformation processes such as nanoindentation albeit still at very high deformation rates and low temperatures. A large number of simulations have been recently carried out on FCC metals to investigate the relation between first dislocation nucleation and incipient plasticity [6-8]. Zhong and Zhu [9] demonstrated that nucleation, gliding, and interaction of Shockley partial dislocations (SPDs) are involved in the early stages of the FCC structures' plasticity. Quantitative analysis of dislocation multiplication during the early stages of plastic deformation was performed by Begau et al. [10]. Li et al. [11] studied defect generation during nanoindentation of Au single crystals, relating defect nucleation events to the characteristic peaks on the indentation force - depth curve. Fang et al. [12] performed an MD simulation study of the effect of various geometrical test parameters such as indenter tilt angle, indentation velocity, and dislocation slip orientation on the nanoindentation of (001) Al. Other previous studies have demonstrated that the effect of crystal defects on the mechanical properties of small volume samples is quite significant. The effect of surface defects lead to early yield by preferential dislocation nucleation has been studied by Navarro et al. [13]. The effect of pre nano-machining, as a simulation of subsurface crystal damage, was investigated by Zhang et al. [14] who demonstrated that the critical load for dislocation nucleation, i.e. the pop-in load, decreased with increased subsurface crystal damage. In a similar study, Liu et al. [15] concluded that the existence of subsurface stacking fault tetrahedra (SFTs) provide resistance to dislocation nucleation and enhances the "work hardening" effect. Lodes et al. [16] simulated the nanoindentation on a plastically deformed material and concluded that pre-deforming the material leads to a reduction in the indentation size effect and smoother elastic-plastic

transition. Njeim and Bahr [17], in a study of the effect of pre-existing vacancies on dislocation nucleation, reported that higher vacancy concentration resulted into a lower load at the onset of plasticity. Salehinia and Bahr [18] quantified the effect of internal defects on the onset of plasticity in copper. According to their findings, among a variety of moderately sized point defects, SFTs cause the largest reduction in initial yield stress Wang et al. [19] suggested that surface defects are more likely to be responsible for pop-ins during indentation along the <111> and <110> directions while bulk defects contribute to displacement bursts along the <100> directions. In another study, Salehinia and Bahr [20] observed that the temperature sensitivity of the initial yield stress was also significantly influenced by the presence of the internal defects.

While experimental nanoindentation test and numerical simulations have achieved significant results in nanoscale properties, there is still some unanswered question about the effect of initial crystal condition on the incipient plasticity and the evolution of dislocations in early stages of nanoindentation. In this paper MD modeling is used to explore the coupled effects of crystallographic orientation, and pre-existing structural defects on the distribution of pop-in loads and deformation mechanisms during nanoindentation of Au. A general view of the defect generation mechanisms and its evolution during the nanoindentation is provided. The onset of plasticity and its evolution is analyzed by quantifying dislocation density and identifying the dislocation evolution mechanisms. The validity of conventional continuum mechanic work hardening theory; i.e. Taylor hardening model, which has not been previously studied with full atomistic detail, and the effect of orientation on the hardening model is investigated for nanoindentation.

3.2. Methods

In this study, we model the deformation of FCC single-crystal Au. This metal was chosen because of its low yield stress, high crystal symmetry, and low stacking fault energy, which results in its plastic deformation by dislocation glide rather than more complex dislocation glide/twinning mechanisms. Molecular dynamic simulations were performed using the open-source Large-scale Atomic/Molecular Massively Parallel Simulator (LAMMPS) [21]. The simulation performed was the nanoindentation of an Au

volume, $40 \times 30 \times 40$ nm, containing 2,866,906 atoms. The simulation box was large enough that the effect of boundaries on the onset of plasticity was negligible. Three low-indexed surface orientations; [001], [110], and [111] are considered for analysis. Periodic boundary conditions were applied to the atoms along the lateral sides of the Au volume, while those along the top surface of the cell were unconstrained. The atomic positions of the bottom three layers of the sample were fixed, i.e. they are not moving in the course of simulations to avoid the motion of the entire sample. The next four layers at the bottom, as well as the outermost five layers along each lateral side, were kept at a fixed temperature of 300 K by a Nosé-Hoover thermostat [22]. Before performing the nanoindentation, the internal energy of the volume was minimized at 0 K using the conjugate gradient (CG) algorithm, until energy tolerance is less than 10^{-6} eV and a force tolerance of 10^{-8} eV/Å. The system was equilibrated for 80 ps after minimization with the temperature increasing to 300 K with a Nosé-Hoover thermostat [22] followed by 80 ps thermal relaxation at 300K with a barostat ensemble [23], to obtain a well-distributed temperature and pressure profile.

Indentation simulation proceeded with the 8 nm diameter spherical indenter pressing into the Au to a depth of 4 nm at a velocity of 5 m/s followed by complete retraction at 10 m/s. Test simulations with a lower indentation and retraction velocities (1 m/s and 2 m/s respectively) were performed as well, but this alters the results only negligibly. A non-atomic rigid sphere is used as the indenter to save the computation time. The indenter repels all the atoms it contacts, and the interaction potential can be expressed as:

$$F(r) = -k(r - R)^2 \tag{3.1}$$

where k is the specified force constant equal to 10 eV/A^2, r is the distance from the atom to the center of the indenter, and R is the radius of the indenter. The Au embedded-atom method (EAM) potential developed by Foiles et al. [24] is used to simulate the Au–Au atomic interaction. Common neighbor analysis (CNA) [25] is used to analyze the local atomic crystal structure. Dislocation Extract Algorithm (DXA) [26] is applied to identify the dislocation patterns, and the Open Visualization Tool OVITO [27] is utilized to visualize the atomistic configurations.

To verify the accuracy of the MD simulation, the elastic region of the indentation force *P* versus indentation depth *h* curves obtained by MD simulation of [111] oriented Au was compared with the predicted *P-h* curve derived from application of the classic Hertz elastic sphere-flat surface contact solution.

$$P = \frac{4}{3}E^* R^{1/2} h^{3/2}$$ (3.2)

where R is the indenter radius, h is the indentation depth, and E^* is the reduced elastic modulus expressed as[28]:

$$\frac{1}{E^*} = \frac{1 - v_1^{\ 2}}{E_1} + \frac{1 - v_2^{\ 2}}{E_2}$$ (3.3)

E_1, E_2 are the elastic moduli and v_1, v_2 are Poisson's ratios of the Au and spherical indenter, respectively. The elastic modulus and Poisson's ratio of Au gold were taken as 85 GPa and 0.44 [29], and the elastic modulus of the rigid sphere is assumed to be infinitely large. As can be observed in Figure 3.1, the *P-h* curve obtained from MD simulation fits closely to that predicted by the Hertz elastic contact theory and demonstrates the numerical accuracy of the MD simulation. Deviation of the MD simulation from the elastic solution appears at *h* = 0.38 nm and corresponds to the onset of first plastic deformation events.
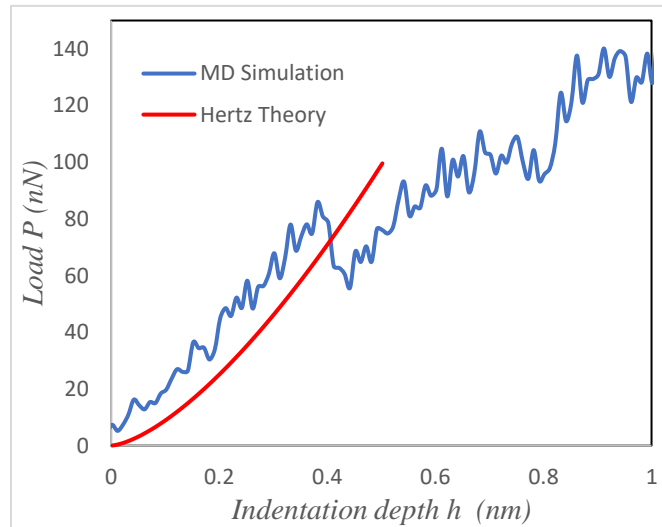
Figure 3.1: Indentation force P versus indentation depth h for the nano-indentation of [111] oriented Au thin film. The results from the MD simulation correspond quite

closely to that predicted by the Hertz elastic contact equations (Eq. 1) up to h = 0.38 nm at which point the first plastic deformation event occurs. The MD simulation predicts a small positive P when h = 0 due to the repulsive force between the indenter and the Au atoms.

3.3. Dislocation nucleation and evolution

Our MD simulations have provided data that allow a detailed analysis of the nucleation, growth, and interaction of crystal defects during the early stages of the nanoindentation of Au. What follows is a description of the ideal case; namely, nanoindentation of initially defect-free [111] oriented Au. We then describe simulations of the nanoindentation of [001] and [110] oriented Au to assess the effect of crystal orientation and finally describe the effect of pre-existing crystal defects on the nanoindentation deformation process.

3.3.1.   Dislocation nucleation and growth in defect-free [111] oriented Au

A typical indentation P vs h curve generated by MD simulation of initially defect-free [111] oriented Au is shown in Figure 3.2. The force P is slightly positive at the beginning of indentation, when $h = 0$, due to repulsive forces between the indenter and the Au atoms. The indentation force increases with increasing h until point "a" when two ($\bar{1}11$) and ($11\bar{1}$) stacking faults are created. These are the leading partial dislocations that expand and intersect to form a full dislocation of b = a/6[$\bar{2}1\bar{1}$] (Figure 3.3a).

The next force drop, point "b" (Figure 3.2), occurs before the formation of a tetrahedral sessile {111} dislocation lock. Each face of the tetrahedron is a stacking-fault with Shockley partial dislocations along the <110> edges of the intersection. Subsequent defect structure evolution is local glides of partial dislocations emerging from the faces of tetrahedron which gradually reconfigure into irregularly shaped clusters of dislocation loops and stacking faults. Appearance and disappearance of partial dislocations occur mainly along the {111}-type slip planes underneath the indenter tip. These multifaceted local dislocation glide results in the highly oscillatory P vs h response shown in Figure 3.2.

As the indentation depth h increases fluctuations in the P vs h response continue and the deformation process is primarily dominated by dislocation nucleation events (Figure 3.2 & Figure 3.3). The defects present in the Au indentation zone are mainly {111} stacking faults (SFs) growing in one of three <110> directions. Figure 3.3c shows the structure of dislocation and stacking faults when $h = 0.692$ nm, in which a (111) stacking fault is created 2.1 nm under the indenter surface and five {111} stacking faults connect it to the indenter surface. As the size of the {111} SFs increase they begin to intersect to form V-shaped locked defect structures. These locks start to glide along the common <110> direction of their constituent planes, resulting in the reduction of the developed (111) plane area. Figure 3d shows the development and glide of one of these locks related to force drop at point "d" (Figure 3.2).

The deformation phenomena consisting of nucleation and growth of SFs and the generation and glide of V-shaped locked defect structures continues until point "e" (Figure 3.2) where the surface of the indentation reaches the (111) plane upon which defect nucleation originally began. From then on, mobile edge dislocation loops are nucleated and grow by glide on the affected {111} planes. This results in an indentation load drop concurrent with the first large loop formation at $h = 1.79$ nm (Figure 3.3e). These loops are embryonic prismatic loops that can later grow and separate from indentation region. During the long period of (i), observed are active appearing and disappearing motions of local dislocation loops along the {111}-type slip planes underneath the indenter tip. These multifaceted local glides of dislocations result in the highly oscillatory response in the load-displacement curve. Figure 3.3 f presents the growth of the main (111) loop related to the point f on the load-displacement curve. These loops keep competing to grow until one of them is finally triggered to evolve into an isolated prismatic dislocation loop. However, due to the instability nature all over the procedure, it is almost impossible to predict precisely when the prismatic loop is emitted.

The first local dislocation loop separates from the dislocation network at the depth of 2.72 nm (point g). Being expelled by the stress field of the matrix, emitted loop starts to move away through the surface along the $[0\bar{1}1]$; the common direction of its four sides (Figure 3.3g). The formation of this half prismatic loop is accompanying the small load

relaxation at point g. From this point on, dislocations can be divided into two groups. The first group of dislocations is those that still stick to the surface beneath the indenter. The second group is closed dislocation loops that move out of the surface indentation volume, along the free surface or deeper into the simulation volume. The energy release in result of the dislocation loop emission leads to the overall re-increase of indenting load during the period of loop glide until the next partial loop is triggered to fully grow, as denoted by (h) in Figure 3.2. The formation of the second half prismatic loop from the tail of the grown (111) loop will result in the sudden drop at point h of the load-displacement curve. This one moves along $[\bar{1}10]$ direction. Prismatic loops glide, either through the thickness or along the surface, play an important role in plastic deformation as they carry deformation energy impulses and thus propagate the permanent deformation far away from the vicinity of indenter tip. As it is observed after the creation of prismatic loops, the shape of the dislocation structure does not change significantly and the deformation mechanism is manlily characterized by the movement of the created loop until it reaches out of the material. The third half prismatic loop is released at d ≈ 3.33 nm and glides along $[\bar{1}01]$ direction, resulting in the load relaxation at point i. Since the thickness of the substrate is thin, the partial dislocation loop in our simulation cannot become a complete prismatic dislocation loop. Figure 3.3 h and i refer to the status of dislocations network after the indentation from the side and bottom view, respectively to reveal the distinct {111} planes along which defect structures propagate and their interactions during the nanoindentation process.

To summarize, three stages are involved in the mechanism of incipient plasticity during nanoindentation of [111]-oriented Au: i) Subsurface nucleation of {111} stacking faults and their growth, formation of tetrahedral sessile dislocation locks with the local glide of complementary dislocations, ii) Intersection of stacking faults, formation of V lock defect structures and embryonic partial dislocation loops, and iii) Extended glide of dislocation loops from the region near the indenter to the bulk Au or the nearby Au surface.

In the case of nanoindentation of fcc metals with higher stacking fault energy, glide, and growth of locks and loops happens with thinner stacking fault planes. To investigate the effect of stacking fault energy upon the nanoindentation deformation process we

reconfigured our MD model to simulate the nanoindentation of [111] oriented Al thin film. The Al embedded-atom method (EAM) potential developed by Mishin et al. [30] was employed in this simulation. Aluminum has a stacking fault energy about four times higher than Au [31, 32]. Figure 3.4 depicts some of the deformation stages of the Al. The deformation is mainly dominated by the development of the embryonic dislocation loops and the emission of half prismatic loops to the surface. In this case, the dislocation loops are surrounded by thinner stacking fault planes compared to Au deformation. These results are consistent with the findings of Tsuru and Shibutani [2].
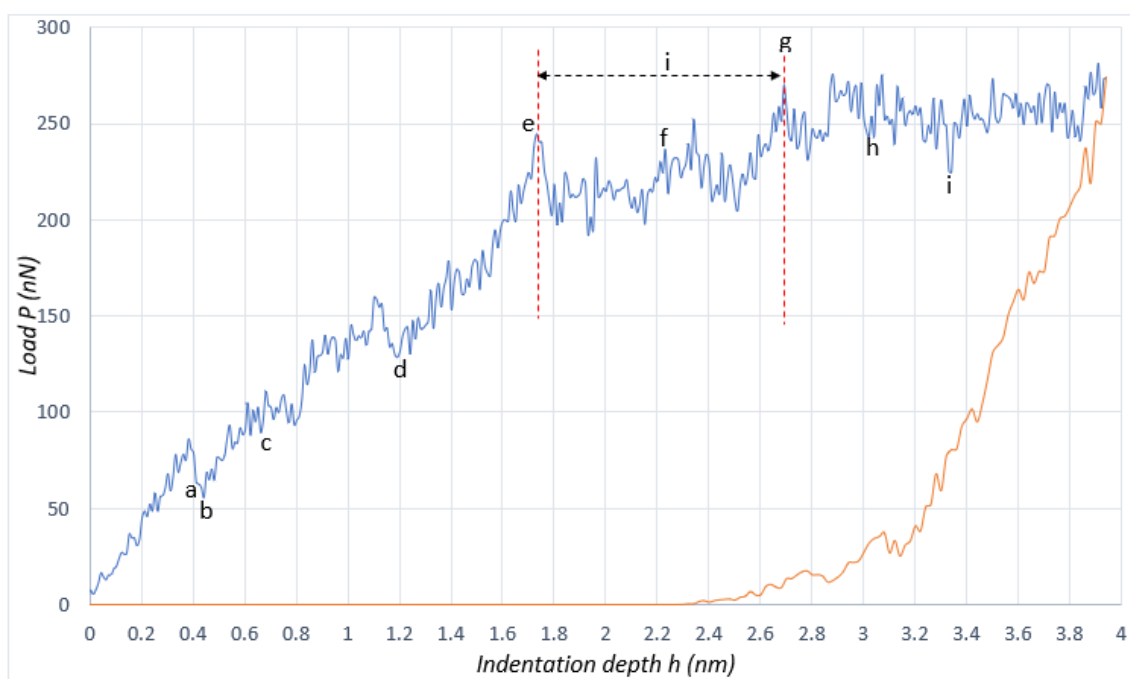
Figure 3.2: MD simulated indentation force P versus indentation depth h for the nano-indentation of [111] oriented Au. Specific force oscillation events are labeled. These events are referred to in the text and the deformed microstructure of the Au corresponding to these events is shown in figure 3.3.
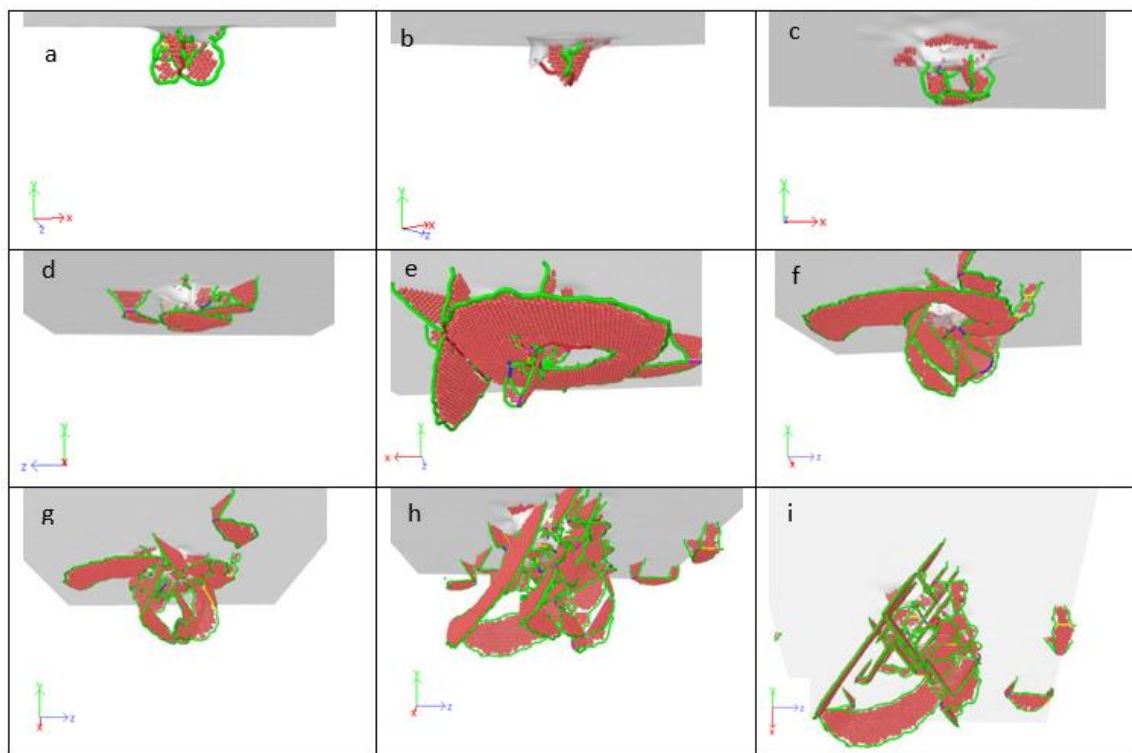
Figure 3.3: MD simulated crystal defect distribution resulting in [111] oriented Au during indentation (Fig. 3.2). (a) Deformation corresponding to Point "a", (b) Deformation corresponding to Point "b", (c) Deformation corresponding to Point "c", (d) Deformation corresponding to Point "d", (e) Deformation corresponding to Point "e", (f) Deformation corresponding to Point "f", (g) Deformation corresponding to Point "g", (h) and (i) dislocations network after the indentation from the side and bottom view.
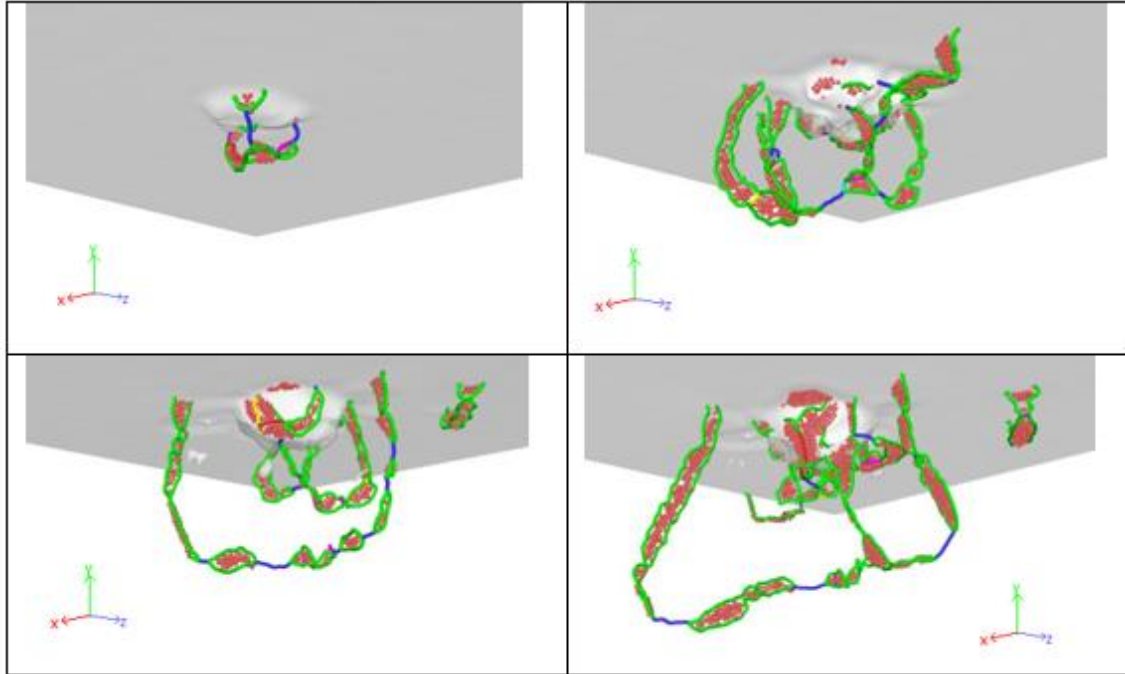
Figure 3.4: MD simulated crystal defect distribution resulting in [111] oriented Al during indentation. (a) depth of 0.692 nm, (b) depth of 1.692 nm, (c) depth of 2.212 nm, (d) depth of 2.852 nm.

3.3.2.   Effect of crystal orientation on the initial plastic event

Nanoindentation of (110) and (001) Au surfaces were simulated using the same loading and computational conditions described previously for [111] oriented Au indentation. The resulting P - h curves are compared in Figure 3.5. As the initial loading curves indicate, the [111] oriented sample is mechanically stiffer than the [110] oriented sample (85.9 nN and 71.3 nN yielding point force, respectively), and the elastic anisotropy is observed in the behavior of Au oriented films. Moreover, the same moduli are observed in the considered orientations. These observations are in good agreement with the literature [4, 33] [9]. The considerable difference in the onset of the plasticity of the [111]- oriented sample with the other orientations can be explained by its lower Schmid factor. As the FCC glide systems $<1\bar{1}0>\{111\}$ are at quite oblique angles to the indentation force direction; the Schmid factor for the [111] oriented sample is only $\sqrt{2/27}$. Since the Schmid factor is $1/\sqrt{6}$ for the (001) and (110) planes (around 1.5 times higher than the one for (111) plane), glide systems are more easily activated for the

(001) and (110) surfaces. After starting the plastic deformation, the effect of orientation decreases for the [111]- and [110]-oriented samples, but the [001]-oriented sample shows a little different behavior with a higher rate of hardening. The difference can be related to the easier and faster formation and emission of prismatic loops in the [001] oriented sample (Figure 3.6).

Figure 3.6 shows snapshots of the dislocation structure beneath indentations of various depths, up to $h = 3.93$nm, for the [001], [110], and [111] oriented Au indentations. The size of the plastic zone and the orientation and direction that the emitted prismatic loops travel varies with crystal orientation. For instance, at the depth of $h = 3.93$nm, indentation on the (001) Au surface results in the emission of a partial dislocation loop that grows in a direction essentially parallel to the indented surface and interacts with the free surface while indentations on the (110) and (111) surfaces are associated with emission of partial dislocation loops on oblique planes that grow in the <110> direction into the bulk Au. The result is that the indentation plastic zone is smaller and more localized around the [001] Au indentation compared to the [110] and [111] indentations. This is consistent with the previous observations of a more localized plastic zone in the [001] than for [110] and [111] indentations in FCC metals [33].
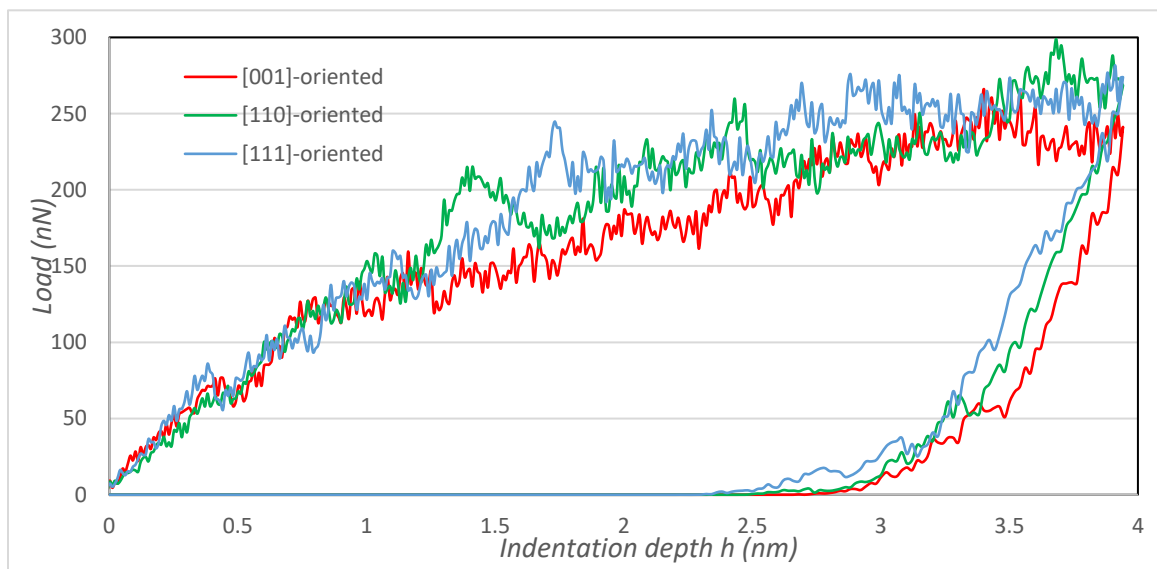
Figure 3.5: MD simulated indentation force P versus indentation depth h for the nano-indentation of Au performed on (001), (110), and (111) surfaces.
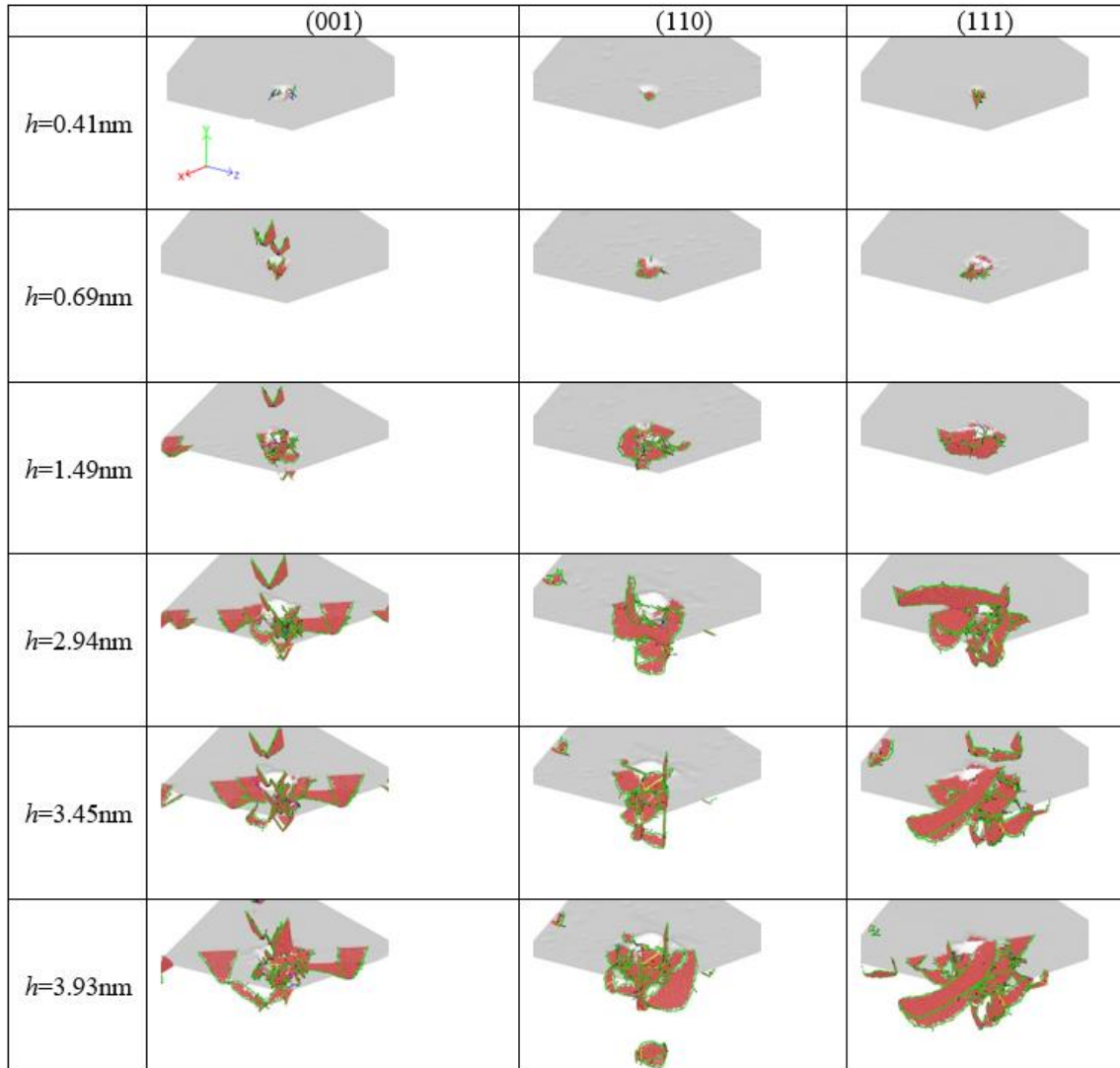
Figure 3.6: Crystal defect distribution at various depths h during MD simulated indentation of (001), (110), and (111) Au surfaces.

As the region below the indentation deforms plastically, a pile-up pattern is formed on the Au free surface (Figure 3.7). The pattern follows the symmetry of the primary $<1\bar{1}0>\{111\}$ dislocation slip.

The indented (001) Au surface (Figure 3.7a) displays slip steps in four directions around the indentation center corresponding to the $\langle 1\ 1\ 0 \rangle$ directions. In more details, the primary (111) and ($1\bar{1}1$) slip planes intersect the surface along the [110] and [$1\bar{1}0$] directions. Thus, a four-fold symmetry arises in the slip steps on the indented (001) Au

surface. Experimental indentation of the [001] oriented FCC samples shows similar slip-step pattern upon the indented surface [34].

The indented (110) Au surface (Figure 3.7b) displays slip steps that extend along four directions however the pattern is different than the four-fold symmetry pattern on (001) Au indented surface. For the (110) surface the primary $(1\bar{1}1)$, and $(11\bar{1})$ slip planes project into the surface along the $[21\bar{1}]$ and $[2\bar{1}1]$ directions, revealing two-fold symmetry pattern on the (110) Au surface [35].

The indented (111) Au surface (Figure 3.7c) displays projection of $(\bar{1}11)$, $(1\bar{1}1)$, and $(11\bar{1})$ active slip planes along the $[01\bar{1}]$, $[10\bar{1}]$ and $[1\bar{1}0]$ on the (111) surface. This results in a slip step pattern with sixfold symmetry on the surface. This is consistent with experimental and FEM simulation results of observed pile-up patterns in the nano-indentation of FCC crystals [35-37].
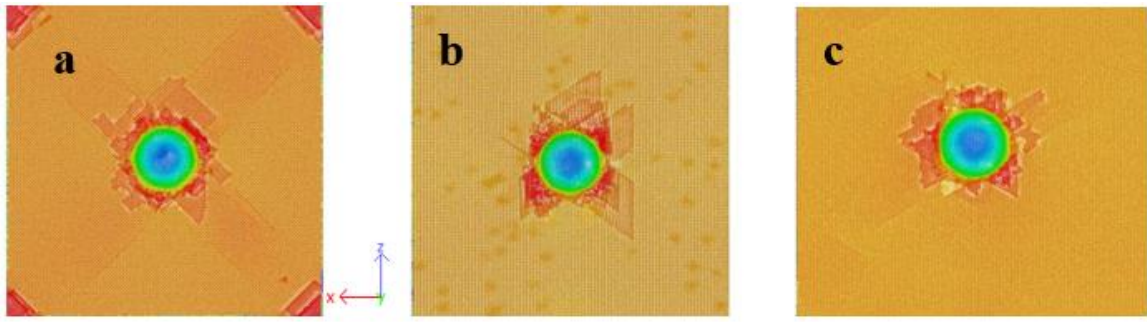
Figure 3.7: The Au surface after nanoindentation, to a depth of h = 3.94 nm, showing anisotropic slip steps resulting from dislocation intersection for (a) (001), (b) (110), and (c) (111) surfaces.

3.4. Dislocation density and plastic zone

The plastically deformed volume beneath an indentation is traditionally assumed to be hemispherical in shape. For a spherical indentation of radius R and indentation depth h, the contact radius $a_c(h)$ is defined as [38]:

$$a_c(h) = \sqrt{R^2 - (R - h)^2} \tag{3.4}$$

The radius of the hemispherical plastic zone beneath the indentation is then determined as $R_{pl} = f\, a_c$ where f is in the range of 0 - 3.5 [39]. Our MD simulations allow us to measure

R_{pl} as the distance to the furthest dislocation in the deformed volume beneath the indenter [40]. The value of f is then obtained by comparing the visualized R_{pl} with the calculated a_c (Figure 3.8). Although f can be taken to be constant and independent of indentation depth when one considers indentation to occur in an isotropic continuum [39], our results suggest that f generally increases with increasing indentation depth, as;

$$f(h) = 2.182(h)^{0.55} \qquad (3.4)$$

where the indentation depth h is expressed in units of nm. Voyiadjis and Yaghoobi [40] also reported similar dependence of f upon h during simulated nano-indentation of Ni thin films.

The total dislocation line length λ in the visualized plastic zone is shown in Figure 3.9 and, in the early stages of indentation ($h < 1.7$ nm), is essentially the same for the [001], [110], and [111] Au orientations. As the h increases, λ grows and its growth rate is greatest in the [111] oriented Au sample. This likely reflects the higher rate of prismatic loops separation form the plastic zone in the [001] and [110] orientation compared to the [111] orientation.

The dislocation density $\rho(h)$ within the indentation plastic zone can now be calculated from the measured $\lambda(h)$ and the calculated plastic zone volume $V_{pl}(h)$ as;

$$\rho(h) = \frac{\lambda(h)}{V_{pl}(h)} \qquad (3.5)$$

where

$$V_{pl}(h) = \frac{2\pi}{3}R_{pl}{}^3 - V_{indent} = \frac{2\pi}{3}\left((R_{pl})^3 - R^3\right) \qquad (3.6)$$

where $R_{pl} = fa_c$. Incorporating our expressions for plastic zone volume ($V_{pl}(h)$) and having the dislocation length ($\lambda(h)$), we can calculate the instantaneous dislocation density as a function of indentation depth (Figure 3.10).
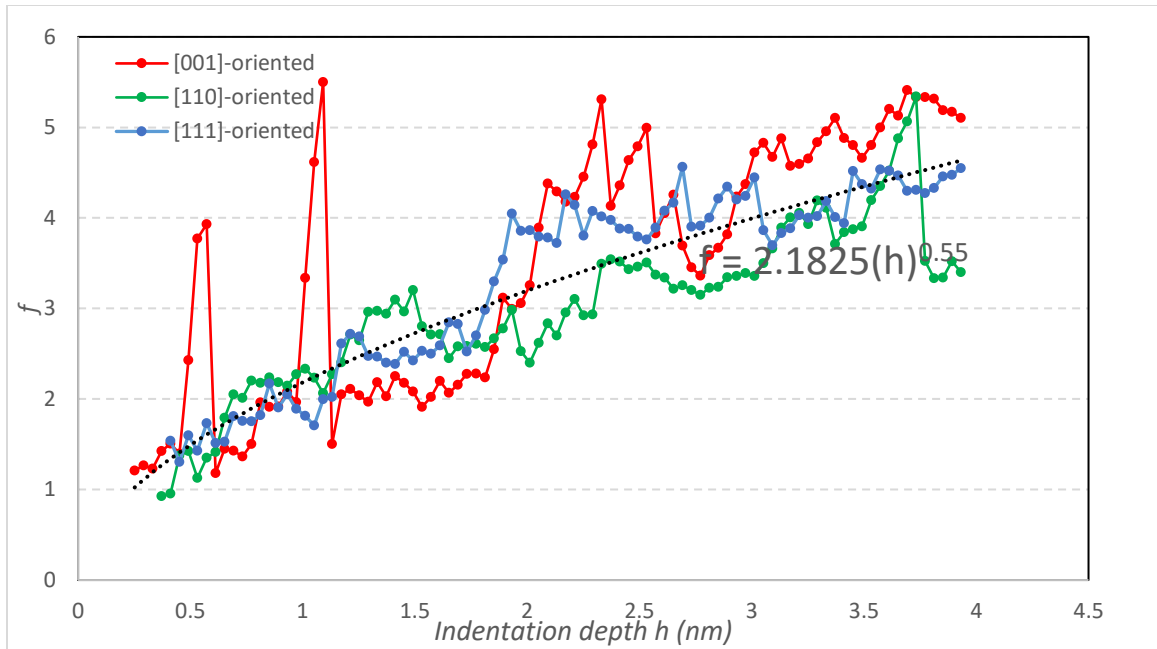
Figure 3.8: Correlation parameter f relating the measured hemispherical plastic zone radius Rpl to the indentation contact radius ac versus indentation depth h for MD simulations of nanoindentations performed on (001), (110), and (111) Au surfaces.
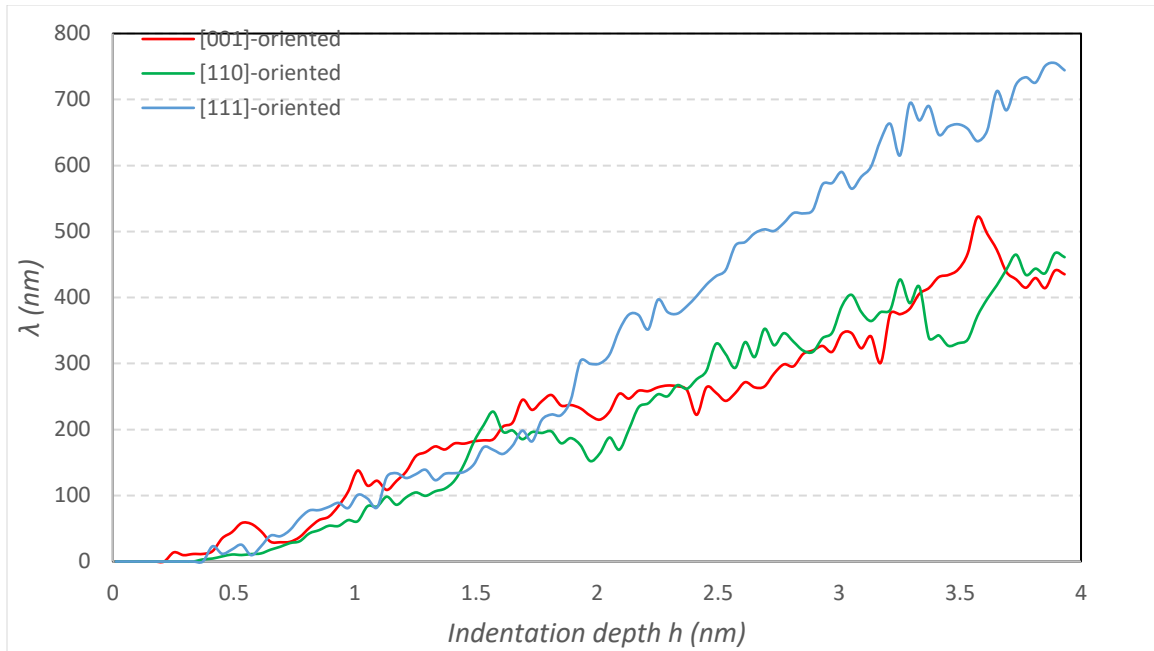
Figure 3.9: Dislocation length based on indentation depth for [001], [110] and [111] orientations.
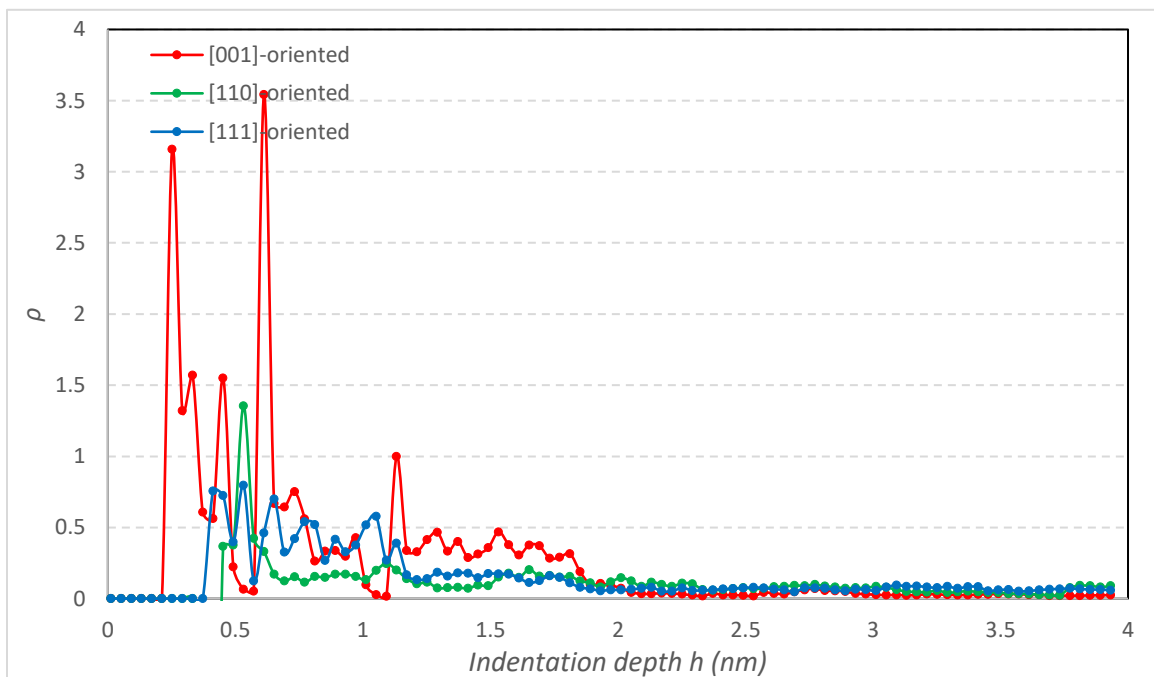
Figure 3.10: Dislocation density based on indentation depth for [001], [110] and [111] orientations.

In the next step, the nanoindentation hardness is calculated by dividing the indentation force, provided by the MD simulation, by the contact area as defined by the indentation contact radius $a_c(h)$ (Eq. 3.3). The variation of hardness with the indentation depth is shown in Figure 3.11. Based on conventional theories of plasticity, the nanoindentation hardness is related to the dislocation density when there is enough dislocation length in the plastic zone to activate forest hardening behavior [41]. To investigate the relationship between hardness and dislocation density at the early stages of plasticity, the indentation hardness total dislocation line length and dislocation density within the indentation plastic zone is plotted versus indentation depth for the [111]-oriented sample (Figure 3.12). The indentation hardness displays a stochastic behavior at the early stages of deformation. As the total dislocation line length in the plastic zone increases, the indentation hardness decreases, and it follows the same trend of dislocation density after a certain depth of indentation (around 2.1 nm).
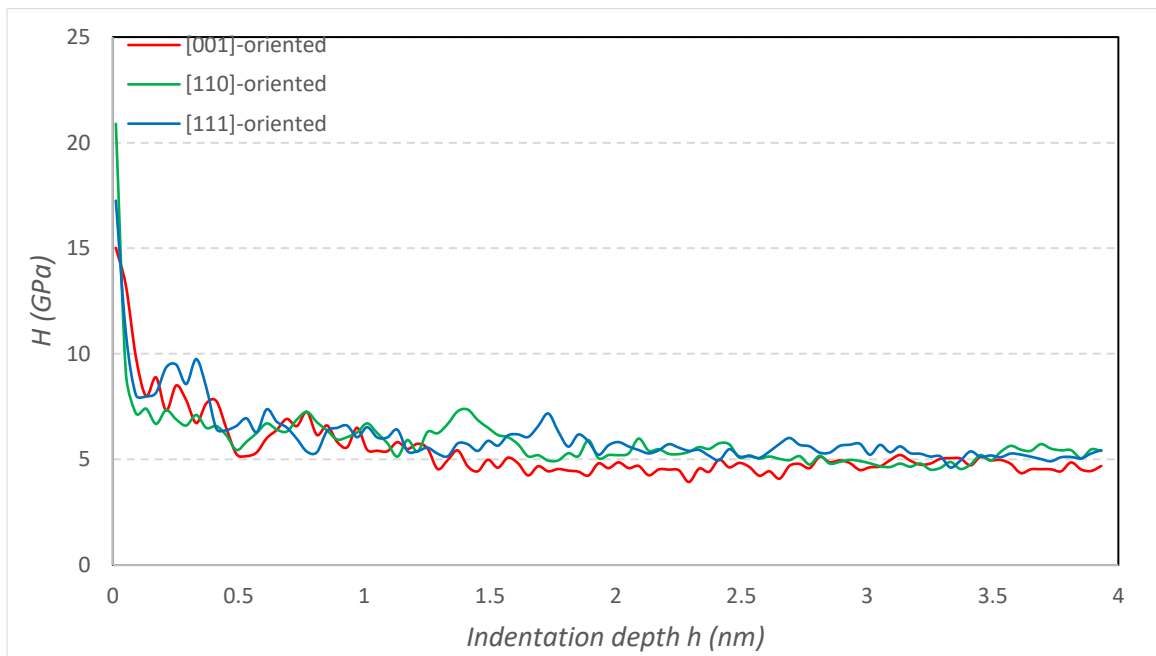
Figure 3.11: Hardness based on indentation depth for [001], [110] and [111] orientations.
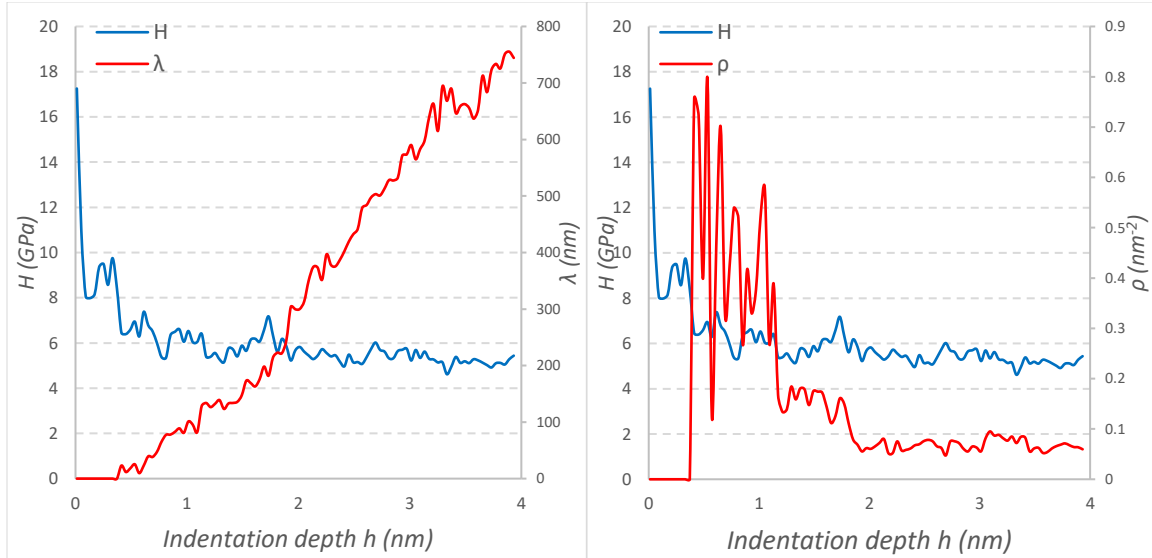
Figure 3.12: The relation of hardness and (a) total dislocation lengths in the plastic zone (b) dislocation density for the [111] oriented sample.

We can now use the *H(h)* and *ρ(h)* data from the MD simulations to assess the accuracy of the well-known Taylor hardening model in describing the deformation in the early stages of nanoindentation. The Tylor hardening model represents a classical continuum mechanics-based, description of dislocation hardening and expresses *H* as a function of dislocation density ρ as;

$$H = 3\sqrt{3}\alpha\mu b\sqrt{\rho} \tag{3.6}$$

where α, μ and b are an empirical constant, the shear modulus, and the Burgers vector, respectively. The empirical constant is in the range of 0.3–0.5 [42] and is affected by many factors, e.g. deformation, deformation rate, temperature, dislocation distribution, crystal orientation, alloying, etc. [42]. Therefore, according to the Taylor hardening model, the hardness is directly related to $\sqrt{\rho}$ when the dislocation density is high and the deforming volume is large enough to be considered as a continuum free from the influence of external boundaries. However, the question then arises about how accurate is the Taylor hardening model, eq.(3.6), when the deforming volume is very small and the dislocation density is low in the early stages of the nanoindentation process. It is obvious that the Taylor hardening expression, eq. (3.6), cannot predict the hardness before the dislocation nucleation, i.e. when ρ = 0. Figure 3.13 depicts the MD simulation results of

indentation hardness H and $\sqrt{\rho}$ versus indentation depth h for indentations made in Au of different crystal orientations. From Figure 3.13, it is apparent that, after a certain indentation depth of about 2 nm, there is a linear relation between hardness H and $\sqrt{\rho}$. The coefficient of this relationship is different for the three orientations considered. Looking at the Taylor hardening equation (eq. 3.6), the coefficient is related to the empirical constant and shear modulus, which both are orientation dependent. The average shear modulus and the magnitude of the Burgers vector are 27 GPa and 0.288 nm for Au [43]. The value of empirical constant is different for FCC metals based on the type of dislocation distribution [42]. Assuming that plasticity mainly happens by reaction between primary and loop-shaped forest dislocations, as shown in Figure 3.3 (f-i), after around 2 nm indentation depth, the empirical constant is $\alpha = 0.57$ [42]. When these values for a, m, and b are applied in eq. 6, the resulting average $H - \sqrt{\rho}$ proportionality constant becomes 23.03 which is close to the values shown in Figure 3.13. Combining coefficients and constants of eq. 3.6, we can express the $H - \sqrt{\rho}$ relationship as;

$$H = A\sqrt{\rho} \tag{3.7}$$
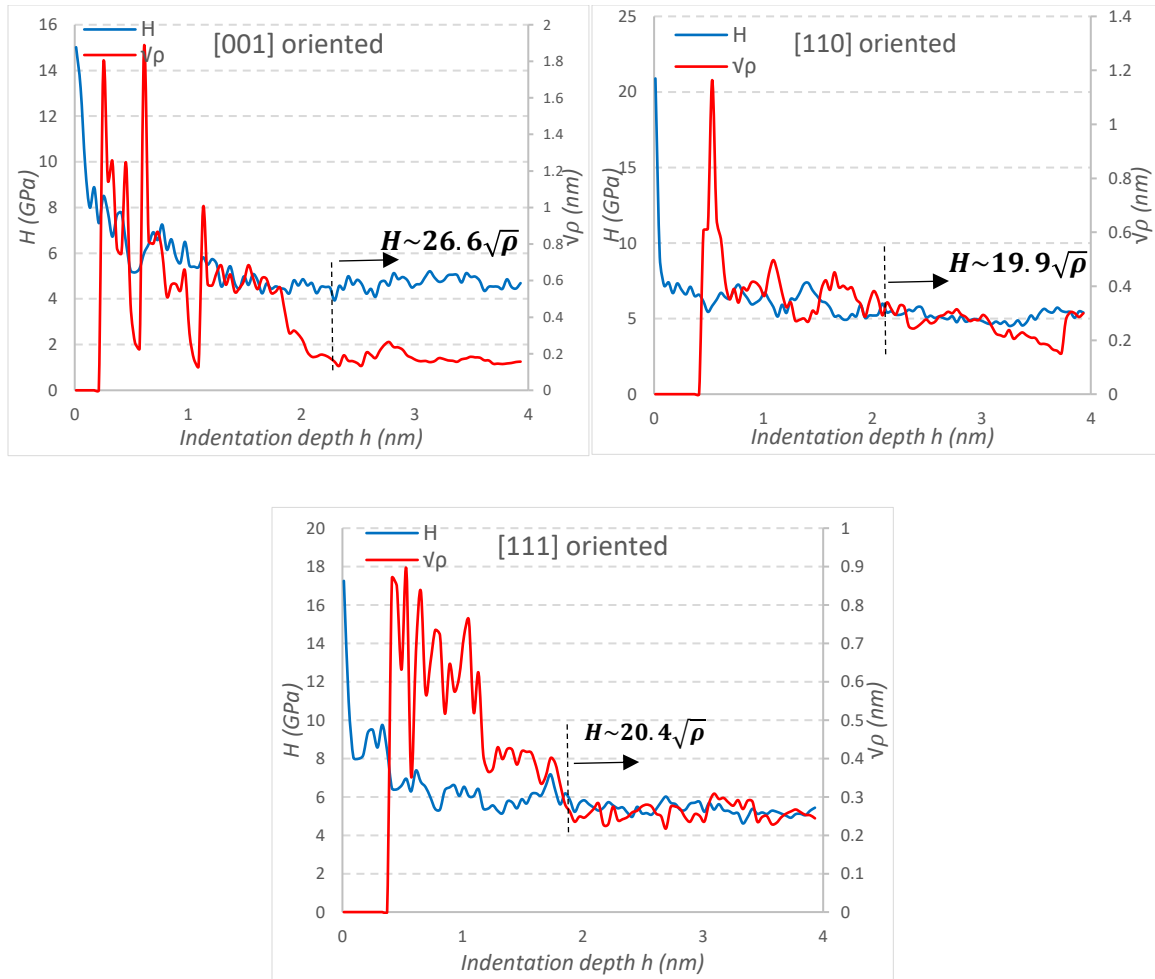
Figure 3.13: The relation of nanoindentation hardness and √ρ for (a) [001], (b) [110], (c) [111] oriented Au samples.

3.5. Effect of pre-existing defects

The presence of pre-existing crystal defects alters the deformation behavior of a single crystal. Here, pre-existing stacking faults (SFs) were introduced into our MD simulation to understand their effect on the mechanical response during the nanoindentation of Au. The pre-existing SFs were created by first forming a perfect crystal atomic structure, which was then stabilized using the conjugate gradient (CG) method. Stacking fault platelets were then generated by relaxation of a circular Frank loop platelet of vacancies on {111} planes, located at different points in the sample. Depending on the initial diameter of the vacancy platelet and the crystal orientation, a network of stacking fault

planes and tetrahedrons sized between 2 to 2.5 nm was developed after equilibrating the system at 300 K for 160 ps (Figure 3.14).
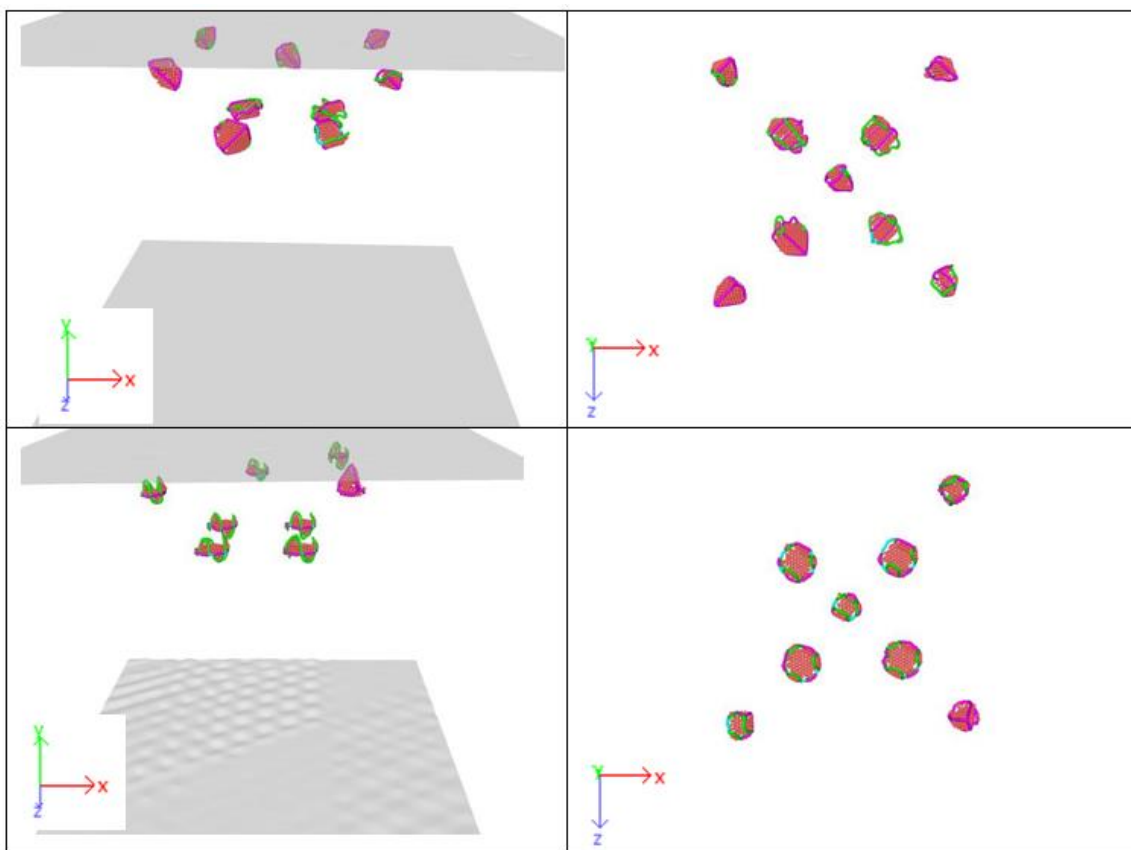
Figure 3.14: Side and top view of the pre-existing stacking fault defects introduced into the a, b) [001] oriented Au, c, d) [111] oriented Au samples.

Figure 3.15 and 3.16 compare the resulting indentation load-displacement curves of [001]- and [111]-oriented Au crystals with- and without-pre-existing SF defects. The presence of pre-existing defects affects the mechanical response differently based upon the specific crystal orientation relative to the indentation direction. For example, for the [111]-oriented sample, a 14.5% load drop is observed at the onset of plasticity; that is the point where the first dislocation is nucleated, while only 5.2% load drop is observed for the [001]-oriented samples.

The inset images in Figure 3.15 and 3.16 illustrate the dislocation distribution within the Au at various points during the indentation process. The dislocation distribution is clearly

quite complex and variable with dislocation loop nucleation occurring beneath the indenter and interaction of these dislocations with themselves and with the pre-existing SFs to create new dislocations some of whom are sessile while others are mobile. As an example, the pre-existed SFT beneath the indenter accelerates the onset of plasticity at the [001]-oriented sample, by reacting with the nucleated dislocations and annihilating through the surface (h=0.442nm). On the other hand, for the [111]-oriented sample, the stacking fault under the pit starts to develop and form a network of dislocation, while it is still separated from the deformation surface and seems to decelerate the onset of plasticity (Figure 3.16). The plastic zone develops and grows faster in result of having pre-existing defects in the crystal. This is observed in both Figure 3.15 and 3.16, at different deformation depths. The first complete prismatic loop is emitted at the 2.49nm indentation depth for the [111]-oriented crystal with pre-existing defects and glides through the martial along with $<0\,0\,\bar{1}>$ direction. However, no complete prismatic loop is generated at the plastic zone of the defect-free crystal until the depth of 3.94 nm.

A phenomenon that can be observed in the deformation of the [001]- and [111]-oriented crystals with pre-existing defects, is the lower load-drop at incipient plasticity and smoother transition from elastic to plastic deformation. The reason can be the heterogeneous activation of pre-existing faults under the surface in contrast to the homogeneous nucleation of critical defects in the defect-free crystal. This is consistent with the results of indenting a pre-deformed crystal [14, 16]. However, the [110]-oriented sample yields with a big pop-in in the presence of pre-existed stacking faults in the crystal (Figure 3.17b).
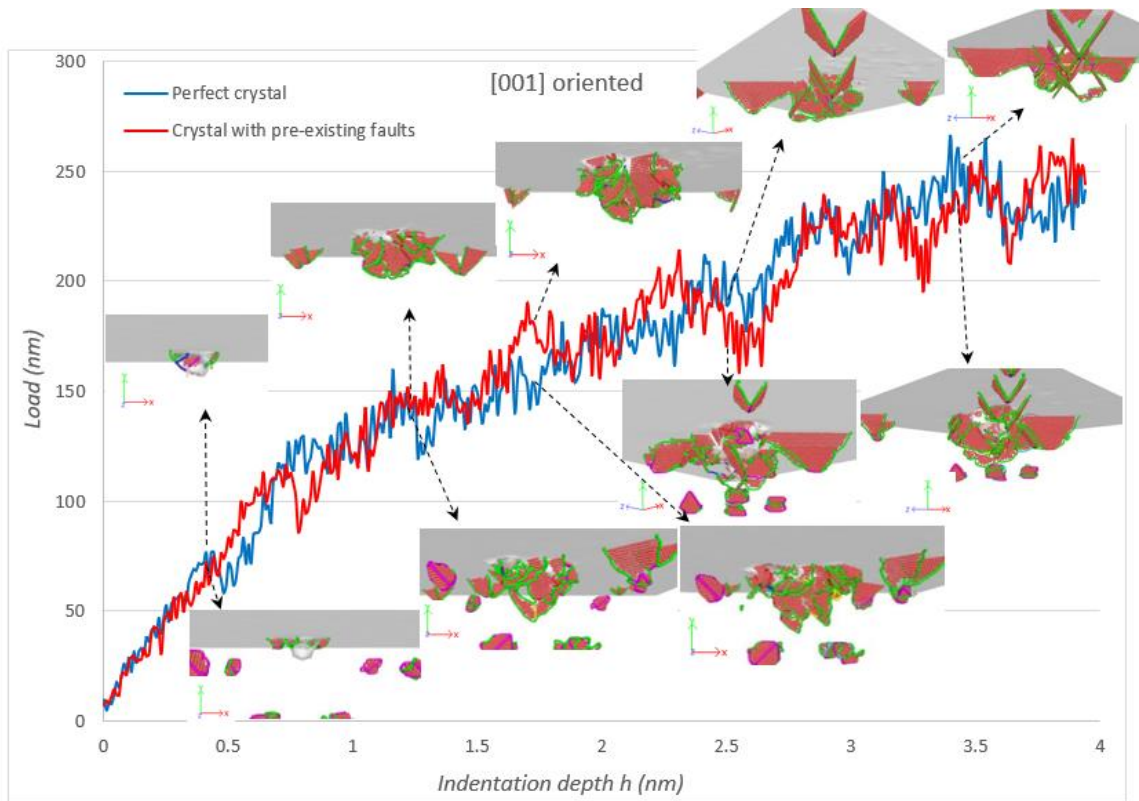
Figure 3.15: Comparison of the defect distribution in the indentation of [001] oriented a) pristine crystal, b) crystal with pre-existing faults.
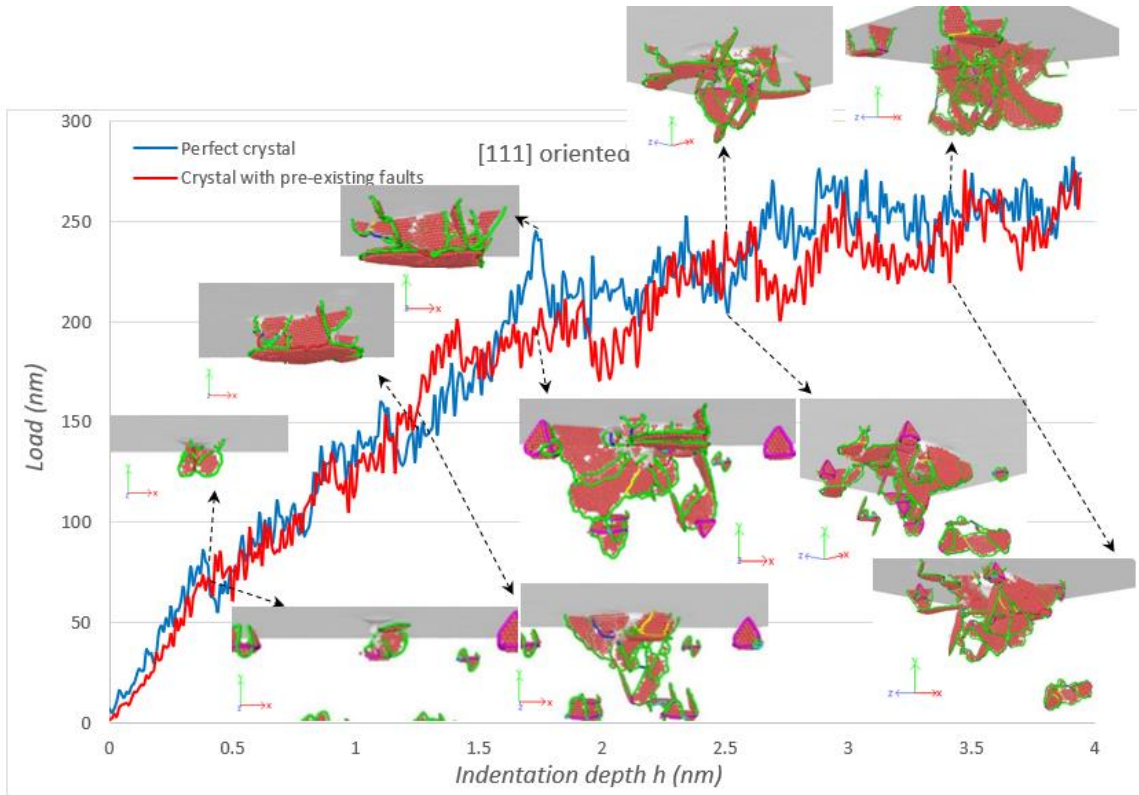
Figure 3.16: Comparison of the defect distribution in the indentation of [111] oriented a) pristine crystal, b) crystal with pre-existing faults.

The same analysis of H and $\sqrt{\rho}$ as a function of indentation depth h as shown in Section 3.4 can be performed on the Au samples containing pre-existing faults (Figure 3.17). As stated for the pristine Au samples, a linear relation is observed between H and $\sqrt{\rho}$ after a certain indentation depth of samples with pre-existing faults. The coefficients of the H-$\sqrt{\rho}$ relationships are decreased for the Au samples containing pre-existing SFs compared to the pristine Au samples of the same crystal orientation. This could be related to the lower shear modulus (μ) values or empirical coefficient (α) of the Taylor hardening rule (eq. 3.6) for the samples with pre-existing faults. Thirteen different scenarios have been proposed by Lavrentev [42] which related the magnitude of α to the dislocation distribution within a plastically deforming material. Although it is not clear which scenario is applicable to the Au samples simulated in our study, one clear fact is that crystal orientation has a higher impact on the magnitude of the parameter A (eq. 3.7) in

samples with pre-existing faults. In other words, the coefficient *A* in eq. 3.7 is more dependent on the crystal orientation in the presence of pre-existing crystal defects.
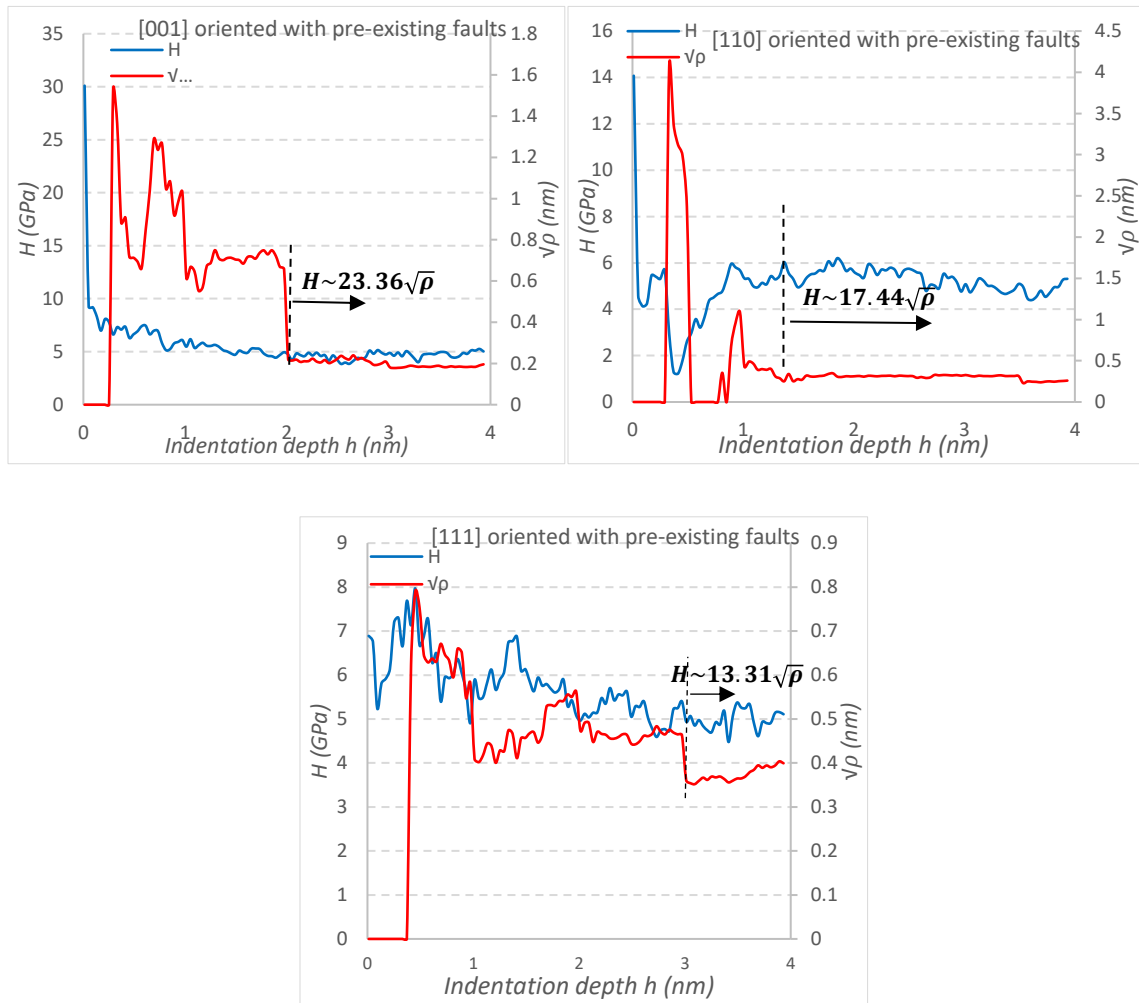
Figure 3.17: The relation of hardness and √ρ for (a) [001], (b) [110], (c) [111] oriented samples in the presence of the pre-existing faults.

Conclusions

Molecular dynamic simulations were used to investigate the effect of crystallographic orientation on the incipient plasticity of fcc Au single crystals during nanoindentation in the presence, and absence, of pre-existing stacking fault defects. The following conclusions can be drawn from this study;

- Size effect during nanoindentation is initially controlled by homogeneous nucleation of dislocations, growth, and development of stacking faults, formation, and glide of V-shape locks, development, and interaction of loops and emission of half prismatic dislocation loops along the free surface or complete prismatic loops into the crystal.

- The dislocation length and density within the nanoindentation plastic zone are highly variable during the initial stage of the deformation process. When the nanoindentation depth is greater than about 2 nm the dislocation density becomes less variable and the indentation hardness H is directly proportional to $\sqrt{\rho}$ thus conforming to the classical Taylor hardening expression for yield stress as a linear function of $\sqrt{\rho}$ where its coefficient A is dependent upon crystal orientation.

- The size of the plastic zone is strongly dependent upon the crystal orientation of the indented surface and is smaller for [001] orientation than those of [110] and [111] orientations. Unlike what has been previously assumed, the relation between the plastic zone size and the indentation contact radius is not constant and changes with indentation depth up to 4 nm.

- The sensitivity of crystal yield point to pre-existing crystal faults depends on the crystallographic orientation. An immediate plastic deformation without pop-in behavior was observed in the nanoindentation [001]-oriented sample with pre-existing faults. Pre-existing defects can either result in one significant yield event ([110]-oriented sample) or initiate a series of tiny events before one big discontinuity in the load-displacement curve ([001]-oriented sample).

- As with tests performed on pristine Au crystals, nanoindentation performed on crystals with pre-existing stacking fault defects also displayed indentation hardness H which conforms to the classical Taylor hardening expression for yield stress as a linear function of $\sqrt{\rho}$ however, the presence of the stacking fault defects increases the variability of the coefficient A for the crystal orientations studied.

The results and analyses presented in this paper provide new information useful in the development of dislocation-based continuum theories. It must be noted however that the

atomistic simulations performed were, by necessity, conducted under exceptionally high indentation loading rates and associated high strain rates. The effect of strain rate on the operative mechanisms of the plasticity of nanometer-scale volumes of ductile metals remains an area still to be studied.

References

[1] H.Y. Liang, C.H. Woo, H.C. Huang, A.H.W. Ngan, T.X. Yu, Dislocation nucleation in the initial stage during nanoindentation, Philos Mag 83(31-34) (2003) 3609-3622.

[2] T. Tsuru, Y. Shibutani, Anisotropic effects in elastic and incipient plastic deformation under (001), (110), and (111) nanoindentation of Al and Cu, Phys Rev B 75(3) (2007).

[3] J. Jin, S.A. Shevlin, Z.X. Guo, Multiscale simulation of onset plasticity during nanoindentation of Al (001) surface, Acta Mater 56(16) (2008) 4358-4368.

[4] G. Ziegenhain, H.M. Urbassek, A. Hartmaier, Influence of crystal anisotropy on elastic deformation and onset of plasticity in nanoindentation: A simulational study, J Appl Phys 107(6) (2010).

[5] K.J. Van Vliet, J. Li, T. Zhu, S. Yip, S. Suresh, Quantifying the early stages of plasticity through nanoscale experiments and simulations, Phys Rev B 67(10) (2003).

[6] J. Li, K.J. Van Vliet, T. Zhu, S. Yip, S. Suresh, Atomistic mechanisms governing elastic limit and incipient plasticity in crystals, Nature 418(6895) (2002) 307-310.

[7] B. Shiari, R.E. Miller, W.A. Curtin, Coupled atomistic/discrete dislocation simulations of nanoindentation at finite temperature, J Eng Mater-T Asme 127(4) (2005) 358-368.

[8] K.J. Kim, J.H. Yoon, M.H. Cho, H. Jang, Molecular dynamics simulation of dislocation behavior during nanoindentation on a bicrystal with a Sigma=5 (210) grain boundary, Mater Lett 60(28) (2006) 3367-3372.

[9] Y. Zhong, T. Zhu, Simulating nanoindentation and predicting dislocation nucleation using interatomic potential finite element method, Comput Method Appl M 197(41-42) (2008) 3174-3181.

[10] C. Begau, A. Hartmaier, E.P. George, G.M. Pharr, Atomistic processes of dislocation generation and plastic deformation during nanoindentation, Acta Mater 59(3) (2011) 934-942.

[11] Y.Z. Li, A. Goyal, A. Chernatynskiy, J.S. Jayashankar, M.C. Kautzky, S.B. Sinnott, S.R. Phillpot, Nanoindentation of gold and gold alloys by molecular dynamics simulation, Mat Sci Eng a-Struct 651 (2016) 346-357.

[12] T.H. Fang, W.Y. Chang, J.J. Huang, Dynamic characteristics of nanoindentation using atomistic simulation, Acta Mater 57(11) (2009) 3341-3348.

[13] V. Navarro, O.R. de la Fuente, A. Mascaraque, J.M. Rojo, Uncommon dislocation processes at the incipient plasticity of stepped gold surfaces, Phys Rev Lett 100(10) (2008).

[14] J.J. Zhang, T. Sun, A. Hartmaier, Y.D. Yan, Atomistic simulation of the influence of nanomachining-induced deformation on subsequent nanoindentation, Computational Materials Science 59 (2012) 14-21.

[15] H.T. Liu, X.F. Zhu, Y.Z. Sun, W.K. Xie, Evolution of stacking fault tetrahedral and work hardening effect in copper single crystals, Appl Surf Sci 422 (2017) 413-419.

[16] M.A. Lodes, A. Hartmaier, M. Goken, K. Durst, Influence of dislocation density on the pop-in behavior and indentation size effect in CaF2 single crystals: Experiments and molecular dynamics simulations, Acta Mater 59(11) (2011) 4264-4273.

[17] E.K. Njeim, D.F. Bahr, Atomistic simulations of nanoindentation in the presence of vacancies, Scripta Mater 62(8) (2010) 598-601.

[18] I. Salehinia, D.F. Bahr, The impact of a variety of point defects on the inception of plastic deformation in dislocation-free metals, Scripta Mater 66(6) (2012) 339-342.

[19] W. Wang, Y. Zhong, K. Lu, L. Lu, D.L. McDowell, T. Zhu, Size effects and strength fluctuation in nanoscale plasticity, Acta Mater 60(8) (2012) 3302-3309.

[20] I. Salehinia, D.F. Bahr, Mechanical behavior of FCC single crystals at finite temperatures in the presence of point defects, Mat Sci Eng a-Struct 588 (2013) 340-346.

[21] S. Plimpton, Fast Parallel Algorithms for Short-Range Molecular-Dynamics, J Comput Phys 117(1) (1995) 1-19.

[22] S. Nose, A Unified Formulation of the Constant Temperature Molecular-Dynamics Methods, J Chem Phys 81(1) (1984) 511-519.

[23] W.G. Hoover, Constant-pressure equations of motion, Physical Review A 34(3) (1986) 2499-2500.

[24] S.M. Foiles, M.I. Baskes, M.S. Daw, Embedded-Atom-Method Functions for the Fcc Metals Cu, Ag, Au, Ni, Pd, Pt, and Their Alloys, Phys Rev B 33(12) (1986) 7983-7991.

[25] H. Tsuzuki, P.S. Branicio, J.P. Rino, Structural characterization of deformed crystals by analysis of common atomic neighborhood, Comput Phys Commun 177(6) (2007) 518-523.

[26] A. Stukowski, K. Albe, Extracting dislocations and non-dislocation crystal defects from atomistic simulation data, Model Simul Mater Sc 18(8) (2010).

[27] A. Stukowski, Visualization and analysis of atomistic simulation data with OVITO-the Open Visualization Tool, Model Simul Mater Sc 18(1) (2010).

[28] H.R. Hertz, The principles of mechanics (Slovak translation of H.R. Hertz's with annotations and introduction), Filozofia 57(6) (2002) 444-453.

[29] J.D. Kiely, J.E. Houston, Nanomechanical properties of Au (111), (001), and (110) surfaces, Phys Rev B 57(19) (1998) 12588-12594.

[30] Y. Mishin, D. Farkas, M.J. Mehl, D.A. Papaconstantopoulos, Interatomic potentials for monoatomic metals from experimental data and ab initio calculations, Phys Rev B 59(5) (1999) 3393-3407.

[31] F.I. Grace, M.C. Inman, Influence of stacking fault energy on dislocation configurations in shock-deformed metals, Metallography 3(1) (1970) 89-98.

[32] P.C.J. Gallagher, The influence of alloying, temperature, and related effects on the stacking fault energy, Metall Trans 1(9) (1970) 2429-2461.

[33] I. Salehinia, S.K. Lawrence, D.F. Bahr, The effect of crystal orientation on the stochastic behavior of dislocation nucleation and multiplication during nanoindentation, Acta Mater 61(5) (2013) 1421-1431.

[34] E. Carrasco, O.R. de la Fuente, M.A. Gonzalez, J.M. Rojo, Dislocation cross slip and formation of terraces around nanoindentations in Au(001), Phys Rev B 68(18) (2003).

[35] Y. Wang, D. Raabe, C. Kluber, F. Roters, Orientation dependence of nanoindentation pile-up patterns and of nanoindentation microtextures in copper single crystals, Acta Mater 52(8) (2004) 2229-2238.

[36] S.P. Ju, C.T. Wang, C.H. Chien, J.C. Huang, S.R. Jian, The nanoindentation responses of nickel surfaces with different crystal orientations, Mol Simulat 33(11) (2007) 905-917.

[37] Y. Liu, B. Wang, M. Yoshino, S. Roy, H. Lu, R. Komanduri, Combined numerical simulation and nanoindentation for determining mechanical properties of single crystal copper at mesoscale, J Mech Phys Solids 53(12) (2005) 2718-2741.

[38] I.A. Alhafez, C.J. Ruestes, Y. Gao, H.M. Urbassek, Nanoindentation of hcp metals: a comparative simulation study of the evolution of dislocation networks, Nanotechnology 27(4) (2016).

[39] K. Durst, B. Backes, M. Goken, Indentation size effect in metallic materials: Correcting for the size of the plastic zone, Scripta Mater 52(11) (2005) 1093-1097.

[40] G.Z. Voyiadjis, M. Yaghoobi, Large scale atomistic simulation of size effects during nanoindentation: Dislocation length and hardness, Mat Sci Eng a-Struct 634 (2015) 20-31.

[41] A.A.H. Ameri, N.N. Elewa, M. Ashraf, J.P. Escobedo-Diaz, P.J. Hazell, Estimation of Dislocation Density in Metals from Hardness Measurements, Springer International Publishing, Cham, 2017, pp. 441-449.

[42] F.F. Lavrentev, The Type of Dislocation Interaction as the Factor Determining Work-Hardening, Mater Sci Eng 46(2) (1980) 191-208.

[43] J.F. Rodriguez-Nieva, C.J. Ruestes, Y. Tang, E.M. Bringa, Atomistic simulation of the mechanical properties of nanoporous gold, Acta Mater 80 (2014) 67-76.

Chapter 4

4. The effect of grain boundary on the local incipient plastic deformation of FCC metals during nanoindentation

The effect of grain boundaries on the deformation mechanisms becomes increasingly important as the volume of deformation reaches to submicron and nanoscale. The current work investigates the impact of grain boundaries on the incipient plasticity of small scale deformations of FCC metals. For this purpose, the behavior of single and bi-crystal Au thin films during nanoindentation are studied, using large scale atomistic simulation. Various symmetric <1 1 0> tilt GBs with a wide range of misorientation angles are included to analyze the effect of GB geometry on the nano-scale plasticity mechanisms. Potentially, GBs can act as a source, sink, or obstacle for lattice dislocation, depending on their geometry, energy level, and distance from the deformation zone. The role of the heterogeneous nucleation and emission of dislocations from grain boundaries on the plasticity and hardness of bicrystals is analyzed. According to the simulation results, the intrinsic free volume involved in the grain boundary region is associated with dislocation nucleation at the GB. The volume of the plastic zone generated beneath the tip and the way it grows is strongly dependent on the GB structure. Dislocation nucleation occurs predominantly and in the early stages of indentation at GBs with dissociated interface structural unit, before the interaction of lattice dislocation and GB. Coherent twin boundaries display the lowest effect on the bicrystal hardness. The impact of GB decreases as the depth of indentation increases, and bicrystal samples present the same behavior as single crystals at higher strains. Based on our results, there is a strong correlation between the interfacial boundary energy and its effect on the bicrystal hardness. GBs with lower interfacial energy offer a higher barrier against slip transmission and nucleation at the GB. Moreover, the distance of the GB from the indentation surface plays an essential role in the GB effect on plasticity, and as it is expected, the GB effect decreases as its distance from the indentation surface increases.

4.1. Introduction

Deformation is mainly controlled by the interaction of dislocation with grain boundaries in bulk polycrystalline metals and it is well known that pile-up of dislocation at grain boundaries increases strength of materials with lower grain sizes. This effect is very well described by Hall-Petch [1, 2] theory. However, as the grain size decreases to the nano-scale sizes, the Hall-Petch model can not describe the material behavior and GB involves deformation through another mechanism such as acting as a source of dislocation nucleation, sliding and rotating during the deformation [3]. According to Yamakov et al. [4-7] results, as the grain size decreases, the overall dislocation activity and its effect on producing strain decreases rapidly until, a GB-based deformation process dominates the deformation in nanocrystalline metals.

One of the most effective techniques to capture local yielding and studying the effect of grain boundaries on the mechanical response is nanoindentation since it can make local deformation near or at the border of grains. Indenting near grain boundaries resulted in specific pop-ins in the load-displacement curves and interpreted as transfer of deformation to the adjacent grain [8], however there is still not a clear understanding on the dislocation-grain interaction and its effect on the small scale deformation. Since the size of the nanoindenter tip is in the nano scale (~100 nm) and deformation happens in a small volume of material, it is almost impossible to analyze the deformation experimentally and advance of atomistic level simulations have provided a powerful tool to understand underlying mechanisms.

Spearot et al's [9] simulations indicate that the orientation of the opposing lattice regions and the presence of certain structural units are two features of the interface structure the stress required for dislocation nucleation during the tensile deformation. Based on Tschopp and McDowell [10] studies on the dislocation nucleation mechanisms for asymmetric $\Sigma 3$ Cu boundaries show that nucleation is preceded by dislocation dissociation from the boundary. Then, dislocations nucleate in only one crystal on its maximum Schmid factor slip plane(s).

Lilleodden et al [11] study on the gold bi-crystal with a Σ79, 34° tilt boundary showed that high angle grain boundaries are a ready source of dislocations in nanoindentation deformation. Prismatic dislocation loops merged into the grain boundary without transmission into the adjacent grain or reflection, in Kim et al.'s [12] simulation of Ni bicrystal with a Σ 5 (210) grain boundary. Instead, interaction of dislocations and the grain boundary resulted a series of atom shifts near the grain boundary, leading to the grain boundary migration [12].

It is show in Hasnaoui et al.'s [13] study that when the grain size is bigger than the indenter size, GBs can emit, absorb and repel dislocations, depending on their local structure and stress distribution. Jang and Farkas [14] observed transmission of dislocation across the grain boundary during nanoindentation of bi-crystal Ni thin film, leaving a step in the boundary plane. Tsuru et al. [15] studied the incipient plasticity of various types of grain boundaries subjected to nanoindentation. They found that the mechanisms of dislocation nucleation at the grain boundary are strongly related to the static grain-boundary stability and its fault energy during slip deformation. Sangid et al. [16] showed that the grain boundary energy barrier for the slip–GB interaction is highly affected by the character and the structure of the GB. As they concluded GBs with lower static interfacial energy provide a higher barrier against slip transmission and nucleation at the GB. Zhang et al. [17] indicated that stress state can play a significant role in the deformation mechanisms of nanocrystalline materials. Their simulations on the tensile deformation of symmetric and asymmetric ∑5 tilt GBs of Cu bicrystal revealed that once the maximum tensile stress has been reached, dislocations are nucleated and emitted into both grains of the symmetric GBs, while this emission occurs only at the lower grain region in the asymmetric GBs at the beginning, and then the slip systems in the upper grain can be activated [17].

The effect of grain boundary on the elastic modulus, hardness and maximum shear stress of Fe biocrystal was investigated by Talaei et al [18]. According to their results, dislocation loops merged into the grain boundary without transmission into the adjacent grain.

Voyiadjis and Yaghoobi [19] concluded that dislocation nucleation at grain boundary can severely affect the strength of thin film, if it happens at the very early stages of indentation. According to their results the grain boundary doesn't change the mechanical response at larger indentation depths when the forest hardening mechanism is dominant and source exhaustion becomes inactive.

Kuhr and Aifantis [20] focused on determining the grain boundary vs grain interior yield stresses by performing MD nanoindentation near and on Σ5 tilt grain boundaries of BCC Fe nanocrystals. As they observed, adding C segregants resulted higher strength in the GB through the pinning effect, which made twin formation more difficult, and inhibited GB migration.

Published studies have revealed that the mechanical behavior and deformation mechanisms are mainly related to the GB structure and various scholars have focused their studies on a certain geometry of GB. Moreover, most of the atomistic studies on the effect of GB on deformation mechanisms are limited to the tensile tests without local deformation and interaction of lattice dislocation with GB. Therefore, the role of the GB on the local deformation and the complex interaction of lattice dislocations and GB geometry is still not fully studied. In this study the correlation of GB structure and properties with locally small scale plasticity is studied by analyzing interaction of lattice nucleated dislocations with various GB structures ranging high range of energy levels.

4.2. Methodology

Classical MD simulations are performed using the Large-scale Atomic/Molecular Massively Parallel Simulator (LAMMPS) [21]. Au thin films with dimensions of $40 \times 30 \times 40$ nm in the x, y and z directions are considered to simulate the nanoindentation behavior of Au single and bicrystals. Each sample has around 2,866,900 atoms depending on the grain boundaries geometry. The periodic boundary condition is applied to the lateral surfaces and the position of the bottom three layers of the sample were fixed. The next four layers at the bottom are kept at a fixed temperature of 300 K by a Nosé-Hoover thermostat.

A 2 fs time step was used for the integration and periodic boundary conditions applied in lateral directions. Bicrystals were constructed by creating two separate grains with symmetric misorientations about [1 $\bar{1}$ 0] tilt axis. Periodic boundary conditions are used along with the x and z directions and the indentation surface is modeled as free surface.

Stable configurations are achieved through a combination of molecular statics and molecular dynamics. A molecular statics calculation carried out using energy minimization with the conjugate gradient (CG) algorithm. Several in-plane rigid body translations; ie. the top and bottom grains are rigidly translated relative to each other; are carried out to achieve the minimum energy configuration of GBs. The final relaxed structures are obtained by CG method with an energy tolerance of 10^{-25}eV and a force tolerance of 10^{-25}eV/Å. The system was equilibrated for 80 ps after minimization with the temperature increasing from 1 K to 300 K and it relaxed at 300K for 80 ps, before initiation of the process. The minimum GB energy for the four considered grain boundaries are calculated using EAM potential and reported in Table 4.1. Equilibrium GB configurations are shown in Figure 4.1, using Centrosymmetry parameter [22]. Dislocation Extract Algorithm (DXA) [23] is adopted to identify the dislocation patterns and the Open Visualization Tool OVITO [24] is utilized to visualize the atomistic configurations.

Relaxed samples are indented using a rigid spherical indenter with an 8 nm diameter tip. The indenter moves downwards and penetrates into the film with a constant velocity of 5 m/s, until the maximum depth of 4 nm; equal to the indenter radius. The retraction of the indenter is simulated analogously to the penetration. An indenter with non-atomistic repulsive sphere is used to save the computation time. The indenter repels all the atoms it contacts, and the interaction potential can be expressed as;

$$F(r) = -k(r - R)^2 \tag{4.1}$$

where k is the specified force constant equal to 10 eV/A^2, r is the distance from the atom to the center of the indenter, and R is the radius of the indenter. The Au embedded-atom method (EAM) potential developed by Foiles et al. [25] is used to simulate the atomic interaction of Au–Au. EAM potential is a common method to simulate metallic systems using MD [26]. Dislocation Extract Algorithm (DXA) [23] is adopted to identify the

dislocation patterns, and the Open Visualization Tool OVITO [24] is utilized to visualize the atomistic configurations.

Table 4.1: The energy level of different [1 $\bar{1}$ 0] symmetric GBs of Au bicrystal.

Boundary	Misorientation angle θ (°)	Boundary energy γ_{GB} (mJ m^{-2})
Σ19 (1 1 6)	26.5	518
Σ9 (1 1 4)	38.9	491
Σ139 (3 3 11)	42.2	452
Σ11 (1 1 3)	50.5	214
Σ33 (2 2 5)	58.9	356
Σ3 (1 1 2)	70.5	404
Σ17 (2 2 3)	86.6	407
Σ3 (1 1 1)	109.5	2
Σ171 (11 11 10)	114.5	222
Σ11 (3 3 2)	129.5	479
Σ291 (11 11 7)	131.5	517
Σ9 (2 2 1)	141.1	551
Σ19 (3 3 1)	153.5	554
Σ73 (6 6 1)	166.6	466

Σ9 (1 1 4) θ=38.9°   Σ139 (3 3 11) θ=42.2°

86

Σ11 (1 1 3) θ=50.5º

Σ33 (2 2 5) θ=58.9º

Σ3 (1 1 2) θ=70.5º

Σ3 (1 1 1) θ=109.5º

Σ171 (11 11 10) θ=114.5º

Σ11 (3 3 2) θ=129.5º

Figure 4.1: Initial equilibrium structures of the Au <1 1 0> symmetric tilt GBs obtained by the energy minimization. The structures are viewed along with the [1 $\bar{1}$ 0] tilt axis and are colored based on the CNA parameter. Atoms with a perfect fcc structures are shown in blue color and the structural units are highlighted by solid lines and marked by C, D, and E.

Calculated GB energy is shown in Figure 4.2 as a function of the misorientation angle. The curve has minimums and cusps at 50.5° and 109.5° misorientation angles which are related to the Σ11 (1 1 3) and Σ3 (1 1 1) structures that have only preferred units in their geometry. Moreover, Σ3 (1 1 1) represents a coherent twin boundary.
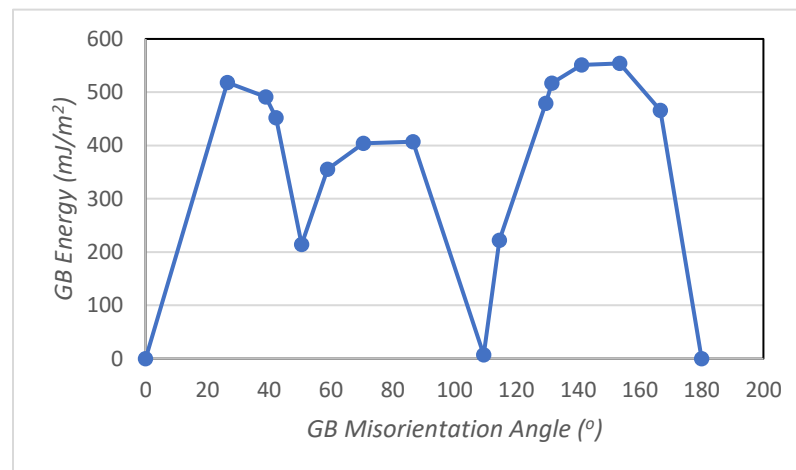
Figure 4.2: The energy of Au <1 1 0> tilt GBs as a function of the misorientation angle at 0K.

4.3. Results and discussion

4.3.1. Mechanical response

Figure 4.3 compares the load-displacement curve of the nanoindentation of Au single and bicrystals for different GB structures. The grain boundary is located 2nm below the indentation surface in all of the bicrystals. In order to include the effect of lattice orientation the behavior of each bicrystal was compared to the single crystal with the same lattice orientation. Since the behavior of single and biocrystals becomes more similar to the indentation depth increases, diagrams only show the first 2 nm depth of indentation. The observed load drops on the onset of plasticity of all tested bicrystals correspond to dislocation nucleation and the critical values of bicrystals which is apparently smaller than that of a single crystal. According to Tsuru et al.'s [27] study, the critical hardness value which is obtained by dividing the indentation load to the contact area is one of the key indicators of dislocation nucleation because of the linear relation of maximum shear stress and the hardness. However, the difference in the behavior of single and biocrystals becomes more significant after nucleation and in result of the interaction of the nucleated dislocations with grain boundary.
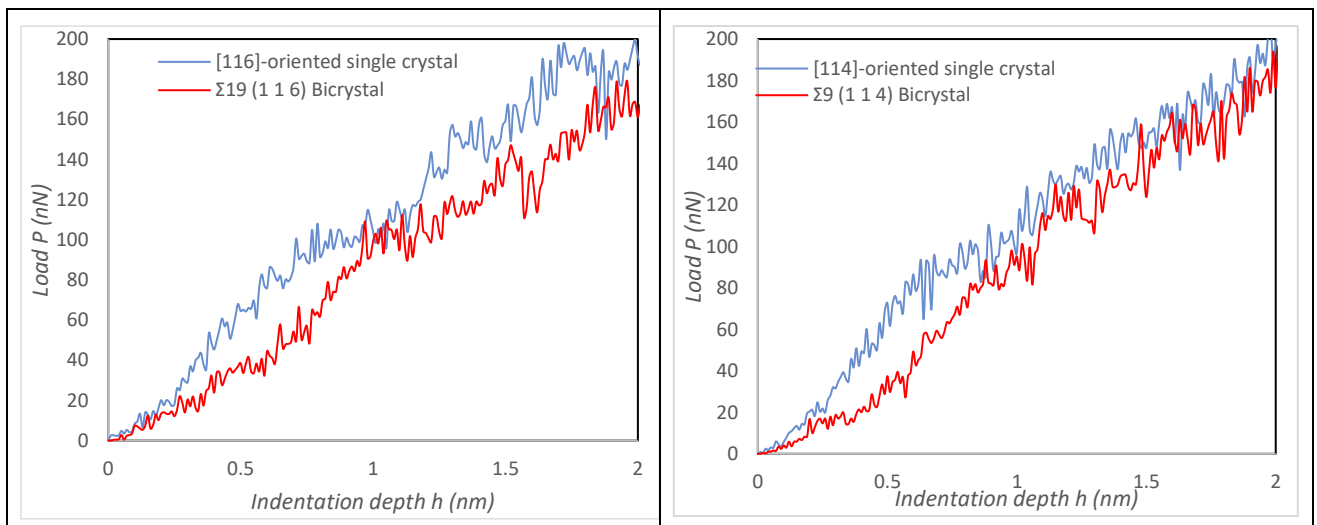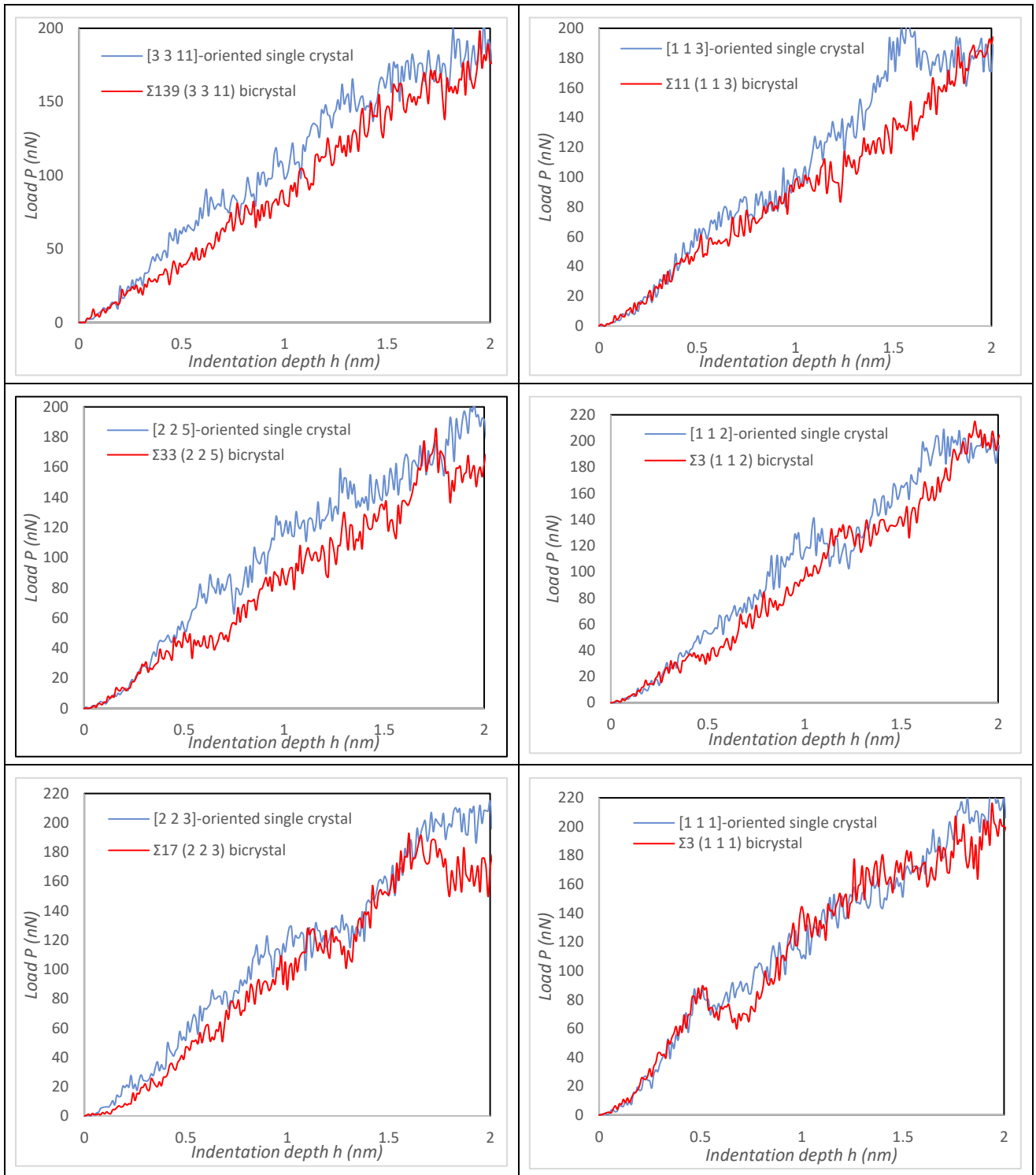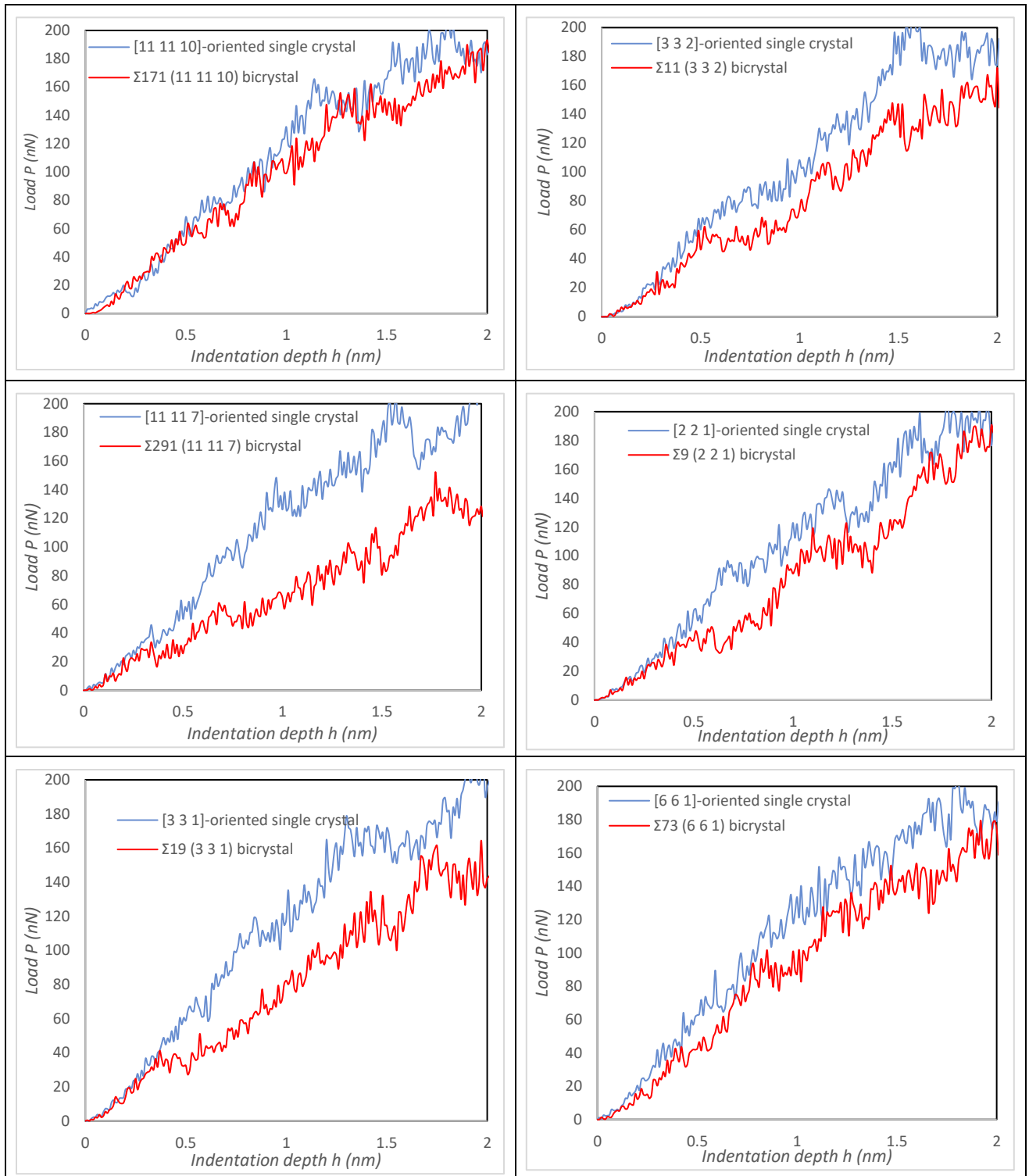
Figure 4.3: Comparison of force-displacement curve for Au biocrystals with the same orientation single crystals (the distance of GB and indentation surface is 2nm).

To compare the effect of different GBs on the mechanical properties of bicrystals, the amount of average hardness a the first 2nm indentation depth is presented in Figure 4.4 for various GB misorientation angles. As it is observed in Figure 4.4, having a grain boundary in the structure generally decreases the hardness value and weaken the crystal. This effect is more significant in lower misorientation angles and it decreases as the misorientation angle increases up to 109.5°. In another word the strength of the bicrystal increases and becomes closer to the single crystal as the misorientation angle increases up to 109.5°. This hardness decrease in result of the presence of grain boundary is related to the higher energy of the atoms in the GB than the lattice atoms and the easier nucleation of dislocations. The amount of hardness decrease raises abruptly when misorientation angle exceeds 109.5° that could be related to the intrinsic GB structure of grains with misorientation angle higher than 109.5°, as they have E units in their structures which will affect the deformation mechanism [28, 29]. It is also worth to note that according to Figure 4.4, Σ3 (1 1 1) shows the lowest reduction in hardness or presents the strength close to single crystal which is in result of its simple structure and very low boundary energy. The dislocation nucleation at the grain boundary and the deformation mechanism are reviewed in next sections based on the misorientation angle.
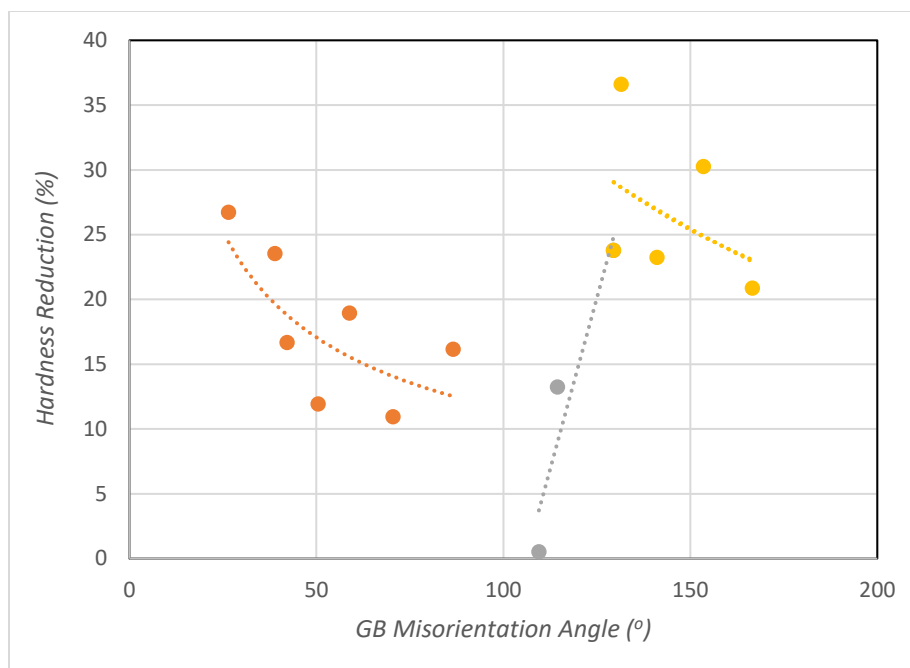
Figure 4.4: The amount of average hardness reduction in the result of the presence of GBs with different misorientation angles.

4.3.2.   Deformation mechanisms

4.3.2.1   Grains with misorientation angle θ<109°

Two grain boundary structures, Σ11 (113) θ=50.5° and Σ3 (112) θ=70.5° are considered to study the effect of grain boundaries with misorientation angles less than 109° on the dislocation nucleation and evolution during nanoindentation. Figure 4.5 compares the deformation process of a [113] oriented single crystal with a bicrystal with a Σ11 (113) GB located 2.6nm from the indentation surface. As it was shown in fig 1, Σ11 (113) has a simple geometry consisting of C structural units and the boundary energy is a local minimum (first cusp in Figure 4.2). As it can be observed in Figure 4.5, the Shockley partial dislocations (SPDs) are nucleated along the (1 1 $\bar{1}$) plane for the bicrystal (the green lines represent Shockley partial dislocation lines (SPDLs)) and extend, forming inclined stacking faults (SFs), similar to single crystal. The atoms in the figure identified as HCP and "other" lattice structure atoms were removed for clarity. As it is observed, all the SPDLs slip on inclined {111} planes rather than on the plane parallel with the GB. Stacking faults mainly grow on the (1 1 1) and (1 1 $\bar{1}$) planes as they are the primary slip

systems $(SF_{(1\,\bar{1}\,1)}^{max} = SF_{(1\,1\,\bar{1})}^{max} = 0.429$. Another interesting factor in the indentation of sample with $\Sigma 11$ (113) GB is that there is no misfit dislocations at the boundary after equilibrating the sample at 300K and before deformation. As the plastic zone develops and the amount of energy at the grain boundary increases, a network of small partial dislocations gets activated in the boundary. This soften the sample effectively as it can be seen in Figure 4.5 (depth 1.092 nm) and results to a strength reduction of 47% at 1.46nm depth. The activation of dislocation network at the grain boundary happens at the 1.092nm, 1.452nm, and 1.892nm indentation depth for the samples in them the distance of grain boundary is 2.6nm, 4nm, and 5.7nm from the surface, respectively.
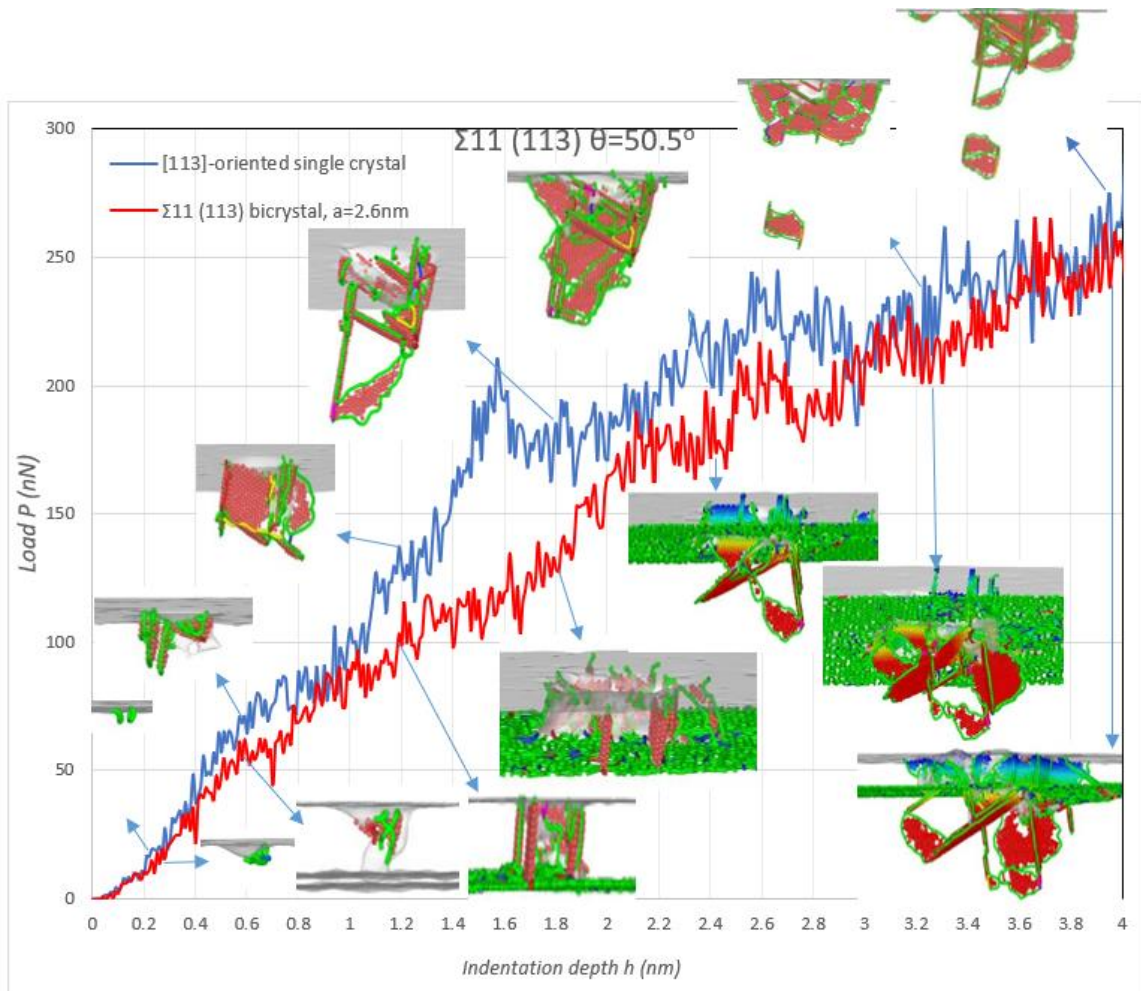
Figure 4.5: Deformation mechanism of a sample with Σ11 (113) θ=50.5° GB at 300K. Atoms are colored based on their positions regarding the GB after passing the GB (Loops that passed GB are shown in red color).

Grains with misorientation angles of 50.5°<θ<109.5° have dissociated dislocations in their structures which will result to the evolve of dissociated facet faults in the grain boundary even in the areas out of plastic zone. Figure 4.6 compares the deformation of [1 1 2]-oriented single crystal with a biocrystal sample with Σ3 (112) GB located 4nm from the surface of indentation. Dissociated GB dislocations are observed at the GB before the deformation due to the structure of the GB (Figure 4.1). As it has been described by Tsuru et al. [15], in unstable grain boundaries dislocations are initially activated in the heterogeneous region and then move of the inner region. As it is observed, the onset of plasticity starts with nucleation of Shockley partial dislocations on the $(\bar{1}\bar{1}\bar{1})$ plane and it

continues with the growth of the SPDs till they reach the grain boundary. As the plastic zone reaches the boundary new parallel PSDs are nucleated at the inner part of the grain boundary and in the bottom of the plastic zone and the grain boundary plays as source of dislocation nucleation. This can be clearly observed in Figure 4.7a which shows the dislocation structure at the depth of 1.09 nm. The nucleation of the new dislocations decreases the strength significantly at the range of 1-2 nm depth. After the interaction of lattice dislocations and the GB dislocations, the plasticity mainly continues with the dislocation nucleation at sources in the grain boundary or close to it. The other interesting factor which happens here is the growth of the intrinsic stacking fault planes of the grain boundary along the highest Schmid factor; (111) planes (Figure 4.7b). As Tschopp and McDowell [30] described, this happens when a GB dissociated partial dislocation is emitted into the adjacent lattice. It appears as a partial dislocation loop, starting at a single point upon the dissociated partial dislocation line defect. Several scenarios have been considered by Tschopp and McDowell [30] to describe this phenomena which are not included here.

As the distance of the $\Sigma 3$ (112) boundary from surface increases, less softening happens in the load-displacement curve as it is expected (Figure 4.8). This is due to the higher Confined Layer Slip (CLS) dominant plasticity in sample with higher distance of grain boundary from surface (Figure 4.9).
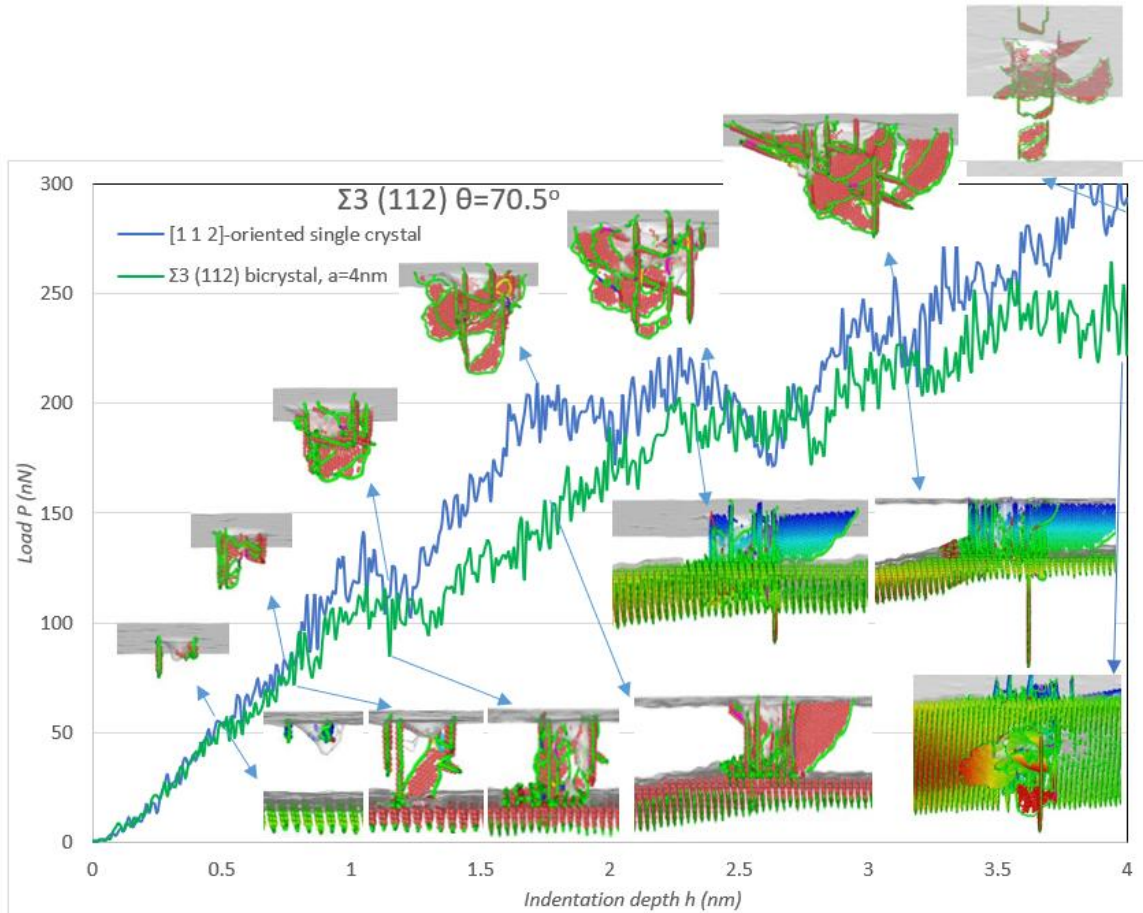
Figure 4.6: Deformation mechanism of a sample with Σ3 (112) θ=70.5° GB at 300K. Atoms are colored based on their positions regarding the GB after passing the GB (Loops that passed GB are shown in red color).
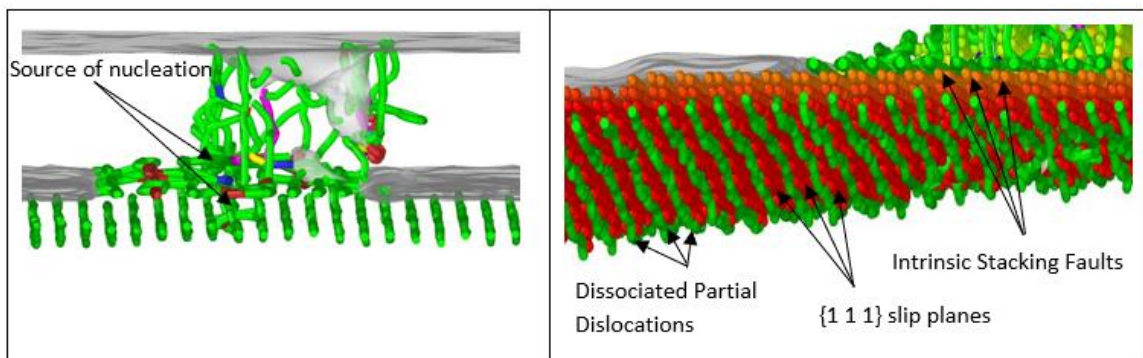
Figure 4.7: a) Dislocation nucleation sites at the Σ3 (112) GB, b) Nucleation of dislocation loops at Σ3 (112) boundary with dissociated partial dislocations on the maximum Schmid factor {1 1 1}.
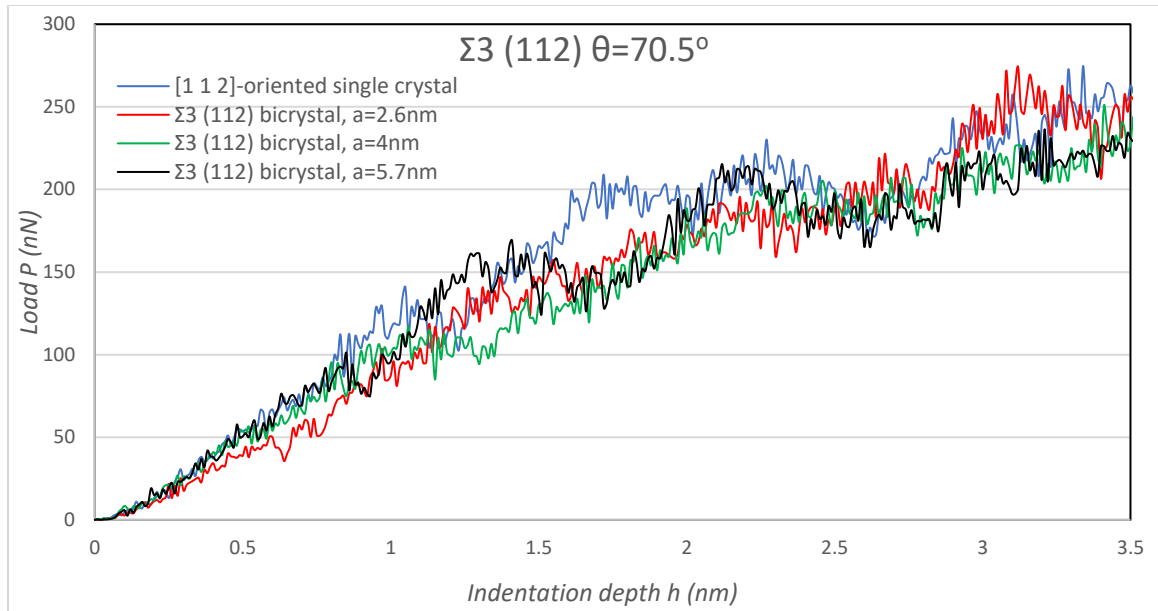
Figure 4.8: Effect of the Σ3 (112) GB distance from the indentation surface on the sample strength.
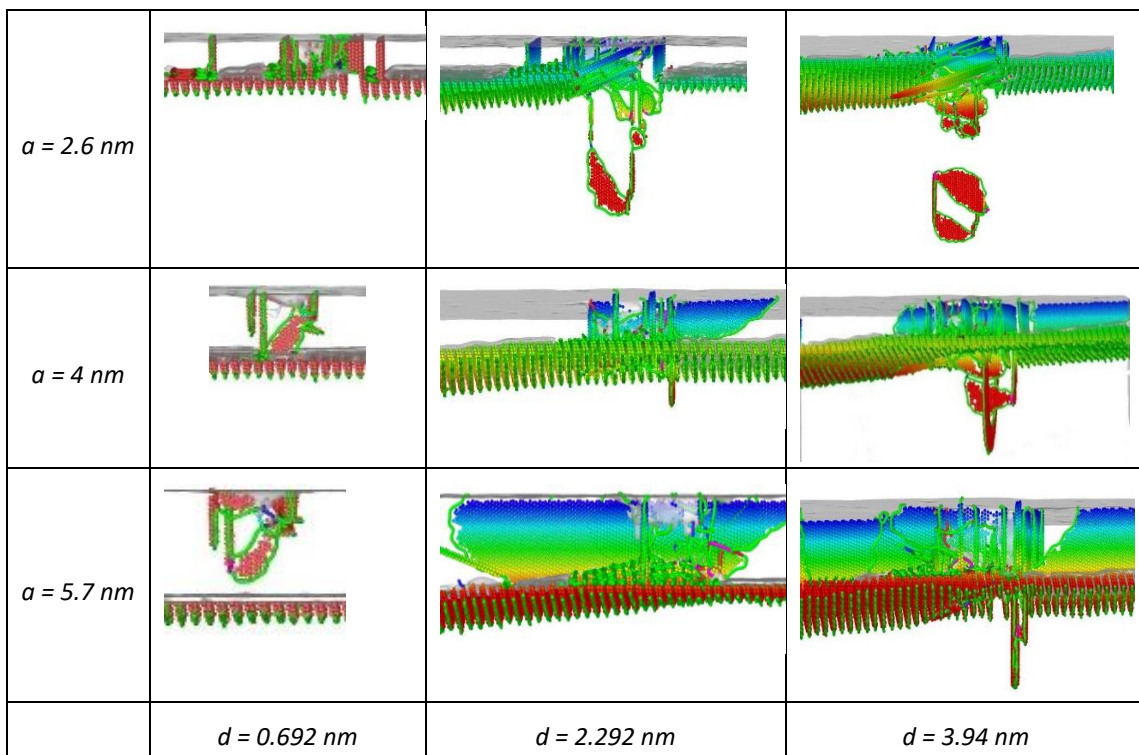
Figure 4.9: Fault structure at different indentation depths "d" based on a Σ3 (112) GB located a distance "a" from the indentation surface.

4.3.2.2   Grains with misorientation angle 109º <θ<114.5º

Σ3 (111) is expected to behave like a single crystal (bulklike behavior) due to its simple structure and very low energy which shows it is much more coherent than the other grain boundaries. Load-displacement curves of the [111] oriented single crystal and the samples with Σ3 (111) grain boundary prove this and not a significant difference is observed in the strength and critical pressure of them. Comparing the flow behavior of 109º oriented single and bicrystal, it can be observed that Shockley partial dislocations (SPDs) are nucleated along the $(11\bar{1})$ plane for the bicrystal and extend, forming inclined stacking faults (SFs), similar to the single crystal. However, the nucleated SPDs grow faster in the bicrystal until they reach the grain boundary. As it is observed, all the Shockley partial dislocation lines (SPDLs) slip on inclined {111} planes rather than on the plane parallel with the TB. The softening behavior is also observed for the bicrystal after the dislocation nucleation as it is expected [31]. Comparing the dislocation structure at point b shows that the shaped stacking fault in the grain boundary starts to glide and grow in the boundary instead of having more SPD nucleation in the single crystal. The reason could be related to the lower fault energy of the grain-boundary sliding rather than stacking-fault energy due to the low energy of this boundary, which makes the glide happens in the boundary with less required energy for nucleation [15].

 Comparing the microstructure at point c with point b, reveals that the plasticity mainly includes the following mechanisms for the structure with Σ3 (111) TB rather than the single crystal:

(1) after the incipient plasticity some new SPDs nucleate forming inclined slips on the main slip planes; (2) some TB atoms which are surrounded by dislocation lines move downwards, forming twinning partial slips. This can be clearly observed by color coding the atoms based on the position of TB. All the red and yellow atoms have been moved downward against the position of TB. Figure 4.11 represents a closer view of the displaced atoms from the bottom view. It should be noted that the indentation force overally increases even in the presence of dislocation nucleation and glides due to the increase of contact area. Figure 4.12 presents three snapshots as a dislocations merge into the grain boundary (Figure 4.12a), disturbing the periodicity of the boundary (Figure

4.12b) and transmit across the boundary (Figure 4.12c). This phenomena clearly shows that the GB can imply resistance against dislocation movement and decrease the plastic deformation, which is in consistent with the well-known Hall Petch theory on the grain size strengthening. It is also noticeable that the interaction of dislocation and grain boundary makes a step in the grain boundary (Figure 4.12b and c). As Jang and Farkas [14] described, this is due to the different direction of Burgers vectors of lattice dislocations at two adjacent grains. According to their Burgers vector analysis, the lattice dislocation in grain I merged into the grain boundary and it is dissociated into another lattice dislocation in grain II and a grain boundary dislocation with a DSC (displacement shift complete) vector, resulting a step in the grain boundary.

Twin Partial Slips (TPSs) extend horizontally with increasing force resulting softening and some slip planes ({111} ones) developed between the TB and surface with Burgers vector parallel to the TB. These slip of dislocation which is confined between the TB and surface has been referred as confined-layer slip, CLS, by You et al. [32] and causes strengthening based on equation 4.2 and 4.3. However, as mentioned due to the lower fault energy of the grain-boundary sliding rather than stacking-fault energy loop nucleation happens far later in the bicrystal comparing to the single crystal.

$$H = H_0 + H_{strengthen} - H_{soften} \tag{4.2}$$

$$H = H_0 + H_{CLS} - H_{TPS} - H_{PSPTB} - H_{DN} \tag{4.3}$$

where H_0 is the hardness of single-crystal, H_{CLS} corresponds to the confined layer slip effect (or blocking of dislocations at interface), H_{TPS}, is related to the twinning partial slip, H_{PSPTB}, is partial slip parallel with twin boundary, and H_{DN} is the effect of dislocation nucleation at the grain boundary.

As the indenter proceeds dislocations nucleated from the Frank sources near the TB along the slip planes inclined to the TB and cross as it is observed in point d of Figure 4.10. From then on the plasticity continues by nucleation and growth of loops rather than twin partial slip. These loops are nucleated on three active slip planes $(11\bar{1})$, $(\bar{1}11)$, and $(1\bar{1}1)$

which are the primary slip systems with the maximum Schmid factor 0.314, similar to the [111] oriented single crystal.
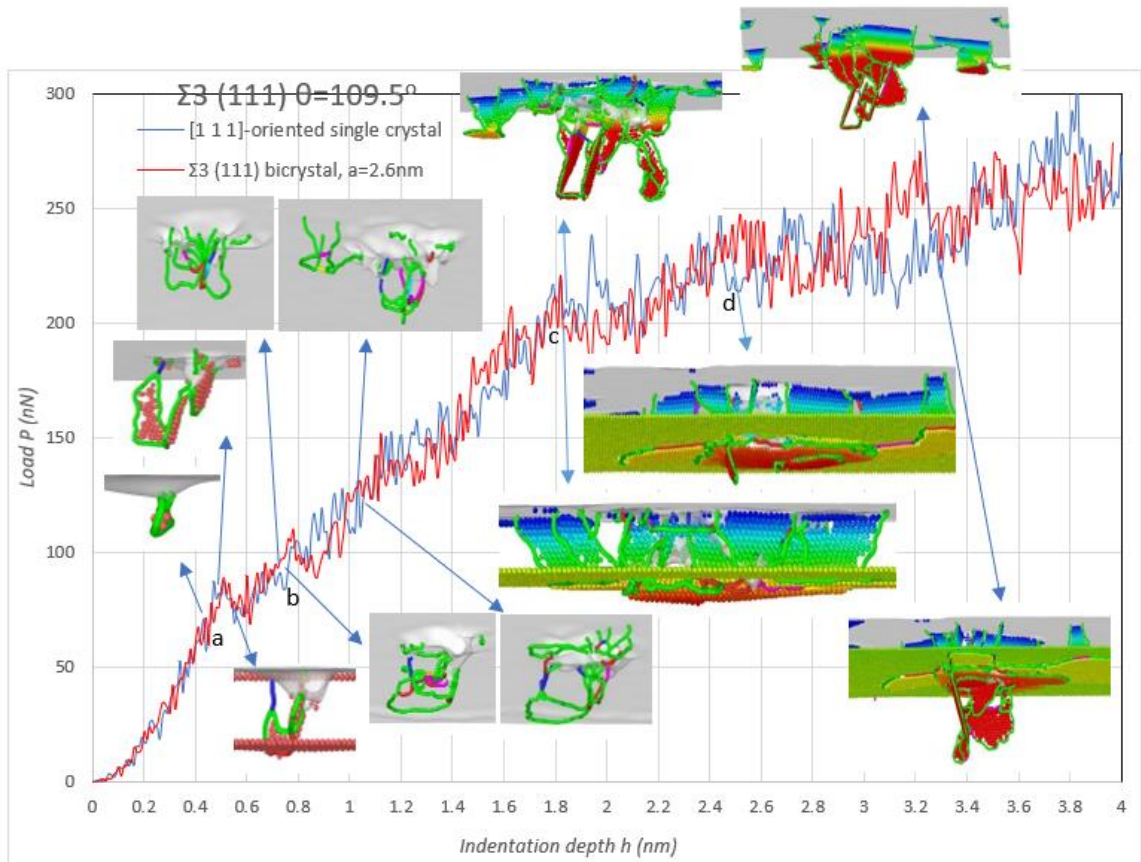
Figure 4.10: Deformation mechanism of a sample with Σ3 (111) θ=109.5° GB at 300K. Atoms are colored based on their positions regarding the GB after passing the GB (Loops that passed GB are shown in red color).
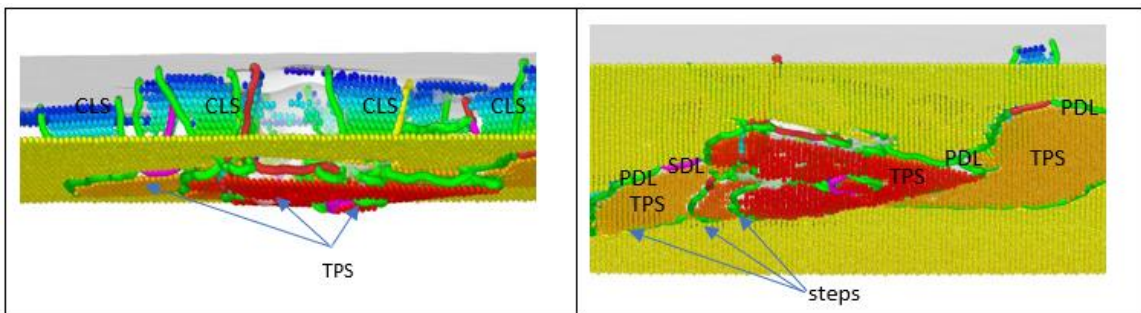
**Figure 4.11: a) Formation of CLS and TPS in the indentation of Σ3 (111) bicrystal, b)Buttom view of the Σ3 (111) twin indicating the partial slip of twin atoms and creation of step at the boundary in result of slip.**
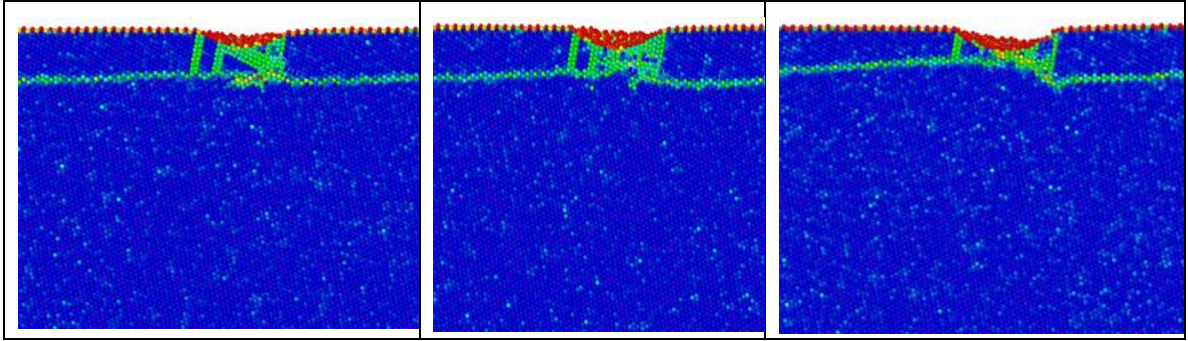
Figure 4.12: Interaction of the lattice dislocations with a Σ3 (111) twin boundary before (a), during (b) and after (c) the transmission of a dislocation across the grain boundary.

Figure 4.13 compares the deformation of the samples in them the TB has different distances from the surface. Looking at Figure 4.13, it is observed that the distance of the TB doesn't affect elasticity significantly. However, as the distance between the TB and surface decreases the TPS mechanism happens sooner and sample shows higher softening as it is clear around the 1.2 nm indentation depth. Increasing the distance of TB and surface would result in the CLS dominant plasticity and the creation of more slip planes around the pit (Figure 4.13).

	d = 0.532 nm	d = 1.77 nm	d = 3.292 nm	d = 3.94 nm
a = 2.6 nm				
a = 4 nm				
a = 5.7 nm				

Figure 4.13: Effect of the distance of the TB with the surface on the TPS and fault formation at various depths of indentation.

$\Sigma171$ (11 11 10) $\theta=114.5^{\circ}$ GB has only a small deviation in lattice orientation from the $\Sigma3$ (111) twin boundary. This structure of GB can be described as a vicinal twin boundary [33] in which the 5° misorientation angle is compensated by distorted E structural units and dissociated D units to provide a symmetrical structure. Based on the Rittner and Seidman [34] study, E units can be represented as cores of alternating a/3 <1 1 1> dislocations or disconnections and dissociated D units can be defined as a/6 <1 1 2> Shockley partial dislocations. Figure 4.14 represents some snapshots of the nanoindentation of the bicrystal with $\Sigma171$ (11 11 10) GB. It worth to mention that the a/3 <1 1 1> disconnections have been reported in HRTEM studied of fcc metals [35, 36]. Disconnections in GB and dissociated partials can be observed in fig. 8 before the deformation and it is interesting that unlike the GBs with $50.5^{\circ}<\theta<109.5^{\circ}$, here the dissociated facet is along the primary slip planes of the grains and this will result to the rapid propagation of pre-nucleated Shockley dislocations and intrinsic stacking faults. Twin partial slip and split of intrinsic stacking faults in the region that TPS happens in observed in Figure 4.14 b-f.
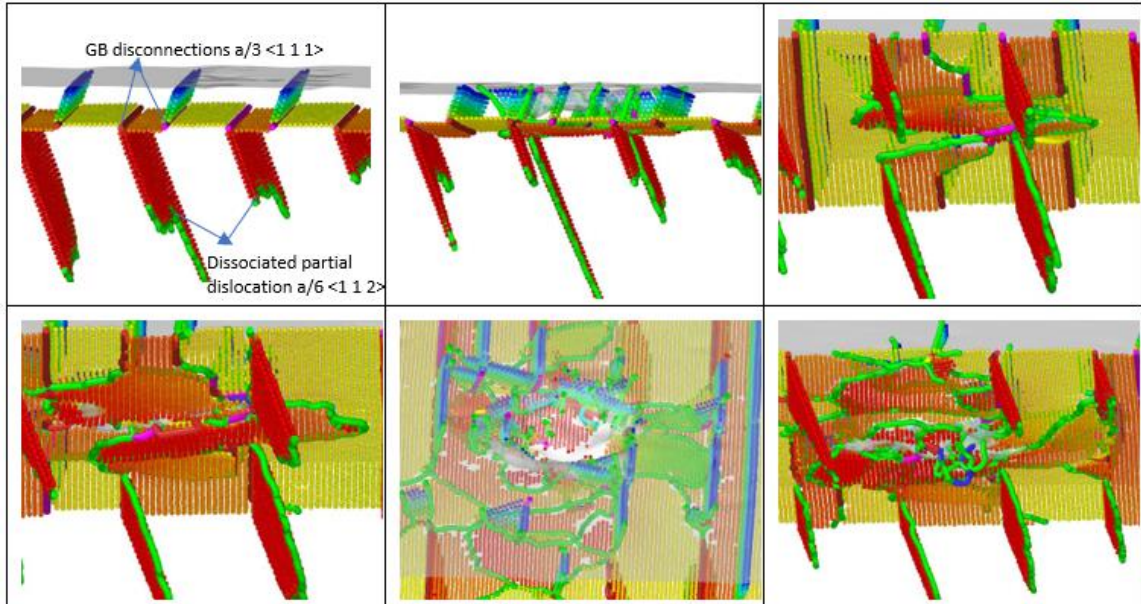
Figure 4.14: Snapshots of the deformation of bicrystal sample with Σ171 (11 11 10) GB located 1.9nm below the indentation surface a) h=0, b) h= 1.28nm side view, c)h=1.28nm bottom view, d) h= 1.68nm, e) h= 2.41nm top view, f) h=2.41nm bottom view.

4.3.2.3 Grains with misorientation angle θ>114.5º

As it was shown in Figure 4.1, all the GBs with θ>109.5º have E units in their structures. According to Spearot's[37] study on copper grain boundaries containing E structural unit, the natural morphology of the interface porosity with respect to the primary dislocation slip systems will result in the easy emission of Shockley partial dislocations from boundaries during uniaxial tension. Based on Spearot's[37] conclusion, the emission of SPDs that are nucleated directly from E structural units is facilitated by the collapse of the free volume at the interface. Figure 4.15 shows the nucleation and propagation of Shockley partial dislocations on the (1 1 1) and (1 1 1) planes, even in the regions far from the pit area.
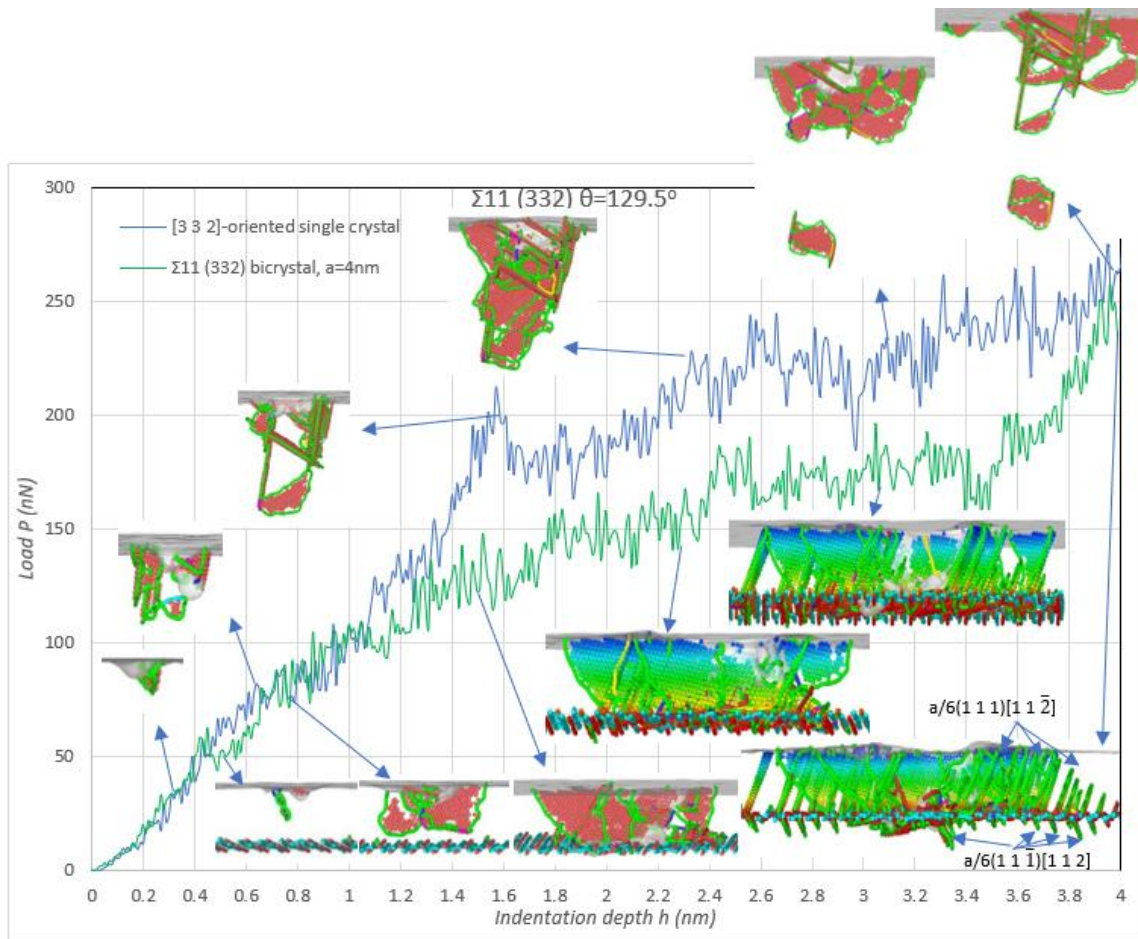
Figure 4.15: Deformation mechanism of a sample with Σ11 (332) θ=129.5o GB at 300K. Atoms are colored based on their positions regarding the GB after passing the GB (Loops that passed GB are shown in red color), Cyan color lines at the grain boundary are intrinsic Frank dislocations with a/3 <1 1 1> Burgers vector.

The dependence of the hardness decrease to the distance of the grain boundary from the indentation surface is summarized in Figure 4.16. As it is observed the highest decrease happens when the indentation is applied near the grain boundary. The grain boundaries have little influence on the hardness at distance higher than 8 nm from the indentation surface (the size of indenter diameter is 8 nm). Moreover, the hardness decrease is more apparent at the distance of 2.6nm for the GBs with θ<109.5°.
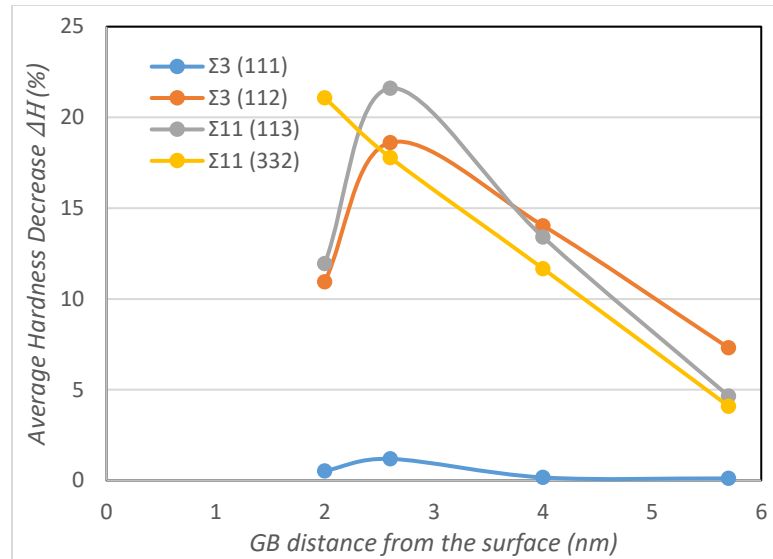
Figure 4.16: Average hardness decrease in relation to the distance between the indentation surface and the grain boundary for several bicrystals.

4.3.3. Effect of grain boundary energy on the indentation hardness

Based on the results, GB structure plays an important role in the process of dislocation nucleation from GB and the interaction of lattice dislocations with the GB. The larger free volume of E units in the structure of GBs with θ>109.5° results in high boundary energy and provides sufficient room for rearranging GB atoms during deformation to nucleate dislocations and accommodate local deformation. The average of hardness decreases at the first 2nm indentation depth is plotted in Figure 4.17, based on the GB energy. Since Σ3(1 1 1) twin boundary has a simple structure and stable level of energy, no dislocation nucleation happens in the grain boundary, but rather slip of dislocations and twin partial slip is observed during the indentation. The amount of hardness reduction increases with GB energy and samples with low level of GB energy and more stable structure presents closer behavior to single-crystal samples and requires higher stress for dislocation nucleation at the grain boundary. The relation of hardness decrease and GB energy follows an exponential equation as follows;

$$\Delta H = H_0 Exp(a\gamma_{GB}) \tag{4.4}$$

Where, H_0 is a material property, mostly related to the stacking fault energy and *a* is constant. The values of H_0 and *a* are 1.54 and 0.0057 considering all the GBs with various misorientation angles. However, the dependence of the ΔH to the GB energy increases if GB structures were considered separately based on the θ≤109.5° or θ≥109.5° as is observed in Figure 4.18. Nevertheless, the relation of ΔH and GB energy follows very close trends in both cases.
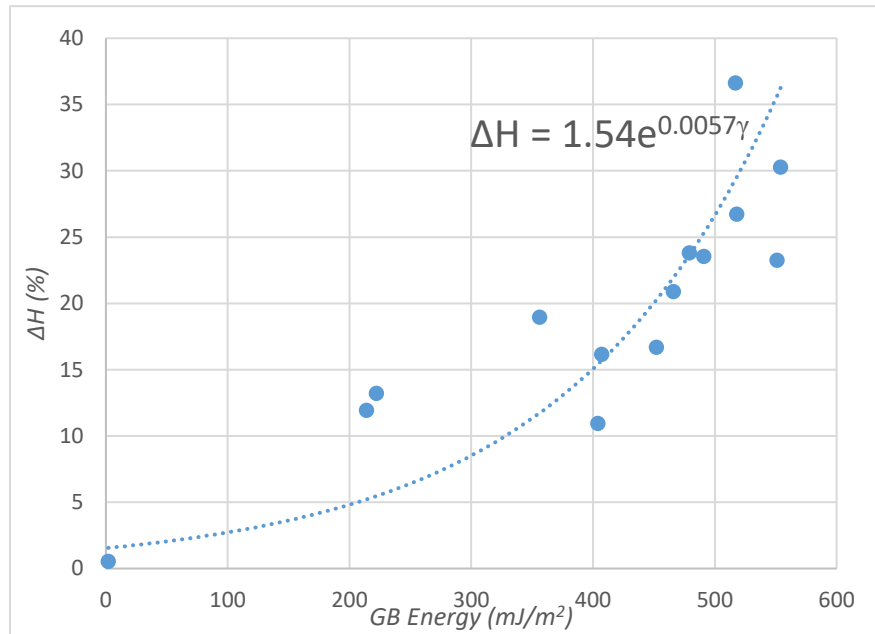
Figure 4.17: The amount of average hardness decrease as a function of GB energy for all of the misorientation angles.
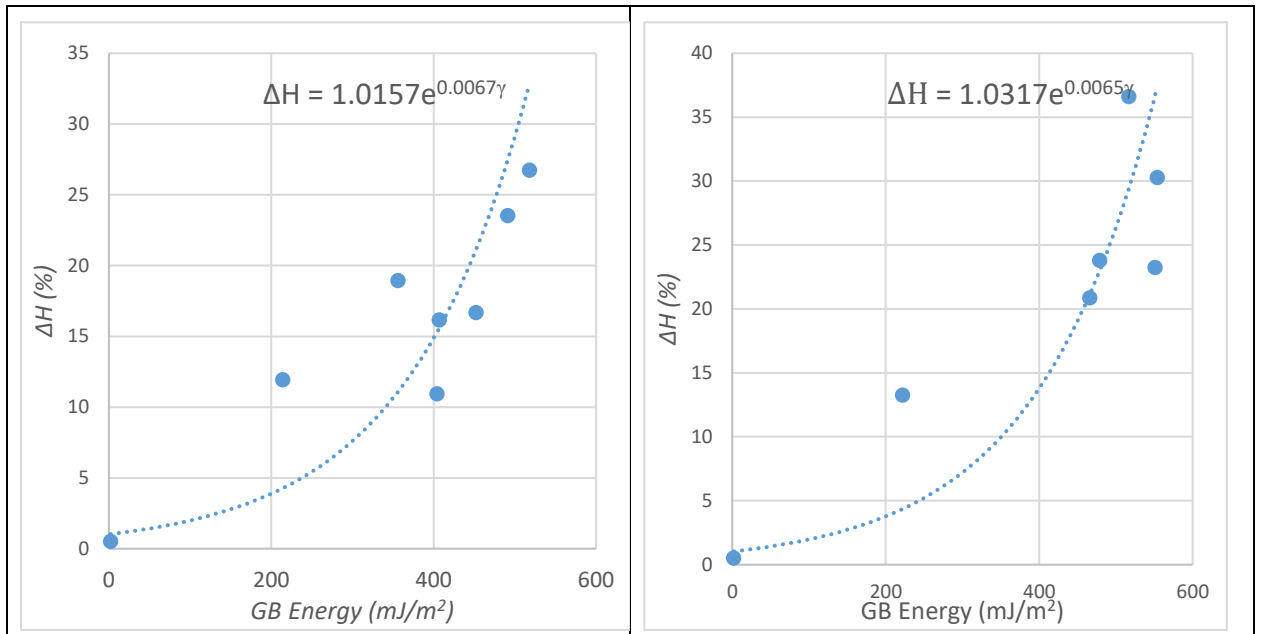
Figure 4.18: The amount of average hardness decrease as a function of GB energy for a) GBs with θ≤109.5º, b) GBs with θ≥109.5º

Conclusions

Atomistic simulations were used to study the operative mechanisms of: i) dislocation slip-GB interaction and ii) nucleation of the partial dislocations from symmetric tilt grain boundaries and their influence on the local deformation of nano-scale volumes of FCC metals. Results of the nanoindentation of single and bicrystal samples show that the incipient yield occurs at a lower load in all the bicrystal samples compared to the perfect crystals. However, the yielding mechanisms vary considerably for the different grain boundaries. The smallest effect was observed for the coherent Σ3(1 1 1) twin boundary and this is consistent with its simple structure and low GB energy. The results of the slip-GB interaction show that the transmission of lattice dislocation across the GB introduces a step at the GB plane due to the different orientations of the adjacent grains. The effect of the GB on the indentation force – depth response decreases with increasing indentation depth. When the indentation depth was greater than about 3.5 nm the bicrystal samples presented the same force-depth response as the single crystals.

Intrinsic stacking faults and dissociated high-energy GB interface structures resulted in dislocation nucleation at GBs in the early stages of deformation. The larger free volume of E units in the structure of GBs with $\theta > 109.5^\circ$ leads to the higher boundary energy and provides sufficient room for rearranging GB atoms during deformation to nucleate dislocations and accommodate local deformation. A strong exponential correlation was observed between the interfacial boundary energy and its effect on the bicrystal strength. More stable structures present closer behavior to single-crystal samples and require higher stress for dislocations to cross, or nucleate at, the grain boundary.

References

[1] E.O. Hall, The Deformation and Ageing of Mild Steel .3. Discussion of Results, P Phys Soc Lond B 64(381) (1951) 747-753.

[2] N.J. Petch, The Cleavage Strength of Polycrystals, J Iron Steel I 174(1) (1953) 25-28.

[3] T.T. Zhu, A.J. Bushby, D.J. Dunstan, Materials mechanical size effects: a review, Mater Technol 23(4) (2008) 193-209.

[4] V. Yamakov, D. Wolf, S.R. Phillpot, H. Gleiter, Deformation twinning in nanocrystalline Al by molecular dynamics simulation, Acta Mater 50(20) (2002) 5005-5020.

[5] V. Yamakov, D. Wolf, S.R. Phillpot, H. Gleiter, Dislocation-dislocation and dislocation-twin reactions in nanocrystalline Al by molecular dynamics simulation, Acta Mater 51(14) (2003) 4135-4147.

[6] V. Yamakov, D. Wolf, S.R. Phillpot, A.K. Mukherjee, H. Gleiter, Deformation mechanism crossover and mechanical behaviour in nanocrystalline materials, Phil Mag Lett 83(6) (2003) 385-393.

[7] D. Wolf, V. Yamakov, S.R. Phillpot, A. Mukherjee, H. Gleiter, Deformation of nanocrystalline materials by molecular-dynamics simulation: relationship to experiments?, Acta Mater 53(1) (2005) 1-40.

[8] K.E. Aifantis, W.A. Soer, J.T.M. De Hosson, J.R. Willis, Interfaces within strain gradient plasticity: Theory and experiments, Acta Mater 54(19) (2006) 5077-5085.

[9] D.E. Spearot, M.A. Tschopp, K.I. Jacob, D.L. McDowell, Tensile strength of $< 100 >$ and $< 110 >$ tilt bicrystal copper interfaces, Acta Mater 55(2) (2007) 705-714.

[10] M.A. Tschopp, D.L. McDowell, Dislocation nucleation in Sigma 3 asymmetric tilt grain boundaries, Int J Plasticity 24(2) (2008) 191-217.

[11] E.T. Lilleodden, J.A. Zimmerman, S.M. Foiles, W.D. Nix, Atomistic simulations of elastic deformation and dislocation nucleation during nanoindentation, J Mech Phys Solids 51(5) (2003) 901-920.

[12] K.J. Kim, J.H. Yoon, M.H. Cho, H. Jang, Molecular dynamics simulation of dislocation behavior during nanoindentation on a bicrystal with a Sigma=5 (210) grain boundary, Mater Lett 60(28) (2006) 3367-3372.

[13] A. Hasnaoui, P.M. Derlet, H. Van Swygenhoven, Interaction between dislocations and grain boundaries under an indenter - a molecular dynamics simulation, Acta Mater 52(8) (2004) 2251-2258.

[14] H. Jang, D. Farkas, Interaction of lattice dislocations with a grain boundary during nanoindentation simulation, Mater Lett 61(3) (2007) 868-871.

[15] T. Tsuru, Y. Kaji, D. Matsunaka, Y. Shibutani, Incipient plasticity of twin and stable/unstable grain boundaries during nanoindentation in copper, Phys Rev B 82(2) (2010).

[16] M.D. Sangid, T. Ezaz, H. Sehitoglu, I.M. Robertson, Energy of slip transmission and nucleation at grain boundaries, Acta Mater 59(1) (2011) 283-296.

[17] L. Zhang, C. Lu, K. Tieu, Atomistic Simulation of Tensile Deformation Behavior of Sigma 5 Tilt Grain Boundaries in Copper Bicrystal, Sci Rep-Uk 4 (2014).

[18] M.S. Talaei, N. Nouri, S. Ziaei-Rad, Grain boundary effects on nanoindentation of Fe bicrystal using molecular dynamic, Mech Mater 102 (2016) 97-107.

[19] G.Z. Voyiadjis, M. Yaghoobi, Role of grain boundary on the sources of size effects, Computational Materials Science 117 (2016) 315-329.

[20] B.R. Kuhr, K.E. Aifantis, Interpreting the inverse Hall-Petch relationship and capturing segregation hardening by measuring the grain boundary yield stress through MD indentation, Mat Sci Eng a-Struct 745 (2019) 107-114.

[21] S. Plimpton, Fast Parallel Algorithms for Short-Range Molecular-Dynamics, J Comput Phys 117(1) (1995) 1-19.

[22] C.L. Kelchner, S.J. Plimpton, J.C. Hamilton, Dislocation nucleation and defect structure during surface indentation, Phys Rev B 58(17) (1998) 11085-11088.

[23] A. Stukowski, K. Albe, Extracting dislocations and non-dislocation crystal defects from atomistic simulation data, Model Simul Mater Sc 18(8) (2010).

[24] A. Stukowski, Visualization and analysis of atomistic simulation data with OVITO-the Open Visualization Tool, Model Simul Mater Sc 18(1) (2010).

[25] S.M. Foiles, M.I. Baskes, M.S. Daw, Embedded-Atom-Method Functions for the Fcc Metals Cu, Ag, Au, Ni, Pd, Pt, and Their Alloys, Phys Rev B 33(12) (1986) 7983-7991.

[26] G. Ziegenhain, H.M. Urbassek, A. Hartmaier, Influence of crystal anisotropy on elastic deformation and onset of plasticity in nanoindentation: A simulational study, J Appl Phys 107(6) (2010).

[27] T. Tsuru, Y. Shibutani, Y. Kaji, Fundamental interaction process between pure edge dislocation and energetically stable grain boundary, Phys Rev B 79(1) (2009).

[28] L. Zhang, C. Lu, K. Tieu, X. Zhao, L. Pei, The shear response of copper bicrystals with Σ11 symmetric and asymmetric tilt grain boundaries by molecular dynamics simulation, Nanoscale 7(16) (2015) 7224-7233.

[29] L. Smith, D. Farkas, Deformation response of grain boundary networks at high temperature, J Mater Sci 53(8) (2018) 5696-5705.

[30] M.A. Tschopp, D.L. McDowell, Grain boundary dislocation sources in nanocrystalline copper, Scripta Mater 58(4) (2008) 299-302.

[31] X.Y. Li, Y.J. Wei, L. Lu, K. Lu, H.J. Gao, Dislocation nucleation governed softening and maximum strength in nano-twinned metals, Nature 464(7290) (2010) 877-880.

[32] Z.S. You, X.Y. Li, L.J. Gui, Q.H. Lu, T. Zhu, H.J. Gao, L. Lu, Plastic anisotropy and associated deformation mechanisms in nanotwinned metals, Acta Mater 61(1) (2013) 217-227.

[33] A.G. Frøseth, P.M. Derlet, H. Van Swygenhoven, Vicinal twin boundaries providing dislocation sources in nanocrystalline Al, Scripta Mater 54(3) (2006) 477-481.

[34] J.D. Rittner, D.N. Seidman, <110> symmetric tilt grain-boundary structures in fcc metals with low stacking-fault energies, Phys Rev B 54(10) (1996) 6999-7015.

[35] S.M. Foiles, D.L. Medlin, Structure and climb of 13 111 twin dislocations in aluminum, Materials Science and Engineering: A 319-321 (2001) 102-106.

[36] E.A. Marquis, D.L. Medlin, Structural duality of $1/3 < 111 >$ twin-boundary disconnections, Phil Mag Lett 85(8) (2005) 387-394.

[37] D.E. Spearot, Evolution of the E structural unit during uniaxial and constrained tensile deformation, Mech Res Commun 35(1) (2008) 81-88.

Chapter 5

5. The effect of crystal orientation on the size effects of nano-scale fcc metals

The present work investigates the dominant mechanisms of size effects in the plasticity of fcc metallic samples. Compression of nanopillars with different nanoscale diameters reveals that three different mechanisms, including; dislocation exhaustion, dislocation starvation, and dislocation interaction are controlling the plasticity of Au nanopillars with different orientations The simulation results show that the plasticity always starts with the nucleation of dislocations at free surface, and the crystal orientation affects the subsequent microstructural evolution and flow behavior. Frequent dislocation interactions in orientations with more slip systems ([100] and [111]) result in the later activation of dislocation starvation mechanism while the less chance of dislocation interaction in [110] orientation will result to the sooner dislocation starvation mechanism activation. The high symmetry of [111] orientation will result in the activation of a high density of dislocation loops, which their interaction will lead to the less serrated stress-strain response than the ones for two other orientations. Based on the results the Schmid factor of leading and trailing partials plays a decisive role in leading to the twinning deformation or slip deformation. [100]-oriented pillars deform by the glide of the twin boundary planes while [110] and [111] oriented pillars deform by the slip of stacking fault loops and planes. A significant difference is observed in the strength of pillars of the same size with different orientations. The power-law equation exponent is completely dependent on the crystal orientations, and a week or no size effect is observed in the compression of [100]- and [110]-oriented Au pillars with sizes less than 40 nm. The results of the compression of pillars with rigid constraining layers show that in the absence of free surface the nucleation of initial dislocations happens in much higher stress and trapping of dislocations in the pillar will result in the smooth increase of stress with strain. The compression of rigid coated and Pt coated nanopillars show that the observed orientation based behaviour and size scale effects decrease by confining the free surface.

5.1. Introduction

Nano-size materials are now regularly being fabricated for a wide variety of applications. These systems exhibit mechanical properties that can be quite significantly different from their macroscopic counterparts. Classic continuum mechanics based theories do not accurately describe their mechanical strength and deformation behaviour primarily because the sample size, being similar in scale to discrete crystal imperfections within the sample, invalidates the assumption of an elastic continuum. There is thus a need for understanding the fundamental operative plastic deformation mechanisms in such samples. Such an understanding must be arrived at with new experimental data and novel computation-based deformation modelling approaches.

Size effects on the mechanical properties of metallic samples was initially described in terms of the necessary existence of large strain gradients present within sample in result of nonhomogeneous loading condition of some micromechanical testing techniques such as micro/nano- bending [1, 2], torsion [3], and indentation testing [4-6]. These observations of increased strength and work-hardening rates in small metal samples have been theoretically attributed to the presence of increased dislocation density, which is "geometrically necessary" to accommodate these large localized strain gradients within the small volumes of deformation [7-12]. However, a strong size effect was observed by Uchic et al. [13, 14] even in the absence of strain gradients, in the micro compression of cylindrical samples. Their results showed a strong increase in the flow stress with decreasing the size of micropillars prepared using focused ion beam (FIB) machining. From then on different scholars have tried to describe the material behavior and operating mechanisms in the deformation of small-sized materials. In studies involving the compression of mesoscopic scale Ni single crystals, Dimiduk et al. [15] were the first to report that the flow stress is a stochastic quantity for small volumes (characteristic dimensions below ~20 μm) and intrinsic size effects may play a more important role in plasticity of this scale than gradient-induced storage of geometrically necessary dislocations (GNDs).

One of the theories for describing length-scale dependence of the strength of metals was made by Greer et al. [16] who explained the phenomena in terms of the dislocation starvation model. According to this model, if the rate of dislocation annihilation at the free surfaces is greater than that of dislocation nucleation and multiplication in a small crystal, then a "dislocation starvation" mechanism will occur, in which the crystal is constantly drained from mobile dislocations, and plasticity is only promoted by the nucleation of new dislocations at elevated stress [17]. This condition can be considered as a special case of "source exhaustion" hardening mechanism which dominates when there is insufficient mobile dislocation density to accommodate plastic deformation [18]. Such a source-limited deformation has been observed during in situ TEM nanocompression and tensile testing of MgO nanocubes, and Mo alloy nanofibers [19, 20].

Other theories, such as the source truncation and the weakest link theories, have also been developed to describe length-scale dependent incipient deformation processes that can occur in the absence of large strain gradients [21-24]. In the source truncation model, a Frank Read dislocation source is truncated by the sample surface and leaves behind two half sources whose length and thus operating stress is limited by sample size [25, 26]. The number of possible low-stress slip planes (number of large dislocation length sources) decreases with sample size based on the weakest link theory and higher stress is needed to activate short dislocation sources which were un-activated in larger samples [27].

In situ transmission electron microscope compression tests of Wang et al. [28] on Al pillars showed two contrasting regimes underlying the large strain bursts. For small pillars (D = 80 to 300 nm) incipient plastic deformation occurred by sudden dislocation generation, characterized by high collapse stresses and dislocation-free post-collapse microstructure while larger pillars (D = 300 to 1000 nm) displayed incipient plastic deformation occurring at relatively low-stress with retention of the dislocation network after the strain burst. Liang et al. [29] conducted compression tests on single-crystalline micropillars (D = 0.5 to 3 μm) of a twinning-induced plasticity (TWIP) steel. According to their observation, the plastic deformation of their pillars was driven by twinning mainly by twin growth in one single twinning system, suggesting that the size effect

should be related to twinning deformation rather than dislocation gliding. In-situ TEM deformation performed on micron-sized Ni single crystals by Samaee et al. [30] indicated that small-scale plasticity is mainly controlled by the conversion of sparse tangled dislocations, located in the test sample prior to deformation, into stable single-arm sources and the successive operation of these sources. Wang et al. [31] in situ atomic-scale observations of Pt nanocrystals plastic deformation indicated that full dislocation mechanism dominated plasticity of nanocrystals of size above ~6 nm. However, the plastic deformation was dominated by the dislocation-free mechanism for nanocrystals of diameters below ~2 nm. Zhao et al.'s [32] STEM observations of deformed [011] oriented Cu micropillars showed the formation of fractal geometry dislocation cells in pillars larger than 1µm while dislocations were not retained in the smaller pillars.

Mechanical tests of submicron-size samples, such as those described above, are very difficult to perform and are ultimately limited by the spatial resolution, image stability, and load/displacement resolution of the test equipment. To study the actual operative deformation mechanisms occurring in such samples one must resort to numerical simulation of the deformation process. Between simulation techniques, discrete dislocation dynamics (DDD) simulation and the molecular dynamics (MD) simulation appeared as effective methods for the description of plasticity and deformation mechanisms in materials. DDD simulation of the deformation of FCC single crystals performed by Zhou et al. [33] have indicated that below a critical size, which depends upon the initial dislocation density, nucleation of surface dislocations is required to accomplish plastic deformation due to the loss of internal dislocation sources resulting from operation of a "dislocation starvation hardening" process. Only when the sample size is larger than a critical size does conventional multiplication of internal dislocation sources occur during plastic flow. Based on Cui et al.'s [34] simulation on the Ni single crystal micropillars with diameters from 200 nm to 800 nm, intermittent strain burst is mainly controlled by the operation of single-arm sources (SAS) and the length of the stable single-arm source is proportional to the sample size. Using 3D DDD simulations, El-Awady [18] predicted that operative deformation mechanism changes from dislocation-source strengthening to forest hardening at a critical dislocation density based upon the sample size. Ryu et al. [35] found that dislocation surface nucleation is the

dominant operative deformation mechanism in micropillars with diameters less than 200 nm, while the operation of single-arm dislocation sources governs the deformation process when the pillar diameter is larger than 1 μm. Between these diameters, both deformation mechanisms occur in a stochastic way. Leung et al. [36] modelled the deformation of single crystal nanowires using a method based on the dynamics of dislocation-density functions. Their findings indicate that specimens smaller than about 4000b deform by a dislocation depletion mechanism where the total dislocation density remains essentially constant throughout the deformation process while for intermediate-sized samples, between 4000b and 8000b, dense dislocation clusters affect the operative mechanism of deformation according to the weakest-link deformation concept. DDD simulation of the effect of strain rate, sample size and dislocation sources on the deformation behavior of sub-micron pillars has been performed by Hu et al.[37]. They observed that there is a transition from dislocation multiplication to surface dislocation nucleation as the strain rate increase for pillars smaller than D = 400 nm dimeter.

Molecular dynamics MD simulations, performed by Sansoz [38], of the deformation of sub-75 nm diameter Cu pillars with high initial dislocation densities and showed that neither dislocation-exhaustion nor dislocation source-truncation processes significantly contribute to the size dependence of <1 1 1> oriented samples, whereas the observed length-scale dependence of the incipient flow stress can be related to emission of new dislocations from small immobile defects inside the pillars. Compared to DDD simulations, MD modelling has the capability of considering cross-slip precisely, which is an important mechanism in the plasticity of metallic confined volumes. Moreover, the mechanism of dislocation nucleation from free surfaces can be precisely modeled with MD simulation [39]. Constant strain rate MD simulations performed by Weinberger and Tucker [40] showed that single-arm dislocation sources can be created and destroyed by interaction with dislocations nucleated from grain boundaries and free surfaces [40, 41]. Xu et al. [42] studied the effect of crystal orientation on the operative deformation mechanisms of Al nanopillars and observed that a dislocation-starvation state is not readily achievable when deforming a crystal along high symmetry orientations but can be achieved when deforming along lower symmetry orientations. Yaghoobi and Voyiadjis [39] MD simulations on the Ni nanopillars showed that the deformation dominant

mechanism is independent of the strain value and is affected only by the pillar size. Rohith et al.'s [43] MD simulation on the tensile behaviour of Cu nanowires showed two stages irrespective of deformation temperature and strain rates; dislocation exhaustion at early stages of deformation followed by dislocation starvation at high strains. Korchuganov et al. [44] proposed an atomic model for the nucleation of dislocation and twins based on the local reversible fcc→bcc→fcc transformation. As they suggested the local internal stresses at the defect nucleation zones are high enough to be able to decrease the stability of the initial structure and provide the possibility of fcc→bcc transfer.

Although different theories have been proposed to explain the operative mechanisms by which incipient plasticity occurs in nanoscale volumes of ductile metal, a clear understanding of the combined effect of fundamental parameters such as crystal orientation and crystal surfaces is still missing. In this study, the effect of these parameters is investigated with MD simulation of Au nanopillars compression, focusing on the changes in the dislocation density and stress and development and movements of the crystal defects.

5.2. Methods

Molecular dynamics simulation is performed using the open-source Large-scale Atomic/Molecular Massively Parallel Simulator (LAMMPS) [45] to study the behavior of Au, Pt, and Pt coated Au nanopillars. The Au and Pt embedded-atom method (EAM) potential developed by Foiles et al. [46] is used to simulate the Au–Au and Pt-Pt atomic interaction. EAM alloy potential developed by O'Brien et al. [47] is used to simulate Au-Pt interaction at Pt coated Au nanopillars. A range of pillar sizes has been used to evaluate the effect of surface/volume ratio. The diameter of pillars ranges from 7nm to 40nm and the height/diameter ratio was kept 2 for all of them. The simulated systems contained approximately 38,000 to 6,570,000 atoms, depending on their size. Energy minimization was performed by the conjugate gradient (CG) method and simulations are performed in constant NVT ensemble with a velocity-Verlet integrator and temperature is controlled at 300 K by the Nosé–Hoover thermostat. The perfect crystal arrangement of

the pillars and spheres were relaxed for 60 ps at zero force to minimize the potential energy.

Common neighbor analysis (CNA) [48] is used to analyze the local atomic crystal structure. Dislocation Extract Algorithm (DXA) [49] is applied to identify the dislocation patterns and the Open Visualization Tool OVITO [50] is utilized to visualize the atomistic configurations.

5.3. Plastic deformation mechanisms

5.3.1. [111]-oriented nanopillars

Figure 5.1 presents the stress-strain response of compression of a 25nm diameter Au nanopillar along [111] orientation. As it is observed there is a big pop-in after the initial yield and the plastic flow stress fluctuate within a certain range after the first drop. To have a better understanding of the observed plastic behavior of Figure 5.1, the evolution of microstructure is investigated in detail during the compression (Figure 5.2). Atoms on the perfect fcc lattice are hidden for clarity and atoms on hcp lattice are shown in red. In some of the snapshots all the atoms are hidden and only dislocations have been presented to make it more clear. Shockley, stair-rod, Hirth, and Frank partial dislocations and perfect dislocations are presented in green, purple, yellow, Cyan, and blue, respectively. Before the major drop, Shackley and stair-rod partial dislocations are nucleated at the intersection of pillar and substrate around the edges of the pillar (Figure 5.2a and b). However, they are not stable and annihilate at the surface with force increase. New dislocations are nucleated from surface of the pillar and start to grow at the strain 0.04461 as is shown in Figure 5.2c. As the force increases, new dislocations nucleated from the surface and from the pinning points inside the pillar and stacking faults grow along the {111} planes. These pinning points are results of the cross slip of the dislocations already nucleated from the surface. Figure 5.3d presents the nucleated dislocations from the surface and internal sources. High rate of dislocation nucleation from the internal pinning points and from the surface will result to a sudden increase of dislocation density at the crystal (Figure 5.3 and Figure 5.2e) and thus a significant drop at the stress-strain curve. Figure 5.2f shows a top view from the dislocation network of the point f at the stress

strain curve in which a huge amount of small stacking fault planes are nicely aligned along the {111} planes. This indicates that dislocations do not leave the sample immediately, rather they multiply by cross-slip. This continues until point g where all the crystal is full of small stacking faults and the amount of stress drops to around 50Mpa. Elongation of these small dislocations which most of them are pinned at their ends provides the dislocation length required to sustain the imposed plastic flow. Growth of stacking faults and annihilation of dislocations at the surface as well as reaction of dislocations which shuts off internal sources, will result to the exhaustion hardening and increase of the strength as noted by point h. This gradual decrease of dislocation density is denoted as a dislocation exhaustion stage in Figure 5.3. A slight increase in flow stress is associated with exhaustion stage. Nucleation of dislocations is required after this point to provide enough dislocations for deformation due to the loss of internal nucleation sources. However, dislocation density remains low and almost constant with increasing strain which indicates that the nanopillar is depleted of dislocations. In this stage, the deformation is mainly controlled by nucleation of dislocations at the surface or internal pinning points and annihilation of them at the surface or truncation of nucleated single arm dislocations and dislocation starvation dominates the plasticity. The marginal fluctuations of dislocation density indicates that the rate of dislocation annihilation and rate of dislocation nucleation are almost the same.
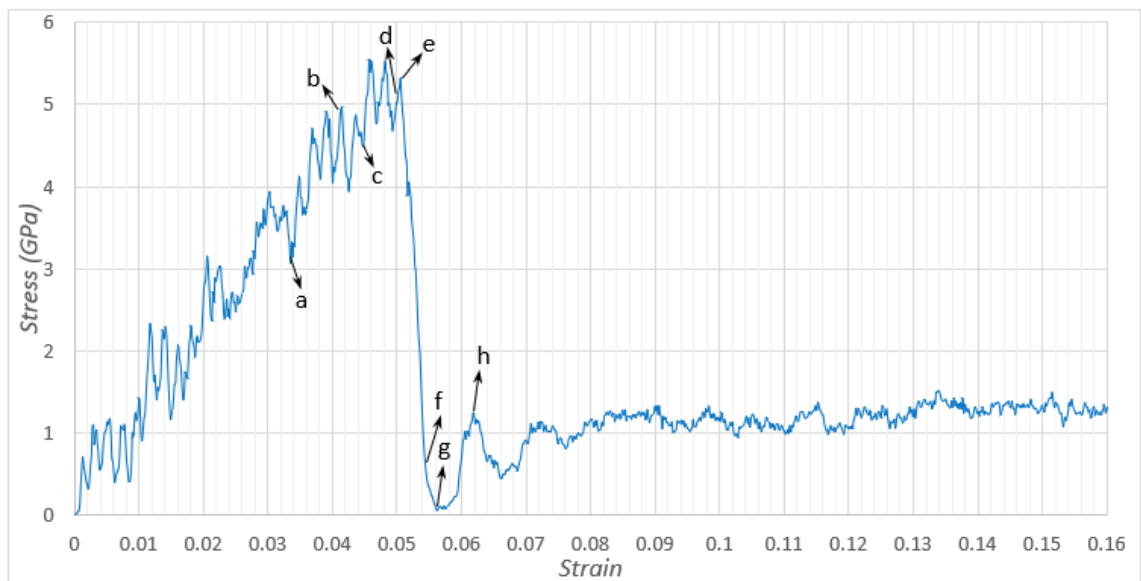
Figure 5.1: Flow behavior of the [111]-oriented 25nm Au pillar (T=300K).
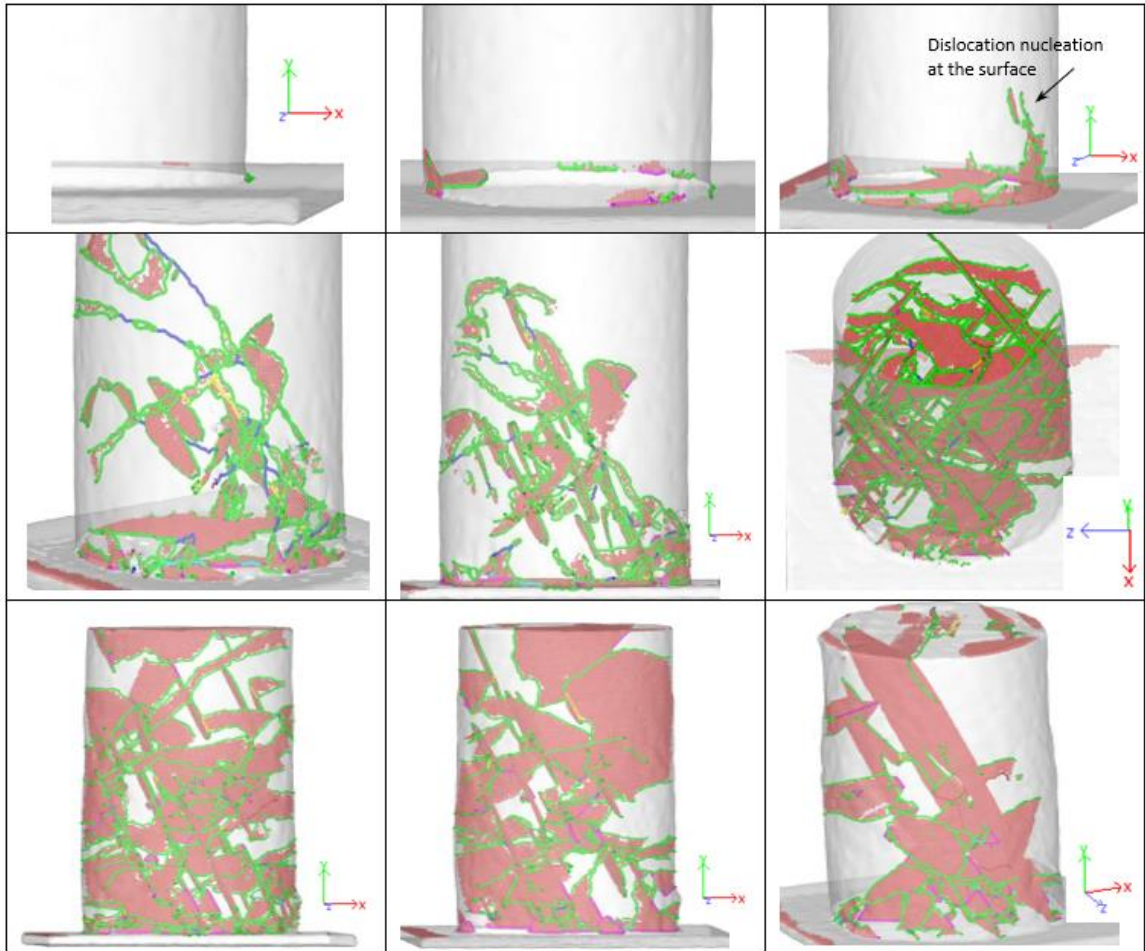
Figure 5.2: Snapshots of the microstructural evolution of [111]-oriented 25nm pillar (figures are corresponded to the points of figure 5.1).
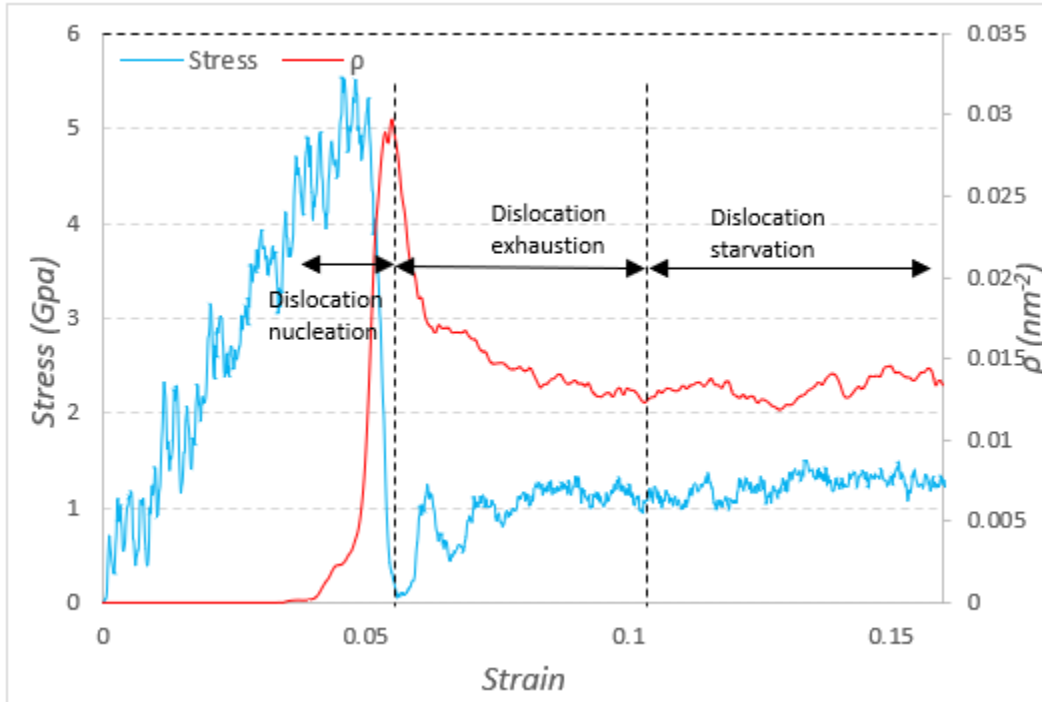
Figure 5.3: Variation of flow stress and dislocation density during the deformation of [111]-oriented 25nm Au pillar, indicating the deformation mechanisms domination ranges.

To have a better idea of the effect of the free surface, the diameter of the pillar is decreased to 10nm to increase the effect of surface (surface/volume ratio is increased from 0.1799 nm^{-1} to 0.4494 nm^{-1} by decreasing the pillar diameter from 25nm to 10nm). What is observed is the same nucleation sites at the early stages of plasticity. However, a higher rate of nucleation is observed from the internal pinning points which are created due to the cross slip. Figure 5.4a shows one of these points in which lots of single-arm dislocations are pinned to it at one of their ends. However, their vicinity to the surface makes them deactivate in a short time and nucleation continues at other pinning points and surface. Figure 5.4b shows the dislocation network at the strain of 0.7955, where the pillar is heavily deformed and the high density of dislocations is active at the deformation volume (Figure 5.5). As the force increases and stacking fault planes grow, some of the dislocations leave the sample and the dislocation density decreases. Moreover, internal nucleation sources shut off due to the truncation at surface and interaction of dislocations (Figure 5.5, 5.4c). Looking at Figure 5.5, it is obvious that the deformation behavior of

the small pillar (10nm diameter) at dislocation starvation range is dominated by dislocation nucleation at the surface or activation of internal sources and annihilation of dislocations at surface. This is clear by comparing stress and dislocation density as the strength drops by increase of dislocation density and rises with dislocation density decrease, indicating that the deformation is mainly nucleation based driven. As the dislocation density decreases, plasticity mainly continues by the growth of stacking faults surrounded by single arm dislocations (Figure 5.4d). The next main drop of stress happens when the number of nucleated dislocations from the upper corner of pillar increases (Figure 5.4e and Figure 5.5).
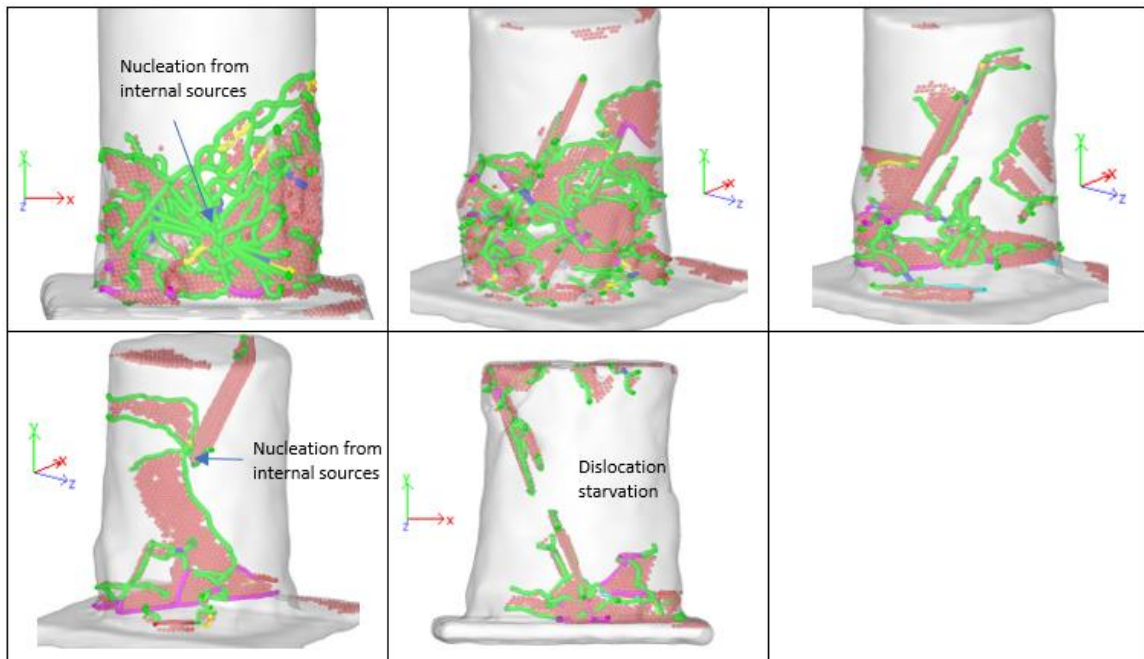
Figure 5.4: Snapshots of the microstructural evolution of [111]-oriented 10nm pillar, indicating the effect of internal nucleation sources and dislocation starvation mechanism.
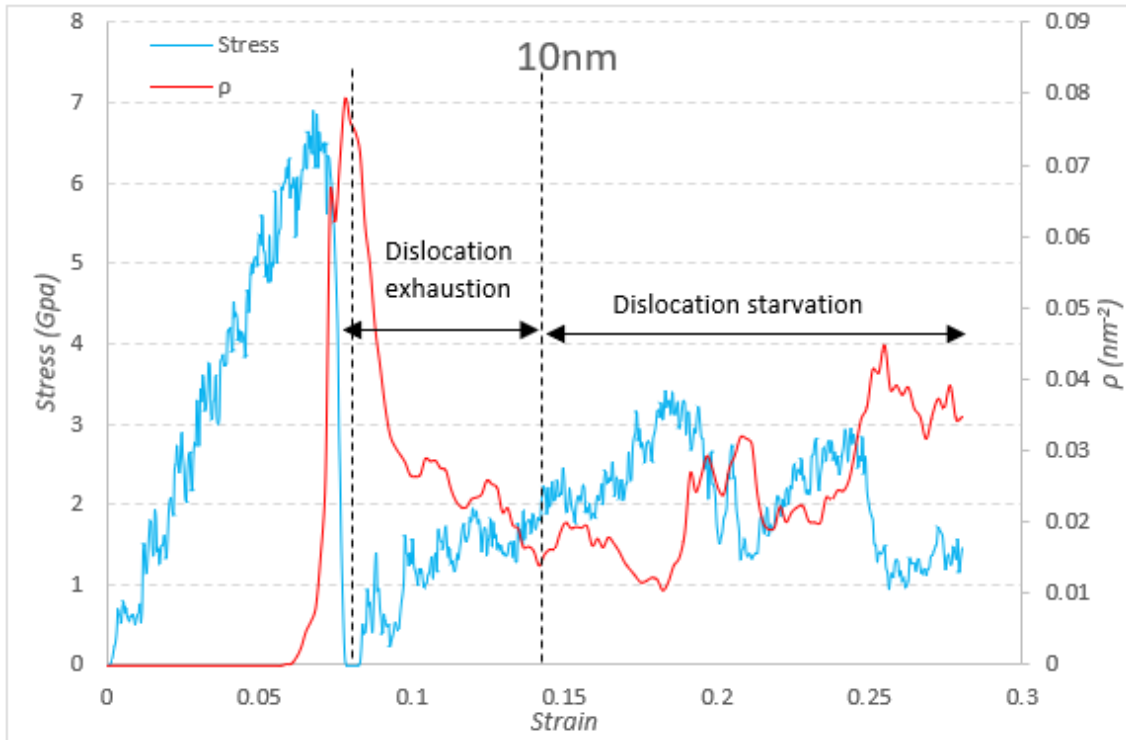
Figure 5.5: Variation of flow stress and dislocation density during the deformation of [111]-oriented 10nm Au pillar, indicating the deformation mechanisms domination ranges.

For the 40nm pillar, nucleation starts from the bottom of the pillar and its surface similar to 25nm one (Figure 5.6a). The dislocation structure before and after the large pop-in (strains 0.05435 and 0.05752) are shown in Figure 5.6b and c). Figure 5.7 compares the flow stress of [111] oriented pillars with different diameters. As it is clearly observed, the smallest pillar shows significantly higher strength than the other two diameters. This could be related to the higher surface/volume ration in the 7nm pillar, which will result in a higher rate of dislocation annihilation. More pop-in events in the 10nm pillar than the other two ones approve this.
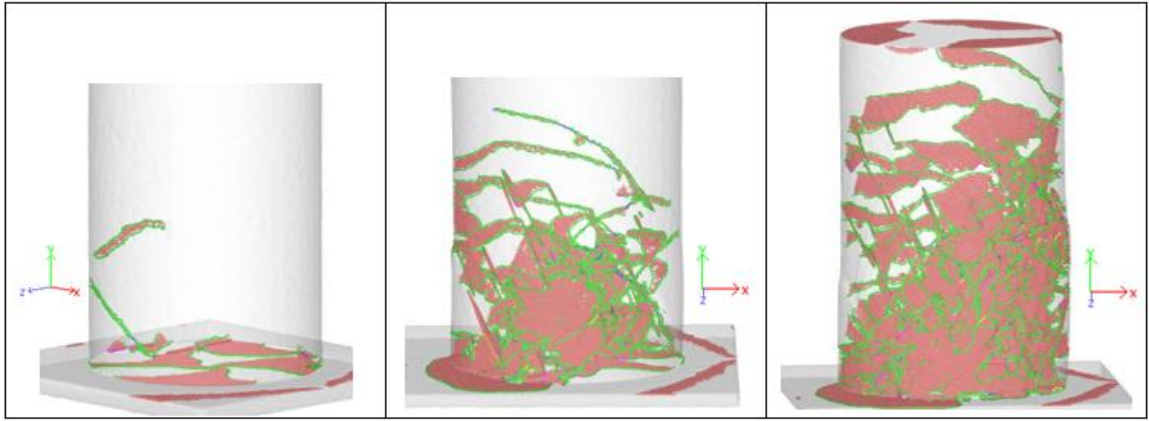
Figure 5.6: Snapshots of the microstructural evolution of [111]-oriented 25nm pillar.
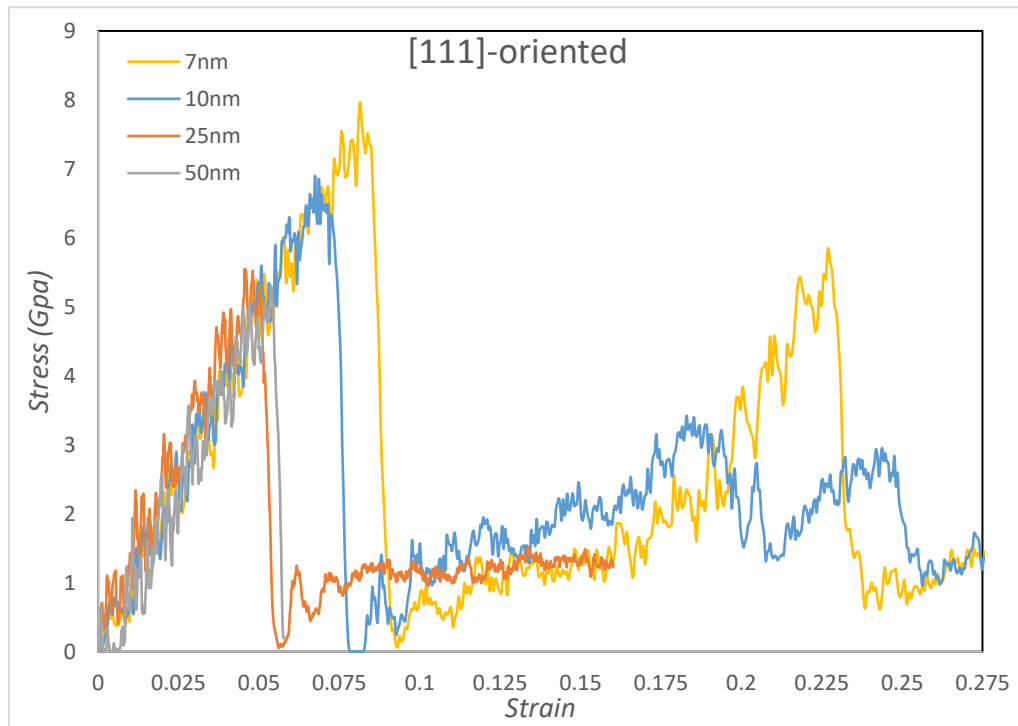
Figure 5.7: Effect of sample size on the flow behavior of [111]-oriented Au nanopillars.

5.3.2. [100]-oriented nanopillars

Two other orientations are studied to understand the effect of orientation on the size effects. Figure 5.8 shows the stress-strain curve of the compression of the pillar oriented along the <100> direction. During the elastic deformation, Shockley partial dislocations nucleate from the surface as is observed in Figure 5.9a, however, they are not stable and

annihilate at the surface after nucleation. The glide of one of the nucleated dislocations will result in the first slip event on the (111) plane (Figure 5.9b) and stops stress increase as shown by point b. Activation of two adjacent parallel slip planes by glide of two nucleated dislocations on the ($\bar{1}$11) plane will from a micro-twin as shown in Figure 5.9c. As the deformation proceeds different slip events happens on the {111} planes and intersect to each other, resulting to the increase of dislocation density and stress release (point d). With the increase of strain, twin partials glide on two twin boundaries in mutually opposite directions resulting the twin boundaries move away from each other and growth of twin as shown in Figure 5.9e. Continuous propagation of twin boundaries along the pillar length gradually reorients the twinned region. However, not all of the nucleated twins in the crystal grow and slip is activated in many of them. The interaction of twins, disrupts the twin growth. Generally, the probability of twin-twin interaction increases when the slip is activated on more than one twin, which affects the twin growth and reorientation process (Figure 5.9f) [51]. The interaction of twins and slip planes will result to lock for twin growth and twin and fault slip and it will increase the stress required to continue the deformation (Figure 5.9g).
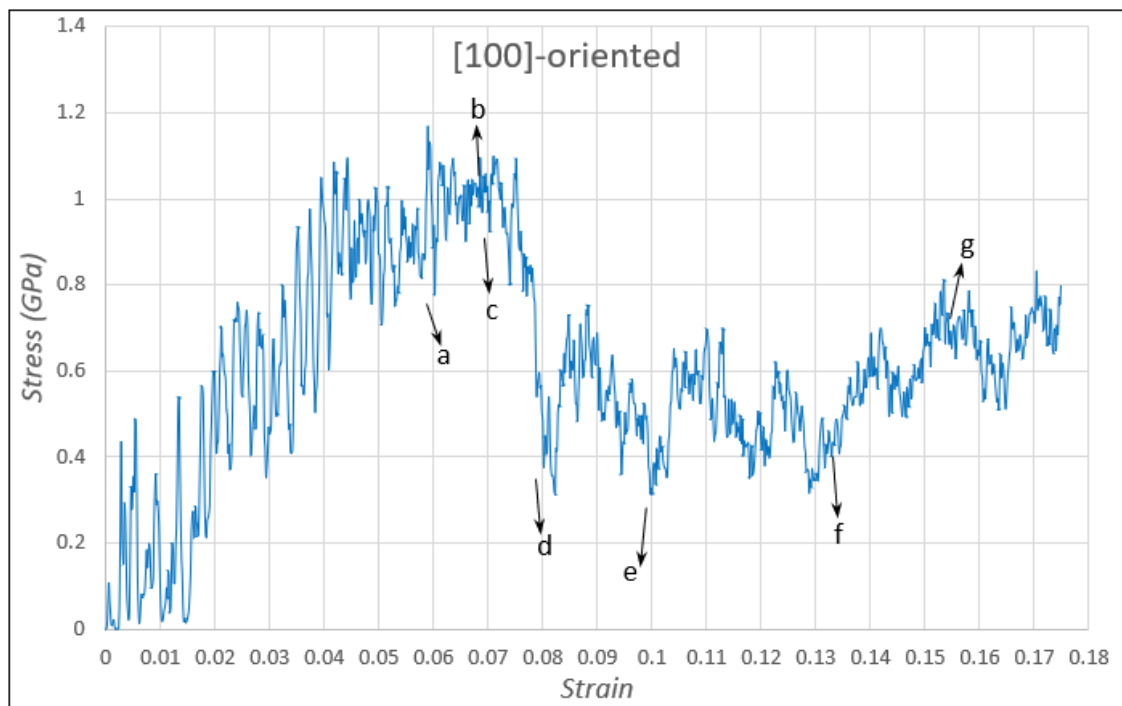
Figure 5.8: Flow behavior of the [100]-oriented 25nm Au pillar (T=300K).
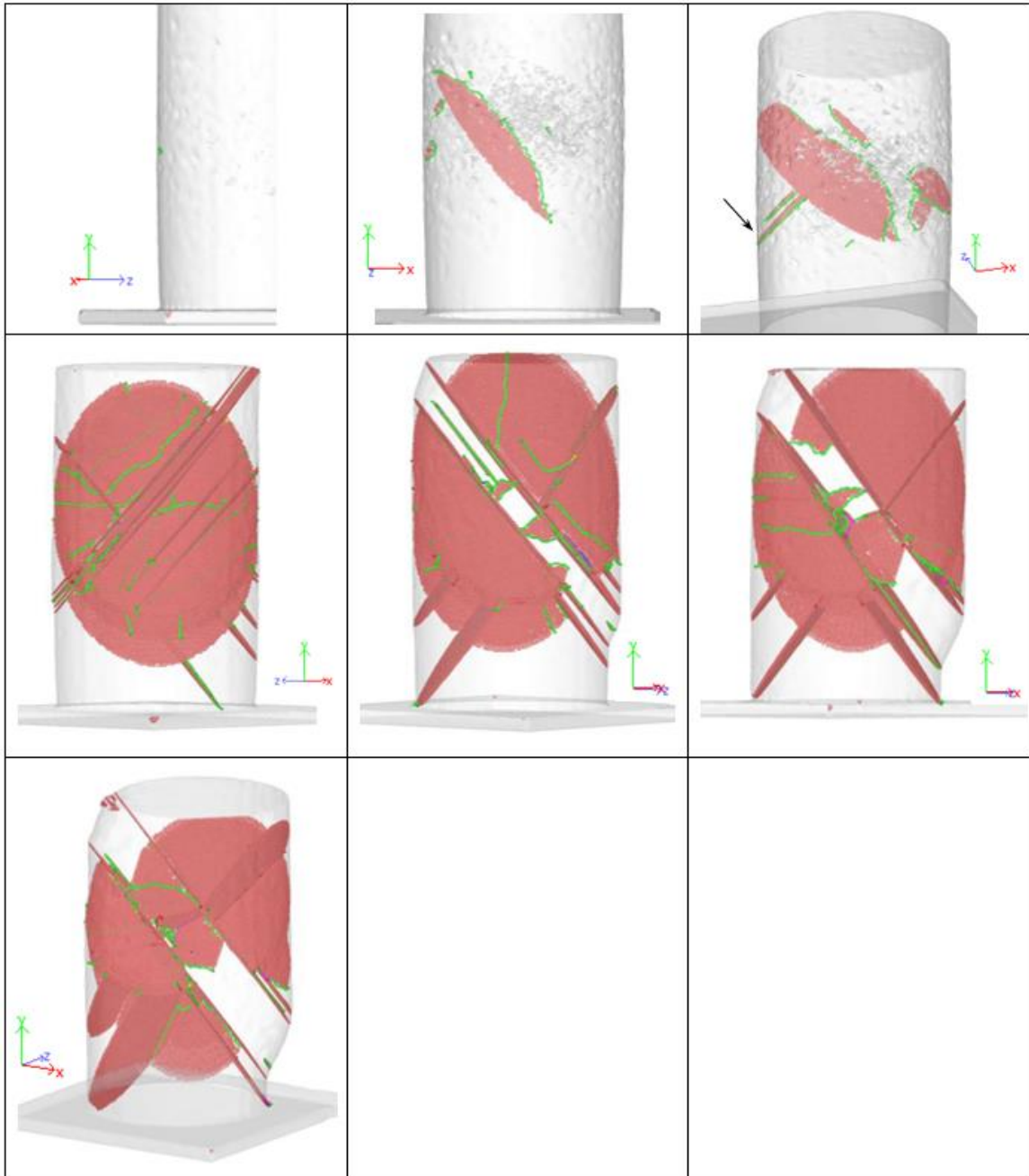
Figure 5.9: Snapshots of the microstructural evolution of [100]-oriented 25nm pillar, indicating the creation and growth of micro-twin (figures are corresponded to the points of fig. 8).

Almost the same mechanism is observed in compression of the smaller pillar (10nm) with same orientation. Figure 5.10a shows the growth of ($\bar{1}$11) twin interacting slipping (111) twin. However, unlike 25nm diameter pillar in which more than one slipping twin was

interaction with growing twin, here interaction of one slipping twin does not impede the boundary migration of growing twin (Figure 5.10b). The increasing strain will result in the annihilation of slip activated twin dislocations on the surface and twin boundary planes as is observed in Figure 5.10c. Looking at the snapshots of pillar deformation for 10 and 25nm pillars and comparing the trend of dislocation density changes for them (Figure 5.11), it is concluded that when the dislocation starvation mechanism is reached, the rate of nucleation is higher than the rate of dislocation annihilation for the smaller pillars and as the pillar size increases, the rate of nucleation and annihilation become closer, resulting fewer jumps in the dislocation density changes with strain.
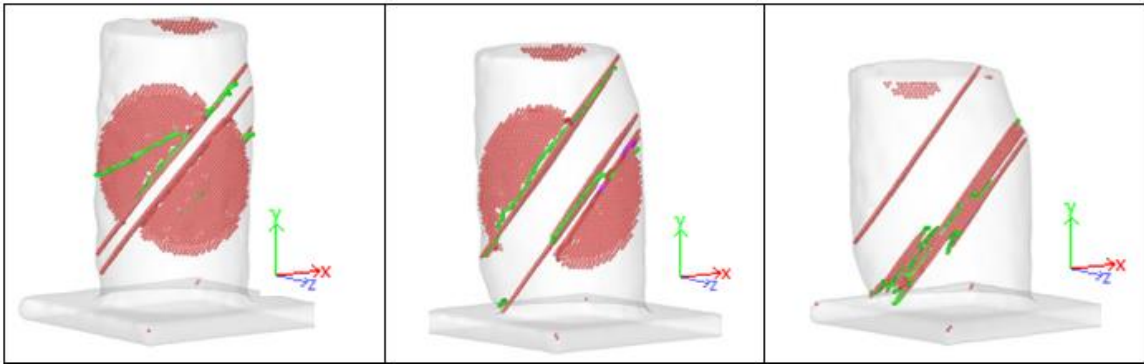
Figure 5.10: Snapshots of the microstructural evolution of [100]-oriented 10nm pillar, indicating the creation and growth of micro-twin and dislocation starvation state.
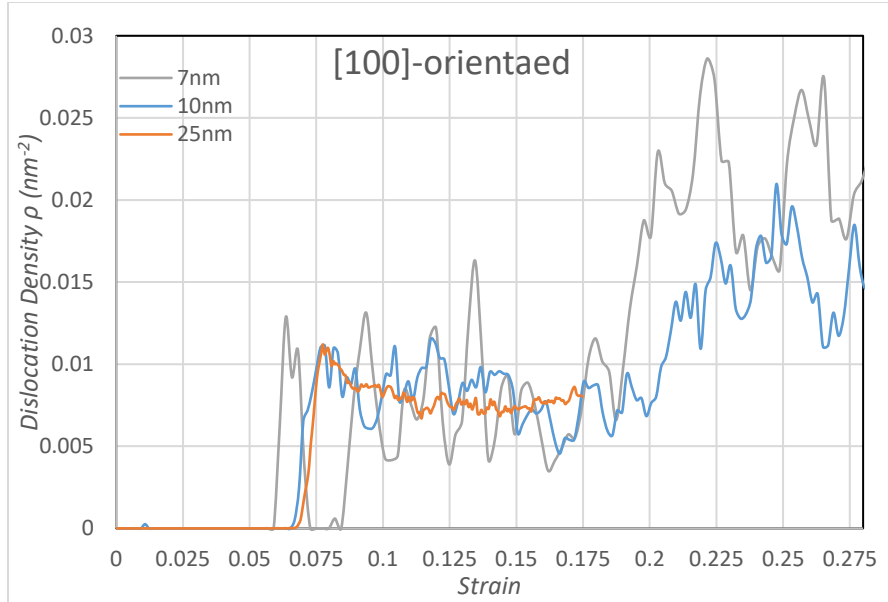
Figure 5.11: The effect of pillar size on the rate of dislocation nucleation and annihilation rates of [100]-oriented nanopillars.

For the [100] oriented 40nm pillar, two partial dislocations nucleate at the bottom of the pillar, activating (111) and (11$\bar{1}$) slip planes (Figure 5.12a). As they grow, they intersect each other at <1$\bar{1}$0> common vector (Figure 5.12b). This stops the growth of (111) slip plane, however, the (11$\bar{1}$) slip plane continues to grow and two other slip planes get activated (Figure 5.12c). Activation of a parallel adjacent plane to the (11$\bar{1}$) will result in the twin formation at the strain of 0.04381as shown in Figure 5.12d. The deformation mainly happens by the reorientation of crystal between twin boundaries and its interaction with slip planes as shown in fig. e. All of four intersecting slip planes can be clearly observed in Figure 5.12e. The increasing strain will result in the activation and growth of more twins as is observed in Figure 5.12f. Figure 5.13 shows the regions of the activity of dislocation exhaustion and starvation mechanisms for [100]-oriented 10nm and 25nm pillars. The lower probability of dislocation-defect interaction and higher image stress in smaller pillars results in the higher rate of the dislocation exhaustion ad lower resident time of dislocations in the pillars.
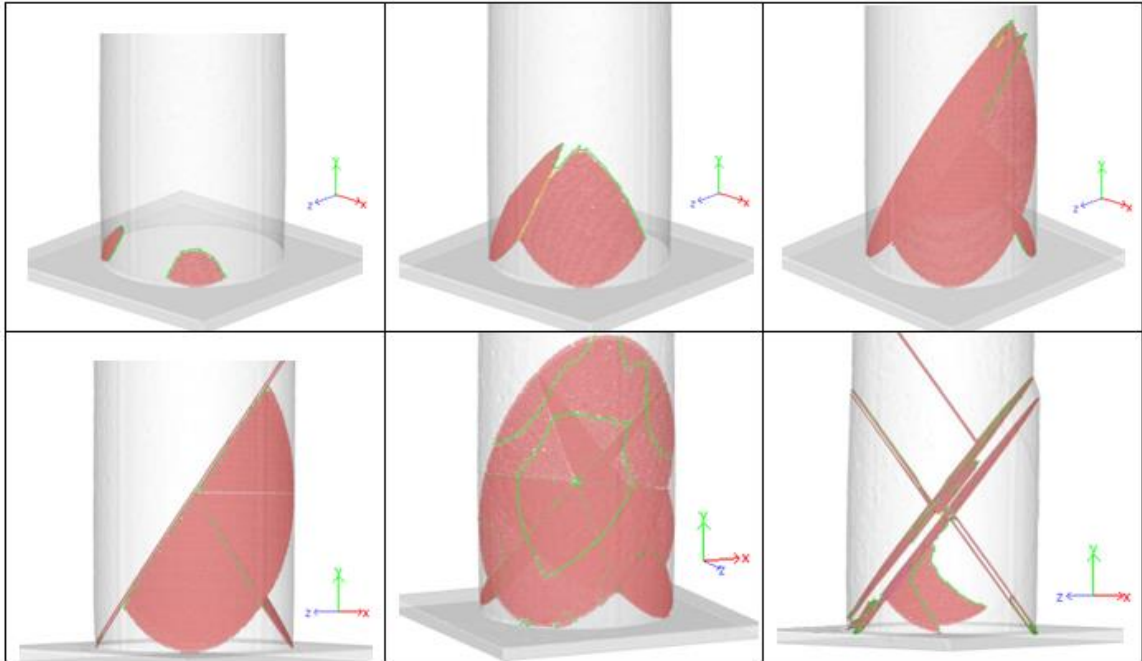
Figure 5.12: Snapshots of the microstructural evolution of [100]-oriented 40nm pillar, indicating the interaction of slip planes and the creation of locks and glide of micro twin boundary planes.
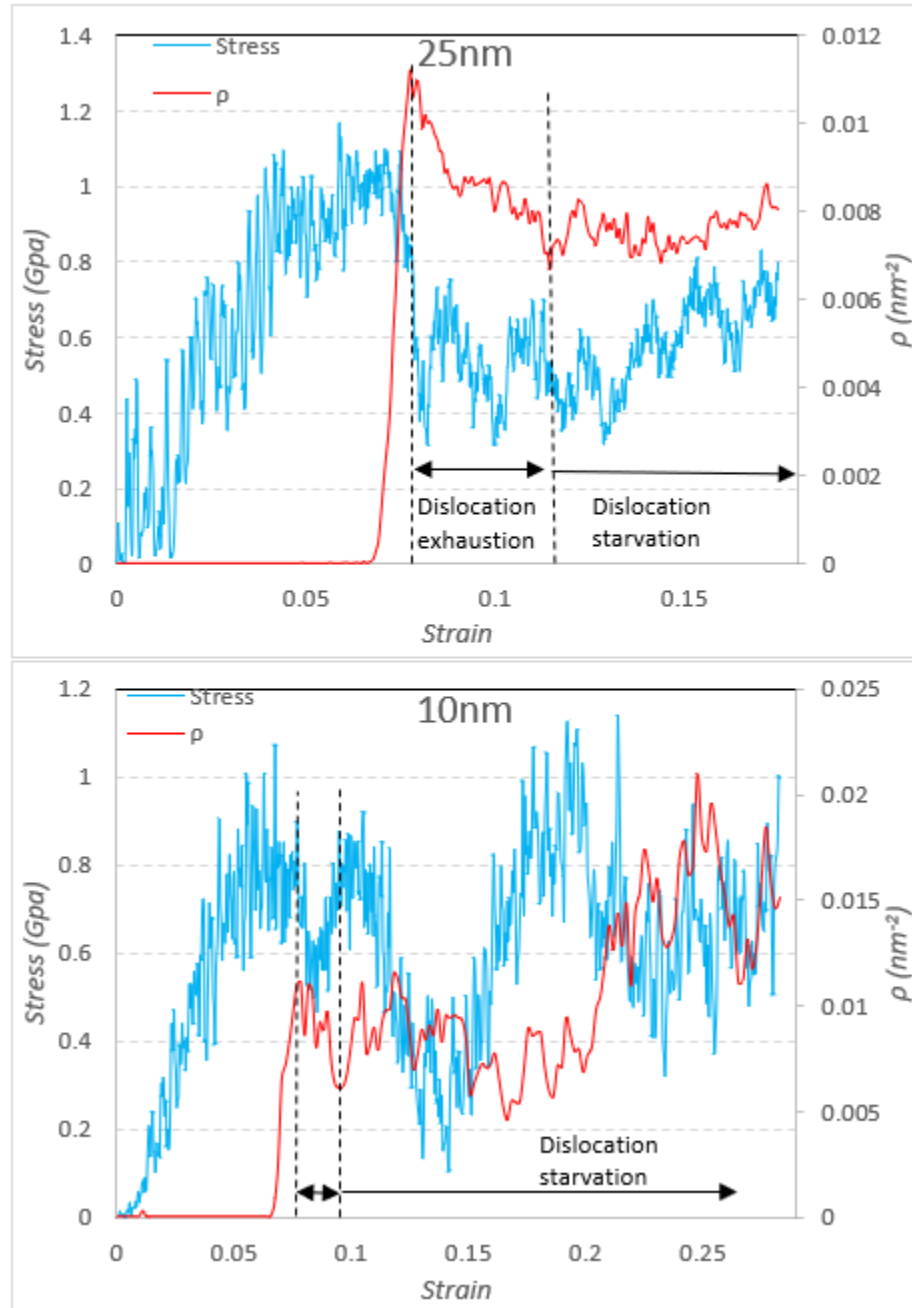
Figure 5.13: Regions of dislocation exhaustion and starvation mechanisms domination in the plasticity of [100]-oriented 25 and 10 nm pillars.

5.3.3.   [110]-oriented nanopillars

Figure 5.14 shows the stress-strain curve of the compression of the 25nm diameter pillar oriented along the <110> direction. The first Shockley partial dislocation nucleates at the strain of 0.0302 at the bottom corner of the pillar and develops on the $(11\bar{1})$ plane. Figure

5.15a shows the development of the resulted loop corresponding to the point an on the stress-strain curve. The second loop nucleates at the strain of 0.352 on the other side of the pillar bottom and moves on the (111) plane. Figure 5.15b represents the development of the second loop related to point b of the stress strain curve. The next dislocation nucleates at the strain of 0.03833 at the bottom corner of the pillar on the (11$\bar{1}$) plane. Figure 5.15c shows the dislocation structure of point c. Dislocation slip on the (11$\bar{1}$) and (111) planes continue until a step is created on the surface of the pillar at the intersection of slip planes and surface (Figure 5.15d). After major yield the stress drops to 0.99GPa at point e. Intersection of slip planes increased the stress as it shown in Figure 5.15f. However, as dislocations move to the surface and density of dislocations at the intersection point decreases, dislocations move easier on the slip planes and the stress drops (Figure 5.15g). Activation of parallel slip planes expands the plastic deformation and makes the surface step bigger (Figure 5.15h). Figure 5.15i shows the deformed pillar after 0.166 compression strain.
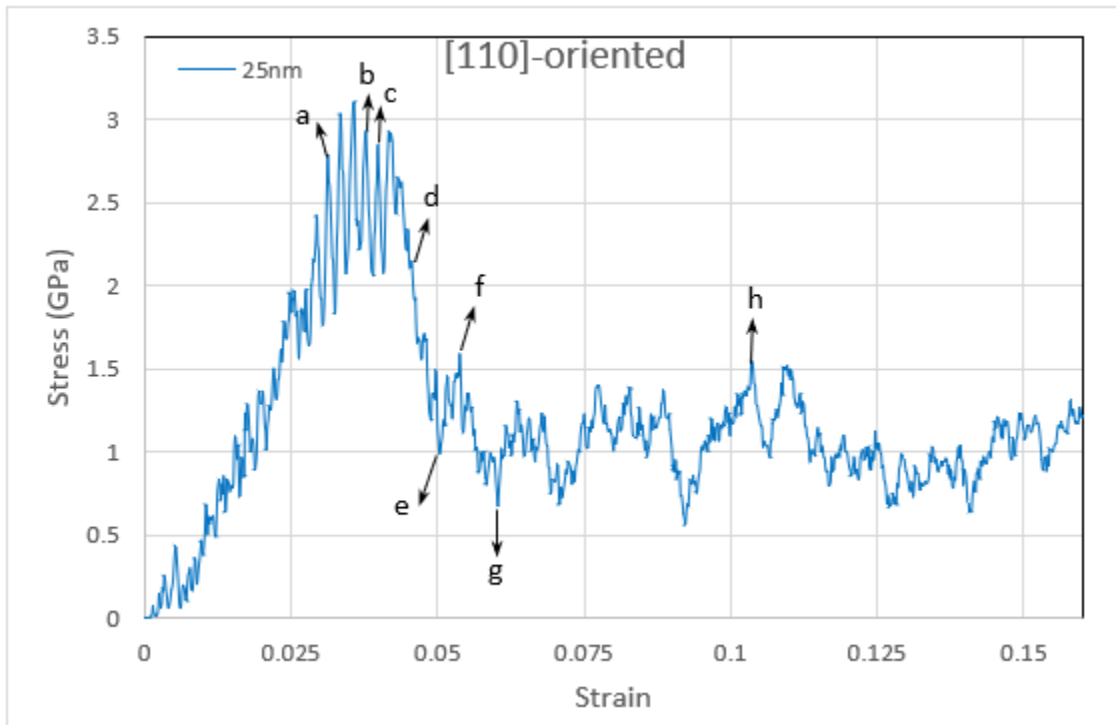

Figure 5.14: Flow behavior of the [110]-oriented 25nm Au pillar (T=300K).
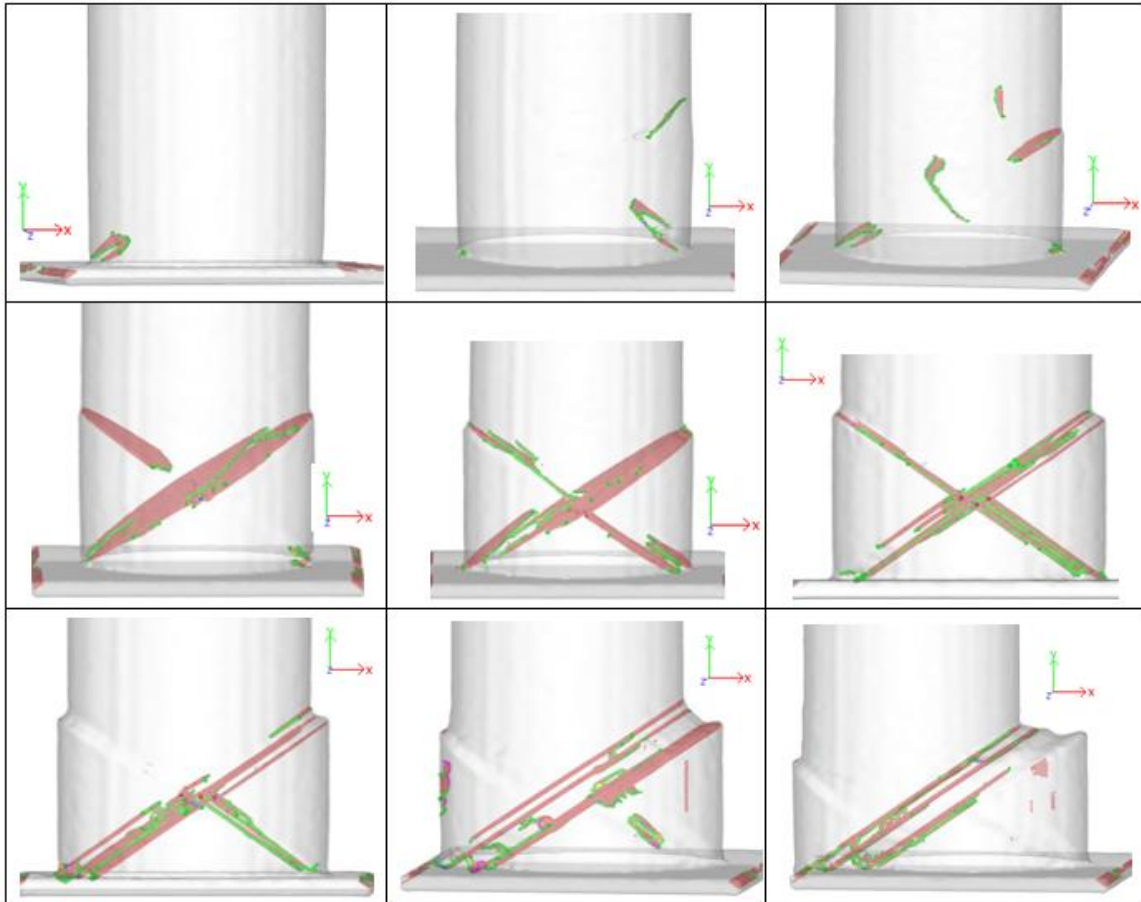
Figure 5.15: Snapshots of the microstructural evolution of [110]-oriented 25nm pillar, indicating the step creation on the pillar surface due to the slip of stacking fault loops, and reaching the dislocation starvation state (figures correspond to the points of 5.14).

For the smaller pillar (10nm diameter) the plasticity starts with nucleation of Shockley partials at the top and bottom of the pillar. Figure 5.16 shows the structure of dislocations and slip lanes at the strains of 0.067, 0.142 and 0.212. As it is observed the plastic deformation is mainly controlled by local slips due to the stacking fault planes. Considering dislocation density changes in Figure 5.17, it is observed that for the 10 nm [110] oriented pillar, after the initial yield and plasticity which happens by the dislocation nucleation at the surface, source exhaustion happens very fast and dislocation starvation becomes the dominant mechanism from low strains. For 25nm pillar, stress drops and raises with increases and decreases of dislocation density reveals that although plasticity

is mainly controlled by the slip loops, annihilation of dislocations at the surface and thus slip planes results to source limited or dislocation starvation mechanism domination.
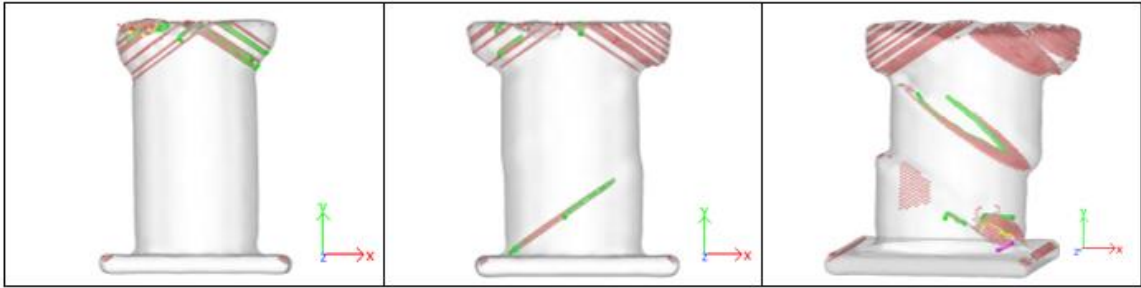
Figure 5.16: Snapshots of the microstructural evolution of [110]-oriented 10nm pillar, indicating the local deformation due to the local slips and the high rate of dislocation exhaustion.
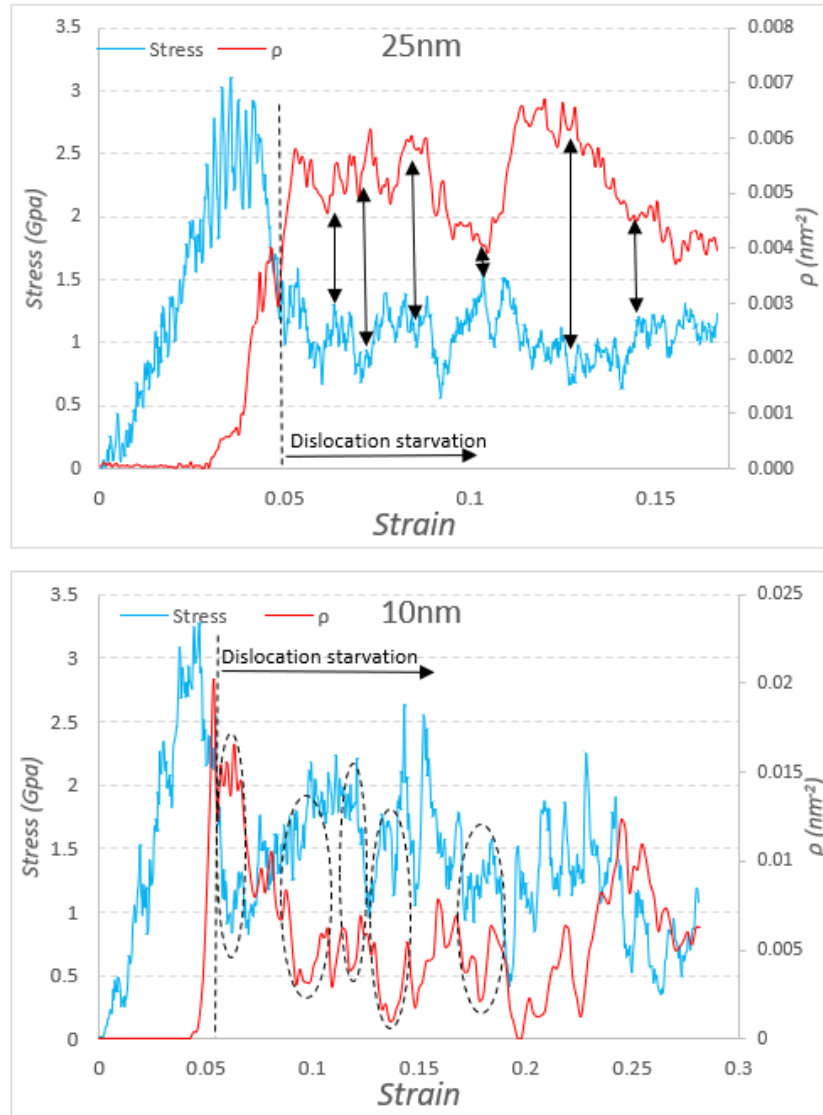
Figure 5.17: The effect of dislocation nucleation and exhaustion on the stress fluctuation of [110]-oriented 25 and 10nm pillars.

5.4. Orientation effect on deformation mechanism

As was observed in the last section, the 25nm diameter [100] oriented sample was deformed basically by formation of twins and glide of twin boundaries while [110] and [111] oriented samples with same diameter were mainly deformed by the slip mechanism. These three high symmetry orientations define corners of a standard stereographic triangle. The analyze of the formation of partial dislocations and stacking faults can illuminate the reason of the orientation based plasticity mechanism.

When applied stress to the crystal is higher than its yielding point, the first slip happens with the formation of an intrinsic stacking fault (ISF) and leading partial dislocation. To preserve the deformation, the second slip usually happens in one of the two following ways. In the first case, the leading partial is followed by the activation of a trailing partial on the same slip plane. This will result in the slip by perfect dislocation or slip mechanism. In the second case, the nucleated leading partial followed by the nucleation of additional leading partials on parallel slip planes. The nucleation of the next partial dislocation on a plane immediately above the first partial plane, will result in twinning. Otherwise, slip occurs by partial dislocations. Formation of leading partial and trailing partial on the same glide plane or leading partial and twinning on the successive plane will result in the dislocation slip (DS) or deformation twinning (DT) mechanisms activation, respectively. Typically for all metals, the energy barrier for the twinning partial formation ($\gamma_{utf} - \gamma_{sf}$) is higher than energy barrier for trailing partial ($\gamma_{usf} - \gamma_{sf}$) formation. Therefore, the activation of DT mechanism needs more energy than DS mechanism. However, the required stress for slip activation is dependent on many other parameters such as testing condition and sample properties and thus the higher energy barrier of DT activation does not necessarily imply that higher stress is needed to activate this mechanism. One of the most important parameters that can affect the activation of trailing partial or twinning partial is the Schmid factor (m). If the leading partial Schmid factor (m_L) is greater than that for the trailing partial (m_T), it will be difficult for the trailing partial to nucleate after the leading partial nucleation and deformation occur by the slip of the partial dislocations or twining depending to the second slip plane. If the m value of the trailing partial is greater than the leading partial, nucleation of trailing partial follows immediately and combines with the already nucleated leading partial, forming a full dislocation without extensive stacking fault generation and therefore the deformation happens by dislocations slip. The values of Schmid factor for leading (m_L) and trailing (m_T) partials are summarized in table 1 for three considered orientations of Au nanopillars. As it is observed $m_L > m_T$ for the [100]-oriented nanopillar and thus leading partials are nucleate and emitted from the surface on parallel slip planes, resulting in the formation of parallel stacking faults and micro-twins. For the other two orientations, nucleation of full dislocations from the surface will result in the slip deformation and

interaction of full dislocations. The same mechanism is observed in the deformation of Platinum samples with different orientations (Figure 5.18).

Table 5.1: Schmid factor analysis for different nanopillar orientations.

Loading axis	Number of slip systems	m_L	m_T	Predicted mechanism	Observed mechanism (10nm pillar)	Observed mechanism (25nm pillar)	Observed mechanism (40nm pillar)
[100]	8	0.471	0.236	Partial slip / twinning	twinning	twinning	twinning
[110]	4	0.236	0.471	Full slip	Full slip	Full slip	Full slip
[111]	6	0.157	0.314	Full slip	Full slip	Full slip	Full slip
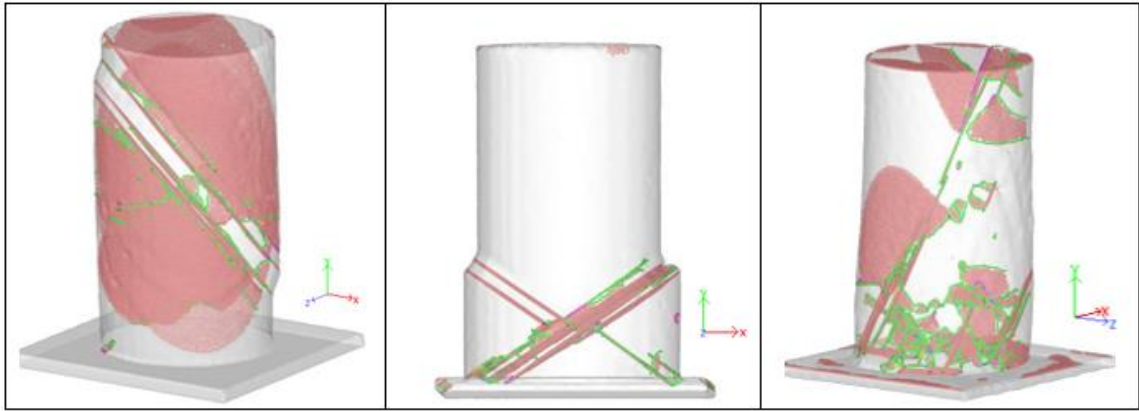
Figure 5.18: Microstructure of a) [100]-oriented, b) [110]-oriented, and c) [111]-oriented 25nm Pt nanopillars, indicating the micro-twin glide, stacking fault plane and loop slip, and slip and dislocation interaction activation respectively.

5.5. Effect of orientation on the size scale properties

Figure 5.19 compares the flow curves of pillars with different orientations for 3 diameters. As it is observed pillars with different orientations present completely deferent behavior specially at elastic region. The effect of orientation decreases as the pillar dimeter increases. [111]-oriented pillar shows the biggest pop-in event for all the considered dimeters. Less stress fluctuations in the [100] oriented pillars than the other two orientations could be related to their deformation mechanism in which stacking faults on four intersecting planes bounded by partial dislocations and micro-twins contribute to plasticity. High frequency of dislocation interactions in this case results to a more mean-

field flow environment and thus a less stress fluctuation. Moreover, activation of higher slip systems in the [100] orientation (8 slip systems) after initial yield will impede the mobile dislocations to escape before a complex interaction happens. For the [001] and [110]-oriented pillars, most of the defects are in the form of dislocation locks and they work as obstacles to further dislocation glides.

[111] oriented pillar shows the highest strength which is related to the lower Schmid factor for the dislocation nucleation and activation of slip planes on this orientation than the other two orientations.

Size dependent strengthening has been frequently reported in literature for submicron pillars. Based on this theory the flow stress increases as the pillar dimeter decreases with a power law equation; $\sigma \propto D^{-m}$, where D is the pillar diameter and m lies between 0.35 to 1 for fcc metals [52]. Double logarithmic plot of yield strength- pillar dimeter is shown in Figure 5.20 for Au and Pt nanopillars with different orientations. The value of exponent m is 0.246 and 0.109 for [111] and [110]-oriented Au nanopillars respectively. For the [001] oriented Au pillars however, the yield strength increases with increasing pillar diameter with the exponent of 0.058. Almost the same results are observed for the Pt nanopillars and the value of m exponent is 0.248, and 0.182 for the [111] and [110]-oriented Pt nanopillars respectively. The yield strength of [001]-oriented Pt nanopillars increases with increasing pillar diameter with the exponent of 0.047. As it is observed the exponent value here is much smaller than the submicron sized pillars [53], especially for the [110] and [100] orientations. One possible reason could be the size of the pillars, where the reported pillars in the experiments are usually larger than 200nm and the experimentally fabricated pillars in this range of size should have pre-existing dislocations. The Taylor interaction of the pre-existing dislocations can result to the increase of m exponent value, as it was observed for our [111] oriented pillar. According to the previous studies, the size dependence of the flow stress in single crystals of fcc micropillars is mainly related to the strain hardening effects after slip activation [54, 55]. However, since in the early stages of plasticity, the deformation is mainly governed by source exhaustion specially for the [110] and [100] pillars, not a strong size effect is

supposed to be observed. This confirms Sansoz [38] hypothesis that little to no size effect takes place during dislocation exhaustion regime.
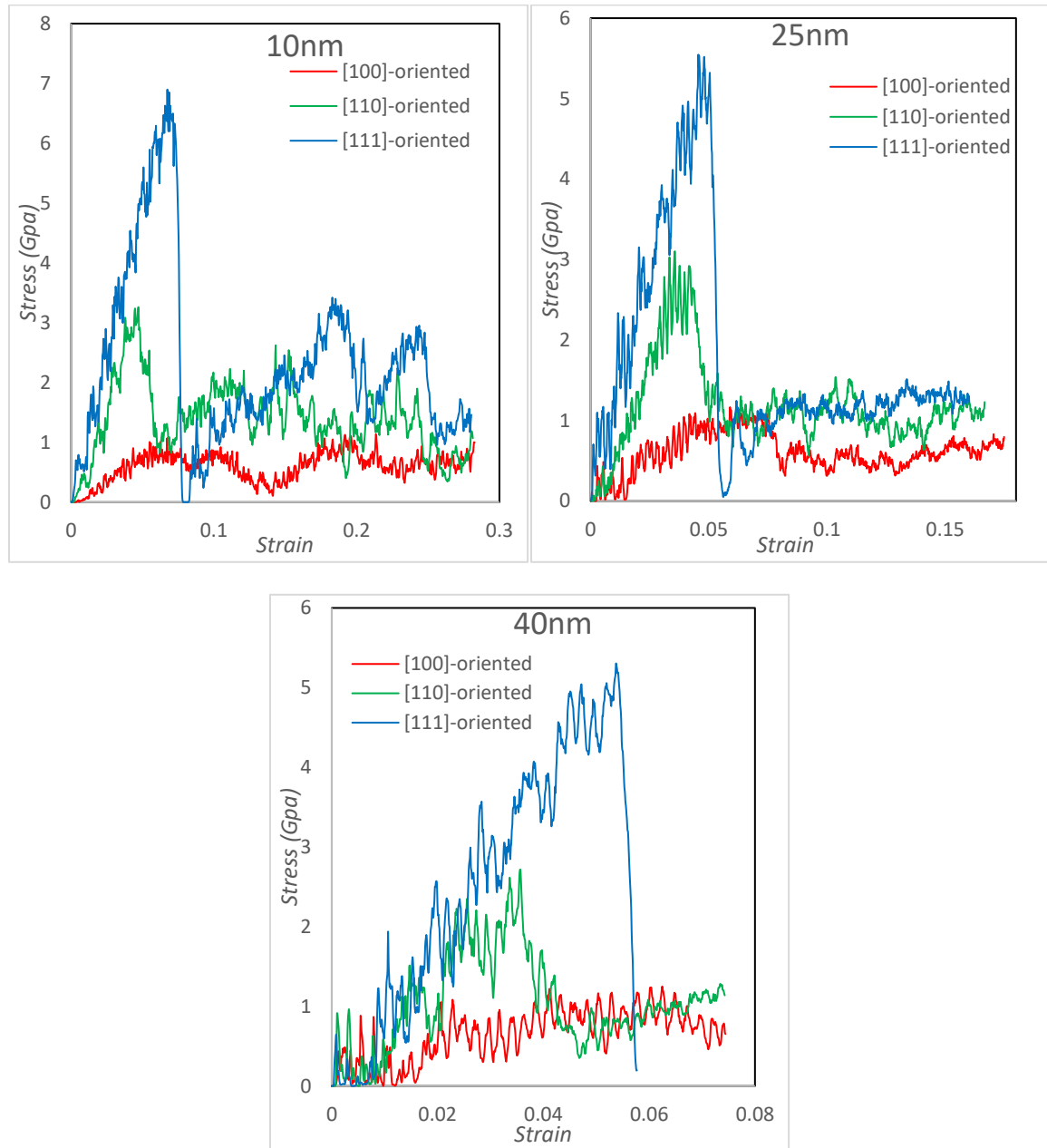
Figure 5.19: Effect of crystal orientation on the flow behavior of a) 10 nm, b) 25 nm, and c) 40 nm Au nanopillars.
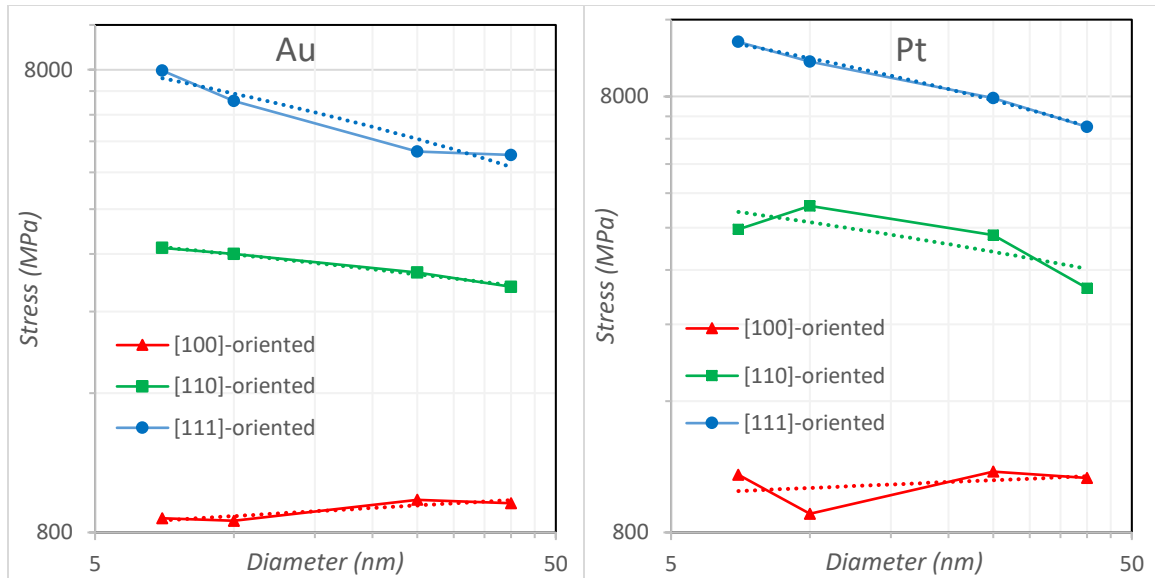
Figure 5.20: Log-Log plot of pillar yield strength vs its dimeter based on the crystal orientation for a) Au, and b) Pt nanopillars.

5.6. Effect of constraining layer

To have a better understanding of the effect of surface on the dislocation nucleation and starvation, the surface of the pillars was confined by applying a rigid layer on the surface. Therefore, dislocations can not annihilate at the surface and are trapped in the pillar. Figure 5.21 displays the stress-strain curves of the pillars with confined layers. As it is observed since the surface is confined in a rigid layer and there is no free surface, the first nucleation happens at higher stress than the sample with free surface and after nucleation dislocations are trapped in the pillar. Trapped dislocations in the pillar will prevent dislocation exhaustion mechanism to be activated and the interaction of dislocations will result in the increase of stress with strain without serrations. These results also indicate that serrated behavior in plasticity of nanopillars is in result of dislocation nucleation and annihilation. Figure 5.22 shows the microstructural evolution of 25nm diameter pillars with different orientations in the condition of having a rigid constraining layer. As it is observed after the dislocation nucleation the density of dislocation grows very fast as none of the dislocations can leave the sample. Figure 5.23 shows the effect of orientation on the 10nm pillars with constraining layer. It is observed that in the absence of free

surface the behavior of pillars with different orientations are close and it can be concluded that the significant orientation effect in Figure 5.19 is in result of the different rate of dislocation nucleation from free surface and annihilation at free surface.
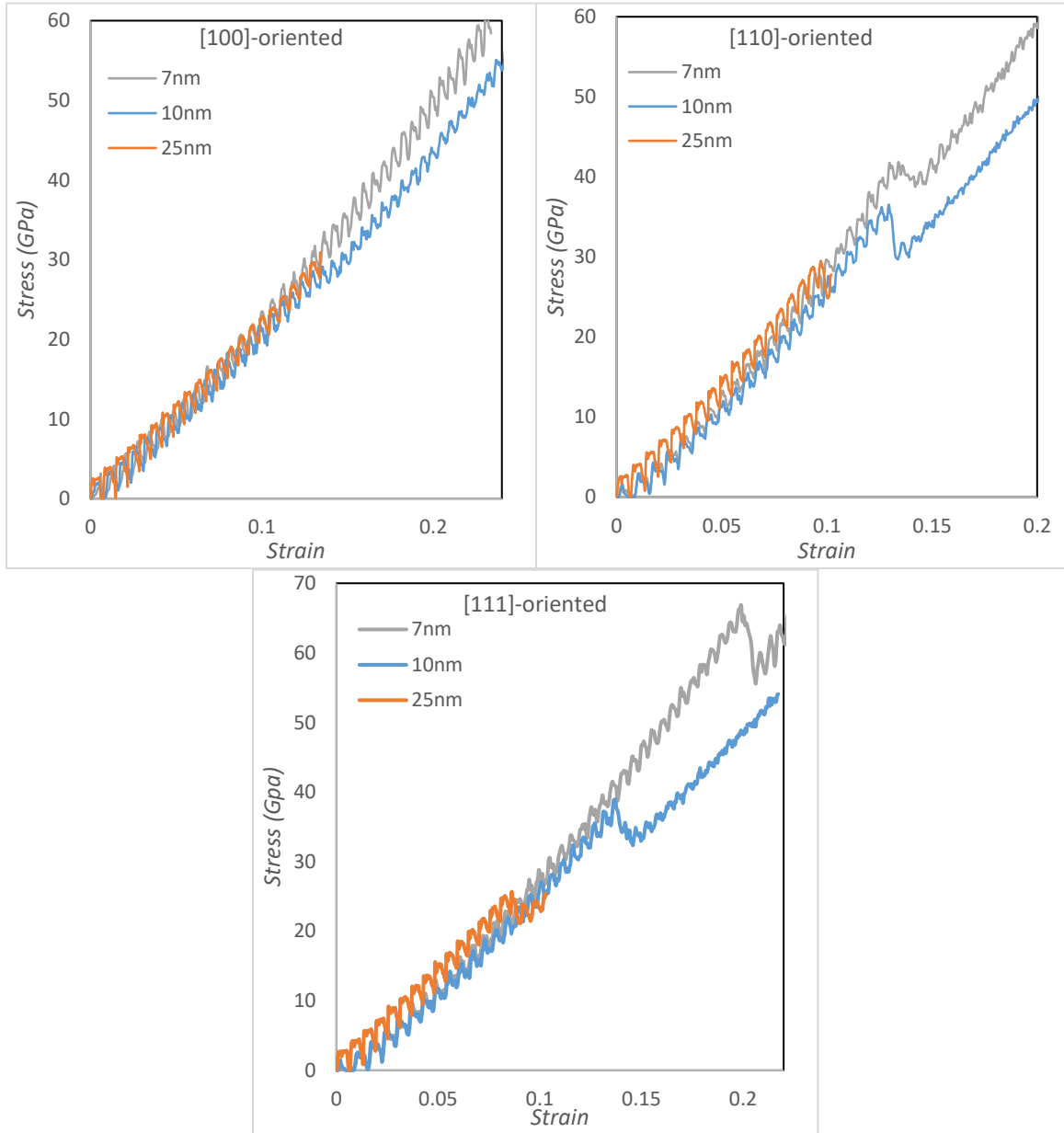
Figure 5.21: Flow behavior of rigid coated samples with different orientations.
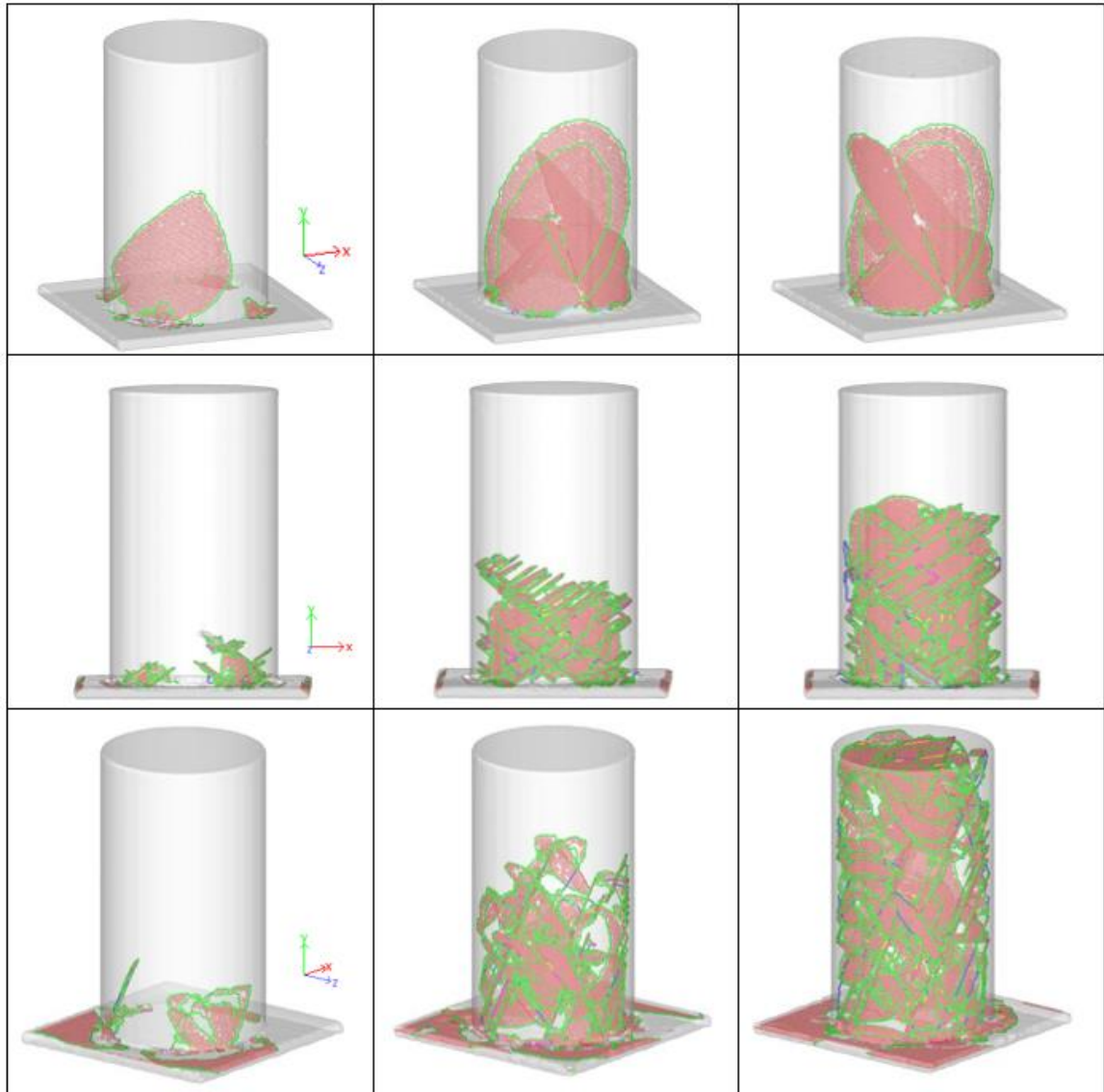
Figure 5.22: Microstructural evolution of rigid coated samples a) [100]-oriented at ε=0.097, b) [100]-oriented at ε=0.107, c) [100]-oriented at ε=0.134, d) [110]-oriented at ε=0.096, e) [110]-oriented at ε=0.098, f) [110]-oriented at ε=0.102, g) [111]-oriented at ε=0.084, h) [111]-oriented at ε=0.087, i) [111]-oriented at ε=0.096.
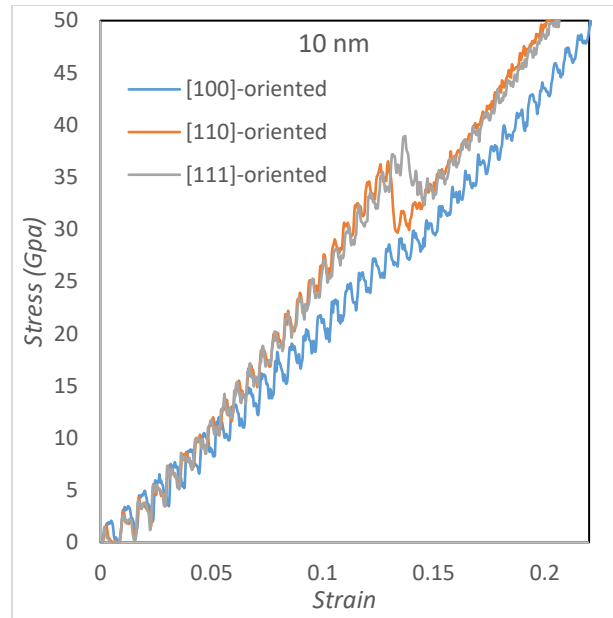
Figure 5.23: Effect of orientation on the behavior of the 10nm rigid coated samples.

To have a closer estimation of the effect of the constraining layer, we have coated samples with a layer of platinum. The thickness of coating layer is about 5% of the pillar diameter. In this case the surface of the pillar is confined with a layer that can deform and act as free surface. However, since the main deformation happens by the Au atoms and volume, the exhaustion of the slipped faults will be stopped by the Pt layer. Figure 5.24 compares the stress-strain curves of the Pt coated with non-coated 10nm Au pillars. The coated samples show higher strength than the non-coated samples with [001] and [110] orientations. However, the coated [111]-oriented sample yields at a lower strength than the non-coated sample. As it is shown in Figure 5.25, the boundary of Au and Pt is covered with sessile dislocations due to the crystal misfit. This initial structure can lead to lower yield strength depending on the orientation of slip systems with the boundary layer. That could be a reason why we are observing lower strength in the coated [111]-oriented nanopillar. As it is observed the slip planes are developed on the same slip planes as the non-coated samples. However, as the glide happens many of the dislocations interact with the dislocation network on the boundary layer and that leads to the lower rate of dislocation exhaustion at the surface.
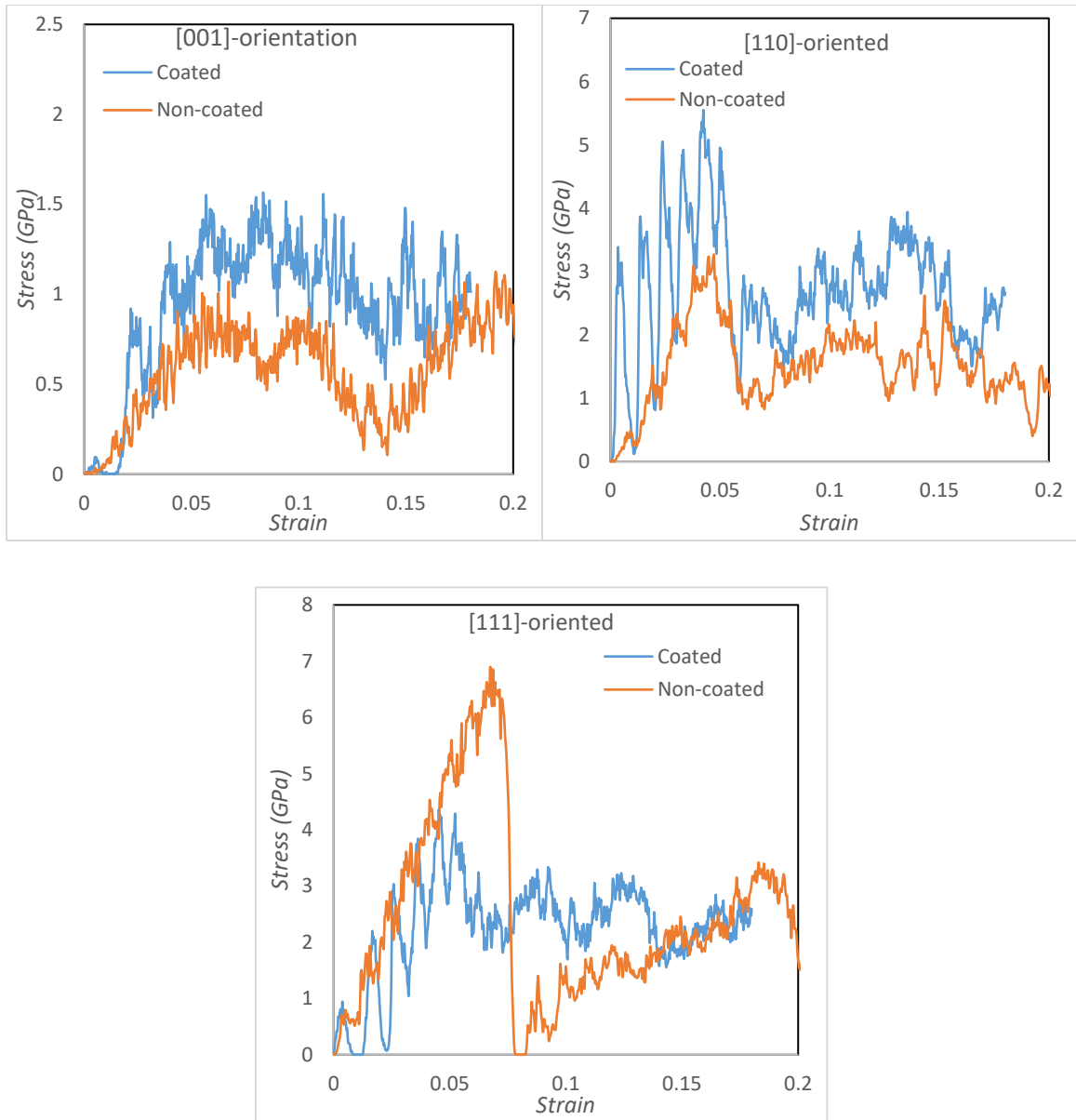
Figure 5.24: Effect of Pt coating layer on the flow behavior of the 10nm Au pillars in different orientations.
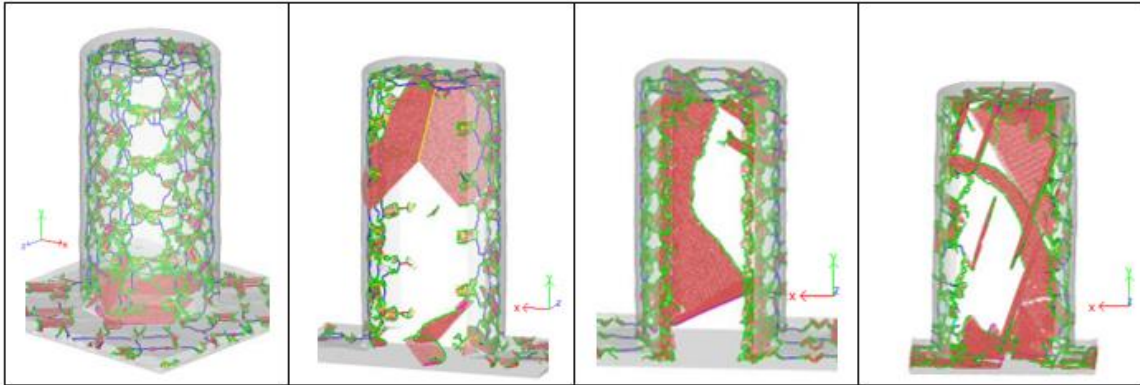
Figure 5.25: Microstructural evolution of 25nm Pt coated samples a)initial structure of [001]-oriented sample, b) [001]-oriented at ε=0.031, c) [110]-oriented at ε=0.027 , d) [111]-oriented at ε=0.055. (the cross section of the sample is shown for a more clear image)

Conclusions

Molecular dynamics is used to provide atomic-scale insights into the size and crystallographic orientation effects on the deformation behavior and microstructural evolution of fcc single-crystal nanopillars. The following conclusions can be drawn;

- The yielding of defect-free nanopillars started with the nucleation and propagation of partial dislocations from the free surface and the crystal orientation affects the subsequent microstructural evolution and flow behavior.

- [111]-oriented nanopillars displayed the highest yield strength between the considered orientations. A significant difference is observed in the strength of pillars of the same size with different orientations.

- The deformation mechanism of defect-free nanopillars is strongly orientation dependent. For the [100]-oriented samples stacking faults bounded by partial dislocations and glide of micro-twins boundaries is the dominant deformation mechanism, whereas [110] and [111]-oriented nanopillars deformed by dislocation slip mechanism. Based on the results the Schmid factor of leading and

trailing partials plays a decisive role in leading to the twinning deformation or slip deformation.

- Annihilation of dislocations at the surface of nanopillars after deformation leads to the dislocation starvation mechanism activation in all the three considered orientations. Nucleation of new dislocations from the surface is required to activate new micro-twins or slip systems to sustain the deformation in the dislocation starved situation.

- Dislocation exhaustion rate depends on the nanopillar size and larger nanopillars showed lower exhaustion rate regardless of orientation.

- Frequent dislocation interactions in orientations with more primary slip systems ([100] and [111]) resulted in the later activation of dislocation starvation mechanism while the less chance of dislocation interaction in orientations with fewer slip systems ([110] orientation in our study) resulted to the higher exhaustion rate and sooner domination of dislocation starvation mechanism. The more serrated and fluctuating post-yield flow response of the [110] nanopillars is also in result of the less resident time of dislocations due to the fewer dislocation interactions.

- The high symmetry of [111] orientation resulted in the activation of a high density of dislocation loops which their interaction lead to the less serrated stress-strain response than the other two orientations.

- The effect of orientation on strength decreases as the pillar diameter increases.

- The power-law equation exponent is completely dependent on the crystal orientations and a week or no size effect was observed in the compression of [100] and [110] oriented Au and Pt pillars with sizes less than 40 nm.

- The results of the compression of pillars with rigid constraining layers showed that in the absence of free surface the nucleation of initial dislocations happens in much higher stress and trapping of dislocations in the pillar results in a smooth increase of stress with strain.

- The compression of rigid coated and Pt coated nanopillars show that the observed orientation based behaviour and size scale effects decrease by confining the free surface.

References

[1] V.A. Lubarda, On the analysis of pure bending of rigid-plastic beams in strain-gradient plasticity, European Journal of Mechanics - A/Solids 63 (2017) 43-52.

[2] M. Hashemian, S. Foroutan, D. Toghraie, Comprehensive beam models for buckling and bending behavior of simple nanobeam based on nonlocal strain gradient theory and surface effects, Mech Mater 139 (2019) 103209.

[3] W. Chen, T. Kitamura, X. Wang, M. Feng, Size effect on cyclic torsion of micro-polycrystalline copper considering geometrically necessary dislocation and strain gradient, International Journal of Fatigue 117 (2018) 292-298.

[4] C.J. Campbell, S.P.A. Gill, An analytical model for the flat punch indentation size effect, Int J Solids Struct 171 (2019) 81-91.

[5] G.Z. Voyiadjis, Y. Song, Strain gradient continuum plasticity theories: Theoretical, numerical and experimental investigations, Int J Plasticity 121 (2019) 21-75.

[6] C. Wang, Q.P. Cao, T. Feng, X.D. Wang, D.X. Zhang, S.X. Qu, J.Z. Jiang, Indentation size effects of mechanical behavior and shear transformation zone in thin film metallic glasses, Thin Solid Films 646 (2018) 36-43.

[7] E. Martínez-Pañeda, C.F. Niordson, On fracture in finite strain gradient plasticity, Int J Plasticity 80 (2016) 154-167.

[8] D. Liu, D.J. Dunstan, Material length scale of strain gradient plasticity: A physical interpretation, Int J Plasticity 98 (2017) 156-174.

[9] S. Das, F. Hofmann, E. Tarleton, Consistent determination of geometrically necessary dislocation density from simulations and experiments, Int J Plasticity 109 (2018) 18-42.

[10] P. Lin, J. Nie, Z. Liu, Z. Zhuang, Study of two hardening mechanism caused by geometrically necessary dislocations in thin films with passivation layer, Int J Solids Struct 160 (2019) 59-67.

[11] S. Yuan, Y. Zhu, S. Liang, M. Huang, Z. Li, Dislocation-density based size-dependent crystal plasticity framework accounting for climb of piled up dislocations at elevated temperature, Mech Mater 134 (2019) 85-97.

[12] S. Kalácska, Z. Dankházi, G. Zilahi, X. Maeder, J. Michler, P.D. Ispánovity, I. Groma, Investigation of geometrically necessary dislocation structures in compressed Cu micropillars by 3-dimensional HR-EBSD, Materials Science and Engineering: A 770 (2020) 138499.

[13] M.D. Uchic, D.M. Dimiduk, J.N. Florando, W.D. Nix, Exploring specimen size effects in plastic deformation of Ni3(Al, Ta), MRS Proceedings 753 (2002) BB1.4.

[14] M.D. Uchic, D.M. Dimiduk, J.N. Florando, W.D. Nix, Sample dimensions influence strength and crystal plasticity, Science 305(5686) (2004) 986-989.

[15] D.M. Dimiduk, M.D. Uchic, S.I. Rao, C. Woodward, T.A. Parthasarathy, Overview of experiments on microcrystal plasticity in FCC-derivative materials: selected challenges for modelling and simulation of plasticity, Model Simul Mater Sc 15(2) (2007) 135-146.

[16] J.R. Greer, W.C. Oliver, W.D. Nix, Size dependence of mechanical properties of gold at the micron scale in the absence of strain gradients, Acta Mater 53(6) (2005) 1821-1830.

[17] J.R. Greer, W.D. Nix, Nanoscale gold pillars strengthened through dislocation starvation, Phys Rev B 73(24) (2006).

[18] J.A. El-Awady, Unravelling the physics of size-dependent dislocation-mediated plasticity, Nature Communications 6(1) (2015) 5926.

[19] I. Issa, J. Amodeo, J. Réthoré, L. Joly-Pottuz, C. Esnouf, J. Morthomas, M. Perez, J. Chevalier, K. Masenelli-Varlot, In situ investigation of MgO nanocube deformation at room temperature, Acta Mater 86 (2015) 295-304.

[20] C. Chisholm, H. Bei, M.B. Lowry, J. Oh, S.A. Syed Asif, O.L. Warren, Z.W. Shan, E.P. George, A.M. Minor, Dislocation starvation and exhaustion hardening in Mo alloy nanofibers, Acta Mater 60(5) (2012) 2258-2264.

[21] T.J. Flanagan, O. Kovalenko, E. Rabkin, S.-W. Lee, The effect of defects on strength of gold microparticles, Scripta Mater 171 (2019) 83-86.

[22] P. Zhang, O.U. Salman, J.-Y. Zhang, G. Liu, J. Weiss, L. Truskinovsky, J. Sun, Taming intermittent plasticity at small scales, Acta Mater 128 (2017) 351-364.

[23] D. Kiener, A.M. Minor, Source Truncation and Exhaustion: Insights from Quantitative in situ TEM Tensile Testing, Nano Lett 11(9) (2011) 3816-3820.

[24] A. Rinaldi, P. Peralta, C. Friesen, K. Sieradzki, Sample-size effects in the yield behavior of nanocrystalline nickel, Acta Mater 56(3) (2008) 511-517.

[25] T.A. Parthasarathy, S.I. Rao, D.M. Dimiduk, M.D. Uchic, D.R. Trinkle, Contribution to size effect of yield strength from the stochastics of dislocation source lengths in finite samples, Scripta Mater 56(4) (2007) 313-316.

[26] S.I. Rao, D.M. Dimiduk, M. Tang, T.A. Parthasarathy, M.D. Uchic, C. Woodward, Estimating the strength of single-ended dislocation sources in micron-sized single crystals, Philos Mag 87(30) (2007) 4777-4794.

[27] J.A. El-Awady, M. Wen, N.M. Ghoniem, The role of the weakest-link mechanism in controlling the plasticity of micropillars, J Mech Phys Solids 57(1) (2009) 32-50.

[28] Z.J. Wang, Q.J. Li, Z.W. Shan, J. Li, J. Sun, E. Ma, Sample size effects on the large strain bursts in submicron aluminum pillars, Appl Phys Lett 100(7) (2012).

[29] Z.Y. Liang, J.T.M. De Hosson, M.X. Huang, Size effect on deformation twinning in face-centred cubic single crystals: Experiments and modelling, Acta Mater 129 (2017) 1-10.

[30] V. Samaee, R. Gatti, B. Devincre, T. Pardoen, D. Schryvers, H. Idrissi, Dislocation driven nanosample plasticity: new insights from quantitative in-situ TEM tensile testing, Sci Rep-Uk 8 (2018).

[31] L. Wang, J. Teng, Y. Wu, J. Zou, G. Yu, Z. Zhang, X. Han, Size dependence of dislocation activities and independence on theoretical elastic strain limit in Pt nanocrystals revealed by atomic-resolution in situ investigation, Materials Today Nano 2 (2018) 1-6.

[32] X.X. Zhao, J. Wu, Y.L. Chiu, I.P. Jones, R. Gu, A.H.W. Ngan, Critical dimension for the dislocation structure in deformed copper micropillars, Scripta Mater 163 (2019) 137-141.

[33] C.Z. Zhou, I.J. Beyerlein, R. LeSar, Plastic deformation mechanisms of fcc single crystals at small scales, Acta Mater 59(20) (2011) 7673-7682.

[34] Y.N. Cui, P. Lin, Z.L. Liu, Z. Zhuang, Theoretical and numerical investigations of single arm dislocation source controlled plastic flow in FCC micropillars, Int J Plasticity 55 (2014) 279-292.

[35] I. Ryu, W. Cai, W.D. Nix, H.J. Gao, Stochastic behaviors in plastic deformation of face-centered cubic micropillars governed by surface nucleation and truncated source operation, Acta Mater 95 (2015) 176-183.

[36] P.S.S. Leung, H.S. Leung, B. Cheng, A.H.W. Ngan, Size dependence of yield strength simulated by a dislocation-density function dynamics approach, Model Simul Mater Sc 23(3) (2015).

[37] J. Hu, Z. Liu, E. Van der Giessen, Z. Zhuang, Strain rate effects on the plastic flow in submicron copper pillars: Considering the influence of sample size and dislocation nucleation, Extreme Mech Lett 17 (2017) 33-37.

[38] F. Sansoz, Atomistic processes controlling flow stress scaling during compression of nanoscale face-centered-cubic crystals, Acta Mater 59(9) (2011) 3364-3372.

[39] M. Yaghoobi, G.Z. Voyiadjis, Size effects in fcc crystals during the high rate compression test, Acta Mater 121 (2016) 190-201.

[40] C.R. Weinberger, G.J. Tucker, Atomistic simulations of dislocation pinning points in pure face-centered-cubic nanopillars, Model Simul Mater Sc 20(7) (2012).

[41] G.J. Tucker, Z.H. Aitken, J.R. Greer, C.R. Weinberger, The mechanical behavior and deformation of bicrystalline nanowires, Model Simul Mater Sc 21(1) (2013).

[42] S. Xu, Y.F. Guo, A.H.W. Ngan, A molecular dynamics study on the orientation, size, and dislocation confinement effects on the plastic deformation of Al nanopillars, Int J Plasticity 43 (2013) 116-127.

[43] P. Rohith, G. Sainath, V.S. Srinivasan, Effect of size, temperature and strain rate on dislocation density and deformation mechanisms in Cu nanowires, Physica B: Condensed Matter 561 (2019) 136-140.

[44] A.V. Korchuganov, A.N. Tyumentsev, K.P. Zolnikov, I.Y. Litovchenko, D.S. Kryzhevich, E. Gutmanas, S. Li, Z. Wang, S.G. Psakhie, Nucleation of dislocations and twins in fcc nanocrystals: Dynamics of structural transformations, J Mater Sci Technol 35(1) (2019) 201-206.

[45] S. Plimpton, Fast Parallel Algorithms for Short-Range Molecular-Dynamics, J Comput Phys 117(1) (1995) 1-19.

[46] S.M. Foiles, M.I. Baskes, M.S. Daw, Embedded-atom-method functions for the fcc metals Cu, Ag, Au, Ni, Pd, Pt, and their alloys, Phys Rev B 33(12) (1986) 7983-7991.

[47] C.J. O'Brien, C.M. Barr, P.M. Price, K. Hattar, S.M. Foiles, Grain boundary phase transformations in PtAu and relevance to thermal stabilization of bulk nanocrystalline metals, J Mater Sci 53(4) (2018) 2911-2927.

[48] H. Tsuzuki, P.S. Branicio, J.P. Rino, Structural characterization of deformed crystals by analysis of common atomic neighborhood, Comput Phys Commun 177(6) (2007) 518-523.

[49] A. Stukowski, K. Albe, Extracting dislocations and non-dislocation crystal defects from atomistic simulation data, Model Simul Mater Sc 18(8) (2010).

[50] A. Stukowski, Visualization and analysis of atomistic simulation data with OVITO-the Open Visualization Tool, Model Simul Mater Sc 18(1) (2010).

[51] P. Rohith, G. Sainath, B.K. Choudhary, Effect of orientation and mode of loading on deformation behaviour of Cu nanowires, Comput Condens Matte 17 (2018).

[52] S.W. Lee, S.M. Han, W.D. Nix, Uniaxial compression of fcc Au nanopillars on an MgO substrate: The effects of prestraining and annealing, Acta Mater 57(15) (2009) 4404-4415.

[53] J.Y. Kim, J.R. Greer, Tensile and compressive behavior of gold and molybdenum single crystals at the nano-scale, Acta Mater 57(17) (2009) 5245-5253.

[54] R. Maass, S. Van Petegem, D.C. Ma, J. Zimmermann, D. Grolimund, F. Roters, H. Van Swygenhoven, D. Raabe, Smaller is stronger: The effect of strain hardening, Acta Mater 57(20) (2009) 5996-6005.

[55] D. Kiener, A.M. Minor, Source-controlled yield and hardening of Cu(100) studied by in situ transmission electron microscopy, Acta Mater 59(4) (2011) 1328-1337.

Chapter 6

6.   Deformation mechanism of micron scale spheres

The size and strain rate dependence of the plastic behavior of micron-scale samples is investigated using the micro-compression of Au microspheres. Four different diameters of Au spheres (750 nm, 1.5 µm, 2.2 µm, 3 µm) have been tested at room temperature. The amount of yield stress was observed to increase with decreasing the sphere diameter (the yield point increases from 24MPa to 407MPa for 3 µm and 0.7 µm spheres, respectively with a loading rate of 0.05mN/s). The apparent activation volume remains almost constant, ranging $1.6\text{-}2.4b^3$ with changes of strain up to 20% for the smallest sphere while it ranges 8.6-10.6 b^3, 9.4-10.2 b^3, and 8.9-10.5 b^3 for the 1.5µm, 2.2µm, and 3µm diameter spheres respectively. These results indicate that the operative mechanism in the deformation of considered spheres is dependent on their size. Our obtained data for apparent activation volume and activation energy suggest that the dislocation-obstacle limited glide mechanism is dominant or the main role of the deformation of larger spheres while the smallest sphere deformed by dislocation nucleation and starvation mechanism.

6.1. Introduction

Metallic micropillar samples fabricated by focused ion beam (FIB) have been used extensively to study the mechanical behavior of micron-scale samples [1-3]. These experiments approved the "smaller stronger" theory in the micron-scale sample, indicating that the strength of the sample increases as the sample size gets smaller. However, some microstructural defects such as dislocation loops, Ga atoms and inions, and precipitates are introduced to the sample through the FIB machining [4]. Several new techniques have been proposed to fabricate micro-scale samples without implementing microstructural defects into the sample. Some of these techniques include molecular beam epitaxy, solid-state dewetting and electroplating, which are able to fabricate samples without introducing defects [5-8].

Experimental and numerical studies of deformation of nearly perfect micro-scale samples show a generally stochastic yielding accompanied by displacement bursts when the applied stress is load-controlled. These bursts are mainly due to the cooperative dislocation processes involving large number of dislocations. Operation of these mechanisms results to the strain energy release which is mainly balanced by the energy created from dislocation processes, and thermal dissipations.

The size and strain rate dependence mechanical behavior of Au microspheres fabricated by electroplating and dewetting technique is studied in this chapter. Au microspheres with size different diameters (750 nm, 1.5 µm, 2.2 µm, 3 µm) were fabricated ebeam lithography and dewetting technique. Uniaxial micro compression tests were performed on the microspheres at room temperature in different loading rates using nano-indentation testing machine equipped with a flat-punch indenter.

The details of the experimental procedure and the results are discussed in the subsequent sections.

6.2. Sample Preparation

Gold microspheres with different diameters were fabricated on a (0001)-oriented sapphire (α-Al_2O_3) surface. A positive photoresist layer (A8 PMMA) was spin-coated on the O_2 plasma cleaned sapphire surface and E-beam lithography was used to project a grid of 1 to 10.0 µm diameter circles upon the photoresist. A polycrystalline Au film of 100 to 600 nm thickness was deposited by e-beam evaporation after the removal of photoresist. The remaining photoresist was then removed and the resulting Au cylinders, of 1.5 to 12.0 µm diameter and 0.1 to 0.6 µm height, were annealed in-vacuum at 1050 ºC (Figure 6.1). Au cylinders dewetted from the sapphire substrate during annealing and some of them took the form of facetted single-crystal spheres of 0.5 to 5.0 µm diameter and some of them were polycrystals (Figure 6.2). About 50 Au microspheres were fabricated for each diameter. The resulted spheres are faceted along the {111} close pack planes which have the threefold rotational crystallographic symmetry [9, 10].

Since the sapphire substrate is nonconductive and the fabricated microspheres were equidistant and also not connected to each other, around 10~15 nm layer of Cr was deposited on the microsphere pattern surface for SEM imaging. Post- imaging, Cr layer was removed with Nitric acid to perform compression tests on the microspheres. Coated spheres were fabricated in the same procedure. Just in a final step, a 60-90 nm thickness W layer has been deposited on the surface by sputtering technique.
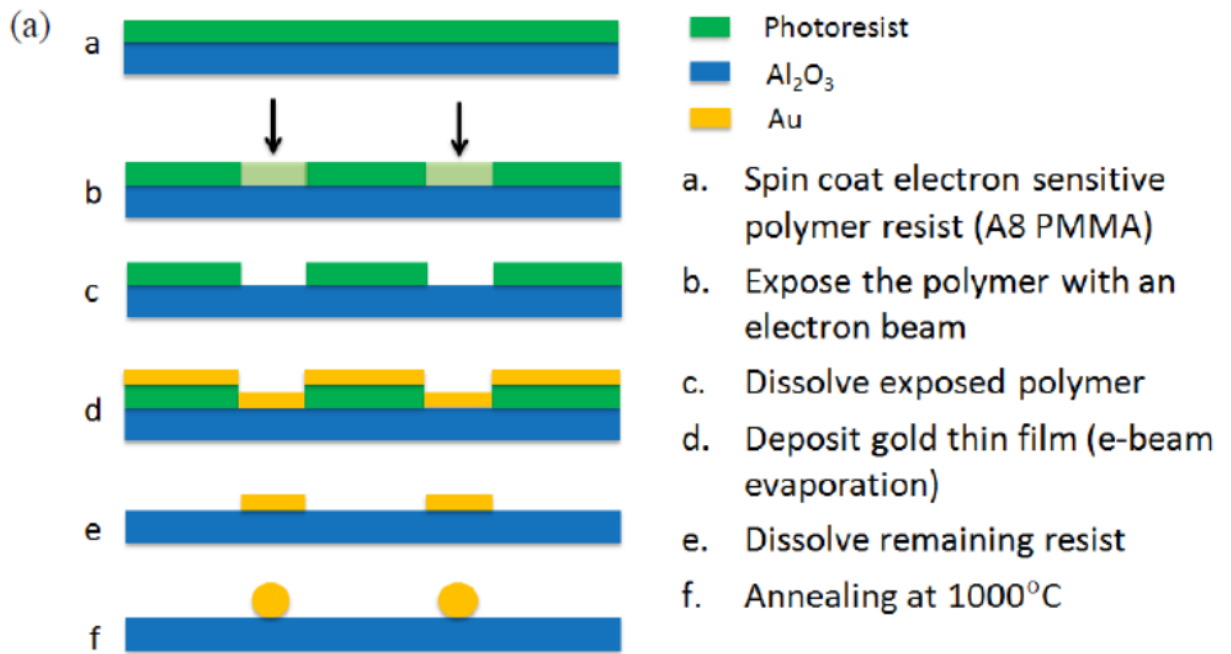
Figure 6.1: Schematic diagram of the steps of Au microspheres fabrication [11].
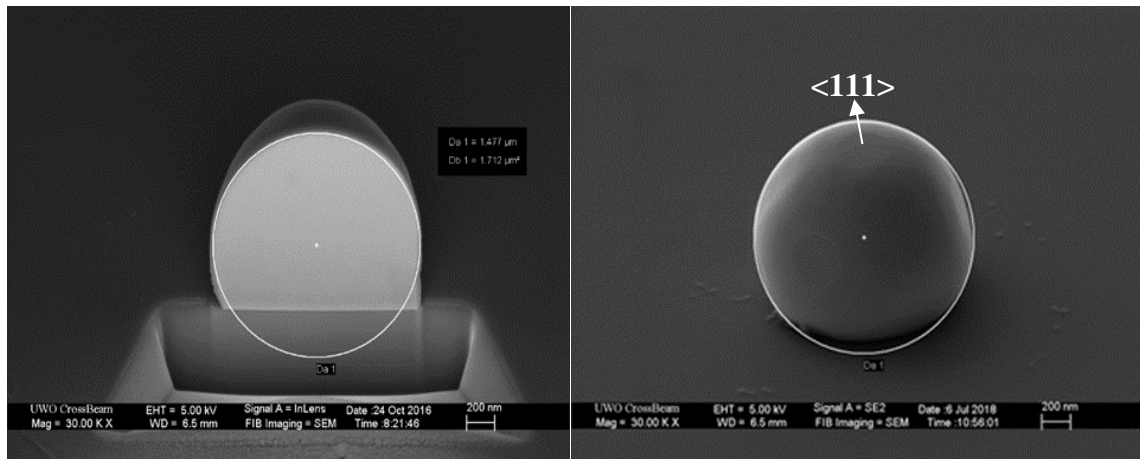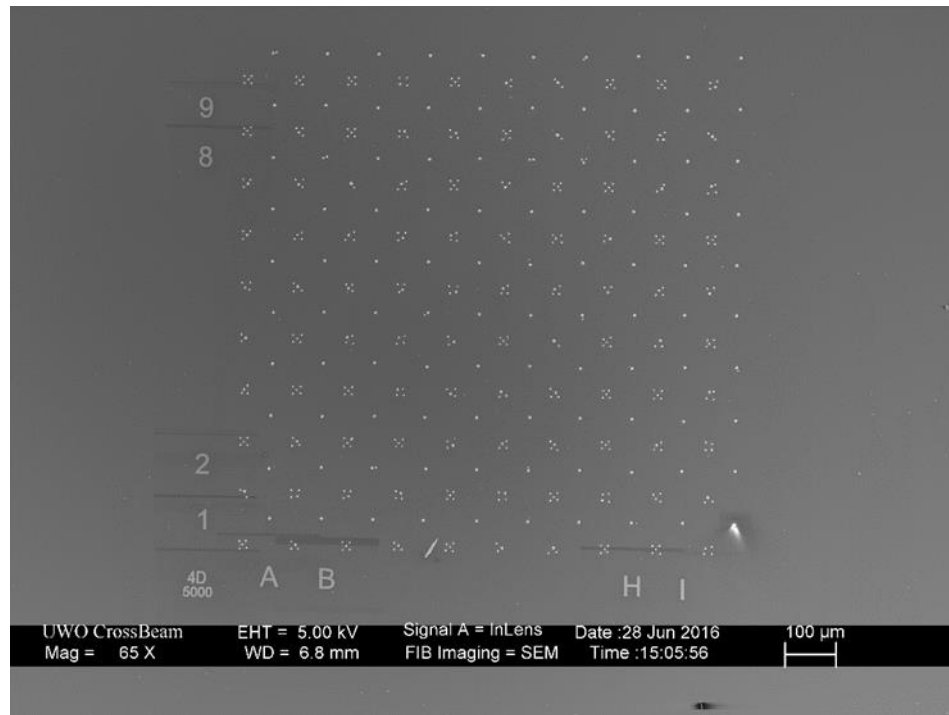
Figure 6.2: The SEM image of a) the array of 5 µm spheres, b) cross-section of one of the spheres 5 b) facets of the fabricated sphere.

6.3. Micro-Compression Tests of Au Spheres

The uniaxial micro-compression testing of Au microspheres carried out in this study was performed with an instrumented indentation machine manufactured by Micro Materials Ltd (Wrexham, UK) [12]. A 9 µm diameter diamond flat punch indenter was used to compress spheres. The machine can apply up to 20 N force with a precision of 100 µN. The capacitance displacement gauge has a displacement range of about 50 µm. We

started the compression with 500 nm spheres. The loading rate ranged from 0.005 mN/s to 0.5mN/s.

6.4. Results

Measured load-displacement curves are shown in Figure 6.3 for different pillar diameters based on the loading rates. A strong loading rate dependence is observed for the 0.7 μm diameter sphere. The effect of loading rate decreases as the sphere diameter increases from 0.7 to 2.2 μm. However, the behavior of 3 μm diameter sphere shows the loading rate dependency. Moreover, the discrete jumps are observed in the smaller spheres which is related to the dislocation nucleation and annihilation events as discussed in the previous chapter. Figure 6.4 shows the SEM images of the deformed sample indicating the trace of {111}<110> slip lines corresponding to the deformation.
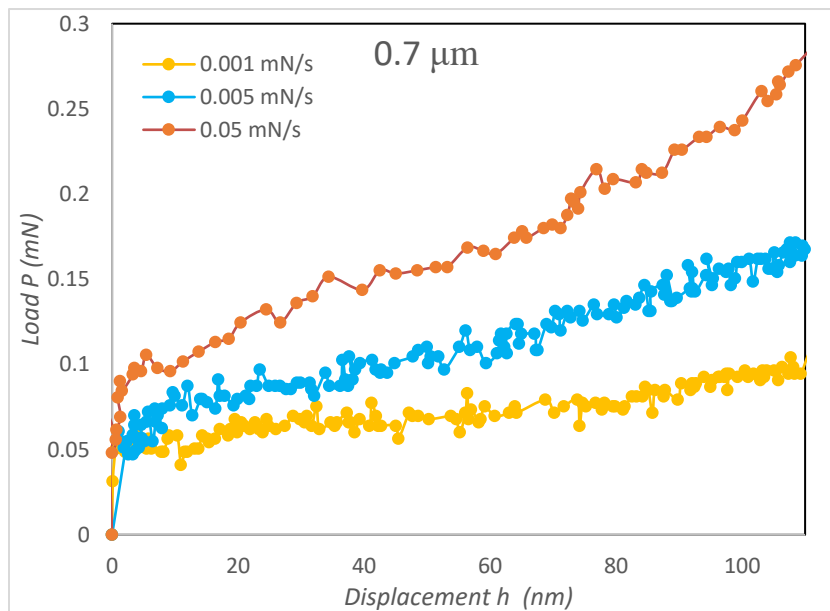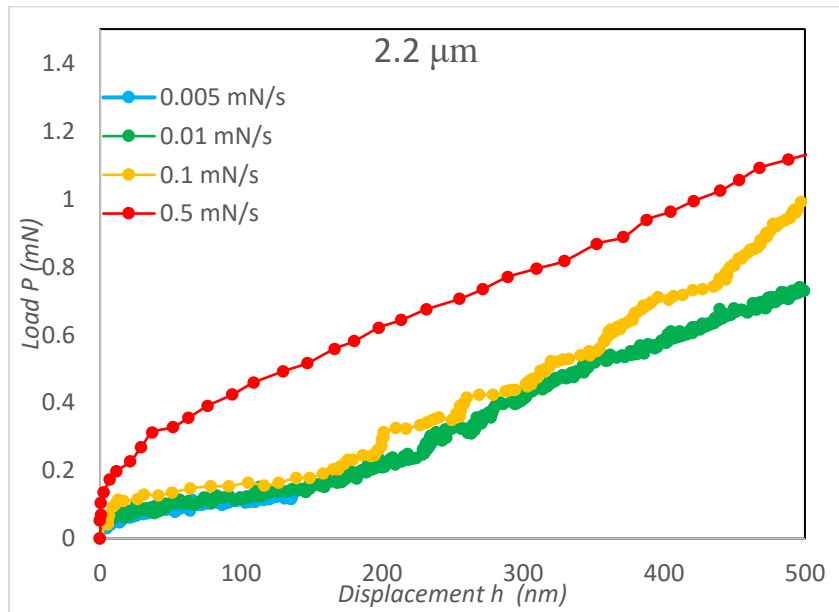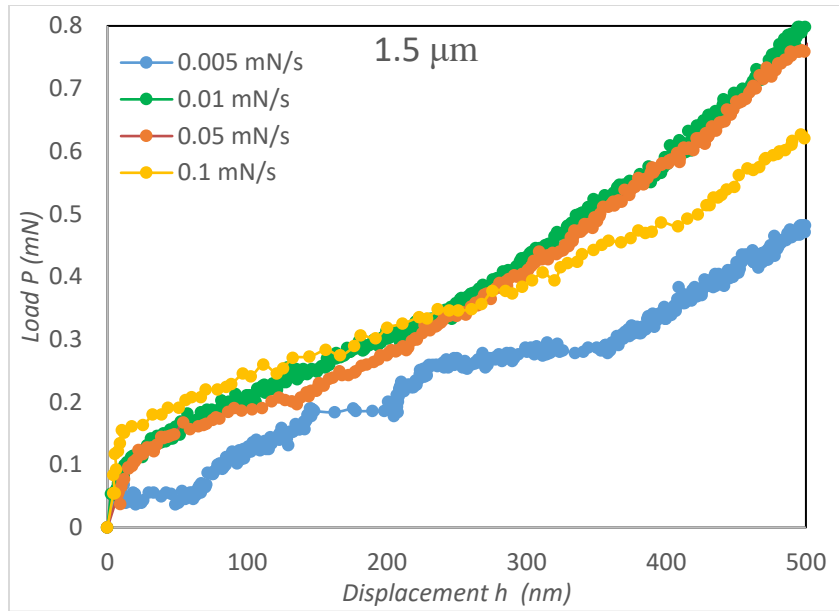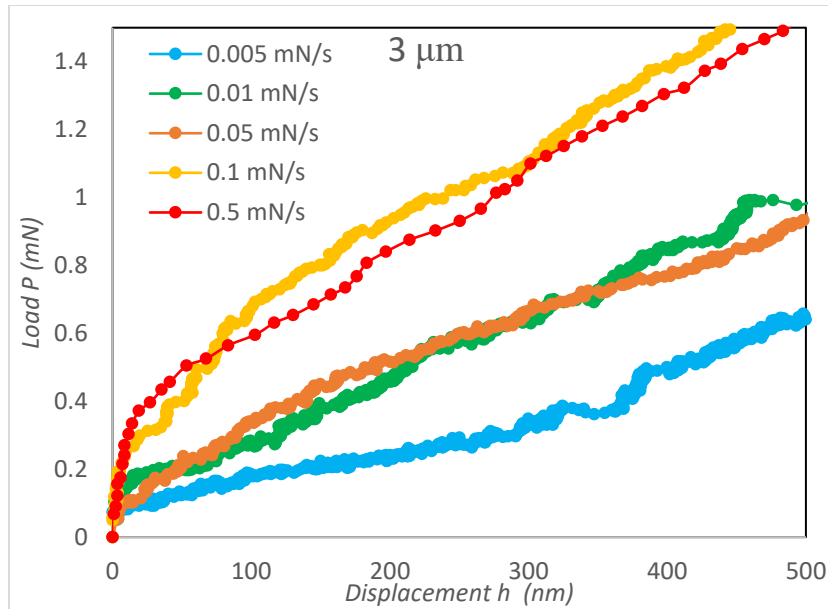
Figure 6.3: The effect of loading rate on the measured load-displacement curves for spheres with a) 0.7 µm, b) 1.5 µm, c) 2.2µm, d) 3 µm dimeter.
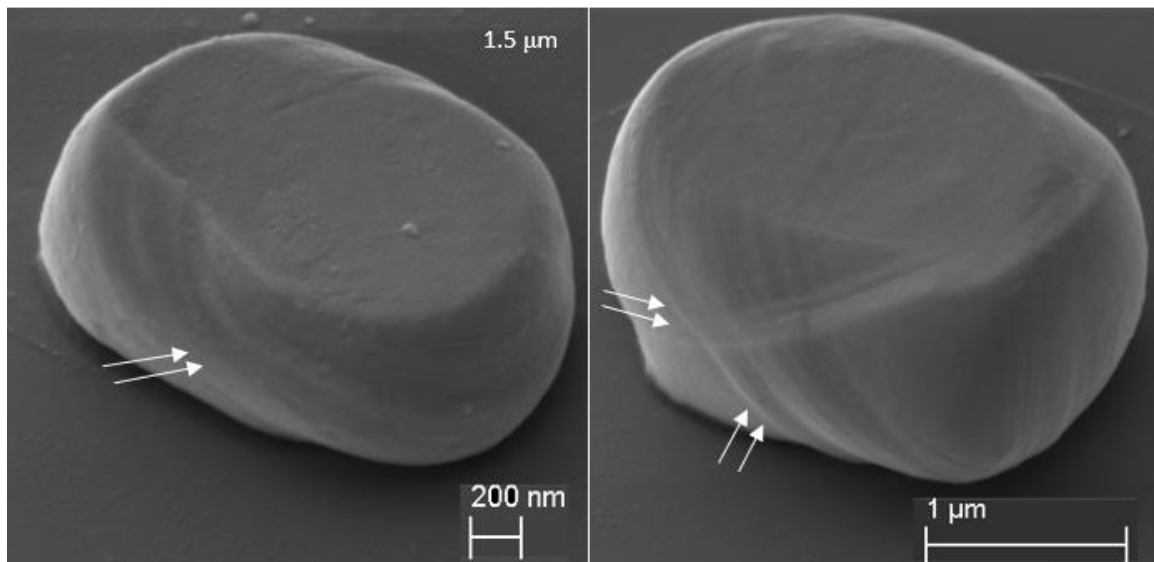
Figure 6.4: SEM images of the deformed microspheres indicating the slip lines of the {111}<110> slip systems.

6.4.1. Stress-Strain Curve

To be able to compare the flow behavior of spheres with different diameters, load-displacement data should be converted to stress-strain data. To obtain representative equivalent stress, the initial radius of the sphere should be converted to the effective

radius. This can be accomplished using volume conservation, assuming an increasing pancaking of sphere to more closely resemble a right cylinder [13]. Therefore;

$$\frac{4}{3}\pi r_0^3 = \pi r_{eff}^2 (h_0 - \delta) \tag{6.1}$$

where h_0 is equal to the original diameter of the sphere, $h_0 = 2r_0$, thus;

$$r_{eff} = 1.155 r_0 \left[\frac{r_0}{2r_0 - \delta}\right]^{0.5} \tag{6.2}$$

The average stress of the equivalent volume can be then calculated using the equivalent cylinder with $A = \pi r_{eff}^2$. This method has been used by various scholars to calculate the average stress on the micro and nano spherical shaped particles [13-15]. Although using this theory will result in the lower bond estimation of the stress amount, it will be useful for analyzing force-displacement data since the behavior of the spheres are being compared together and relative to each other.
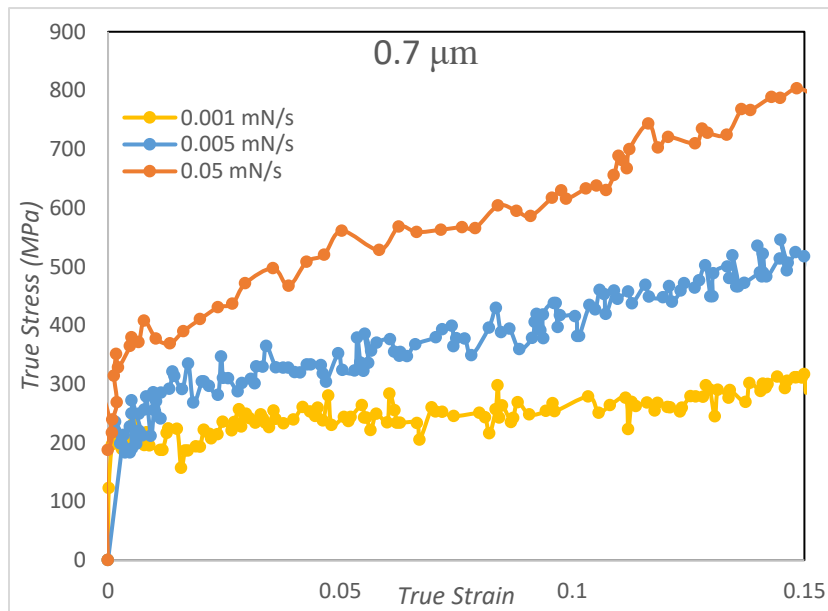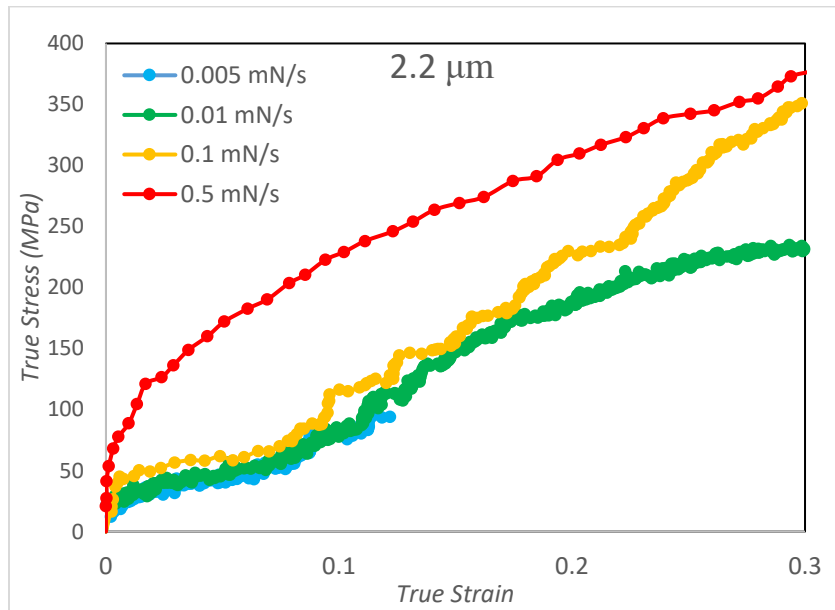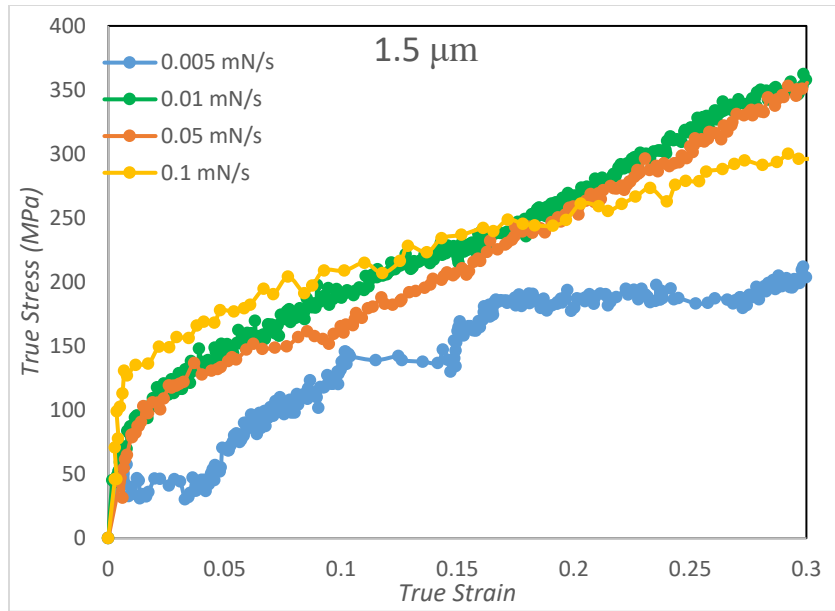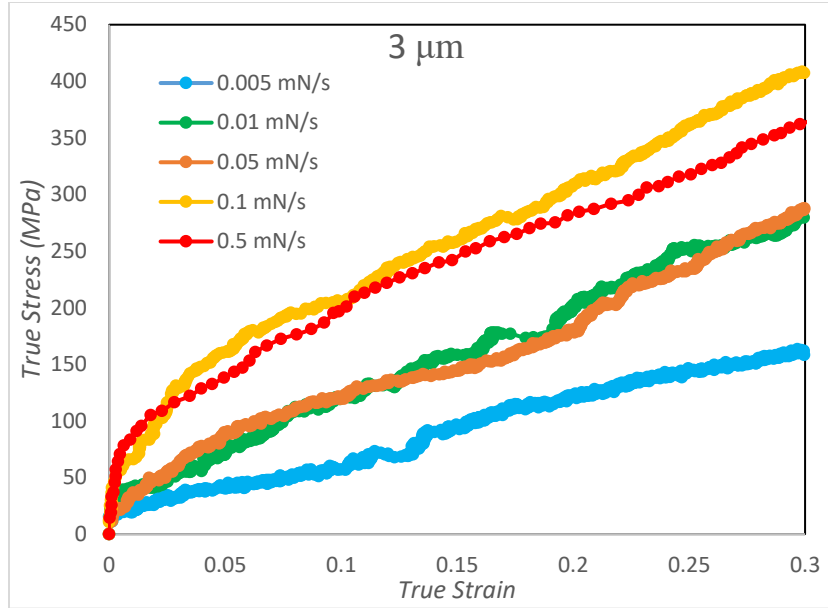
Figure 6.5: Flow behavior of a) 0.7 µm b) 1.5 µm, c) 2.2 µm, d) 3 µm diameter spheres at different strain rates.

6.5. Discussion

As it is observed in stress-strain curves the sensitivity to strain rate is very significant in the 0.7 µm sphere as the observed strength increases more than three times when the strain rate increases from 0.001 mN/s to 0.05 mN/s. Moreover, the amount of yield stress decreases with increase of sphere diameter for a particular strain and strain rate which is consistent with reported results about scale-dependent plasticity [16-21]. The relation of flow stress with strain, strain rate, and temperature can be described by Arrhenius relation as follows [22];

$$\sigma = A\varepsilon^n \dot{\varepsilon}^m exp\left[-\frac{Q}{RT}\right]$$

(6.3)

where A is a material constant, ε and ἐ are strain and strain rate, n is the strain hardening exponent, m is the strain rate sensitivity, Q is the activation energy, T is the temperature, and R is the universal gas constant. Figure 6.6 shows the strain hardening constant for 3 diameters of spheres at various strain rates. As it is observed the amount of n constant increases as the sphere size increases. This means that after yielding point the strain hardening which is in result of forest hardening mechanism increases with diameter of

spheres. In other words, it approves that the deformation mechanism converts to forest hardening as the sphere diameter increases.

Figure 6.7 shows the variation strain rate sensitivity constant (m) at five values of strains of 3 different dimeters of spheres. As it is observed the values of m are higher for the 0.7 µm sphere than the ones for the other two bigger diameters.
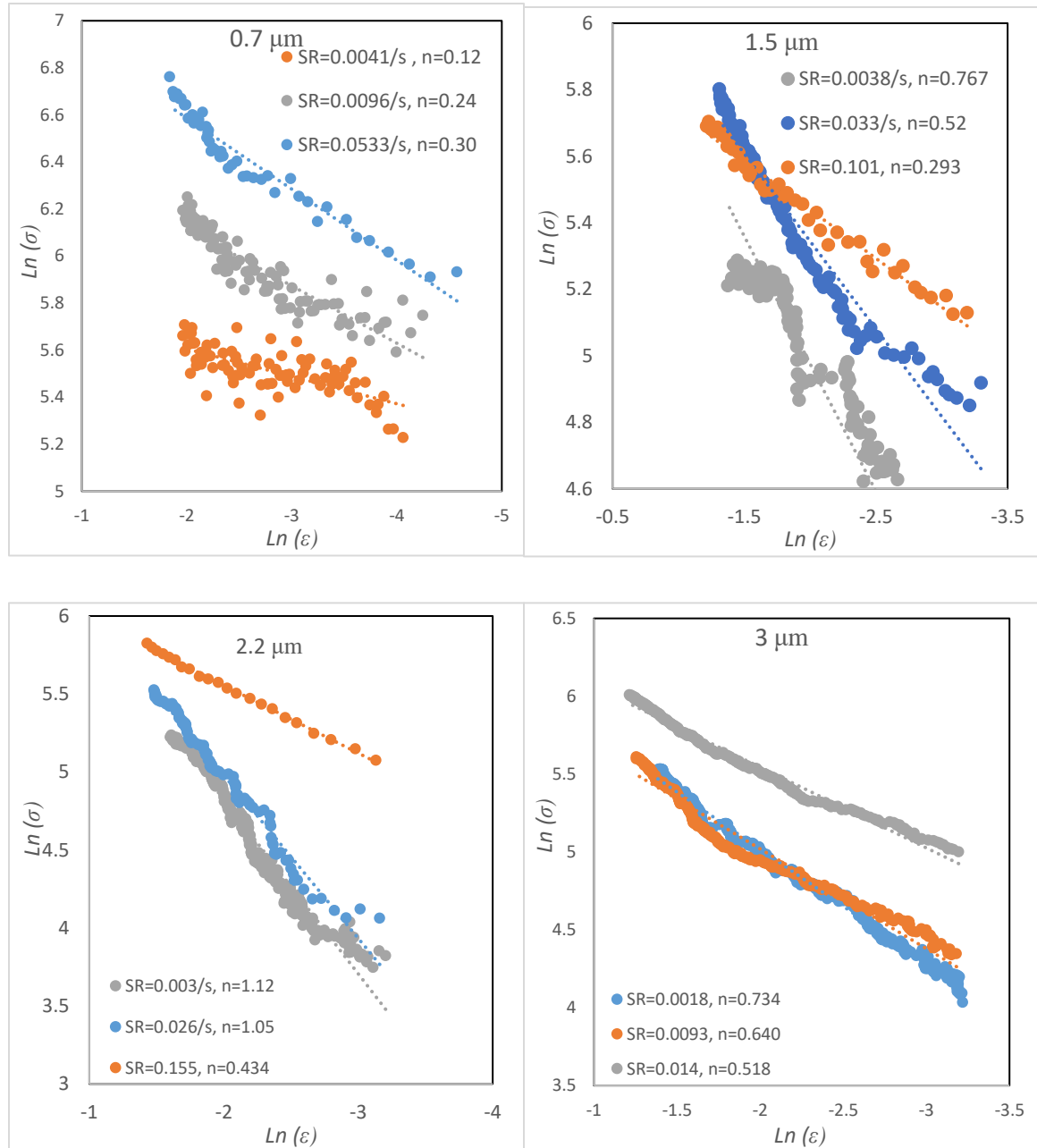
Figure 6.6: Comparing strain hardening constant for different diameters of spheres.
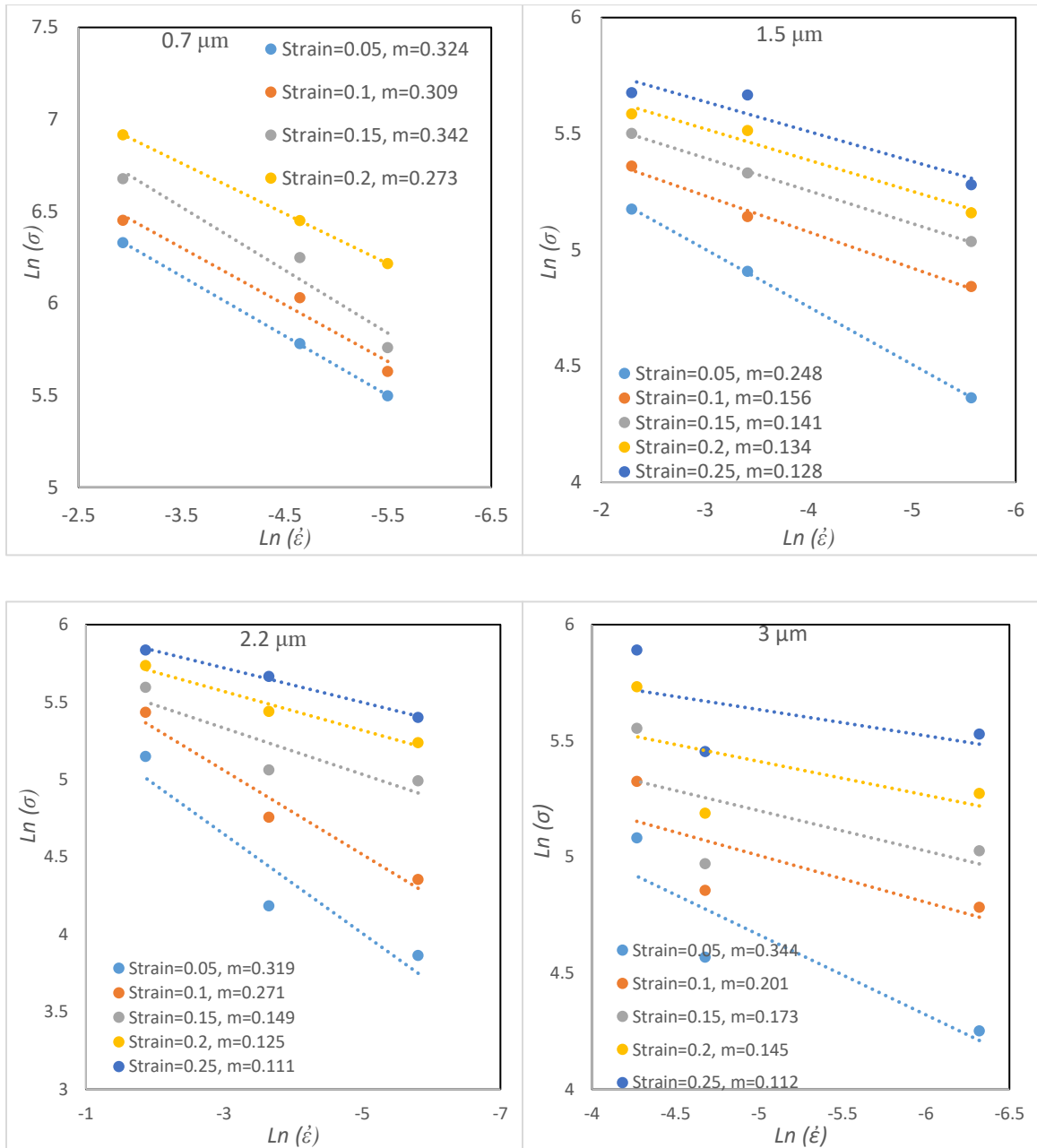
Figure 6.7: Comparing strain rate sensitivity constant for spheres with different diameters.

Figure 6.8 summarized the values of strain hardening constant (n) of all the sphere diameters as a function of strain rate. As it is observed the value of strain hardening constant is higher for the bigger spheres and it has the lowest values for the 0.7 μm sphere. This indicated that the mechanism of deformation is different for the 0.7 μm sphere than the bigger spheres and as the sphere size increases it follows the forest

hardening behavior as bulk material. Moreover, the values of n are more strain rate dependent on the bigger sphere diameters.

Figure 6.9 plots the values of strain rate sensitivity constant (m) for all of the considered sphere diameters as a function of strain. It is observed that the value of m decreases as the deformation and strain increases for all of the spheres. Moreover, the strain rate sensitivity has the highest values for the smallest sphere, indicating that material behavior is more strain rate sensitive in the smaller diameter sphere. The higher values of strain rate sensitivity for 0.7 μm sphere than the values for other dimeters indicates that the deformation behavior is different for the 0.7 μm dimeter sphere than the others. Jennings et al. [23] study on the strain-rate sensitivity in single-crystalline Cu nanopillars showed that both of the strain rate and sample size are affecting the compressive strength of single-crystalline Cu nanostructures. According to their results a clear strain rate sensitivity is observed in the small pillars (75nm and 125nm dimeters), related to the operation of surface dislocation sources of a highly thermal nature [23]. The same results were reported by Zhu et al. [24] and Schneider et al. [25].
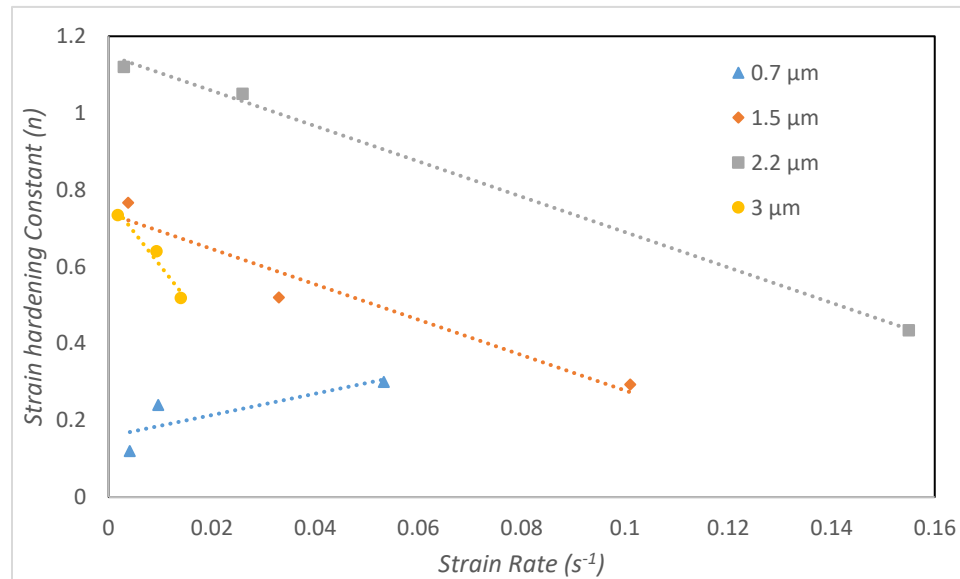
Figure 6.8: Strain hardening constant for different sphere diameters.
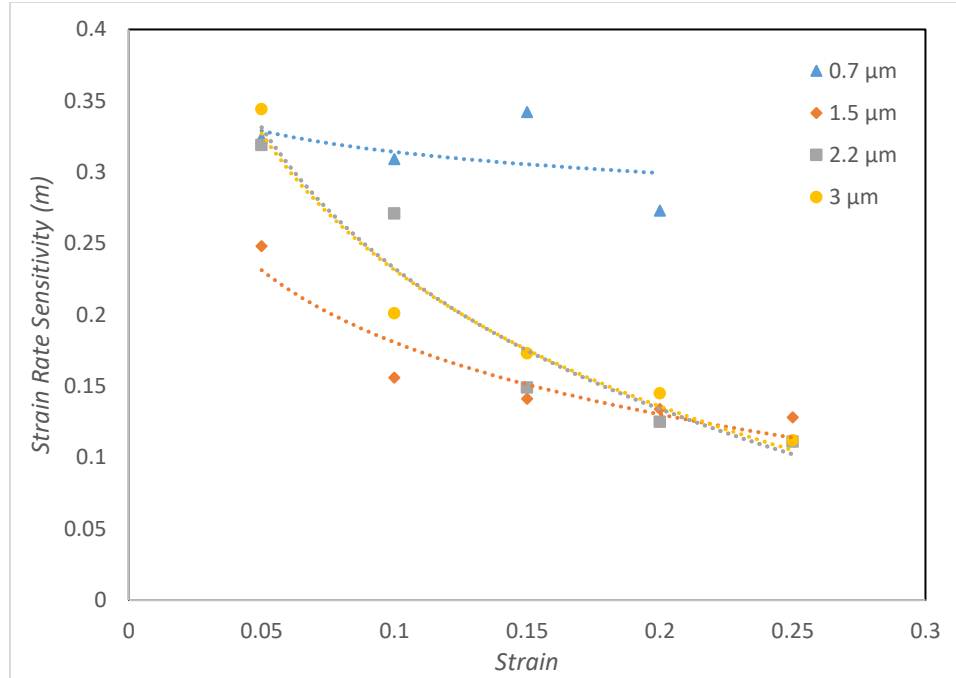
Figure 6.9: Strain rate sensitivity for different sphere diameters.

In pure metals, such as gold spheres of this study, different obstacles, such as dislocation interactions and point defects often block dislocation motions and thermal activation energy is needed to overcome these barriers. The strength for preventing dislocation glide is defined by the apparent activation volume, V^* [26]. Since the behavior of our studied small spheres is different than the bigger ones, dislocation nucleation from the surface is likely to have a significant contribution to their deformation process and thus contribute to their activation volume. The apparent activation volume is related to the strain rate sensitivity based on the following equation [27];

$$V^* = \sqrt{3}kT \left(\frac{\partial ln\dot{\varepsilon}}{\partial \sigma}\right) = \frac{\sqrt{3}kT}{m\sigma} \tag{6.4}$$

where k is Boltzmann's constant and T is the temperature (298.85K for our experiments). The apparent activation volume of the considered spheres is calculated based on the above equation regarding the applied strain. The calculated amounts of V^* were normalized based on the Au Burgers vector (b_{Au}=0.288 [28]). The value of V^* remains almost independent of the strain for the 0.7 diameter sphere, ranging 1.6-2.4b^3. It ranges 8.6-10.6 b^3, 9.4-10.2 b^3, and 8.9-10.5 b^3 for the 1.5μm, 2.2μm, and 3μm diameter spheres respectively. As it is observed as the sphere diameter increases the range of apparent

activation volume changes and its dependence on the strain increases. This means that as the sphere diameter increases, a higher amount of energy is needed to continue the deformation in higher strains and pass the barriers of dislocation motion. These barriers which are activated in higher strains are dislocation interactions and forest hardening [25, 26]. So, the higher strain dependency of apparent activation volume in larger spheres indicates that they are deforming mainly by forest hardening mechanism. The range of calculated apparent activation volume for the 0.7 μm sphere is consistent with the reported values of V^* for the FCC metals by Mook et al. [29], and is an indication of dislocation nucleation events during the deformation.
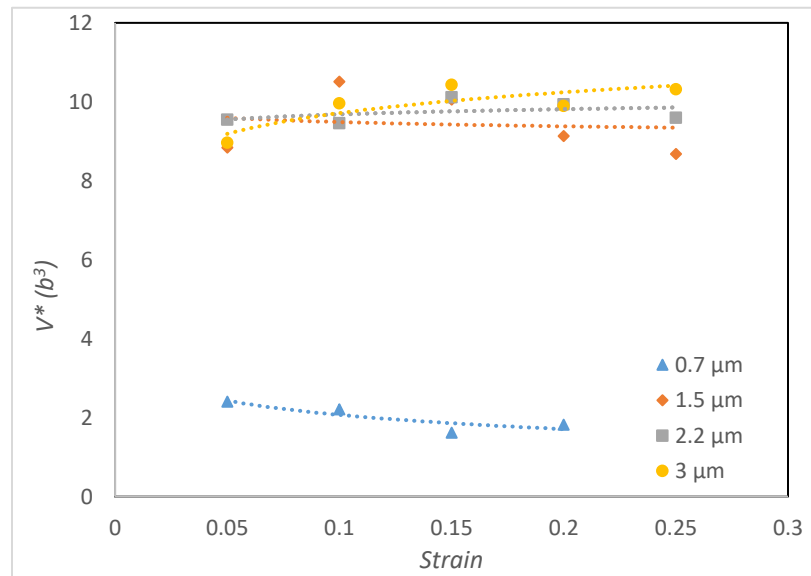
Figure 6.10: Apparent activation volume as a function of strain for different sphere diameters.

The amount of required energy for a dislocation to overcome an obstacle is called apparent activation energy Q* which can be calculated based on the apparent activation volume, using the following equation [30];

$$Q^* = \tau_{oK}V^* \tag{6.5}$$

where τ_{0K} is the athermal contribution to the flow stress, resulting from long-range internal stresses impeding the plastic flow, the temperature dependence of which is weak and mainly due to that of μ (shear modulus) [31]. The amount of τ_{0K} is considered 256 MPa for Au in our calculations [32]. As it is observed in Figure 6.11, the amount of Q*

range between 0.069-0.091 eV for 0.7 μm sphere when strain increases from 5% to 20%. Essentially for the amount of $Q^* < 0.2eV$, dislocation obstacle strength is weak and the glide of dislocation is controlled by lattice resistance [33]. For our larger spheres, the amount of Q^* is between 0.3 and 0.4, which indicates that the mechanism of obstacle0limited dislocation glide is the dominant or a part of the deformation mechanism [33]. Since the fabricated spheres don't have impurities or precipitates and mostly no grain boundaries, the internal obstacle of dislocation glide is dislocation-dislocation interaction and forest hardening in our case.
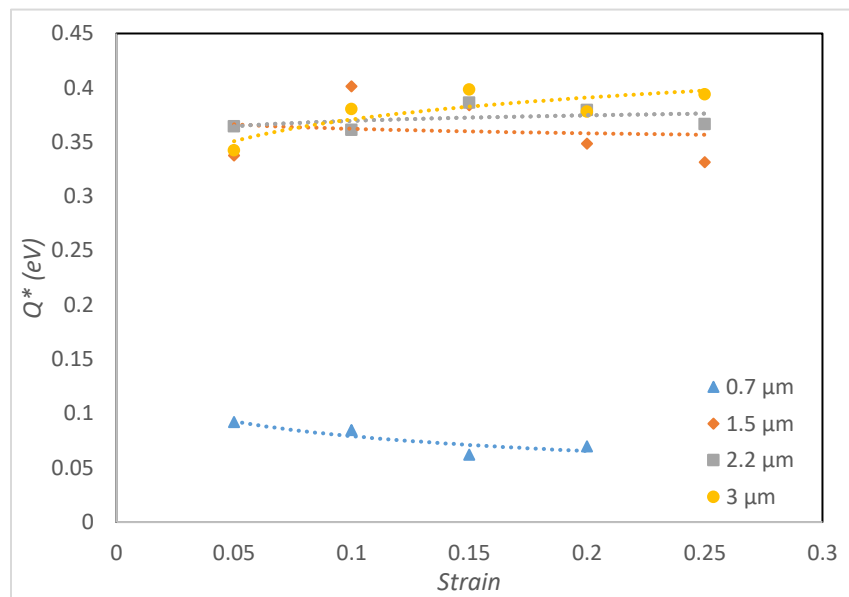
Figure 6.11: Apparent activation energy as a function of strain for different sphere diameters.

Conclusions

In this study, the plastic deformation of sub-micron and micron-sized (0.7 – 3 μm) Au spheres is investigated at room temperature at various strain rates using micro-compression testing. According to our results, the dependence of the flow stress upon strain and strain rate is slightly affected by sphere diameter. Size dependent behavior was observed in the compression of spheres with different diameters and the submicron spheres presented significantly higher strength than the larger spheres at all of the loading rates. Moreover, increasing the rate of deformation resulted in a higher deformation stress

for all of the considered sphere diameters. The results of the calculated apparent activation volume V* and apparent activation energy Q* shows that the deformation mechanism of the smallest spheres (0.7μm diameter) is controlled mainly by dislocation nucleation from free surfaces. The values of V* and Q* for the larger spheres indicate that obstacle limited dislocation glide, which is the typical mechanism in bulk scale deformation of fcc metals, is the operative deformation process for these spheres.

References

[1] M.D. Uchic, D.M. Dimiduk, J.N. Florando, W.D. Nix, Sample dimensions influence strength and crystal plasticity, Science 305(5686) (2004) 986-989.

[2] D.M. Dimiduk, M.D. Uchic, T.A. Parthasarathy, Size-affected single-slip behavior of pure nickel microcrystals, Acta Mater 53(15) (2005) 4065-4077.

[3] C.A. Volkert, E.T. Lilleodden, Size effects in the deformation of sub-micron Au columns, Philos Mag 86(33-35) (2006) 5567-5579.

[4] H. Bei, S. Shim, Effects of focused ion beam milling on the nanomechanical behavior of a molybdenum-alloy single crystal, Appl Phys Lett 91(11) (2007).

[5] G. Richter, K. Hillerich, D.S. Gianola, R. Monig, O. Kraft, C.A. Volkert, Ultrahigh Strength Single Crystalline Nanowhiskers Grown by Physical Vapor Deposition, Nano Lett 9(8) (2009) 3048-3052.

[6] A.T. Jennings, M.J. Burek, J.R. Greer, Microstructure versus Size: Mechanical Properties of Electroplated Single Crystalline Cu Nanopillars, Phys Rev Lett 104(13) (2010).

[7] S. Buzzi, M. Dietiker, K. Kunze, R. Spolenak, J.F. Loffler, Deformation behavior of silver submicrometer-pillars prepared by nanoimprinting, Philos Mag 89(10) (2009) 869-884.

[8] D. Mordehai, M. Kazakevich, D.J. Srolovitz, E. Rabkin, Nanoindentation size effect in single-crystal nanoparticles and thin films: A comparative experimental and simulation study, Acta Mater 59(6) (2011) 2309-2321.

[9] D. Mordehai, S.W. Lee, B. Backes, D.J. Srolovitz, W.D. Nix, E. Rabkin, Size effect in compression of single-crystal gold microparticles, Acta Mater 59(13) (2011) 5202-5215.

[10] S.W. Lee, D. Mordehai, E. Rabkin, W.D. Nix, Effects of focused-ion-beam irradiation and prestraining on the mechanical properties of FCC Au microparticles on a sapphire substrate, J Mater Res 26(14) (2011) 1653-1661.

[11] A.Z.M.A. Islam, Kinetics of Length Scale Dependent Deformation of Gold Microspheres and Micropillars, Mechanical and Materials Engineering, The University of Western Ontario, 2016.

[12] S.G. B. Beake, S. Jones, R. Parkinson, N. Pickford, L. Roberts, and J. Smith, NanoTest Help File, in: M.M. Ltd (Ed.) 2004.

[13] D.D. Stauffer, A. Beaber, A. Wagner, O. Ugurlu, J. Nowak, K.A. Mkhoyan, S. Girshick, W. Gerberich, Strain-hardening in submicron silicon pillars and spheres, Acta Mater 60(6-7) (2012) 2471-2478.

[14] W.M. Mook, J.D. Nowak, C.R. Perrey, C.B. Carter, R. Mukherjee, S.L. Girshick, P.H. McMurry, W.W. Gerberich, Compressive stress effects on nanoparticle modulus and fracture, Phys Rev B 75(21) (2007).

[15] J. Paul, S. Romeis, J. Tomas, W. Peukert, A review of models for single particle compression and their application to silica microspheres, Adv Powder Technol 25(1) (2014) 136-153.

[16] S.W. Lee, S.M. Han, W.D. Nix, Uniaxial compression of fcc Au nanopillars on an MgO substrate: The effects of prestraining and annealing, Acta Mater 57(15) (2009) 4404-4415.

[17] J.R. Greer, C.R. Weinberger, W. Cai, Comparing the strength of f.c.c. and b.c.c. sub-micrometer pillars: Compression experiments and dislocation dynamics simulations, Mat Sci Eng a-Struct 493(1-2) (2008) 21-25.

[18] M.D. Uchic, P.A. Shade, D.M. Dimiduk, Plasticity of Micrometer-Scale Single Crystals in Compression, Annu Rev Mater Res 39 (2009) 361-386.

[19] R. Maass, C.A. Volkert, P.M. Derlet, Crystal size effect in two dimensions - Influence of size and shape, Scripta Mater 102 (2015) 27-30.

[20] R. Gu, A.H.W. Ngan, Size effect on the deformation behavior of duralumin micropillars, Scripta Mater 68(11) (2013) 861-864.

[21] A. Kunz, S. Pathak, J.R. Greer, Size effects in Al nanopillars: Single crystalline vs. bicrystalline, Acta Mater 59(11) (2011) 4416-4424.

[22] A. Kelly, R. Nicholson, Strengthening methods in crystals, (1971).

[23] A.T. Jennings, J. Li, J.R. Greer, Emergence of strain-rate sensitivity in Cu nanopillars: Transition from dislocation multiplication to dislocation nucleation, Acta Mater 59(14) (2011) 5627-5637.

[24] T. Zhu, J. Li, A. Samanta, A. Leach, K. Gall, Temperature and Strain-Rate Dependence of Surface Dislocation Nucleation, Phys Rev Lett 100(2) (2008) 025502.

[25] A.S. Schneider, B.G. Clark, C.P. Frick, P.A. Gruber, E. Arzt, Effect of orientation and loading rate on compression behavior of small-scale Mo pillars, Materials Science and Engineering: A 508(1) (2009) 241-246.

[26] U.F. Kocks, A.S. Argon, M.F. Ashby, Thermodynamics and Kinetics of Slip, Prog Mater Sci 19 (1975) 1-281.

[27] H. Somekawa, C.A. Schuh, Effect of solid solution elements on nanoindentation hardness, rate dependence, and incipient plasticity in fine grained magnesium alloys, Acta Mater 59(20) (2011) 7554-7563.

[28] J.F. Rodriguez-Nieva, C.J. Ruestes, Y. Tang, E.M. Bringa, Atomistic simulation of the mechanical properties of nanoporous gold, Acta Mater 80 (2014) 67-76.

[29] W.M. Mook, M.S. Lund, C. Leighton, W.W. Gerberich, Flow stresses and activation volumes for highly deformed nanoposts, Mat Sci Eng a-Struct 493(1-2) (2008) 12-20.

[30] G. Schoeck, The Activation Energy of Dislocation Movement, physica status solidi (b) 8(2) (1965) 499-507.

[31] Y.M. Wang, A.V. Hamza, E. Ma, Temperature-dependent strain rate sensitivity and activation volume of nanocrystalline Ni, Acta Mater 54(10) (2006) 2715-2726.

[32] A.Z.M.A. Islam, R.J. Klassen, Kinetics of length-scale dependent plastic deformation of gold microspheres, J Mater Res 32(18) (2017) 3507-3515.

[33] H.J. Frost, M.F. Ashby, Deformation-mechanism maps : the plasticity and creep of metals and ceramics, Pergamon Press, Oxford [Oxfordshire]; New York, 1982.

Chapter 7

7. Effect of constraining layer on the plastic deformation of Au microspheres

The effect of having a constraining layer on the plasticity of sub-micron and micron-sized samples is investigated in this chapter. Au single crystalline spheres were coated by a 60-90 nm thickness W and Al_2O_3 layers. The sputtering technique was used to deposit the 80nm W layer on the samples. Atomic layer deposition (ALD) and molecular layer deposition (MLD) techniques were used to deposit 60 nm of Al_2O_3 layer. Microspheres are in different sizes including 0.7μm, 1.5μm, 2.2μm, and 3μm and micro-compression tests were conducted in 5 to 6 loading rates. SEM images of the deformed spheres show micro-cracking in the coated W layer. The force-displacement curves of the coated samples display a significantly higher strength than the non-coated samples. This increase is up to 11 times for the yield strength of the Al_2O_3 coated samples than that for the noncoated samples. Analyses of the apparent activation volume and energy show a significant increase of the V* and Q* amounts for the W coated samples than the noncoated ones. Values of activation energy changed from 0.062-0.091 (eV) to 0.297-0.430 (eV) for the 0.7 μm spheres by having the W coating layer which reflects the activation of dislocation-obstacle mechanism in the coated layer samples and indicates the surface nucleation and exhaustion mechanism activation in the noncoated samples of 0.7 μm dimeter size.

7.1. Introduction

Recent studies on the compression of single-crystalline micro and nano-sized samples have indicated that the strength of crystalline metals, independent of sample size in bulk, increases dramatically as the sample size decreases to the nanoscale [1-10]. As the sample dimension becomes small, the effect of nucleation at the surface becomes significant. Surfaces naturally introduce layers of atoms where their coordination number and the electronic structure are different from that of internal atoms [11]. As a result, the physical and chemical properties of materials can be significantly different near the

surface. The physical change results in a change in the surface energy, residual stress, and vacancy distribution as to facilitate the surface nucleation of defects [11, 12]. The influence of the surface effect on the properties of the sub-micron and nano-scale sample is directly associated with the surface to volume ratio and obviously, the proportion of surface in the total volume of the sample will become higher when the physical dimension of the materials becomes smaller, resulting in increasing significance of the surface nucleation of defects.

One of the methods that can be helpful to evaluate the theories which relates the different mechanical properties of small scale materials to the activation of the surface controlled mechanisms is to constrain the surface with a coating layer. It has been experimentally demonstrated that coating small-scale single-crystalline metallic pillars suppressed the discrete nature of their compressive stress–strain data and resulted in enhanced strengths and in significant storage of dislocations [13]. For example, Greer [14] reported a higher flow stress and a significant amount of linear strain hardening in the alumina coated Au pillars than that for pillars with free surfaces. Numerous dislocations were observed to be trapped at the pillar-coating interface during compression. Ng and Ngan [15] demonstrated that coating aluminium micropillars with W will result to the trapping of dislocations inside the pillar and enhance their interaction and thus decrease the strain bursts and significantly increase the strain hardening behaviour. Jennings et al. [16], observed around 80% higher maximum strengths in 75 nm and 1 μm diameter single-crystalline Cu pillars than the uncoated ones with equivalent diameters [16]. As they concluded, the coating layer inhibits the ability of a dislocation to vanish at the free surface.

Using three-dimensional dislocation dynamics (3DDD) simulations, Zhou et al. [17] explained the significant increase in strength of coated micropillars, demonstrating a fundamentally different strengthening mechanism in coated micropillars than in samples with free surfaces. Lee et al. [18] used a simple numerical model to develop a continuum model for describing the confined plasticity in coated pillars. El-Awady et al. [19] studied the effect of external barrier using 3DDD simulations and concluded that external strong

barrier dramatically increase the dislocation density by an order of magnitude due to trapping dislocations at the barrier.

Building on the previous studies mentioned above, the present work aims to reach a further understanding of the deformation of micron and sub-micron sized samples by comparing the mechanical and deformation behaviour of surface constrained micron-sized spheres with the behaviour of noncoated spheres.

7.2. Sample Preparation

Gold microspheres with different diameters were fabricated on a (0001)-oriented sapphire (α-Al_2O_3) surface. A positive photoresist layer (A8 PMMA) was spin-coated on the O_2 plasma cleaned sapphire surface and ebeam lithography was used to project a grid of 1 to 10.0 μm diameter circles upon the photoresist. A polycrystalline Au film of 100 to 600 nm thickness was deposited by e-beam evaporation after the removal of photoresist. The remaining photoresist was then removed and the resulting Au cylinders, of 1.5 to 12.0 μm diameter and 0.1 to 0.6 μm height, were annealed in-vacuum at 1050 ^{o}C. Au cylinders dewetted from the sapphire substrate during annealing and some of them took the form of facetted single-crystal spheres of 0.5 to 5.0 μm diameter and some of them were polycrystals. About 50 Au microspheres were fabricated for each diameter. The resulted spheres are faceted along the {111} close pack planes which have the threefold rotational crystallographic symmetry [20, 21]. A 60-90 nm thickness W layer has been deposited on the surface by sputtering technique using An Edwards Auto500 sputter deposition tool, equipped with a thickness monitor. To understand the effect of coating technique, a 60nm layer of Al_2O_3 was deposited on the spheres by ALD and MLD technique using Gemstar-8 ALD machine. Figure 7.1 presents the SEM images of the coated samples.
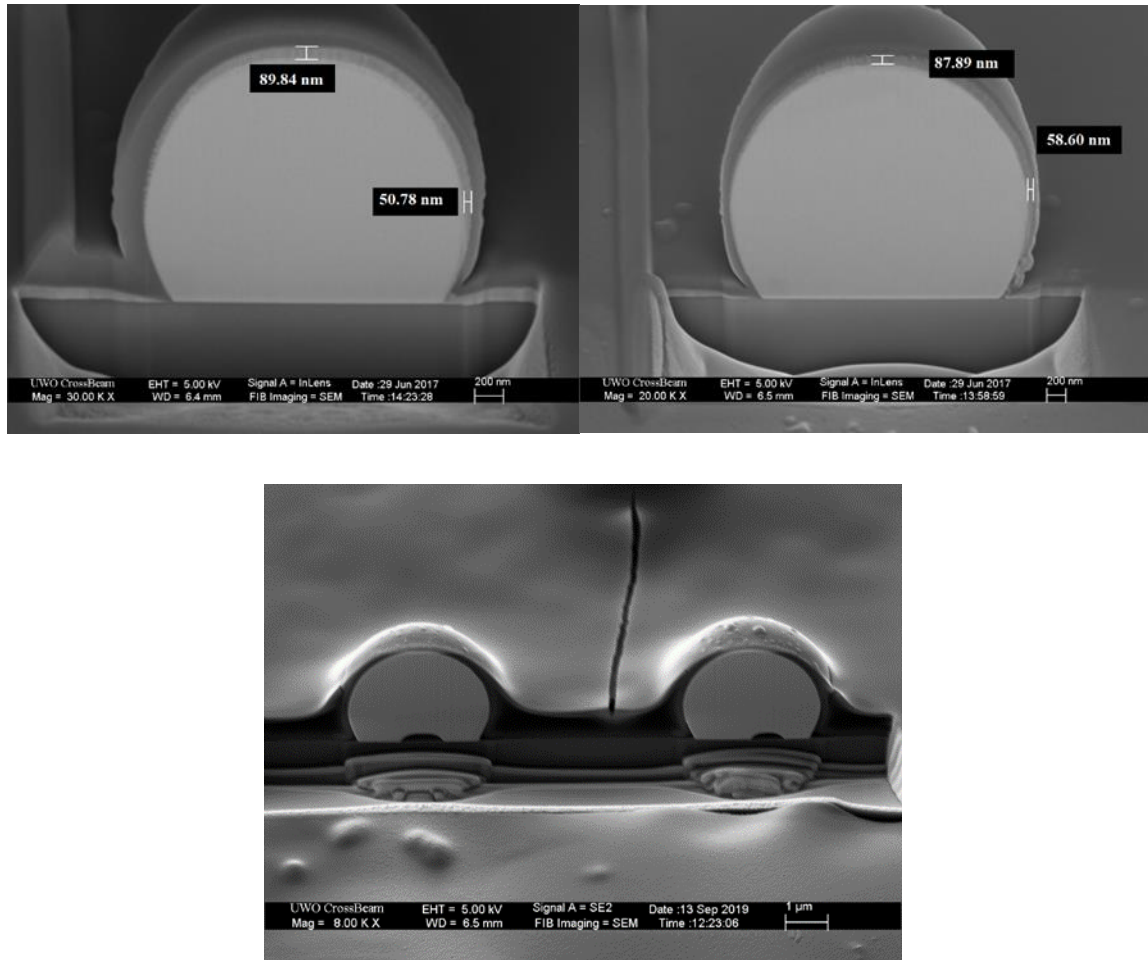
Figure 7.1: SEM images of the cross-sectional view of a) 2.2 µm diameter Au sphere coated with W layer, b) 3 µm diameter Au sphere coated with W layer, and c) 3 µm diameter Au sphere coated with Al₂O₃ layer using ALD technique.

7.3. Micro-Compression Test

The uniaxial micro-compression testing of coated Au microspheres carried out in this study was performed with an instrumented indentation machine manufactured by Micro Materials Ltd (Wrexham, UK) [22]. A 9 µm diameter diamond flat punch indenter was used to compress spheres. The machine can apply up to 20 N force with a precision of 100 µN. The capacitance displacement gauge has a displacement range of about 50 µm. We started the compression with 500 nm spheres. The loading rate ranged from 0.005 mN/s to 0.5mN/s.

7.4. Results

Measured load-displacement curves are shown in Figure 7.2 for different coated pillar diameters based on the loading rates. As it is observed, a strong loading rate dependence is observed for the 0.7 μm diameter coated sphere, similar to the results of non-coated samples (Figure 6.3, chapter 6). Moreover, the flow behavior of the coated spheres is smoother (no-load jumps are observed here) comparing the non-coated samples especially in smaller diameters.
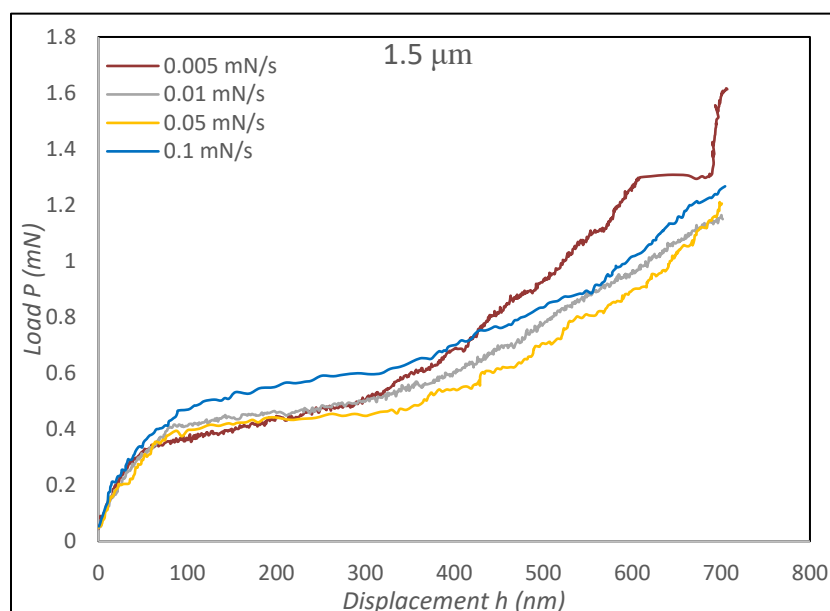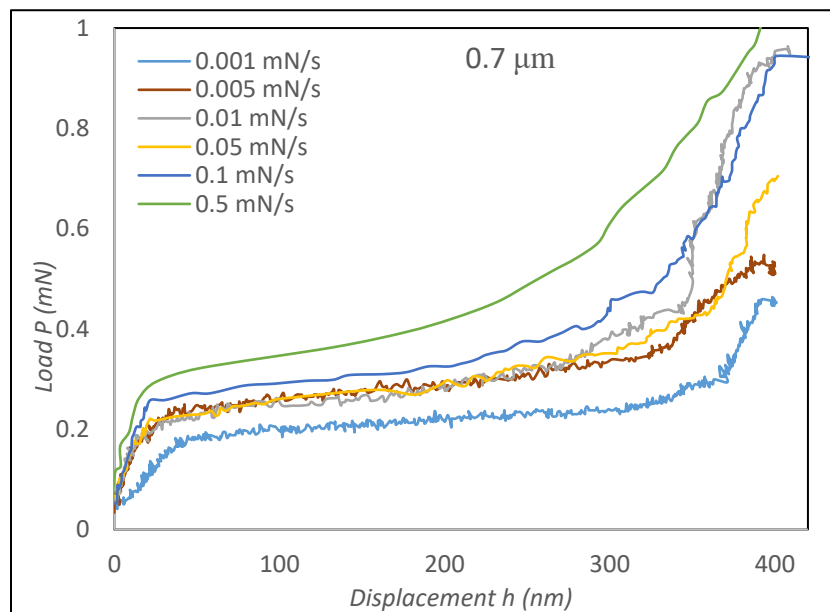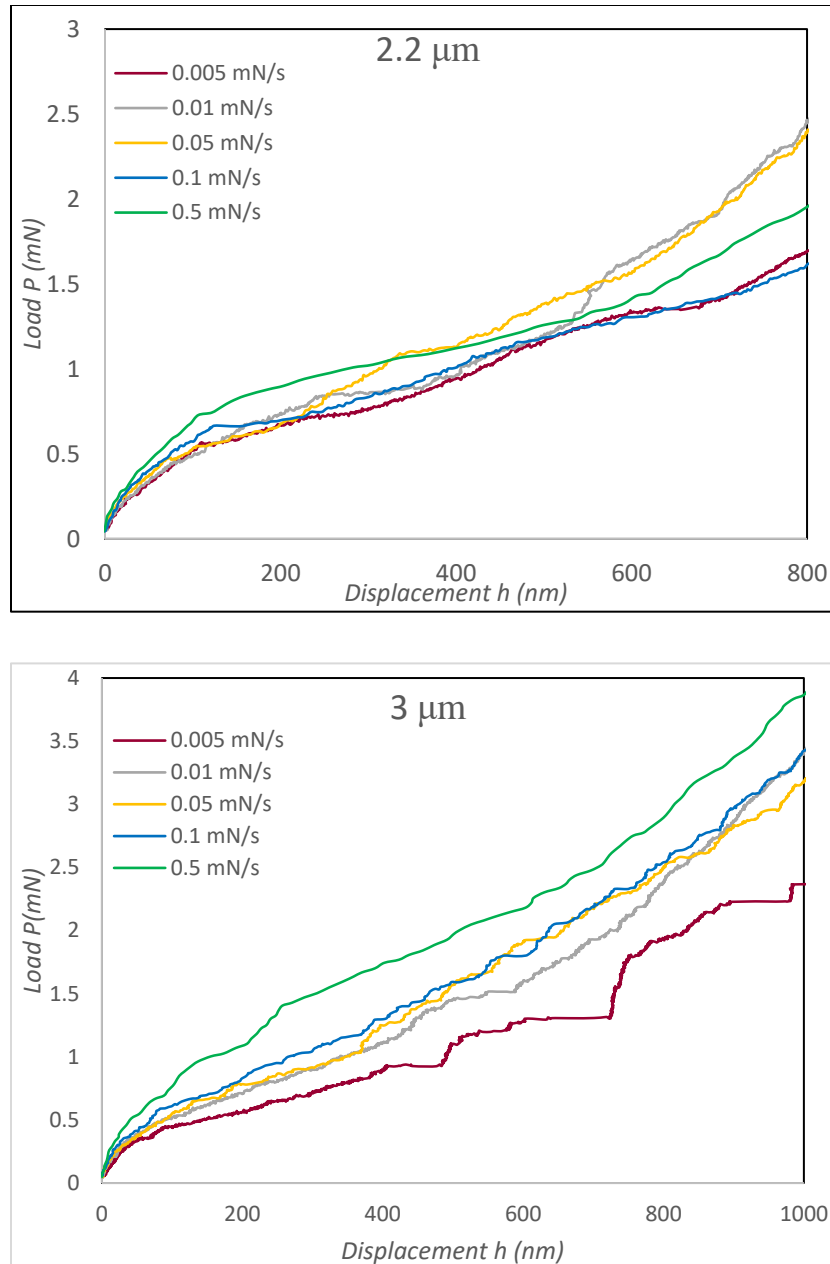
Figure 7.2: The effect of loading rate on the measured load-displacement curves of the W coated spheres with a) 0.7 μm, b) 1.5 μm, c) 2.2μm, d) 3 μm dimeter.

7.5. Discussion

Figure 7.3 compares the load-displacement curves of the coated and non-coated samples at different loading rates. It is observed that the strength increases significantly by having a coated layer. The increase of compression loading due to the W layer, is about 200% for the 1.5 μm diameter spheres, 300% for 2.2 μm diameter spheres, and 175% for 3 μm

diameter spheres and the maximum difference is observed in low strain rates. Samples with Al_2O_3 coated layer shows a significantly (between 4 to 11 times) higher yield strength than the noncoated samples. A it is expected samples which were coated by ALD technique displayed a higher strength than the ones which were coated by MLD technique. Figure 7.4 shows the SEM images of the deformed coated samples. Due to the very brittle nature of Al_2O_3, after its cracking the coating layer mainly detaches from the sphere and the load does not increase for a big range of strain increasing after that.
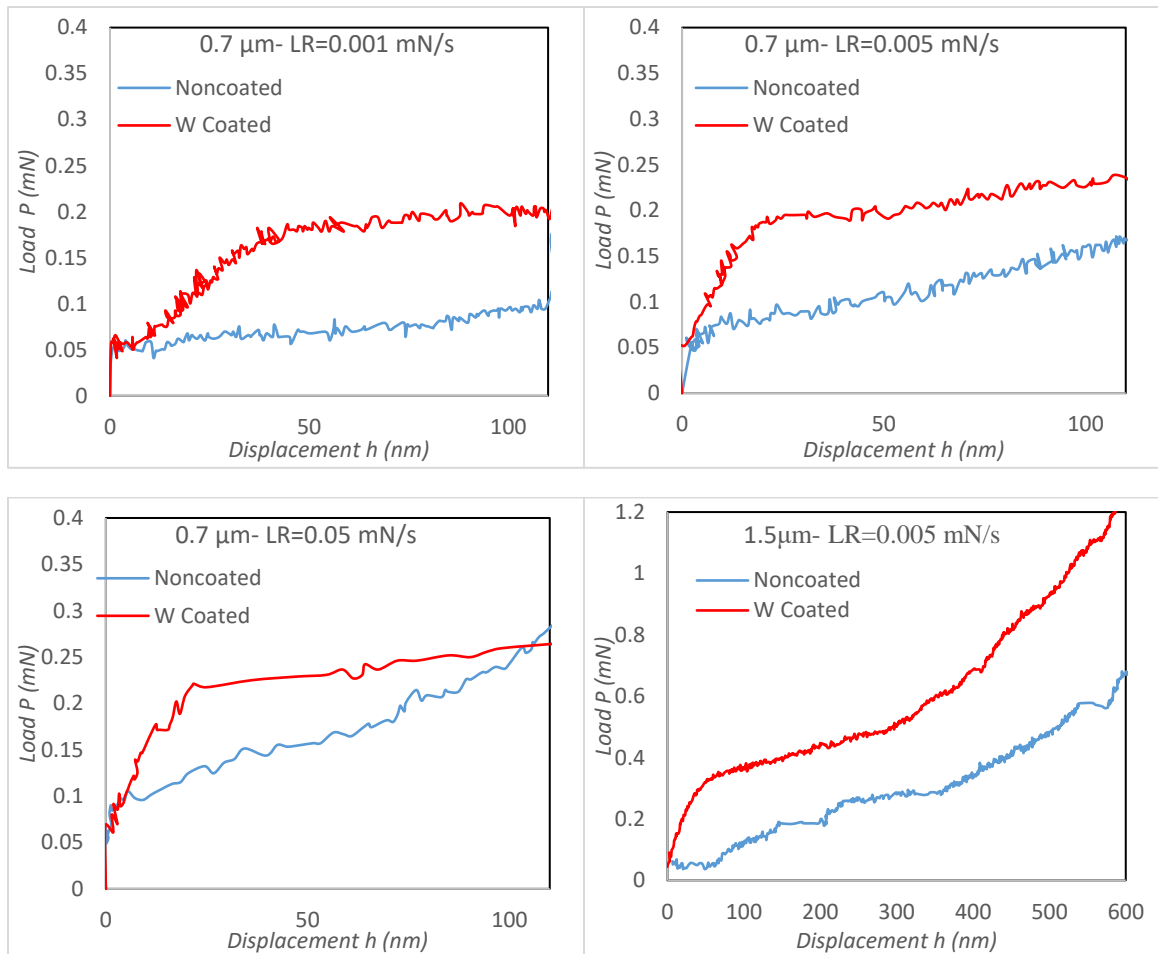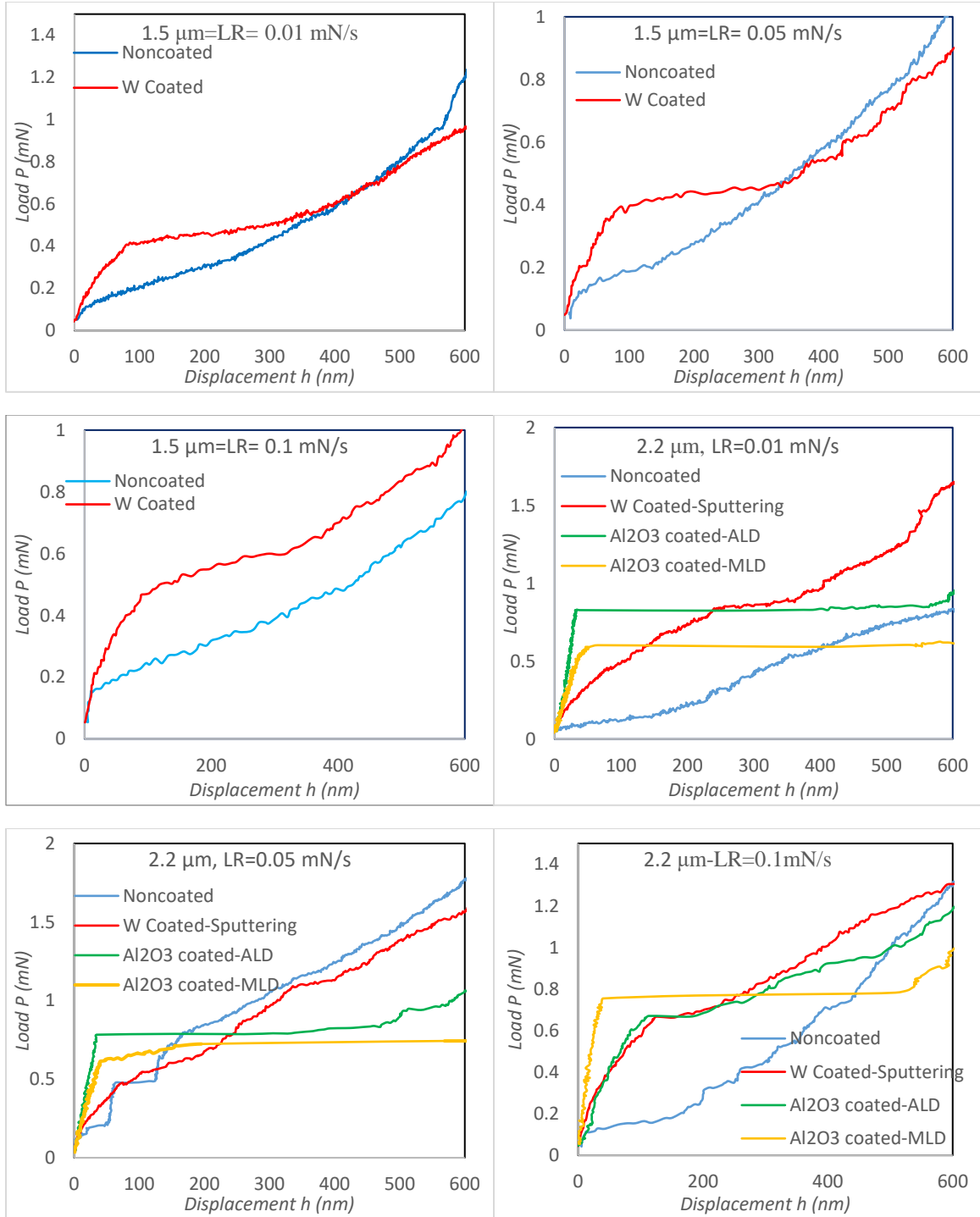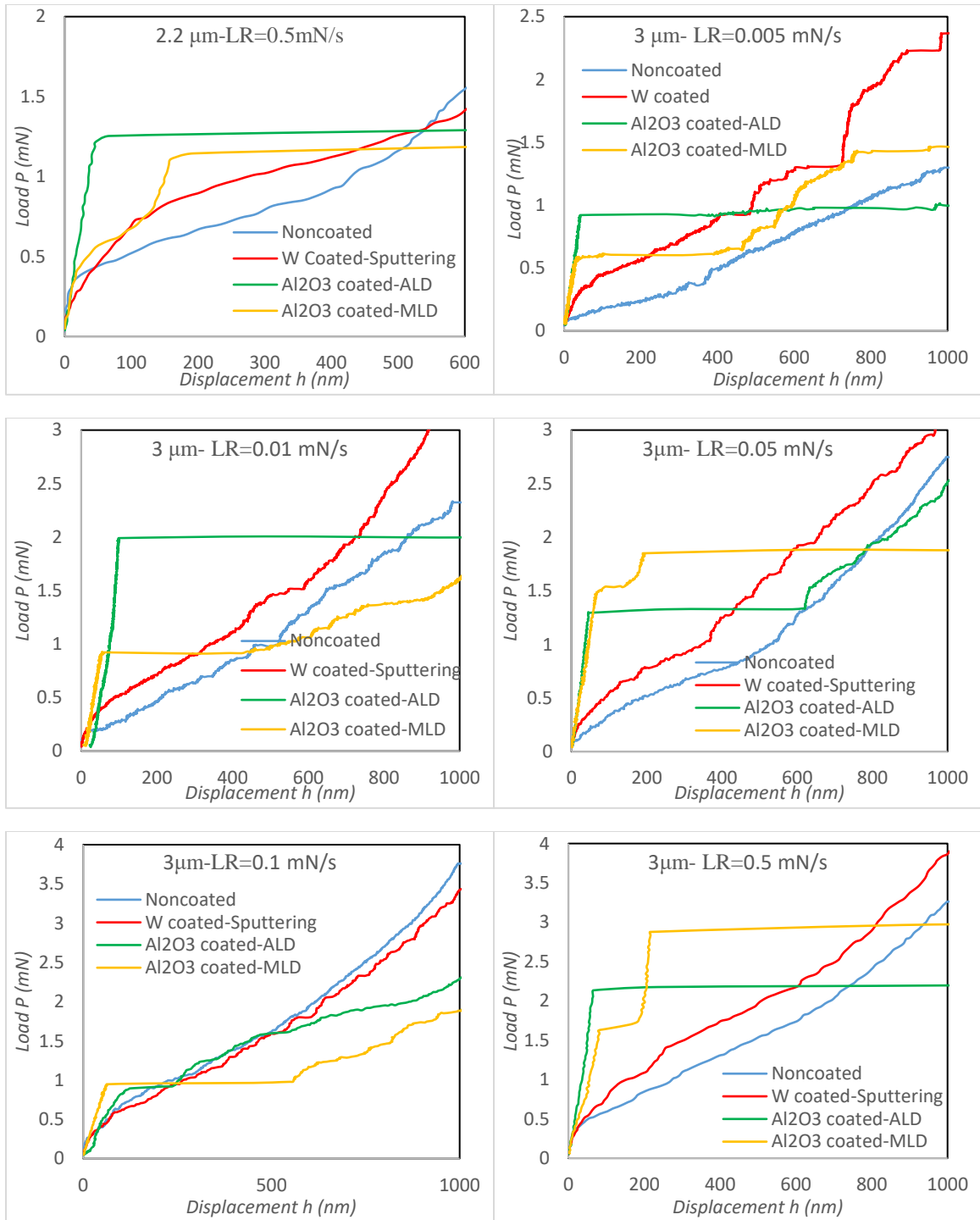
Figure 7.3: Comparison of the behavior of the noncoated and W coated and Al₂O₃ coated samples at different sphere dimeters and loading rates.
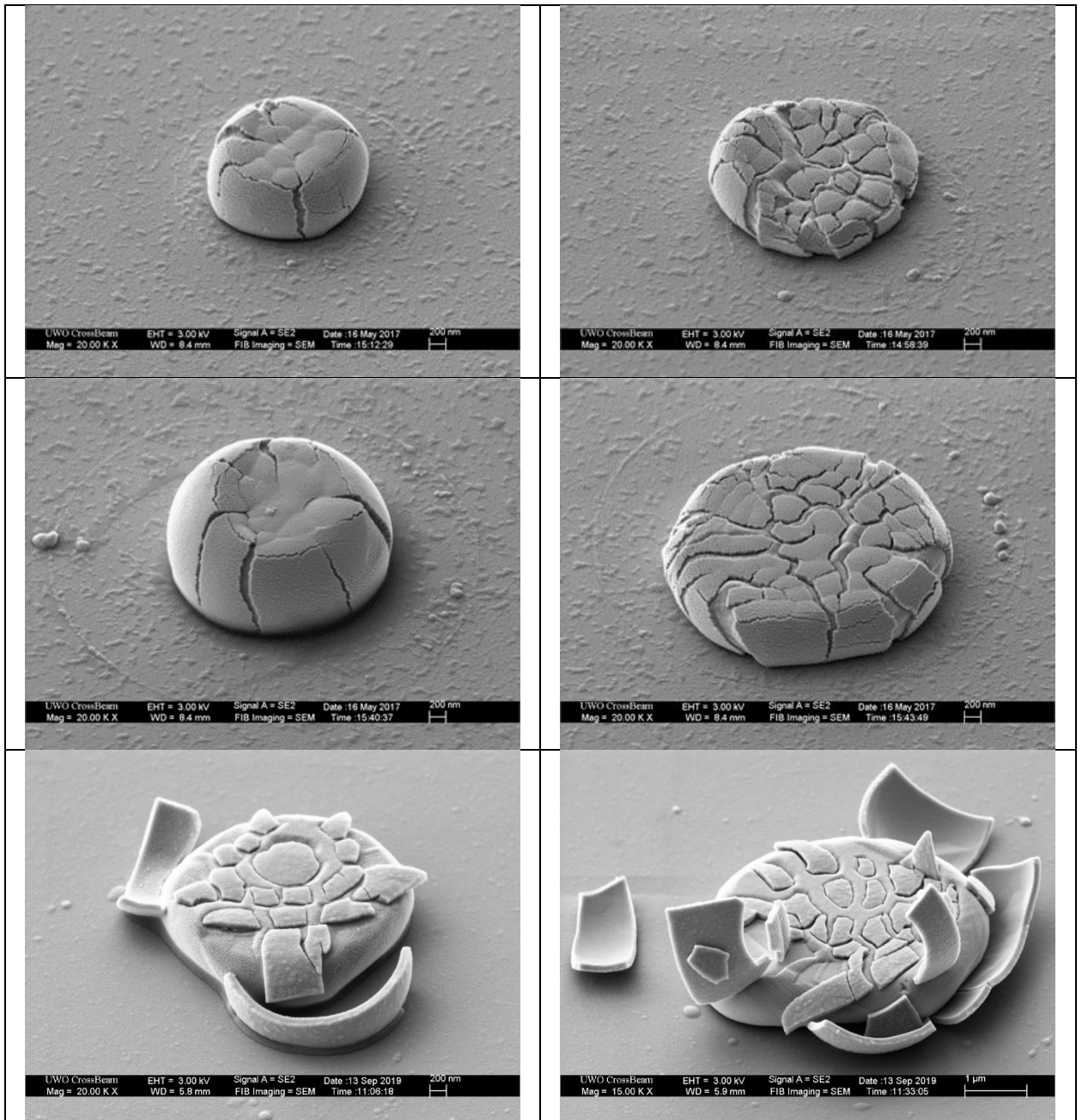
Figure 7.4: . SEM images of the compression a) 1.5 µm W coated sphere after 350 nm compression with 0.05 mN/s loading rate, b) 1.5 µm W coated sphere after 700 nm compression with 0.05 mN/s loading rate, c) 2.2 µm W coated sphere after 500 nm compression with 0.01 mN/s loading rate, d) 2.2 µm W coated sphere after 1000 nm compression with 0.01 mN/s loading rate, e) 2.2 µm Al$_2$O$_3$ coated sphere after 1000 nm compression with 0.005 mN/s loading rate, and f) 3 µm Al$_2$O$_3$ coated sphere after 1400 nm compression with 0.05 mN/s loading rate.

Figure 7.5 shows the strain hardening constant for 4 dimeters of W coated spheres at various strain rates. As it is observed, similar to the results of noncoated sample results (Figure 6.6, chapter 6), the amount of n constant increases as the sphere size increases. This means that the activity of the forest hardening mechanism increases with the diameter of the spheres. Figure 7.6 shows the variation strain rate sensitivity constant (m) at five values of strains for 4 different diameters of W coated spheres.
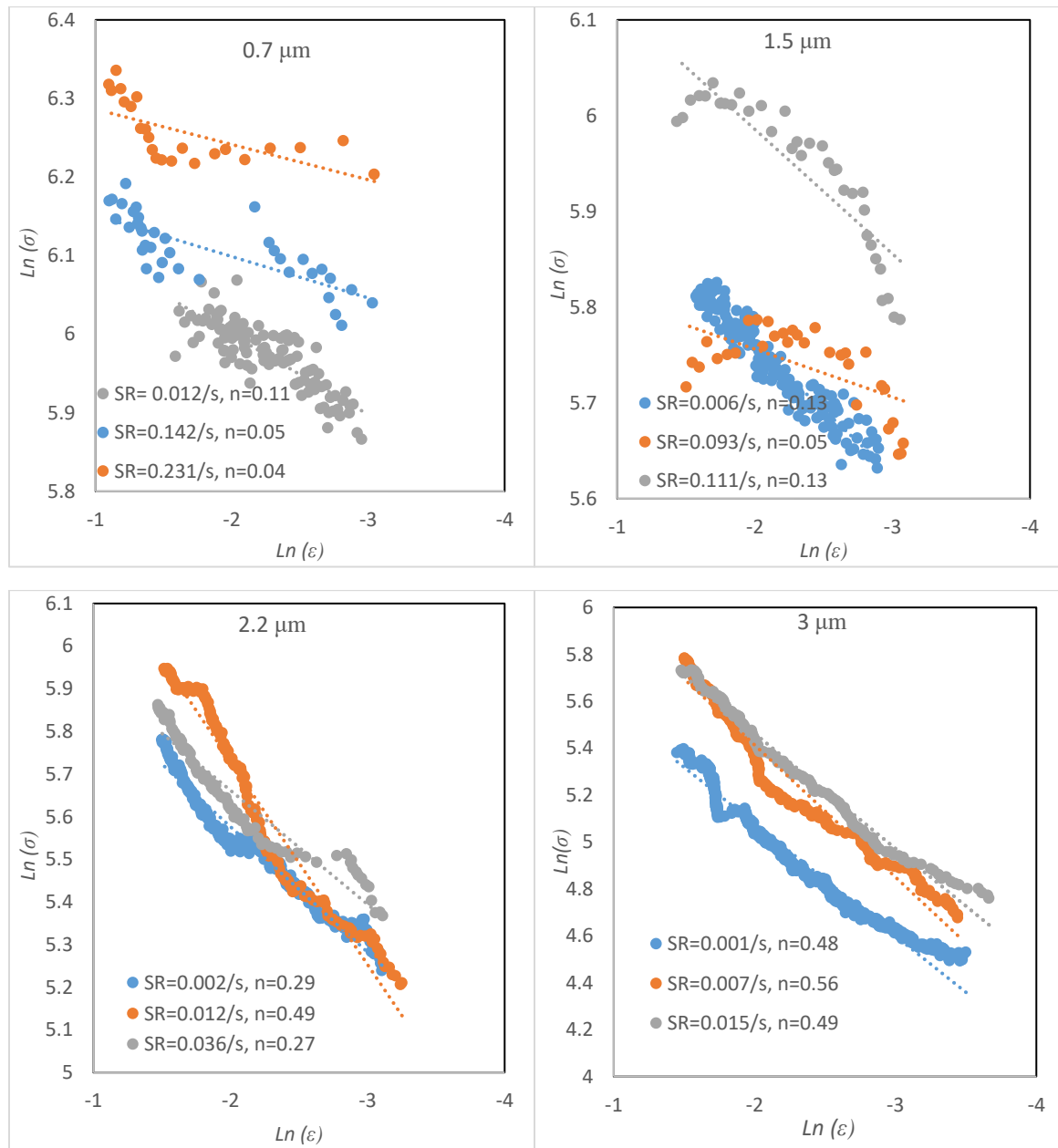
Figure 7.5: Comparing strain hardening constant for different dimeters of W coated spheres.
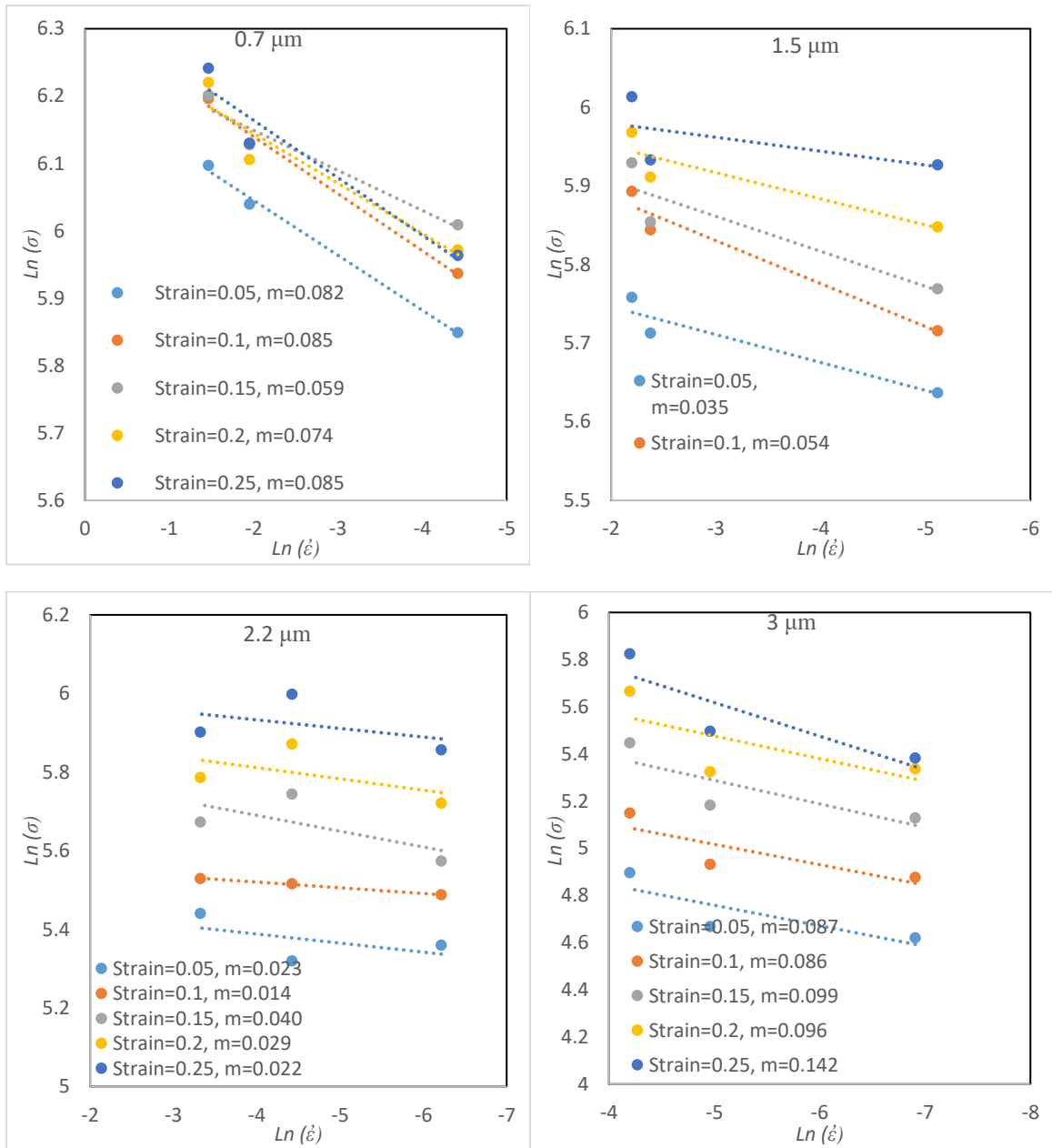
Figure 7.6: Comparing strain rate sensitivity constant for coated spheres with different diameters.

Figure 7.7 summarized the values of strain hardening constant (n) of all the W coated spheres as a function of strain rate. As it is observed the value of strain hardening constant is higher for the bigger spheres and it has the lowest values for the 0.7 μm

sphere. Moreover, the values of n are more strain rate dependent on the bigger sphere diameters.

Figure 7.8 plots the values of strain rate sensitivity constant (m) for all of the considered sphere diameters as a function of strain. It is observed that the value of m is almost constant during the deformation for 0.7 μm, 1.5 μm, and 2.2 μm spheres. However, it increases during the deformation for 3 μm sphere. Comparing these results with the strain rate sensitivity values of the noncoated samples (Figure 6.9, chapter 6), it is clear that the values of m are significantly lower for the coated spheres. As described in chapter 6, the high strain rate sensitivity amounts are related to the activity of surface dislocation sources [23] [24] [25] and the significant decrease of the strain sensitivity in coated samples indicates that the surface dislocation sources are not activated in the coated samples.
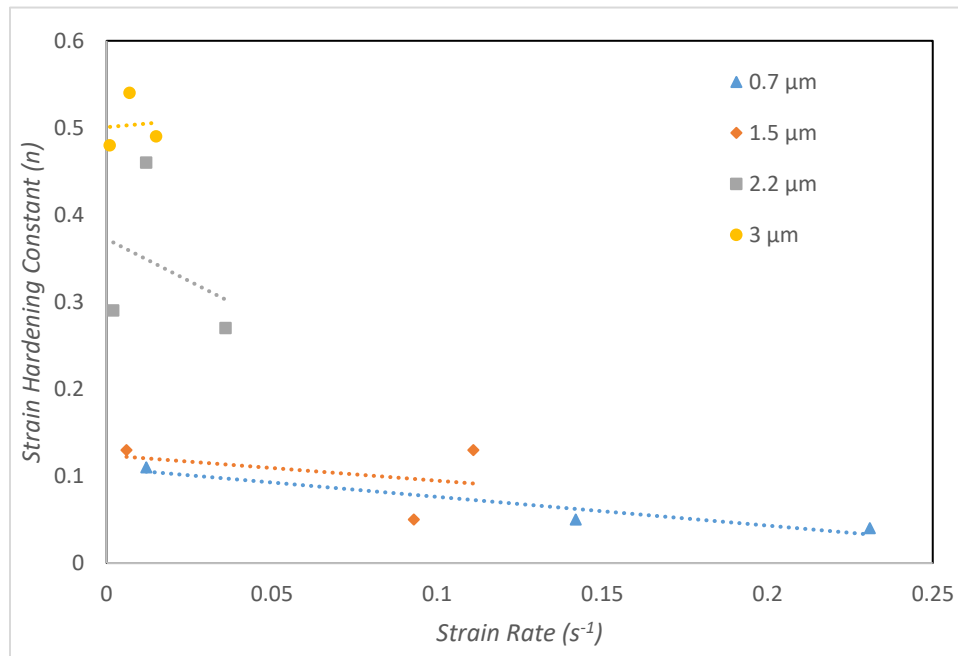
Figure 7.7: Strain hardening constant for the W coated spheres.
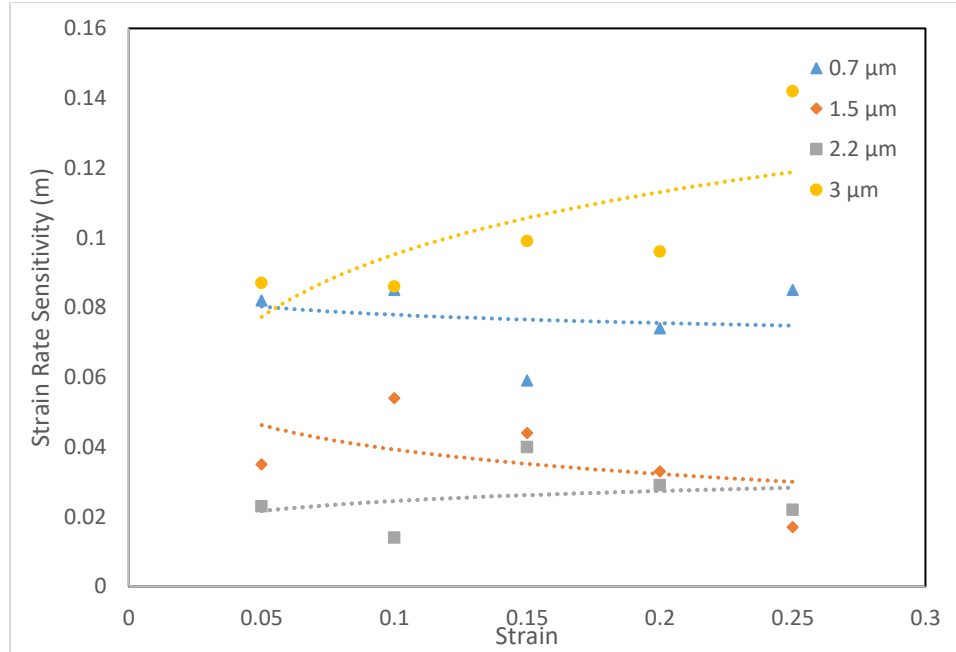
Figure 7.8: Strain rate sensitivity for W coated spheres.

Apparent activation volume, V^*, and apparent activation energy Q^* are calculated for the W coated samples using the equations 6.4 and 6.5, chapter 6. Table 7.1 compares the range of the apparent activation volume energy changes of the coated and noncoated samples. As it is observed the values of V^* increased significantly by having a coating layer. As described in the previous chapter the higher amounts of the V^* is an indication of dislocation-obstacle interaction deformation mechanism [26, 27]. It means that having the coating layer was resulted in confining dislocation in the sphere and not letting them leave the crystal which will increase the dislocation interaction and lead to forest hardening mechanism. It is also worth to note that after the initial yielding cracks appear in the coating layer, but it does not detach from the sphere, otherwise we should have observed big jumps in the load-displacement curves of the coated samples due to the detachment and compression of Au spheres. Thus, the W layer appears to be constraining the annihilation of mobile dislocations from the surface and Au sphere and impeding them to reach the free surface, even after cracking.

Table 7.1: Apparent activation volume ranges for different diameters of W coated and noncoated spheres.

Sphere Diameter	Apparent Activation Volume Range of Noncoated spheres	Apparent Activation Volume Range of coated spheres
0.7 μm	1.6-2.4 b^3	7.8-11.2 b^3
1.5 μm	8.6-10.5 b^3	16.1-46.5 b^3
2.2 μm	9.4-10.2 b^3	31.1-71.6
3 μm	8.9-10.4 b^3	7-26.3

Table 7.2 compares the values of apparent activation energy Q* values of the W coated with noncoated spheres. As discussed in chapter 6, for the amount of Q*<0.2eV, essentially dislocation obstacle strength is weak and the glide of dislocation is controlled by lattice resistance [28]. This is applicable for the 0.7 μm dimeter noncoated spheres. Having a W coating layer on the 0.7 μm spheres results in the Q* to increase over 0.3 eV which is an indication of dislocation-obstacle glide mechanism [28]. The obstacles here are dislocations that are trapped in the sphere due to having the constraining layer. Bigger coated spheres are showing even higher apparent activation energy that suggests the dislocation-dislocation interaction mechanism activation. The distribution of the values of activation energy is displayed in Figure 7.9 for the coated and noncoated samples.

Table 7.2: Apparent activation energy ranges for different diameters of W coated and noncoated spheres.

Sphere Diameter	Activation Energy Range of Noncoated spheres (eV)	Activation Energy Range of coated spheres (eV)
0.7 μm	0.062-0.091	0.297-0.430
1.5 μm	0.331-0.401	0.617-1.776
2.2 μm	0.361-0.386	0.925-2.732
3 μm	0.342-0.398	0.270-1.004
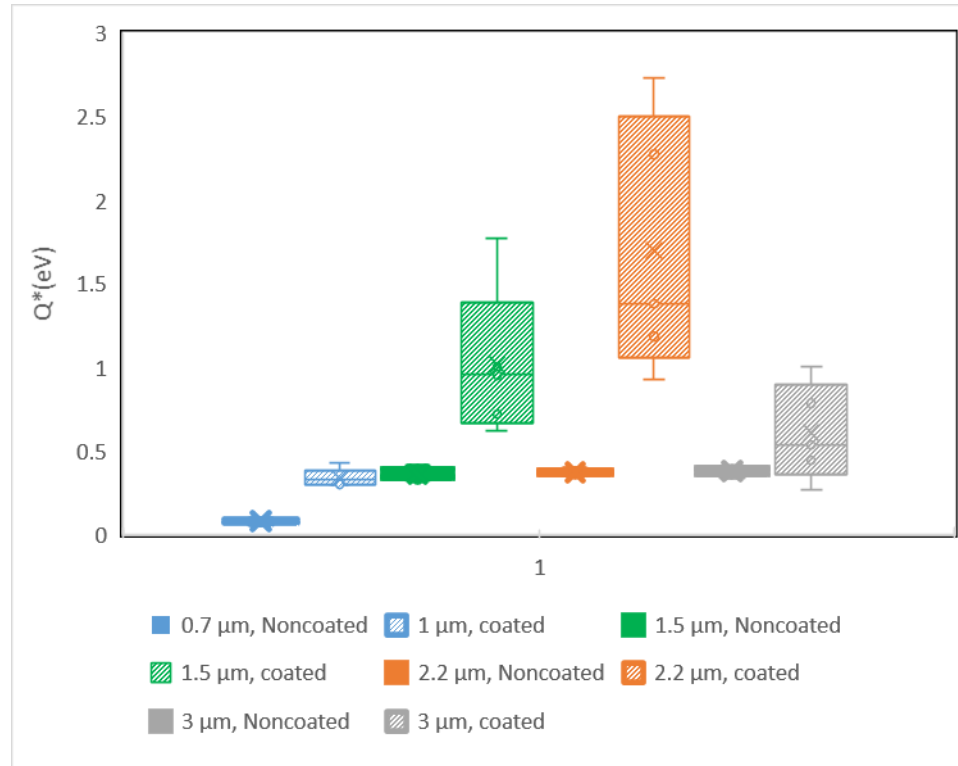
Figure 7.9: Comparing the range of apparent activation energy for the W coated and noncoated samples.

Conclusions

Single crystalline Au spheres with the dimeters of 0.7 μm to 3 μm were coated by a 60 nm constraining layer to investigate the effect of the confining layer on the dislocation surface nucleation and exhaustion mechanisms. The sputtering technique was used to deposit a 80 nm of W layer and ALD and MLD techniques were used to deposit a 60nm layer of Al_2O_3. Having the coated layer resulted to a significant increase in the sphere strength. Samples with ALD 60 nm Al_2O_3 coated layer showed up to 11 times higher yield strength than the noncoated samples. Cracking the Al_2O_3 layer due to its high brittality results to the creep like behavior in the plastic zone deformation of spheres. W layer coated samples also showed a significantly higher strength than the noncoated samples in all the strain rates.

Activation volume, V* increased significantly by having W coating layer on the 0.7 μm, from 1.6-2.4 b^3 to 7.8-11.2 b^3 which indicates that the operating mechanism is changed to

the dislocation-obstacle mechanism. This increase of V* is also observed for the bigger spheres and it reaches the values of 46 b^3 and 71 b^3. Values of apparent activation energy changed from 0.062-0.091 (eV) to 0.297-0.430 (eV) for the 0.7 μm spheres by having the W coating layer which again reflects the activation of dislocation-obstacle mechanism in the samples with constraining layer. The big difference of the V* and Q* values for the coated and noncoated 0.7 μm diameter sphere means that having the 80nm W layer should have changed the deformation mechanism and it means that the 0.7 μm noncoated sample deformed in a mechanism which is based on the effect of the surface dislocation nucleations. These results approve the developed theories in the size-dependent plasticity area that relates the different mechanical properties of submicron-sized materials to the activation of surface dislocation nucleation and annihilation mechanisms.

References

[1] M.D. Uchic, D.M. Dimiduk, J.N. Florando, W.D. Nix, Sample dimensions influence strength and crystal plasticity, Science 305(5686) (2004) 986-989.

[2] J.R. Greer, W.C. Oliver, W.D. Nix, Size dependence of mechanical properties of gold at the micron scale in the absence of strain gradients, Acta Mater 53(6) (2005) 1821-1830.

[3] J.R. Greer, W.D. Nix, Nanoscale gold pillars strengthened through dislocation starvation, Phys Rev B 73(24) (2006).

[4] C.A. Volkert, E.T. Lilleodden, Size effects in the deformation of sub-micron Au columns, Philos Mag 86(33-35) (2006) 5567-5579.

[5] E. Rabkin, H.S. Nam, D.J. Srolovitz, Atomistic simulation of the deformation of gold nanopillars, Acta Mater 55(6) (2007) 2085-2099.

[6] H. Tang, K.W. Schwarz, H.D. Espinosa, Dislocation escape-related size effects in single-crystal micropillars under uniaxial compression, Acta Mater 55(5) (2007) 1607-1616.

[7] C.R. Weinberger, W. Cai, Surface-controlled dislocation multiplication in metal micropillars, P Natl Acad Sci USA 105(38) (2008) 14304-14307.

[8] J.Y. Kim, J.R. Greer, Size-dependent mechanical properties of molybdenum nanopillars, Appl Phys Lett 93(10) (2008).

[9] Z.W. Shan, R.K. Mishra, S.A.S. Asif, O.L. Warren, A.M. Minor, Mechanical annealing and source-limited deformation in submicrometre-diameter Ni crystals, Nat Mater 7(2) (2008) 115-119.

[10] S. Brinckmann, J.Y. Kim, J.R. Greer, Fundamental differences in mechanical behavior between two types of crystals at the nanoscale, Phys Rev Lett 100(15) (2008).

[11] R.C. Cammarata, Surface and Interface Stress Effects in Thin-Films, Prog Surf Sci 46(1) (1994) 1-38.

[12] C.L. Kelchner, S.J. Plimpton, J.C. Hamilton, Dislocation nucleation and defect structure during surface indentation, Phys Rev B 58(17) (1998) 11085-11088.

[13] S.W. Lee, A.T. Jennings, J.R. Greer, Emergence of enhanced strengths and Bauschinger effect in conformally passivated copper nanopillars as revealed by dislocation dynamics, Acta Mater 61(6) (2013) 1872-1885.

[14] J.R. Greer, Effective Use of Focused Ion Beam (FIB) in Investigating Fundamental Mechanical Properties of Metals at the Sub-Micron Scale, MRS Proceedings 983 (2011) 0983-LL08-03.

[15] K.S. Ng, A.H.W. Ngan, Effects of trapping dislocations within small crystals on their deformation behavior, Acta Mater 57(16) (2009) 4902-4910.

[16] A.T. Jennings, C. Gross, F. Greer, Z.H. Aitken, S.W. Lee, C.R. Weinberger, J.R. Greer, Higher compressive strengths and the Bauschinger effect in conformally passivated copper nanopillars, Acta Mater 60(8) (2012) 3444-3455.

[17] C. Zhou, S. Biner, R. LeSar, Simulations of the effect of surface coatings on plasticity at small scales, Scripta Mater 63(11) (2010) 1096-1099.

[18] S.-W. Lee, A.T. Jennings, J.R. Greer, Emergence of enhanced strengths and Bauschinger effect in conformally passivated copper nanopillars as revealed by dislocation dynamics, Acta Mater 61(6) (2013) 1872-1885.

[19] J.A. El-Awady, S.I. Rao, C. Woodward, D.M. Dimiduk, M.D. Uchic, Trapping and escape of dislocations in micro-crystals with external and internal barriers, Int J Plasticity 27(3) (2011) 372-387.

[20] D. Mordehai, S.W. Lee, B. Backes, D.J. Srolovitz, W.D. Nix, E. Rabkin, Size effect in compression of single-crystal gold microparticles, Acta Mater 59(13) (2011) 5202-5215.

[21] S.W. Lee, D. Mordehai, E. Rabkin, W.D. Nix, Effects of focused-ion-beam irradiation and prestraining on the mechanical properties of FCC Au microparticles on a sapphire substrate, J Mater Res 26(14) (2011) 1653-1661.

[22] S.G. B. Beake, S. Jones, R. Parkinson, N. Pickford, L. Roberts, and J. Smith, NanoTest Help File, in: M.M. Ltd (Ed.) 2004.

[23] A.T. Jennings, J. Li, J.R. Greer, Emergence of strain-rate sensitivity in Cu nanopillars: Transition from dislocation multiplication to dislocation nucleation, Acta Mater 59(14) (2011) 5627-5637.

[24] T. Zhu, J. Li, A. Samanta, A. Leach, K. Gall, Temperature and Strain-Rate Dependence of Surface Dislocation Nucleation, Phys Rev Lett 100(2) (2008) 025502.

[25] A.S. Schneider, B.G. Clark, C.P. Frick, P.A. Gruber, E. Arzt, Effect of orientation and loading rate on compression behavior of small-scale Mo pillars, Materials Science and Engineering: A 508(1) (2009) 241-246.

[26] U.F. Kocks, A.S. Argon, M.F. Ashby, Thermodynamics and Kinetics of Slip, Prog Mater Sci 19 (1975) 1-281.

[27] Y.M. Wang, A.V. Hamza, E. Ma, Activation volume and density of mobile dislocations in plastically deforming nanocrystalline Ni, Appl Phys Lett 86(24) (2005).

[28] H.J. Frost, M.F. Ashby, Deformation-mechanism maps : the plasticity and creep of metals and ceramics, Pergamon Press, Oxford [Oxfordshire]; New York, 1982.

Chapter 8

8.   Conclusions

The primary aim of this study was to use simulation and nanomechanical testing techniques to understand the mechanisms of small scale plastic deformation of face center cubic (fcc) crystal structure metals. An atomistic view is presented using molecular dynamics simulations to investigate the dependence of incipient plasticity and governing size-dependent deformation mechanisms on the main microstructural properties of the fcc metals such as crystal orientation, grain boundaries, dislocation density and free surfaces. The following conclusions can be drawn based on our results;

Our simulation results of the incipient plasticity of fcc single crystals in the nanoindentation process in presence and absence of primary defects shows that size effect is initially controlled by homogeneous nucleation of dislocations, growth, and development of stacking faults, formation, and glide of V-shape locks, development, and interaction of loops and emission of prismatic dislocation loops along the free surface or into the crystal. As the indentation depth increases, the dislocation length and density in the plastic zone and sources of nucleation increase which will result in material strength decrease. This will lead to the activation of dislocation interaction mechanisms at higher indentation depths rather than dislocation nucleation and source exhaustion. Strongest dependence of indentation on surface orientation is observed after the onset of plasticity when loops are nucleated in result of different rates of loop emissions and thus load relaxation rates for various orientation. This dependency decreases as the dislocation density increases and forest hardening mechanisms become dominant. The evolution of dislocation structure is different for the three considered orientations and is the reason of differences in the load-displacement curve. The dislocation length and density within the nanoindentation plastic zone are highly variable during the initial stage of the deformation process. When the nanoindentation depth is greater than about 2 nm the dislocation density becomes less variable and the indentation hardness H is directly proportional to $\sqrt{\rho}$ thus conforming to the classical Taylor hardening expression for yield

stress as a linear function of $\sqrt{\rho}$ where its coefficient $\square$ is dependent upon crystal orientation. The size of the plastic zone is strongly dependent upon the crystal orientation of the indented surface and is smaller for [001] orientation than those of [110] and [111] orientations. Unlike what has been previously assumed, the relation between the plastic zone size and the indentation contact radius is not constant and changes with indentation depth up to 4 nm. The sensitivity of crystal yield point to the pre-existing faults depends on the crystallographic orientation. An immediate plastic deformation without pop-in behavior was observed in the nanoindentation [001]-oriented sample with pre-existing faults. Pre-existing defects can either result in one significant yield event ([110]-oriented sample) or initiate a series of tiny events before one big discontinuity in the load-displacement curve ([001]-oriented sample). As with tests performed on pristine Au crystals, nanoindentation performed on crystals with pre-existing stacking fault defects also displayed indentation hardness H which conforms to the classical Taylor hardening expression for yield stress as a linear function of $\sqrt{\rho}$ however, the presence of the stacking fault defects increases the variability of the coefficient *A* for the crystal orientations studied. These results and analyses provide new information useful in the development of dislocation-based continuum theories. It must be noted however that the atomistic simulations performed were, by necessity, conducted under exceptionally high indentation loading rates and associated high strain rates. The effect of strain rate on the operative mechanisms of the plasticity of nanometer-scale volumes of ductile metals remains an area still to be studied.

Based on our results in chapter 2, the incipient yield occurs at a lower load in all the bicrystals than for a perfect crystal. However, the yield mechanisms vary considerably for the different grain boundaries. The smallest effect was observed for the coherent $\Sigma 3(111)$ twin boundary and this is consistent with its simple structure and low GB energy. The results of the slip-GB interaction show that the transmission of lattice dislocation across the GB introduces a step at the GB plane due to the different orientations of the adjacent grains. The effect of the GB on the indentation force – depth response decreases with increasing indentation depth. When the indentation depth was greater than about 3.5 nm the bicrystal samples presented the same force-depth response as the single crystals.

Intrinsic stacking faults and dissociated high-energy GB interface structures resulted in dislocation nucleation at GBs in the early stages of deformation. The larger free volume of E units in the structure of GBs with $\theta > 109.5^\circ$ leads to the higher boundary energy and provides sufficient room for rearranging GB atoms during deformation to nucleate dislocations and accommodate local deformation. A strong exponential correlation was observed between the interfacial boundary energy and its effect on the bicrystal strength. More stable structures present closer behavior to single-crystal samples and require higher stress for dislocations to cross, or nucleate at, the grain boundary.

Our investigation on the size and crystallographic orientation effects on the deformation behavior and microstructural evolution of fcc single-crystal nanopillars showed that the yielding of defect-free nanopillars started with the nucleation and propagation of partial dislocations from the free surface and the crystal orientation affects the subsequent microstructural evolution and flow behavior. A significant difference is observed in the strength of pillars of the same size with different orientations. [111]-oriented nanopillars displayed the highest yield strength between the considered orientations. The deformation mechanism of defect-free nanopillars is strongly orientation dependent. For the [100]-oriented samples stacking faults bounded by partial dislocations and glide of micro-twins boundaries is the dominant deformation mechanism, whereas [110] and [111]-oriented nanopillars deformed by dislocation slip mechanism. Based on the results the Schmid factor of leading and trailing partials plays a decisive role in leading to the twinning deformation or slip deformation. Annihilation of dislocations at the surface of nanopillars after deformation leads to the dislocation starvation mechanism activation in all the three considered orientations. Nucleation of new dislocations from the surface is required to activate new micro-twins or slip systems to sustain the deformation in the dislocation starved situation. Dislocation exhaustion rate depends on the nanopillar size and larger nanopillars showed lower exhaustion rate regardless of orientation. Frequent dislocation interactions in orientations with more primary slip systems ([100] and [111]) resulted in the later activation of dislocation starvation mechanism while the less chance of dislocation interaction in orientations with fewer slip systems ([110] orientation in our study) resulted to the higher exhaustion rate and sooner domination of dislocation starvation mechanism. The more serrated and fluctuating post-yield flow response of the

[110] nanopillars is also in result of the less resident time of dislocations due to the fewer dislocation interactions. The high symmetry of [111] orientation resulted in the activation of a high density of dislocation loops which their interaction lead to the less serrated stress-strain response than the other two orientations. The effect of orientation on strength decreases as the pillar diameter increases. The power-law equation exponent is completely dependent on the crystal orientations and a week or no size effect was observed in the compression of [100] and [110] oriented Au and Pt pillars with sizes less than 40 nm. The results of the compression of pillars with rigid constraining layers showed that in the absence of free surface the nucleation of initial dislocations happens in much higher stress and trapping of dislocations in the pillar results in a smooth increase of stress with strain. The compression of rigid coated and Pt coated nanopillars show that the observed orientation based behaviour and size scale effects decrease by confining the free surface.

Our microcomression experiments on the of sub-micron and micron-sized (0.7 – 3 μm) Au spheres showed that the dependence of the flow stress to the strain and strain rate is slightly affected by the sphere diameter size. Size-dependent behavior was observed in the compression of spheres with different diameters and the submicron spheres presented significantly higher strength than the larger spheres at all of the loading rates. Moreover, increasing the rate of deformation resulted in a higher deformation stress for all of the considered sphere diameters. The results of the calculated apparent activation volume V* and apparent activation energy Q* shows that the deformation mechanism of the smallest spheres (0.7μm diameter) is controlled mainly by dislocation nucleation from free surfaces. The values of V* and Q* for the larger spheres indicate that obstacle limited dislocation glide, which is the typical mechanism in bulk scale deformation of fcc metals, is the operative deformation process for these spheres.

Having the coated layer on the Au spheres resulted in a significant increase in the sphere strength. Samples with 60 nm Al_2O_3 coated layer showed up to 11 times higher yield strength than the noncoated samples. Cracking the Al_2O_3 layer due to its high brittality results in the creep like behavior in the plastic zone deformation of spheres. W layer

coated samples also showed significantly higher strength than the noncoated samples in all the strain rates.

Activation volume, V* increased significantly by having W coating layer on the 0.7 μm, from 1.6-2.4 b^3 to 7.8-11.2 b^3 which indicates that the operating mechanism is changed to the dislocation-obstacle mechanism. This increase of V* is also observed for the bigger spheres and it reaches the values of 46 b^3 and 71 b^3. Values of apparent activation energy changed from 0.062-0.091 (eV) to 0.297-0.430 (eV) for the 0.7 μm spheres by having the W coating layer which again reflects the activation of dislocation-obstacle mechanism in the samples with constraining layer. The big difference of the V* and Q* values for the coated and noncoated 0.7 μm diameter sphere means that having the 80nm W layer should have changed the deformation mechanism and it means that the 0.7 μm noncoated sample deformed in a mechanism which is based on the effect of the surface dislocation nucleations. These results approve the developed theories in the size-dependent plasticity area that relates the different mechanical properties of submicron-sized materials to the activation of surface dislocation nucleation and annihilation mechanisms.

Presented results will lead to a more accurate understanding of the behavior of submicron and nanosized materials such as thin films, micro/nanoparticles, micro/nanodots, micro/nanocoatings, and micro/nanowires. Potential benefits include better understanding and development of new micro and nanotechnology areas such as micro and nanoelectromechanical systems (MEMS) and (NEMS). The better understanding of small scale plasticity will have a significant contribution to the scientific knowledge of plasticity and will affect a broad range of technologies in many industries such as manufacturing and production, and energy.

Curriculum Vitae

Name: Mahdi Bagheripoor

Post-secondary   Iran University of Science & Technology
Education and   Tehran, Iran
Degrees: 2003-2007 B.Sc.

Iran University of Science & Technology
Tehran, Iran
2007-2009 M.Sc.

The University of Western Ontario
London, Ontario, Canada
2015-2020 Ph.D.

Honours and   PSAC 610 Academic Achievement Scholarship
Awards: 2016

Related Work   Teaching Assistant
Experience   The University of Western Ontario
2015-2020

Publications:
Journal papers

- M. Bagheripoor, R.J. Klassen, "The effect of crystal anisotropy and pre-existing defects on the incipient plasticity of FCC single crystals during nanoindentation", Mechanics of Materials, Under review.

- M. Bagheripoor, R.J. Klassen, "The effect of grain boundary on the local incipient plastic deformation of FCC metals during nanoindentation", Computational Materials Science, Under review.

- M. Bagheripoor, R.J. Klassen, "The effect of crystal orientation on the size effects of nano-scale fcc metals", International Journal of Plasticity, Under review.

- M. Bagheripoor, R.J. Klassen, "Length Scale Plasticity: A Review from the Perspective of Dislocation Nucleation", Reviews on Advanced Materials Science 56 (2018) 21-61.

- K.P. Rao, M. Bagheripoor, H. Dieringa, N. Hort, "High Temperature Deformation of Cast ZW11 Magnesium Alloy with Very Large Grain Size", Key Engineering Materials, Vol. 725, 2017, pp.

232-237.

- M. Bagheripoor, H. Bisadi, "An investigation on the roll force and torque fluctuations during hot strip rolling process", Production & Manufacturing Research (Taylor & Francis), Vol. 2, Issue 1, 2014, pp. 128-141.

- M. Bagheripoor, H. Bisadi, "Application of artificial neural networks for the prediction of roll force and roll torque in hot strip rolling Process", Applied Mathematical Modelling (Elsevier), Vol. 37, Issue 7, 2013, pp. 4593-4607.

- M. Bagheripoor, H.Bisadi, "Effects of rolling parameters on temperature distribution in the hot rolling of aluminum strips", Applied Thermal Engineering (Elsevier), Vol. 31, Issue 10, 2011, pp. 1556-1565.

Conference peresentations

- M. Bagheripoor, R.J. Klassen, The effect of grain boundaries on the small-scale plasticity, 31ST Canadian Materials Science Conference, Vancouver, Canada, 10-13 June 2019.

- M. Bagheripoor, R.J. Klassen, Crystal orientation effect on the incipient plasticity of the thin film, CSME 2019, London, Canada, 2-5 June 2019.

- R.J. Klassen, A.Z.M. Ariful Islam, M. Bagheripoor, Role of Surfaces on the Length-scale Dependence of the Incipient Yield Stress of Ductile Metals, Materials Science & Technology 2018, Columbus, USA, 14-18 October 2018.

- R.J. Klassen, A.Z.M. Ariful Islam, M. Bagheripoor, Role of dislocation nucleation on the length-scale dependence of the incipient yield stress of ductile metals, 30th Canadian Material Science Conference, Edmonton, Canada, 19-22 June 2018.

- K.P. Rao, M. Bagheripoor, H. Dieringa, N. Hort, "High temperature deformation processing of dilute magnesium alloy Z1 for bioimplant application", The 9th Pacific Rim International Conference on Advanced Materials and Processing (PRICM9), Kyoto, Japan, 1 - 5 August 2016

- M. Bagheripoor, H. Bisadi, "Grain refinement of aluminum plates by equal-channel angular rolling process",2nd Conference on Applications of Nanotechnology in Sciences, Engineering and Medicine, NTC2011, 16-17 May, 2011, Mashhad, Iran.

- H. Bisadi, M. Bagheripoor, "An Investigation of microstructural evolutions during the hot rolling of aluminum alloys with the aid of finite element method", 11th Iranian Conference on Manufacturing Engineering, ICME 2010, 19-21 Oct, 2010, Tabriz, Iran.

- M. Bagheripoor, H. Bisadi,"Analysis of material deformation behavior in hot flat rolling process with the FEM approach", 11th Iranian Conference on Manufacturing Engineering, ICME 2010, 19-21 Oct, 2010, Tabriz, Iran.

- M. Bagheripoor, H. Bisadi, "An investigation on deformation behavior of pure aluminum during equal channel angular pressing process with the aid of finite element method", 4th Joint Conference of Iranian Metallurgical Engineering Society and Iranian Foundrymen,15-16 Nov, 2010, Tehran, Iran.

- M. Bagheripoor, H. Bisadi, prediction of Recrystallization kinetics in AISI 304 austenitic

stainless steel during and after hot rolling", 4th Joint Conference of Iranian Metallurgical Engineering Society and Iranian Foundrymen, 15-16 Nov, 2010, Tehran, Iran.

- M. Bagheripoor, H. Bisadi, "Roll force and Torque prediction in the hot rolling of aluminum alloys using neural networks ", 19th Annual Conference on Mechanical Engineering, ISME2011, 10-12 May, 2011, Birjand, Iran.

- M. Bagheripoor, H. Bisadi, "Prediction of temperature evolution during hot flat rolling of aluminum alloys", 10th Iranian Conference on Manufacturing Engineering, ICME 2010, 1-3 Mar, 2010, Babol, Iran.

- H. Bisadi, M. Bagheripoor, H. Rezaei, "An investigation on strain inhomogeneity during hot strip rolling of aluminum alloys using finite elements method", 10th Iranian Conference on Manufacturing Engineering, ICME 2010,1-3 Mar, 2010, Babol, Iran.

- H. Bisadi, M. Bagheripoor, H. Rezaei, "Computer simulation of the thermal behaviour of a work roll during hot rolling of steel strips", 10th Iranian Conference on Manufacturing Engineering, ICME 2010,1-3 Mar, 2010, Babol, Iran.

- H. Rezaei, H. Bisadi, M. Bagheripoor, "Efficient eulerian or Lagrangian formulation in the finite element analysis of hot rolling", 10th Iranian Conference on Manufacturing Engineering, ICME 2010, 1-3 Mar, 2010, Babol, Iran.

- M. Bagheripoor, H. Bisadi, "Microstructural development during equal channel angular pressing of aluminium alloys", 2nd Conference in the Manufacturing Engineering, NMEC2009, 28-29 Oct, 2009, Najafabad, Iran.